SPECTROSCOPY AND PHOTOMETRY OF SCATTERED LIGHT ECHOES FROM SUPERNOVAE

SPECTROSCOPY AND PHOTOMETRY OF SCATTERED LIGHT ECHOES FROM SUPERNOVAE

By

BRENDAN SINNOTT, B.Sc.

A Thesis
Submitted to the School of Graduate Studies
in Partial Fulfillment of the Requirements
for the Degree
Doctor of Philosophy

McMaster University

DOCTOR OF PHILOSOPHY (2013)
(Physics and Astronomy)

McMaster University
Hamilton, Ontario

TITLE: Spectroscopy and Photometry of Scattered Light Echoes from Supernovae

AUTHOR: Brendan Sinnott, B.Sc.(University of Toronto)

SUPERVISOR: Professor Douglas Welch, Professor Peter Sutherland

NUMBER OF PAGES: xix, 235

Abstract

We present an observational protocol to observe and interpret asymmetries in stellar explosions using scattered light echoes. Spectroscopy of multiple light echoes are used to observe single astronomical sources from multiple viewing angles, allowing for direct observations of explosion asymmetries, when they exist. We present asymmetry detections for two famous historical supernovae: the ∼25-year-old SN 1987A and the ∼330-year-old Cassiopeia A. In both supernovae we find asymmetries in the first few hundred days of the explosion that appear to be correlated with the geometry of Fe-rich material in the remnant states.

Spectroscopy of SN 1987A light echoes reveals a variation in the Hα line profile as a function of echo azimuth, with maximum asymmetry at position angles 16° and 186°, in agreement with the major-axis of the elongated remnant ejecta. We interpret our asymmetry detection as evidence for a two-sided distribution of high-velocity ^{56}Ni in the first few hundred days of SN 1987A, with the most dominant asymmetry redshifted in the south. For Cassiopeia A, we find evidence for a $\sim$ 4000 km s^{-1} velocity excess in the first hundred days of the explosion, roughly aligned with an Fe-rich outflow in the supernova remnant and approximately opposite in direction to the motion of the compact object.

Core-collapse supernovae have not yet been successfully modelled despite decades of progress in input physics and computing capability. Despite the significance of thermonuclear Type Ia supernovae to cosmology, the progenitor systems and explosion details also remain unclear. Both observational and theoretical work suggest that non-spherical effects are not only common in supernovae, but may in fact aid in generating successful explosions. In addition to offering a new technique for observing supernova asymmetries, spectroscopy of scattered light echoes allows a direct causal connection to be made between stellar explosions and their observed remnant states.

Preface

This thesis includes three previously published articles in Chapters 4, 5, and 6. The references of these publications appear below, as do my specific contributions to each publication.

Chapter 4 originally appeared as "On the Interpretation of Supernova Light Echo Profiles and Spectra" in The Astrophysical Journal as

> "Rest, A., Sinnott, B., Welch, D. L., Foley, R. J., Narayan, G., Mandel, K., Huber, M. E., and Blondin, S. The Astrophysical Journal, **732**, 2 (2011)."

I reduced and analyzed the SN 1987A observations presented in Section 4.5 (as it appears in this thesis), and wrote all text and created the four figures in that section. The idea for the paper was the outcome of analysis on my previous thesis work of SN 1987A, and the model was developed in collaboration with A. Rest during my research visit to Harvard in 2010. I created the portion of the analysis pipeline which performs the data measurements for the paper. A. Rest created the portion of the pipeline that fits the model to the measurements. I was responsible for running the model under many conditions to probe different regions of parameter space, generating the data for roughly half of the 22 included figures. A. Rest was the primary author of the manuscript text, with contributions from all co-authors. D. L. Welch contributed to the manuscript text and helped with guiding the development of the model. R. J. Foley reduced the Cas A spectra and helped contribute to the manuscript.

Chapter 5 originally appeared as "Asymmetry in the Outburst of SN 1987A Detected Using Light Echo Spectroscopy" in The Astrophysical Journal as

> "Sinnott, B., Welch, D. L., Rest, A., Sutherland P. G., and Bergmann, M. The Astrophysical Journal, **767**, 45 (2013)."

I was the primary author of all text and figures in the manuscript. D. L. Welch contributed to the manuscript and was Principal Investigator on the 2006 Gemini observations. A. Rest reduced the SuperMACHO difference images of SN 1987A and contributed to the analysis and interpretation of the light echoes of SN 1987A. P. G. Sutherland contributed to the manuscript and acted in a supervisory role. M. Bergmann designed many of the original Gemini observations and provided guidance for reducing the Gemini multi-object spectra.

Chapter 6 originally appeared as "Direct Confirmation of the Asymmetry of the Cas A Supernova with Light Echoes" in The Astrophysical Journal as

> "Rest, A., Foley, R. J., Sinnott, B., Welch, D. L., Badenes, C., Filippenko, A. V., Bergmann, M., Bhatti, W. A., Blondin, S., Challis, P., Damke, G., Finley, H., Huber, M. E., Kasen, D., Kirshner, R. P., Matheson, T., Mazzali, P., Minniti, D., Nakajima, R., Narayan, G., Olsen, K., Sauer, D., Smith, R. C., and Suntzeff, N. B. The Astrophysical Journal, **732**, 3 (2011)."

A. Rest led the study, with the majority of the manuscript written by A. Rest and R. J. Foley, with contributions from most co-authors. This paper was a companion project to Chapter 4. My contributions involved calculating the flux profiles across the sky for the observed light echoes, determining the inclination of the scattering dust sheets from the data, and helping to model the observed light echo spectra. Although my contribution to the manuscript text was at the $\sim 10\%$ level, without the above data and analysis contributions, the main science result was not possible.

I am the sole author of Chapter 3. Nonetheless, this chapter is heavily influenced by the recent invited review on the topic that was co-authored by A. Rest, D. L. Welch, and me, which originally appeared as "Light Echoes of Transients and Variables in the Local Universe" in the Publications of the Astronomical Society of Australia as

> "Rest, A., Sinnott, B., and Welch, D. L. Publications of the Astronomical Society of Australia, **29**, 466 (2012)."

Acknowledgements

There are many small things that make a supervisor an excellent one. I'm extremely grateful to have been supervised by Doug Welch, who has all those small things. I'm thankful to have had Peter Sutherland contribute to my supervision, providing succinct academic advice that is always accurate. In addition to my committee members, Laura Parker and Alison Sills, I owe thanks to past group members Lindsay Oaster and Brittany McDonald. Armin Rest is much more than a collaborator, and I thank him for that.

A PhD takes a non-trivial amount of time to complete. I can't help but feel indebted to the city of Hamilton and the lengthy list of people who pour their heart into making the downtown a great place to live.

Most of all, I thank my parents, my brothers, and Blair.

Contents

List of Figures

List of Tables

Chapter 1

Introduction

Supernovae (SNe) are remarkable astronomical events. During the first seconds of the explosion, the burst of energy associated with the release of neutrinos can rival the entire stellar output of the observable Universe. In the several months that follow, the luminosity associated with the death of a single star is comparable to that of the entire galaxy from which it originates. Hundreds or even thousands of years later the expanding gas from the explosion can still be observed. The remnant nebulae that are created account for some of the most famous objects in astronomy. Additionally, all elements in the Universe heavier than iron are created in these stellar explosions. At large scales, the chemical enrichment and energy feedback that SNe impart on their surroundings can alter how galaxies evolve with time. And at the largest of scales, observing the violent explosions has led to the discovery that the Universe is expanding at an accelerated rate and that over two thirds of it is filled with dark energy.

Scattered light echoes (LEs) offer a new method to observe SNe. Analogous to mirrors conveniently placed in the sky, LEs reflect photons from the explosion towards Earth that would otherwise never be observed. By seeking out and observing these echoes, we can observe SNe in unusual ways: (1) long after the explosion has faded, since there is a time-delay associated with the echo phenomenon, and (2) from unique viewing angles, since multiple LEs act as different mirrors with which to view the explosion. Both of the above are impossible without (or in the absence of) LEs.

Using spectroscopy of LEs as a tool for studying the outburst light from SNe has been a growing field of astronomy in the last five years. However, sufficient data has not existed to test theories of how spectroscopy of SN LEs should be interpreted. As a result, assumptions have remained in the field which limit the effectiveness of spectroscopy of LEs. This thesis reports a method for interpreting spectroscopic observations of SN LEs using a data set of 18 LE spectra, more than twice the number of previously published SN LE spectra. After testing the method, we present asymmetry detections using the new technique of LE spectroscopy from multiple perspectives on two of astronomy's most famous SNe: SN 1987A and Cassiopeia A (Cas A).

1.1 Astrophysical Motivation

There are multiple reasons why studying SNe is meaningful to astrophysics and why, in particular, scattered LEs are an important tool.

Core-Collapse SN Problem For nearly 50 years we have known that neutrino-driven explosions may be the key to understanding core-collapse SNe (Colgate & White, 1966). However, since the first simulations nearly 30 years ago, the fact remains that the death of massive stars is not sufficiently understood to consistently simulate energetic explosions (Janka, 2012; Burrows, 2013). The result is that we do not reliably know what fraction of stars undergo core-collapse explosions, what fraction produce neutron stars, what fraction produce stellar mass black holes, or how the explosion energy and chemical yield is related to the initial progenitor mass.

Cosmology with Type Ia SNe The discovery that Type Ia (thermonuclear) SNe can act as standard candles based on the shape of their lightcurves (Phillips, 1993) led to measurements of an accelerating Universe and evidence for the existence of dark energy (Riess et al., 1998; Perlmutter et al., 1999). Considering the significance of Type Ia SNe to cosmology, it is highly unfortunate that the progenitor systems are still not known (Maoz & Mannucci, 2012). Uncertainty in the explosion mechanism and the progenitor system may be related to the observed spectral and photometric diversity among Type Ia SNe (Benetti et al., 2005). Better understanding may lead to the reduction of systematic errors in cosmological measurements.

Overcoming Astrophysical Timescales Studying nearby SNe in their remnant state ($\gtrsim$ 20 yr after explosion) gives insight into the chemical composition, distribution, and kinematics of the ejected material, but does not probe the epoch of the explosion. Due to the timescales involved, astronomers typically don't have observational records of the explosion properties that result in observed SN remnants. LEs can overcome this timescale challenge, providing a direct causal connection between properties of the explosion and its $\gtrsim$ 100-year-old remnant state.

A Direct Method for Observing Asymmetries in SNe Current core-collapse models fail at reproducing energetic explosions in one dimension (Burrows, 2013). Multi-dimensional effects such as convection and fluid instabilities are thought to play an important role in the mechanism driving these explosions (Murphy & Burrows, 2008; Nordhaus et al., 2010; Dolence et al., 2013). Polarization measurements tell us most core-collapse SNe show evidence for asymmetry (Wang & Wheeler, 2008), but the physical origin or origins of the asymmetries remain unclear. Coupled with this is the recent connection between SNe and highly asymmetric long-duration gamma-ray bursts (Galama et al., 1998). Since LEs are analogous to mirrors in the sky, they allow a single astronomical source to be viewed from multiple lines of sight. The technique allows for a new, independent, and direct method for studying asymmetries in SNe.

1.2 Structure of Thesis

We begin this thesis by introducing SNe in **Chapter 2**. We describe basic observational properties of SNe, as well as review explosion models. We highlight current theoretical problems in the field, emphasizing asymmetries in SNe. We also provide brief introductions to the two astronomical sources which dominate the thesis: SN 1987A and Cas A.

In **Chapter 3** we introduce the phenomena of scattered LEs and give historical background. We describe the geometry and go over observational signatures. We focus on using spectroscopy of LEs to directly observe the original outbursts of SNe.

Chapter 4 is a comprehensive model for using the photometry of LEs to correctly interpret LE spectroscopy. We present substantial testing of the model's parameter space, as well as brief initial tests using spectroscopy of SN 1987A and Cas A LEs.

The first half of **Chapter 5** uses spectroscopy of SN 1987A LEs to provide observational tests of the model of Chapter 4. The second half of Chapter 5 presents LE spectroscopy from multiple perspectives using the SN 1987A LEs. We present a north/south asymmetry in the original outburst of SN 1987A and discuss possible physical origins.

In **Chapter 6** we demonstrate the power of LE spectroscopy using a more exotic astronomical event: the mid-17$^{\text{th}}$-century SN that led to the famous Cas A SN remnant. We use LE spectroscopy to show an excess velocity in one direction of the Cas A SN and compare to asymmetries in the current remnant and the proper motion of the X-ray point source.

In **Chapter 7** we discuss the future of scattered LEs in astronomy. We address the possible advances in the field that can be realized within the next five years, as well as long-term possibilities for the field. We conclude the thesis by summarizing our contributions.

Bibliography

Benetti, S. and Cappellaro, E. and Mazzali, P. A. and Turatto, M. and Altavilla, G. and Bufano, F. and Elias-Rosa, N. and Kotak, R. and Pignata, G. and Salvo, M. and Stanishev, V. 2005, ApJ, 623, 1011

Burrows, A. 2013, Reviews of Modern Physics, 85, 245

Colgate, S. A. and White, R. H. 1966, ApJ, 143, 626

Dolence, J. C. and Burrows, A. and Murphy, J. W. and Nordhaus, J. 2013, ApJ, 765, 110

Galama, T. J. and Vreeswijk, P. M. and van Paradijs, J. and Kouveliotou, C. and Augusteijn, T. and Böhnhardt, H. and Brewer, J. P. and Doublier, V. and Gonzalez, J.-F. and Leibundgut, B. and Lidman, C. and Hainaut, O. R. and Patat, F. and Heise, J. and in't Zand, J. and Hurley, K. and Groot, P. J. and Strom, R. G. and Mazzali, P. A. and Iwamoto, K. and Nomoto, K. and Umeda, H. and Nakamura, T. and Young, T. R. and Suzuki, T. and Shigeyama, T. and Koshut, T. and Kippen, M. and Robinson, C. and de Wildt, P. and Wijers, R. A. M. J. and Tanvir, N. and Greiner, J. and Pian, E. and Palazzi, E. and Frontera, F. and Masetti, N. and Nicastro, L. and Feroci, M. and Costa, E. and Piro, L. and Peterson, B. A. and Tinney, C. and Boyle, B. and Cannon, R. and Stathakis, R. and Sadler, E. and Begam, M. C. and Ianna, P. 1998, Nature, 395, 670

Janka, H.-T. 2012, Annual Review of Nuclear and Particle Science, 62, 407

Maoz, D. and Mannucci, F. 2012, PASA, 29, 447

Murphy, J. W. and Burrows, A. 2008, ApJ, 688, 1159

Nordhaus, J. and Burrows, A. and Almgren, A. and Bell, J. 2010, ApJ, 720, 694

Perlmutter, S. and Aldering, G. and Goldhaber, G. and Knop, R. A. and Nugent, P. and Castro, P. G. and Deustua, S. and Fabbro, S. and Goobar, A. and Groom, D. E. and Hook, I. M. and Kim, A. G. and Kim, M. Y. and Lee, J. C. and Nunes, N. J. and Pain, R. and Pennypacker, C. R. and Quimby, R. and Lidman, C. and Ellis, R. S. and Irwin, M. and McMahon, R. G. and Ruiz-Lapuente, P. and Walton, N. and Schaefer, B. and Boyle, B. J. and Filippenko, A. V. and Matheson, T. and Fruchter, A. S. and Panagia, N. and Newberg, H. J. M. and Couch, W. J. and Supernova Cosmology Project. 1999, ApJ, 517, 565

Phillips, M. M. 1993, ApJ, 413, L105

Riess, A. G. and Filippenko, A. V. and Challis, P. and Clocchiatti, A. and Diercks, A. and Garnavich, P. M. and Gilliland, R. L. and Hogan, C. J. and Jha, S. and Kirshner, R. P. and Leibundgut, B. and Phillips, M. M. and Reiss, D. and Schmidt, B. P. and Schommer, R. A. and Smith, R. C. and Spyromilio, J. and Stubbs, C. and Suntzeff, N. B. and Tonry, J. 1998, AJ, 116, 1009

Wang, L. and Wheeler, J. C. 2008, ARA&A, 46, 433

Chapter 2

Introduction to Supernovae

The mechanisms driving supernovae (SNe) are primarily a function of stellar mass and can be divided into two categories: core-collapse and thermonuclear runaway.

2.1 Core-Collapse Supernovae

Massive stars spend their lives undergoing successive stages of nuclear burning in their central regions. For stars with $M \gtrsim 10M_{\odot}$, nuclear burning proceeds all the way through to the silicon-burning stage, producing an inert core composed primarily of Fe and Ni (Nomoto, 1987). The star's fate is then sealed as any subsequent nuclear fusion depletes energy from the star. With the silicon-burning stage only lasting on the order of days (Kippenhahn & Weigert, 1990), the star contracts and the Fe core is supported only by electron degeneracy pressure. As outlined in Wheeler et al. (1990), during core-contraction, temperatures rise ($\sim 10^{10}$ K) and neutronization occurs ($p+e^{-} \rightarrow n+\nu_e$), accelerating the collapse as neutrinos immediately escape the star. Photodisintergration of Fe nuclei also occurs, accelerating the collapse further as large fluxes of neutrons and neutrinos are being generated in the process.

Under such extreme conditions in the core, with densities above $\sim 10^{12}$ g cm^{-3}, the diffusion time for neutrinos becomes larger than the dynamical timescale of the collapse (Arnett, 1977). At that stage, the neutrinos are actually trapped in the high-density region. Once nuclear densities are reached ($\sim 2-3 \times 10^{14}$ g cm^{-3}), the collapsing core is abruptly halted due to the repulsive strong force, generating a "bounce shock" which propagates radially outwards away from the core. At this point the inner core has been collapsing homologously at subsonic speeds while the outer core is collapsing at supersonic speeds (Bethe & Wilson, 1985). Theoretically, the bounce shock could completely eject all infalling layers of the star in a successful explosion. In practice, however, the bounce shock loses energy in these "prompt" explosion models and ultimately collapses back in on itself in a failed explosion (Mazurek, 1982; Burrows & Lattimer, 1985).

For stars in the lower mass range of $M \approx 8-10\ M_\odot$, the final state is a degenerate O-Ne-Mg core supported by electron degeneracy pressure (Nomoto, 1984). Electron capture onto ^{24}Mg nuclei causes loss of pressure, with the O-Ne-Mg core undergoing core-collapse to form a degenerate neutron star (NS) (Canal & Schatzman, 1976; Nomoto, 1984, 1987). In this model, so-called "electron capture SNe" can produce explosions in similar fashion to their more massive counterparts (Mayle & Wilson, 1988).

2.1.1 Neutrino-Driven Explosions

The gravitational energy release associated with the collapse down to a NS ($R \sim$ 15 km, $M \sim 1.5\ M_\odot$) is enormous: $\sim 3 \times 10^{53}$ ergs. However, $\sim 99\%$ of the energy is released seconds after core bounce as trapped neutrinos escape. The kinetic energy of the explosion is on the order of $\sim 10^{51}$ ergs, while the radiated photon energy is $\sim 10^{49}$ ergs. Note this latter "small" photon energy still rivals the luminosity output of a billion suns, highlighting just how energetic the phenomenon is.

Colgate & White (1966) first proposed neutrinos as a mechanism for depositing additional energy into the stalled shock wave. In this "delayed explosion" scenario, neutrino heating behind the stalled shock re-energizes the shock wave and results in a successful explosion. Despite the tremendous amount of work done in the field (e.g. Arnett, 1977; Bethe & Wilson, 1985; Wilson, 1985; Burrows & Goshy, 1993; Mezzacappa & Bruenn, 1993; Mezzacappa et al., 2001), successful explosions with energy scales of $\sim 10^{51}$ ergs still elude theorists. However, the computational challenge of accurately simulating a core-collapse should not be minimized. A complete core-collapse model requires general relativistic effects, hydrodynamics, magnetohydrodynamcs (MHD), as well as multi-dimensional, multi-flavour neutrino transport (a 6-dimensional problem).

2.2 Thermonuclear Supernovae

2.2.1 Type Ia

Type Ia SNe show strong Si lines but no H or He signatures in their spectra. Unlike core-collapse SNe, which are locally coupled to regions of high star formation, Type Ia SNe are found in both young and old stellar populations (Hillebrandt & Niemeyer, 2000; Sullivan et al., 2006). Recent work has shown that the rate of Type Ia SNe is positively correlated to the specific star formation rate of the parent galaxy per unit mass (Sullivan et al., 2006; Gao & Pritchet, 2013). The chemical abundances found in Type Ia SNe are consistent with carbon burning in a dense environment (Arnett & Truran, 1969; Arnett, 1969; Nomoto et al., 1997; Woosley, 1997). Lastly, once known corrections are applied, $\sim 85\%$ of observed Type Ia SNe show similar luminosities, lightcurves, and spectra, ultimately suggesting a homogeneous class of progenitors (Hillebrandt & Niemeyer, 2000).

There appears to exist, then, very good evidence that Type Ia SNe are the result of exploding compact degenerate objects, and the best such candidate is a carbon-oxygen white dwarf (CO WD). The very best observational evidence to support this hypothesis came very recently: the discovery of the Type Ia SN 2011fe in the local galaxy M101. Using observations of the expanding shocked envelope at very early times, it was shown that the radius of the progenitor was $R < 0.02R_{\odot}$ with a density $\rho > 10^4$g cm^{-3} (Nugent et al., 2011; Bloom et al., 2012), only leaving degenerate WDs and NSs as possible progenitors. Observations of SN 2011fe by Nugent et al. (2011) also showed conclusive evidence for unburnt high-velocity oxygen in a Type Ia SN for the first time.

The path from WD to explosion is thought to occur when a WD is accreting material in a binary system (Whelan & Iben, 1973). In the most common model, material accretes onto the WD until carbon ignition occurs just prior to reaching the Chandrasekhar mass limit of $\sim 1.4M_{\odot}$ (for small rotation, varying slightly with chemical composition). Because the material is degenerate, the WD has no means to regulate the carbon burning process and this leads to a thermonuclear runaway. The result is an explosion completely destroying the WD and leaving behind no remnant. Much like core-collapse SNe, the details of this process are still not fully understood. What we do know is that the most basic theory, a pure prompt, supersonic detonation, does not work. In that scenario intermediate-mass elements are under-produced (Arnett et al., 1971; Nomoto et al., 1976), in disagreement with observations (Filippenko, 1997). Instead, the initial burning consists of subsonic deflagration that may or may not transition into a delayed supersonic detonation. Some models propose He surface detonations which can trigger carbon ignition for sub-Chandrasekhar masses (e.g. Kromer et al., 2010). The propagating subsonic flames are highly turbulent and pose a significant challenge for theorists.

The exact nature of the companion source that is feeding the accreting WD is not yet known. In “single-degenerate” (SD) explosion models (Whelan & Iben, 1973), the binary companion is either a red giant accreting via a strong stellar wind, or a subgiant/main sequence/He star accreting via Roche-lobe overfill. In the “double-degenerate” (DD) models (Iben & Tutukov, 1984; Webbink, 1984), an explosion is the result of two WDs merging. Arguments exist to support both progenitor channels. For example, the DD model gives a simple explanation for the lack of H lines in

Type Ia spectra. The DD model may also be able to explain recent observations that imply a super-Chandrasekhar WD mass in at least some explosions (Howell et al., 2006; Scalzo et al., 2010; Silverman et al., 2011), since the total mass of the two WDs can exceed the Chandrasekhar limit. However, it remains unclear how the overall homogeneity of Type Ia SNe can remain in the DD model when presumably the total ^{56}Ni varies considerably. Observational evidence exists for the SD model as well (e.g. Chiotellis et al., 2012; Dilday et al., 2012), however, suggesting multiple explosion mechanisms may coexist and explain the diversity of Type Ia SNe.

Unlike core-collapse SNe, no progenitor system of a Type Ia SN has ever been conclusively observed through imaging before or after the explosion. For Tycho, the surviving ex-companion star in a SD model may have been found (Ruiz-Lapuente et al., 2004; González Hernández et al., 2009; Lu et al., 2011), but the finding is still controversial (Kerzendorf et al., 2012b; Shappee et al., 2013). Progenitor limits based on imaging of the historical Type Ia associated with SN 1006 (Kerzendorf et al., 2012a), SNR 0509-67.5 (Schaefer & Pagnotta, 2012; Shappee et al., 2013), and SNR 0519-69.0 (Edwards et al., 2012), appear to disfavor the SD channel. However, Di Stefano & Kilic (2012) notes that ex-companion stars in the SD channel may have evolved below our detection threshold by the time explosion even occurs, due to the timescales of the WD evolution.

2.2.2 Pair Instability

While Type Ia SNe can occur for progenitors with $M \lesssim 8M_{\odot}$, stars in a much higher mass range can also end their lives as thermonuclear SNe. Large stellar masses ($> 100M_{\odot}$) can exist for the first generation of zero-metallicity stars in the Universe (Nakamura & Umemura, 2001). For stars with $M > 260M_{\odot}$, their fate should be a black hole with no SN (Fryer et al., 2001; Heger et al., 2003). However, stars with $140M_{\odot} \lesssim M < 260M_{\odot}$ should end their lives as pair instability supernovae (PI SNe). Stars of such mass produce large He cores ($\sim 45M_{\odot}$) that are affected by electron-positron pair instability, causing collapse and igniting oxygen and silicon burning. The explosive burning provides sufficient energy to reverse the collapse and completely destroy the star in a thermonuclear reaction (e.g. Barkat et al., 1967; Fryer et al., 2001; Heger & Woosley, 2002; Kasen et al., 2011). PI SNe result in tremendous outbursts with ~ 100 times the energy of, and much longer lasting than, Type Ia SNe (Fryer et al., 2001).

Recent studies have illuminated a class of "superluminous" SNe with luminosities an order of magnitude larger than ordinary SNe (Quimby et al., 2011; Gal-Yam, 2012). It has recently been suggested that "pulsational pair instability SNe" with initial stellar masses $96M_{\odot} \lesssim M \lesssim 130M_{\odot}$ may be responsible for these luminous SNe (Woosley et al., 2007). Unlike PI SNe described above, the pair instability here is responsible for cyclic explosive ejections of material into the circumstellar medium (CSM). Woosley et al. (2007) demonstrated that the interaction of successive high-velocity shells of material can produce the significantly higher luminosities in these types of SNe.

2.3 Classification of Supernovae

SNe are classified based on their maximum-light spectra as well as the shape of their lightcurve. Table 2.1 summarizes the key characteristics required for each classification subtype. Figure 2.1 shows the observed rates of different subclasses, based on the volume-limited results of Li et al. (2011). It should be stressed that Type Ia SNe are the only thermonuclear explosions in this classification scheme; all other SN types are driven by gravitational energy in core-collapse.

Table 2.1. Classification of supernovae based on the properties of their maximum-light spectra and lightcurve shape.

Type	Hydrogen	Silicon	Helium	Additional
I	No			
Ia	No	Yes		
Ib	No	No	Yes	
Ic	No	No	No	
II	Yes			
IIP	Yes			Plateau in lightcurve
IIL	Yes			Linear lightcurve
IIb	Yes			Weak H line; resemble Ib at later times
IIn	Yes			Narrow H lines; CSM interaction

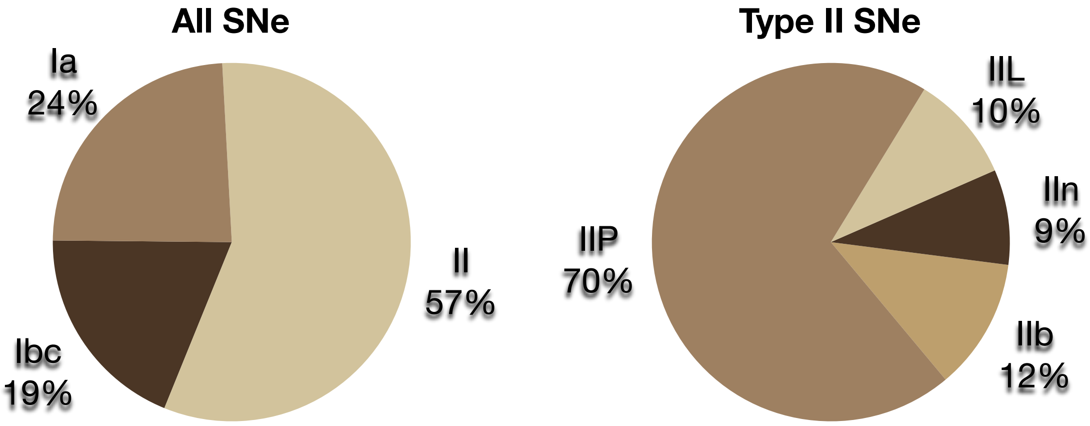

Figure 2.1: Observed rates for the different SN subclasses for all SNe (left) and all Type II SNe (right), from the the volume-limited results of Li et al. (2011). Figure is also adapted from Figure 9 in Li et al. (2011).

2.4 Lightcurves of Supernovae

The first radiation signal of SNe comes in the form of neutrinos. Core-collapse neutrino luminosity is $\sim 10^{52}$ ergs s^{-1} (Nordhaus et al., 2010), while thermonuclear luminosity is $\sim 10^{50}$ ergs s^{-1} (Kunugise & Iwamoto, 2007). Following the initial neutrino burst, SN lightcurves can be powered by radioactive decay (dominated by ^{56}Ni → ^{56}Co → ^{56}Fe), shock-heated envelopes, interaction with CSM material, or a combination of the above. Figure 2.2 shows the overall lightcurve shape for the common SN types.

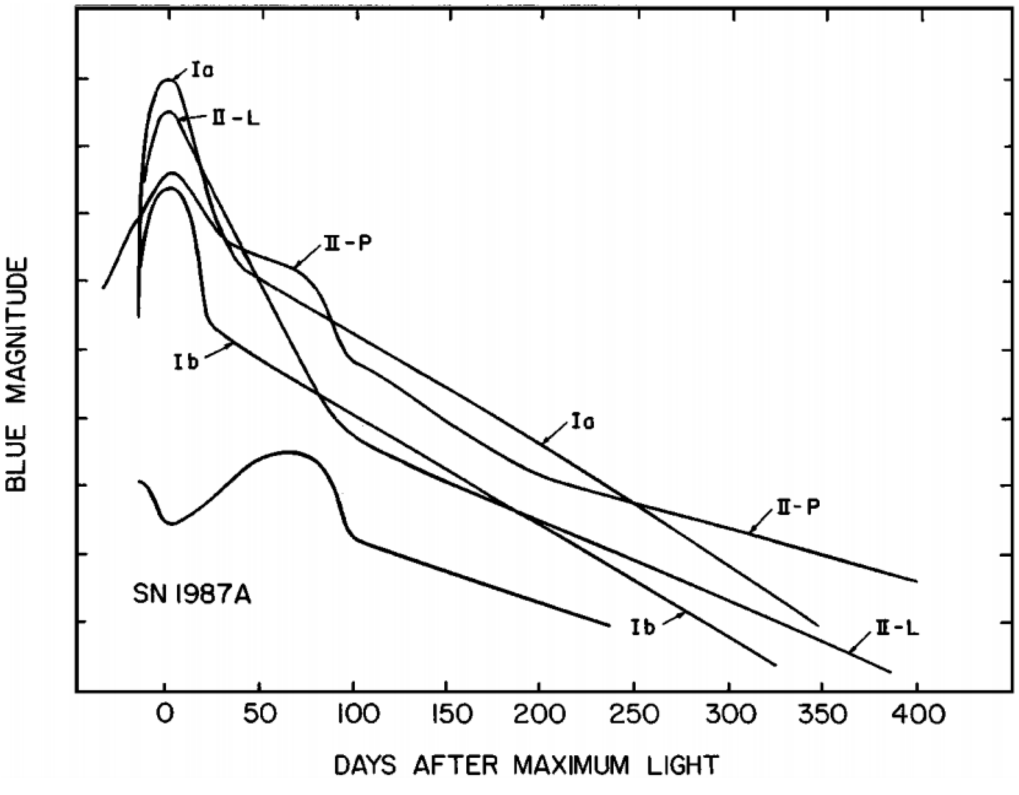

Figure 2.2: Lightcurve templates, showing the overall shapes of lightcurves of SN types Ia, IIL, IIP, Ib, as well as SN 1987A. Figure from Wheeler et al. (1990) and reproduced here with permission.

Type Ia Lightcurves Thermonuclear lightcurves are powered entirely by radioactive decay of newly synthesized ^{56}Ni. The critical reactions are (Arnett, 1982):

$$\begin{aligned} & ^{56}\mathrm{Ni} + \mathrm{e}^- && \rightarrow && ^{56}\mathrm{Co} + \nu_\mathrm{e} + \gamma && (\tau = 6.2^\mathrm{d}) && (2.1) \\ (81\%)\ & ^{56}\mathrm{Co} + \mathrm{e}^- && \rightarrow && ^{56}\mathrm{Fe} + \nu_\mathrm{e} + \gamma && (\tau = 78.8^\mathrm{d}) && (2.2) \\ (19\%)\ & ^{56}\mathrm{Co} && \rightarrow && ^{56}\mathrm{Fe} + \mathrm{e}^+ + \nu_\mathrm{e} + \gamma && (\tau = 78.8^\mathrm{d}) && (2.3) \end{aligned}$$

At very early times the ejecta is opaque. As the the diffusion time lowers in the expanding ejecta the luminosity rises steadily. It reaches a maximum (after $\sim$ 20 days) when the final backlog of energy deposition diffuses through the diluted ejecta. Around maximum light the energy release from ^{56}Co decay matches that of ^{56}Ni (Arnett, 1982) and the lightcurve proceeds onto a radioactive tail powered by ^{56}Co decay. The peak luminosity of thermonuclear SNe is therefore proportional to the amount of ^{56}Ni emitted in the explosion. The width-luminosity relation of Phillips (1993) showed brighter Type Ia SNe have broader lightcurves, forming the foundation of Type Ia SNe as standard candles in cosmology. The standardization of Type Ia SNe allowed for the discovery of an accelerating Universe (Riess et al., 1998; Perlmutter et al., 1999). Additional energy sources for the lightcurves could be luminosity generated via shock interaction with CSM or with a possible progenitor companion (e.g. Kasen, 2010), the latter affecting the lightcurve at very early times.

Core-Collapse Lightcurves Type IIP lightcurves have the most complex shape, showing a plateau of nearly constant luminosity after maximum brightness. Thought to be associated with large H envelopes (Smartt, 2009), Type IIP SNe account for 70% of Type II and 40% of all SNe (Li et al., 2011). After neutrinos comes the arrival of a burst of UV radiation associated with the the shock wave breaking out of the stellar surface (Falk & Arnett, 1977). Subsequent rapid cooling causes a sharp decrease in luminosity before rising to maximum brightness as the photosphere expands. As the shocked ejecta expands, a recombination wave travels inwards through the H envelope. During this phase the luminosity is roughly constant causing a plateau in the observed lightcurve before proceeding onto the radioactive tail (Wheeler et al., 1990; Woosley, 1991). Lightcurves of type IIP, IIL and Ib can be interpreted if the progression from IIP → IIL → Ib corresponds to progenitors with increasing degrees of stripping of their H envelopes. If the three subtypes represent unique progenitors, or if they are of the same origin with a smooth transition between degrees of stripping is an ongoing matter of debate (Heger et al., 2003; Arcavi, 2012).

2.5 Spectra of Supernovae

Due to the large velocities involved ($\sim 10^4$ km s^{-1}) and the existence of an optically thick photosphere surrounded by an optically thin envelope, SN spectral lines are described by P Cygni profiles. Figure 2.3 describes the formation of such line profiles. Photons emitted directly in front of the optically thick photosphere are absorbed by the envelope; the result is blueshifted absorption at the velocity of the photosphere. Photons emitted directly behind the photosphere are occulted and invisible to the observer. Excess photons emitted to the wings of the envelope produce an emission component centred at zero velocity.

The evolution of SN spectra can be understood using Figure 2.3 and considering the optically thick line emitting region. At very early epochs all of the ejecta is optically thick as it expands radially. As the density of the ejecta decreases due to expansion, the photosphere recedes inwards with respect to the homologously expanding ejecta ($r = vt$) (Kirshner & Kwan, 1974). At early epochs, the photosphere is surrounded by a thin envelope, resulting in P Cygni profiles dominated by absorption at high velocities. As the photosphere recedes to reveal inner layers of the ejecta, the emission-to-absorption ratio of the P Cygni line increases steadily. Finally, at nebular epochs when the photosphere recedes to the centre, the entire ejecta is optically thin and pure emission lines are observed. Figure 2.4 shows optical spectra of SN 1987A as

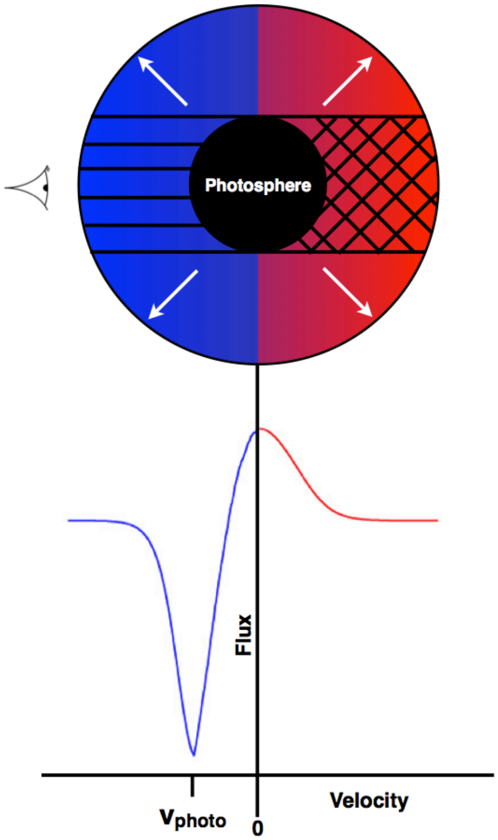

Figure 2.3: Illustration of P Cygni line profile formation. Photons emitted directly in front of the photosphere give rise to a blueshifted absorption component while the region behind the photosphere is invisible to the observer. Photons emitted in other directions provide an emission component centred on the rest wavelength of the line.

a function of time, highlighting the emergence of strong nebular lines at late epochs.

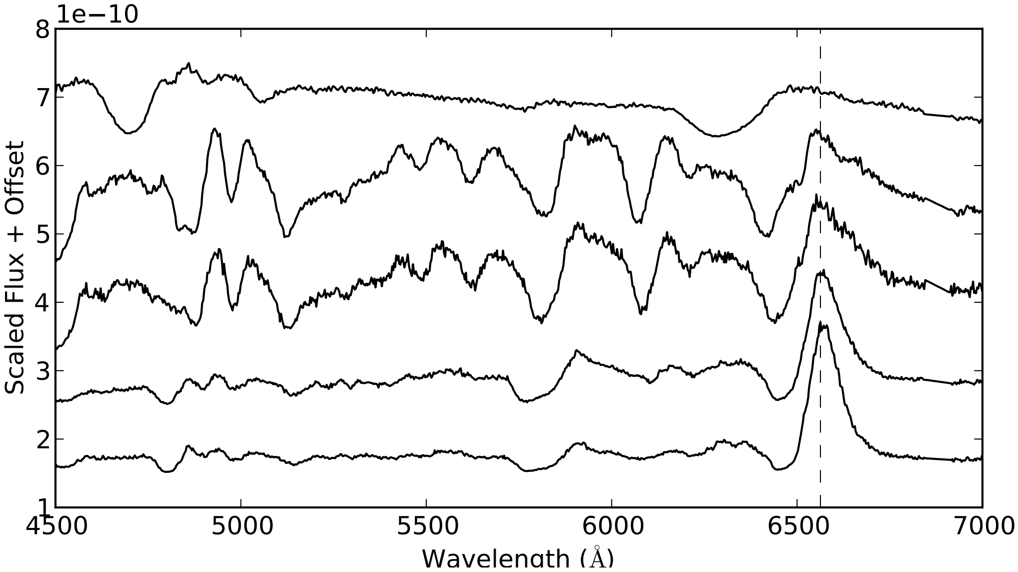

Figure 2.4: Optical spectra of SN 1987A plotted at 10, 40, 60, 140, and 180 days after explosion from top to bottom. Note the transition from an absorption-dominated spectrum at early epochs to an emission-dominated spectrum. The dashed line shows the rest wavelength of the Hα line. Spectra are from Menzies et al. (1987); Catchpole et al. (1987, 1988).

2.6 Asymmetries in Supernovae

Observational evidence suggests that both core-collapse and Type Ia SNe are asymmetric events (Wang & Wheeler, 2008). Interpreting the spectra of SNe in terms of fine-structure as well as velocity, both at photospheric and nebular epochs, asymmetry along the line-of-sight to the SN can be probed (e.g. Chugai et al., 2005; Milisavljevic et al., 2012). Spectropolarimetry observations can also be used to observe asymmetry, predominantly in the plane of the sky. Shapiro & Sutherland (1982) showed the geometry of the line emitting region or the scattering envelope can be inferred using this technique. In spherically symmetric conditions all directions produce the same degree of polarization, so monitoring the Stokes vector results in no net linear polarization. Therefore, observing net continuum or line polarization is evidence for some from of asymmetry in the explosion, be it in the line emitting region, the scattering envelope, or nearby dust. Since maximum polarization occurs for $\sim 90°$ scattering angles, polarization data is naturally biased towards asymmetries in the plane of the sky. There also exists a 180° ambiguity in the measured polarization angle.

2.6.1 Asymmetry in Core-Collapse

Almost all core-collapse SNe sufficiently studied through spectropolarimetry or spectroscopy show evidence for aspherical explosions (e.g. Elmhamdi et al., 2003; Chugai et al., 2005; Leonard & Filippenko, 2005; Wang & Wheeler, 2008; Chornock et al., 2010; Patat et al., 2011; Utrobin & Chugai, 2011). Linear polarization measurements typically show a strong increase in net polarization as the photosphere recedes to reveal the inner layers of the ejecta (Wang & Wheeler, 2008). This is strong evidence that the explosion mechanism itself is intrinsically asymmetric. SN 1987A was an excellent example of an asymmetrical core-collapse SNe, as evidence for asymmetry came in the form of its lightcurve shape, speckle interferometry, continuum polarization, line polarization, the early photospheric spectra, the late nebular spectra, as well as the ejecta distribution in its remnant state. These observations are discussed in detail in Chapter 5. Although SN 1987A is unique in the quality and depth of its observations, the fact remains that the core-collapse explosion process appears to be globally asymmetric.

From a theoretical standpoint, distinguishing between physical assumptions (lack of input physics) versus computational assumptions (lack of dimensionality or sophistication in the input physics) is an aspect of many astronomical problems. However, only recently the field has confirmed the failure of state-of-the-art spherically symmetric core-collapse simulations to generate explosions for $> 10 M_\odot$ progenitors (Burrows, 2013). It appears then, that the missing key for obtaining successful explosions is inherently asymmetric.

The gain region is an important part of a core-collapse explosion, and represents the radius at which the positive energy input is balanced by the energy loss to the proto-neutron star (or black hole). Recent multi-dimensional models show convection and instabilities at early times that effectively increase the radius of the gain region due to asymmetries, thereby lowering the neutrino luminosities required for successful explosions (e.g. Gawryszczak et al., 2010; Hammer et al., 2010; Müller et al., 2012). Whether or not the required energy scales for explosions steadily decreases as a function of dimensionality, as some studies show (e.g. Murphy & Burrows, 2008; Nordhaus et al., 2010), is still unclear. The recently discovered standing accretion shock instability (SASI; Blondin et al., 2003), which causes large low-mode sloshing of the stalled shock, is a good example of how the gain region might be pushed out to larger radii due to aspherical effects.

In addition to the above evidence for asymmetry, there exists the confirmation of a connection between long duration gamma-ray bursts (GRBs) and Type Ib/c SNe (Galama et al., 1998), as well as the large proper motions associated with NSs (Cordes & Chernoff, 1998). Both of these phenomena are presumably deeply rooted in asymmetric core-collapse events (Wheeler et al., 2000; Wongwathanarat et al., 2012). Very recently, Lopez et al. (2013) found evidence for strong jets in the explosion which caused the galactic SNR W49B.

The delayed neutrino-driven mechanism is by far the most mature theory for core-collapse SNe. Naturally, however, the failure of the theory to produce successful $\sim 10^{51}$ ergs explosions has led to competing mechanisms. Due to the overwhelming evidence for asymmetry as described above, many models have emerged where the explosion is at least partially powered by bi-polar jets involving rotation and magnetic fields (e.g. Khokhlov et al., 1999; Wheeler et al., 2000; Akiyama et al., 2003; Couch et al., 2009, 2011). Although the details of these models are still uncertain, future observations of asymmetries in core-collapse SNe could distinguish between models and help unearth the true explosion mechanism.

2.6.2 Asymmetry in Type Ia SNe

Type Ia SNe also show signatures of asymmetry in their polarization data, but to a lesser extent than core-collapse SNe (Wang & Wheeler, 2008). The largest degree of asymmetry is associated with elements produced in subsonic burning (Maeda et al., 2010b), suggesting the origin is an off-centre ignition of the turbulent burning front. Type Ia SNRs (e.g. the Tycho SNR) appear to be more spherical in their remnant stages compared to core-collapse SNRs, consistent with the idea of off-centre ignition in an otherwise spherical explosion.

Although Type Ia SNe can be used as standard candles based on their lightcurves, there does exist spectroscopic diversity among Type Ia SNe that cannot be parametrized by the lightcurve alone (Benetti et al., 2005). Recent work has shown that diversity in the critical width-luminosity relation, as well as spectroscopic diversity, can arise from asymmetrical effects (Kasen et al., 2009; Maund et al., 2010). Asymmetries introduced by an off-centre delayed detonation model seem to provide an explanation (Maeda et al., 2010a, 2011; Maeda, 2012). However, the nature of the companion star in Type Ia progenitor systems is still not known. Asymmetry studies may be similarly fruitful in this area as well (e.g. Kasen, 2010).

2.7 SN 1987A

SN 1987A was a Type II SN discovered on February 24, 1987 in the Large Magellanic Cloud (LMC). It remains the (apparently) brightest SN to be observed since Kepler's SN of 1604, and the brightest to be observed in the era of modern instruments. It is one of the most studied objects in all of astronomy. SN 1987A had many "firsts." It was the first time the progenitor star of a SN was known precisely due to pre-explosion images. Its progenitor was a $\sim 20 M_{\odot}$ blue supergiant star (Arnett et al., 1989; Arnett, 1991), changing our view that only red supergiants would end in core-collapse SNe. Neutrinos were also detected for the first time from an astronomical source other than the Sun, although only 19 were detected in total (Bionta et al., 1987; Hirata et al., 1987). However, this small number of detections was sufficient to confirm the hypothesis that massive stars undergo core-collapse. Although observations were a day too late to detect the UV shock breakout, the rapid cooling period immediately following was detected for the first time in the initial 7 days of the lightcurve (Woosley, 1991).

Due to its blue progenitor, SN 1987A was a peculiar SN. The lightcurve (Figure 2.2 and Figure 2.5) showed no substantial plateau period and took ~ 85 days to slowly rise to its relatively faint maximum brightness. Although it reached a peak apparent magnitude of $\sim +3$ (Arnett et al., 1989), its absolute magnitude was relatively faint at $M_B = -14.7$ (Milone et al., 1988). For comparison, the average brightness of typical SNe is $M_{B,Ia} = -18.49 \pm 0.09$, $M_{B,II} = -16.05 \pm 0.15$, and $M_{B,IIP} = -15.66 \pm 0.16$ for SN Types Ia, II, and IIP, respectively (Li et al., 2011).

SN 1987A surprised once again when the Hubble Space Telescope (HST) revealed concentric circumstellar rings in the immediate CSM. The three rings create an axisymmetric hour-glass shape, with one equatorial ring surrounding the SN ejecta and two roughly equal outer rings of larger radii (Luo & McCray, 1991; Burrows et al., 1995). The material was illuminated by the X-ray flash from the shock breakout and is thought to have originated in a single mass-loss event from a binary system (Podsiadlowski, 1992; Morris & Podsiadlowski, 2007).

SN 1987A is the only SN for which we have observed the explosion with modern instruments and also observed the SNR phase (or at least the beginnings of the bona-fide SNR phase). HST images and integral field spectroscopy reveal an elongated distribution for the inner ejecta (Wang et al., 2002; Kjær et al., 2010). In the most recent study of the ejecta geometry, Larsson et al. (2012) noted that the degree of

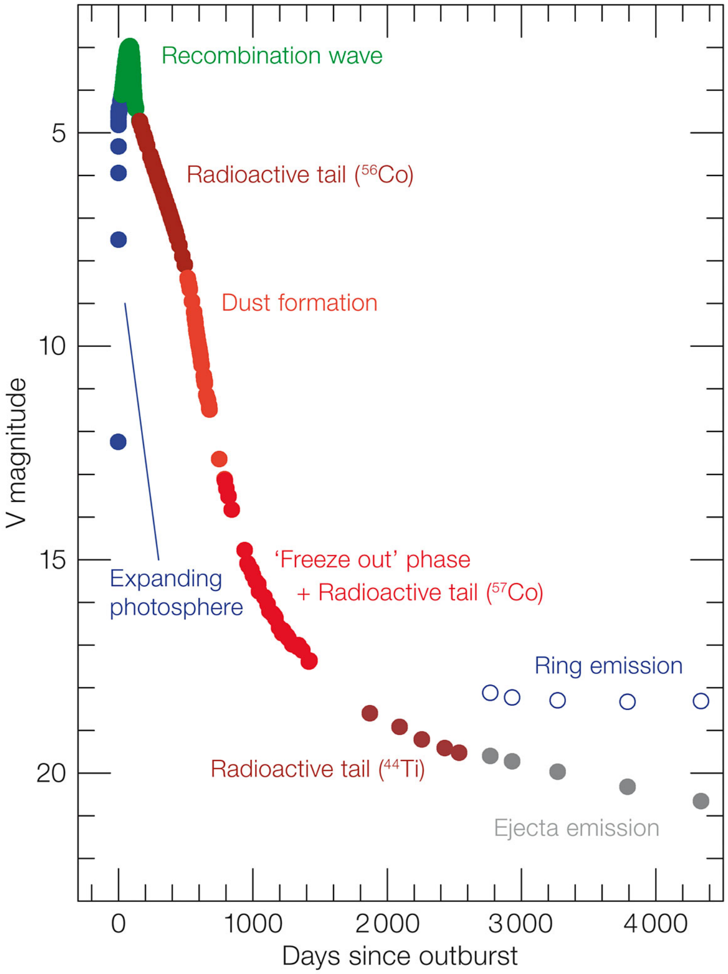

Figure 2.5: Optical lightcurve of SN 1987A for the first ∼ 10 years after core-collapse. Key aspects of the lightcurve are noted in the figure. Image credit: ESO.

asymmetry is higher than current explosion models predict. Linking asymmetries in the original outburst with asymmetries in the SNR is the subject of Chapter 5. Chapter 6 demonstrates how these types of causally-connected asymmetry studies can be extended to additional objects besides SN 1987A.

It should be stressed that although SN 1987A is a peculiar SNe due to its progenitor, other similar SNe have been observed (e.g. Schmitz & Gaskell, 1988; Young & Branch, 1988; Pastorello et al., 2012; Taddia et al., 2012). Most importantly, there is no evidence to suggest that the underlying mechanism driving the core-collapse explosion was unique to SN 1987A. To sweep it under the rug by calling it peculiar would be to discount 25 years of observations which have furthered our understanding of core-collapse supernovae. SN 1987A holds tremendous scientific interest in addition to being the ideal laboratory for the observations discussed throughout this thesis.

2.8 Cassiopeia A

Until recently, Cas A was the youngest known galactic SNR. That title now belongs to the $\sim$ 100-year-old SNR G1.9+0.3 (Reynolds et al., 2008). At a distance of $\sim$ 11000 ly, Cas A is a factor of $\sim$ 15 times closer than SN 1987A. Although the SNR expansion implies a 1681 ± 19 AD origin (Fesen et al., 2006b), there are no historical records of such a SN (Stephenson & Green, 2002). The precursor to the SNR is now known to be a Type IIb core-collapse SNe (Krause et al., 2008, and additionally confirmed by observations in Chapter 6). SNe of Type IIb represent $\lesssim 7\%$ of observed SNe in a volume-limited sample (Figure 2.1; Li et al., 2011).

The overall appearance, chemical composition, and ejecta kinematics all suggest that the Cas A SN was highly asymmetric (Hwang et al., 2004; Fesen et al., 2006b,a; Wheeler et al., 2008; DeLaney et al., 2010). The asymmetry is dominated by three key features:

1. Asymmetric Si-rich outflows, showing a northeast (NE) jet-like feature and southwest (SW) counterpart to that feature (Hughes et al., 2000; Hines et al., 2004; Hwang et al., 2004).

2. Asymmetric Fe-rich outflows in the NW and SE, redshifted and blueshifted, respectively (Hughes et al., 2000; Willingale et al., 2002).

3. An X-ray point source, presumed to be the remnant NS, with a proper motion of $\sim$ 330 km s^{-1} (Thorstensen et al., 2001), aligned within $\sim 30^\circ$ of the SE

Fe-rich outflow (Wheeler et al., 2008).

A debated topic is if the primary axis in the explosion mechanism is represented by the Si-rich NE-SW axis (Hughes et al., 2000; Hwang et al., 2004; Hines et al., 2004; Fesen et al., 2006b; Laming et al., 2006) or by the almost perpendicular Fe-rich NW-SE axis (Burrows et al., 2005; Wheeler et al., 2008; DeLaney et al., 2010). The focus of Chapter 6 is on observing asymmetries in the first few hundred days of the $\sim$ 330-year-old IIb SN and comparing to the above asymmetry features.

Bibliography

Akiyama, S. and Wheeler, J. C. and Meier, D. L. and Lichtenstadt, I. 2003, ApJ, 584, 954

Arcavi, I. 2012, in IAU Symposium, Vol. 279, IAU Symposium, 34–39

Arnett, D. 1991, ApJ, 383, 295

Arnett, W. D. 1969, Ap&SS, 5, 180

——. 1977, ApJ, 218, 815

——. 1982, ApJ, 253, 785

Arnett, W. D. and Bahcall, J. N. and Kirshner, R. P. and Woosley, S. E. 1989, ARA&A, 27, 629

Arnett, W. D. and Truran, J. W. 1969, ApJ, 157, 339

Arnett, W. D. and Truran, J. W. and Woosley, S. E. 1971, ApJ, 165, 87

Barkat, Z. and Rakavy, G. and Sack, N. 1967, Physical Review Letters, 18, 379

Benetti, S. and Cappellaro, E. and Mazzali, P. A. and Turatto, M. and Altavilla, G. and Bufano, F. and Elias-Rosa, N. and Kotak, R. and Pignata, G. and Salvo, M. and Stanishev, V. 2005, ApJ, 623, 1011

Bethe, H. A. and Wilson, J. R. 1985, ApJ, 295, 14

Bionta, R. M. and Blewitt, G. and Bratton, C. B. and Casper, D. and Ciocio, A. 1987, Physical Review Letters, 58, 1494

Blondin, J. M. and Mezzacappa, A. and DeMarino, C. 2003, ApJ, 584, 971

Bloom, J. S. and Kasen, D. and Shen, K. J. and Nugent, P. E. and Butler, N. R. and Graham, M. L. and Howell, D. A. and Kolb, U. and Holmes, S. and Haswell, C. A. and Burwitz, V. and Rodriguez, J. and Sullivan, M. 2012, ApJ, 744, L17

Burrows, A. 2013, Reviews of Modern Physics, 85, 245

Burrows, A. and Goshy, J. 1993, ApJ, 416, L75

Burrows, A. and Lattimer, J. M. 1985, ApJ, 299, L19

Burrows, A. and Walder, R. and Ott, C. D. and Livne, E. 2005, in Astronomical Society of the Pacific Conference Series, Vol. 332, The Fate of the Most Massive Stars, ed. R. Humphreys & K. Stanek, 350

Burrows, C. J. and Krist, J. and Hester, J. J. and Sahai, R. and Trauger, J. T. and Stapelfeldt, K. R. and Gallagher, III, J. S. and Ballester, G. E. and Casertano, S. and Clarke, J. T. and Crisp, D. and Evans, R. W. and Griffiths, R. E. and Hoessel, J. G. and Holtzman, J. A. and Mould, J. R. and Scowen, P. A. and Watson, A. M. and Westphal, J. A. 1995, ApJ, 452, 680

Canal, R. and Schatzman, E. 1976, A&A, 46, 229

Catchpole, R. M. and Menzies, J. W. and Monk, A. S. and Wargau, W. F. and Pollaco, D. and Carter, B. S. and Whitelock, P. A. and Marang, F. and Laney, C. D. and Balona, L. A. and Feast, M. W. and Lloyd Evans, T. H. H. and Sekiguchi, K. and Laing, J. D. and Kilkenny, D. M. and Spencer Jones, J. and Roberts, G. and Cousins, A. W. J. and van Vuuren, G. and Winkler, H. 1987, MNRAS, 229, 15P

Catchpole, R. M. and Whitelock, P. A. and Feast, M. W. and Menzies, J. M. and Glass, I. S. and Marang, F. and Laing, J. D. and Spencer Jones, J. H. and Roberts, G. and Balona, L. A. and Carter, B. S. and Laney, C. D. and Evans, L. T. and Sekiguchi, K. and Hutchinson, G. G. and Maddison, R. and Albinson, J. and Evans, A. and Allen, F. A. and Winkler, H. and Fairall, A. and Corbally, C. and Davies, J. K. and Parker, Q. A. 1988, MNRAS, 231, 75P

Chiotellis, A. and Schure, K. M. and Vink, J. 2012, A&A, 537, A139

Chornock, R. and Filippenko, A. V. and Li, W. and Silverman, J. M. 2010, ApJ, 713, 1363

Chugai, N. N. and Fabrika, S. N. and Sholukhova, O. N. and Goranskij, V. P. and Abolmasov, P. K. and Vlasyuk, V. V. 2005, Astronomy Letters, 31, 792

Colgate, S. A. and White, R. H. 1966, ApJ, 143, 626

Cordes, J. M. and Chernoff, D. F. 1998, ApJ, 505, 315

Couch, S. M. and Pooley, D. and Wheeler, J. C. and Milosavljević, M. 2011, ApJ, 727, 104

Couch, S. M. and Wheeler, J. C. and Milosavljević, M. 2009, ApJ, 696, 953

DeLaney, T. and Rudnick, L. and Stage, M. D. and Smith, J. D. and Isensee, K. and Rho, J. and Allen, G. E. and Gomez, H. and Kozasa, T. and Reach, W. T. and Davis, J. E. and Houck, J. C. 2010, ApJ, 725, 2038

Di Stefano, R. and Kilic, M. 2012, ApJ, 759, 56

Dilday, B. and Howell, D. A. and Cenko, S. B. and Silverman, J. M. and Nugent, P. E. and Sullivan, M. and Ben-Ami, S. and Bildsten, L. and Bolte, M. and Endl, M. and Filippenko, A. V. and Gnat, O. and Horesh, A. and Hsiao, E. and Kasliwal, M. M. and Kirkman, D. and Maguire, K. and Marcy, G. W. and Moore, K. and Pan, Y.

and Parrent, J. T. and Podsiadlowski, P. and Quimby, R. M. and Sternberg, A. and Suzuki, N. and Tytler, D. R. and Xu, D. and Bloom, J. S. and Gal-Yam, A. and Hook, I. M. and Kulkarni, S. R. and Law, N. M. and Ofek, E. O. and Polishook, D. and Poznanski, D. 2012, Science, 337, 942

Edwards, Z. I. and Pagnotta, A. and Schaefer, B. E. 2012, ApJ, 747, L19

Elmhamdi, A. and Danziger, I. J. and Chugai, N. and Pastorello, A. and Turatto, M. and Cappellaro, E. and Altavilla, G. and Benetti, S. and Patat, F. and Salvo, M. 2003, MNRAS, 338, 939

Falk, S. W. and Arnett, W. D. 1977, ApJS, 33, 515

Fesen, R. A. and Hammell, M. C. and Morse, J. and Chevalier, R. A. and Borkowski, K. J. and Dopita, M. A. and Gerardy, C. L. and Lawrence, S. S. and Raymond, J. C. and van den Bergh, S. 2006a, ApJ, 636, 859

——. 2006b, ApJ, 645, 283

Filippenko, A. V. 1997, ARA&A, 35, 309

Fryer, C. L. and Woosley, S. E. and Heger, A. 2001, ApJ, 550, 372

Gal-Yam, A. 2012, Science, 337, 927

Galama, T. J. and Vreeswijk, P. M. and van Paradijs, J. and Kouveliotou, C. and Augusteijn, T. and Böhnhardt, H. and Brewer, J. P. and Doublier, V. and Gonzalez, J.-F. and Leibundgut, B. and Lidman, C. and Hainaut, O. R. and Patat, F. and Heise, J. and in't Zand, J. and Hurley, K. and Groot, P. J. and Strom, R. G. and Mazzali, P. A. and Iwamoto, K. and Nomoto, K. and Umeda, H. and Nakamura, T. and Young, T. R. and Suzuki, T. and Shigeyama, T. and Koshut, T. and Kippen, M. and Robinson, C. and de Wildt, P. and Wijers, R. A. M. J. and Tanvir, N. and Greiner, J. and Pian, E. and Palazzi, E. and Frontera, F. and Masetti, N. and

Nicastro, L. and Feroci, M. and Costa, E. and Piro, L. and Peterson, B. A. and Tinney, C. and Boyle, B. and Cannon, R. and Stathakis, R. and Sadler, E. and Begam, M. C. and Ianna, P. 1998, Nature, 395, 670

Gao, Y. and Pritchet, C. 2013, AJ, 145, 83

Gawryszczak, A. and Guzman, J. and Plewa, T. and Kifonidis, K. 2010, A&A, 521, A38

González Hernández, J. I. and Ruiz-Lapuente, P. and Filippenko, A. V. and Foley, R. J. and Gal-Yam, A. and Simon, J. D. 2009, ApJ, 691, 1

Hammer, N. J. and Janka, H.-T. and Müller, E. 2010, ApJ, 714, 1371

Heger, A. and Fryer, C. L. and Woosley, S. E. and Langer, N. and Hartmann, D. H. 2003, ApJ, 591, 288

Heger, A. and Woosley, S. E. 2002, ApJ, 567, 532

Hillebrandt, W. and Niemeyer, J. C. 2000, ARA&A, 38, 191

Hines, D. C. and Rieke, G. H. and Gordon, K. D. and Rho, J. and Misselt, K. A. and Woodward, C. E. and Werner, M. W. and Krause, O. and Latter, W. B. and Engelbracht, C. W. and Egami, E. and Kelly, D. M. and Muzerolle, J. and Stansberry, J. A. and Su, K. Y. L. and Morrison, J. E. and Young, E. T. and Noriega-Crespo, A. and Padgett, D. L. and Gehrz, R. D. and Polomski, E. and Beeman, J. W. and Haller, E. E. 2004, ApJS, 154, 290

Hirata, K. and Kajita, T. and Koshiba, M. and Nakahata, M. and Oyama, Y. 1987, Physical Review Letters, 58, 1490

Howell, D. A. and Sullivan, M. and Nugent, P. E. and Ellis, R. S. and Conley, A. J. and Le Borgne, D. and Carlberg, R. G. and Guy, J. and Balam, D. and Basa, S.

and Fouchez, D. and Hook, I. M. and Hsiao, E. Y. and Neill, J. D. and Pain, R. and Perrett, K. M. and Pritchet, C. J. 2006, Nature, 443, 308

Hughes, J. P. and Rakowski, C. E. and Burrows, D. N. and Slane, P. O. 2000, ApJ, 528, L109

Hwang, U. and Laming, J. M. and Badenes, C. and Berendse, F. and Blondin, J. and Cioffi, D. and DeLaney, T. and Dewey, D. and Fesen, R. and Flanagan, K. A. and Fryer, C. L. and Ghavamian, P. and Hughes, J. P. and Morse, J. A. and Plucinsky, P. P. and Petre, R. and Pohl, M. and Rudnick, L. and Sankrit, R. and Slane, P. O. and Smith, R. K. and Vink, J. and Warren, J. S. 2004, ApJ, 615, L117

Iben, Jr., I. and Tutukov, A. V. 1984, ApJS, 54, 335

Kasen, D. 2010, ApJ, 708, 1025

Kasen, D. and Röpke, F. K. and Woosley, S. E. 2009, Nature, 460, 869

Kasen, D. and Woosley, S. E. and Heger, A. 2011, ApJ, 734, 102

Kerzendorf, W. E. and Schmidt, B. P. and Laird, J. B. and Podsiadlowski, P. and Bessell, M. S. 2012a, ApJ, 759, 7

Kerzendorf, W. E. and Yong, D. and Schmidt, B. P. and Simon, J. D. and Jeffery, C. S. and Anderson, J. and Podsiadlowski, P. and Gal-Yam, A. and Silverman, J. M. and Filippenko, A. V. and Nomoto, K. and Murphy, S. J. and Bessell, M. S. and Venn, K. A. and Foley, R. J. 2012b, ArXiv e-prints, 1210.2713

Khokhlov, A. M. and Höflich, P. A. and Oran, E. S. and Wheeler, J. C. and Wang, L. and Chtchelkanova, A. Y. 1999, ApJ, 524, L107

Kippenhahn, R. and Weigert, A. 1990, Stellar Structure and Evolution

Kirshner, R. P. and Kwan, J. 1974, ApJ, 193, 27

Kjær, K. and Leibundgut, B. and Fransson, C. and Jerkstrand, A. and Spyromilio, J. 2010, A&A, 517, A51

Krause, O. and Birkmann, S. M. and Usuda, T. and Hattori, T. and Goto, M. and Rieke, G. H. and Misselt, K. A. 2008, Science, 320, 1195

Kromer, M. and Sim, S. A. and Fink, M. and Röpke, F. K. and Seitenzahl, I. R. and Hillebrandt, W. 2010, ApJ, 719, 1067

Kunugise, T. and Iwamoto, K. 2007, PASJ, 59, L57

Laming, J. M. and Hwang, U. and Radics, B. and Lekli, G. and Takács, E. 2006, ApJ, 644, 260

Larsson, J. and Fransson, C. and Kjaer, K. and Jerkstrand, A. and Kirshner, R. P. and Leibundgut, B. and Lundqvist, P. and Mattila, S. and McCray, R. and Sollerman, J. and Spyromilio, J. and Wheeler, J. C. 2012, ArXiv e-prints, 1212.5051

Leonard, D. C. and Filippenko, A. V. 2005, in Astronomical Society of the Pacific Conference Series, Vol. 342, 1604-2004: Supernovae as Cosmological Lighthouses, ed. M. Turatto, S. Benetti, L. Zampieri, & W. Shea, 330

Li, W. and Leaman, J. and Chornock, R. and Filippenko, A. V. and Poznanski, D. and Ganeshalingam, M. and Wang, X. and Modjaz, M. and Jha, S. and Foley, R. J. and Smith, N. 2011, MNRAS, 412, 1441

Lopez, L. A. and Ramirez-Ruiz, E. and Castro, D. and Pearson, S. 2013, ApJ, 764, 50

Lu, F. J. and Wang, Q. D. and Ge, M. Y. and Qu, J. L. and Yang, X. J. and Zheng, S. J. and Chen, Y. 2011, ApJ, 732, 11

Luo, D. and McCray, R. 1991, ApJ, 379, 659

Maeda, K. 2012, in IAU Symposium, Vol. 279, IAU Symposium, 261–268

Maeda, K. and Benetti, S. and Stritzinger, M. and Röpke, F. K. and Folatelli, G. and Sollerman, J. and Taubenberger, S. and Nomoto, K. and Leloudas, G. and Hamuy, M. and Tanaka, M. and Mazzali, P. A. and Elias-Rosa, N. 2010a, Nature, 466, 82

Maeda, K. and Leloudas, G. and Taubenberger, S. and Stritzinger, M. and Sollerman, J. and Elias-Rosa, N. and Benetti, S. and Hamuy, M. and Folatelli, G. and Mazzali, P. A. 2011, MNRAS, 413, 3075

Maeda, K. and Taubenberger, S. and Sollerman, J. and Mazzali, P. A. and Leloudas, G. and Nomoto, K. and Motohara, K. 2010b, ApJ, 708, 1703

Maund, J. R. and Höflich, P. and Patat, F. and Wheeler, J. C. and Zelaya, P. and Baade, D. and Wang, L. and Clocchiatti, A. and Quinn, J. 2010, ApJ, 725, L167

Mayle, R. and Wilson, J. R. 1988, ApJ, 334, 909

Mazurek, T. J. 1982, ApJ, 259, L13

Menzies, J. W. and Catchpole, R. M. and van Vuuren, G. and Winkler, H. and Laney, C. D. and Whitelock, P. A. and Cousins, A. W. J. and Carter, B. S. and Marang, F. and Lloyd Evans, T. H. H. and Roberts, G. and Kilkenny, D. and Spencer Jones, J. and Sekiguchi, K. and Fairall, A. P. and Wolstencroft, R. D. 1987, MNRAS, 227, 39P

Mezzacappa, A. and Bruenn, S. W. 1993, ApJ, 405, 669

Mezzacappa, A. and Liebendörfer, M. and Messer, O. E. and Hix, W. R. and Thielemann, F.-K. and Bruenn, S. W. 2001, Physical Review Letters, 86, 1935

Milisavljevic, D. and Fesen, R. A. and Chevalier, R. A. and Kirshner, R. P. and Challis, P. and Turatto, M. 2012, ApJ, 751, 25

Milone, L. A. and Paolantonio, S. and Briggi, V. and Mendicini, D. and Minniti, E. 1988, Ap&SS, 150, 291

Morris, T. and Podsiadlowski, P. 2007, Science, 315, 1103

Müller, B. and Janka, H.-T. and Marek, A. 2012, ApJ, 756, 84

Murphy, J. W. and Burrows, A. 2008, ApJ, 688, 1159

Nakamura, F. and Umemura, M. 2001, ApJ, 548, 19

Nomoto, K. 1984, ApJ, 277, 791

——. 1987, ApJ, 322, 206

Nomoto, K. and Iwamoto, K. and Nakasato, N. and Thielemann, F.-K. and Brachwitz, F. and Tsujimoto, T. and Kubo, Y. and Kishimoto, N. 1997, Nuclear Physics A, 621, 467

Nomoto, K. and Sugimoto, D. and Neo, S. 1976, Ap&SS, 39, L37

Nordhaus, J. and Burrows, A. and Almgren, A. and Bell, J. 2010, ApJ, 720, 694

Nugent, P. E. and Sullivan, M. and Cenko, S. B. and Thomas, R. C. and Kasen, D. and Howell, D. A. and Bersier, D. and Bloom, J. S. and Kulkarni, S. R. and Kandrashoff, M. T. and Filippenko, A. V. and Silverman, J. M. and Marcy, G. W. and Howard, A. W. and Isaacson, H. T. and Maguire, K. and Suzuki, N. and Tarlton, J. E. and Pan, Y.-C. and Bildsten, L. and Fulton, B. J. and Parrent, J. T. and Sand, D. and Podsiadlowski, P. and Bianco, F. B. and Dilday, B. and Graham, M. L. and Lyman, J. and James, P. and Kasliwal, M. M. and Law, N. M. and Quimby, R. M. and Hook, I. M. and Walker, E. S. and Mazzali, P. and Pian, E. and Ofek, E. O. and Gal-Yam, A. and Poznanski, D. 2011, Nature, 480, 344

Pastorello, A. and Pumo, M. L. and Navasardyan, H. and Zampieri, L. and Turatto, M. and Sollerman, J. and Taddia, F. and Kankare, E. and Mattila, S. and Nicolas, J. and Prosperi, E. and San Segundo Delgado, A. and Taubenberger, S. and Boles, T. and Bachini, M. and Benetti, S. and Bufano, F. and Cappellaro, E. and Cason,

A. D. and Cetrulo, G. and Ergon, M. and Germany, L. and Harutyunyan, A. and Howerton, S. and Hurst, G. M. and Patat, F. and Stritzinger, M. and Strolger, L.-G. and Wells, W. 2012, A&A, 537, A141

Patat, F. and Taubenberger, S. and Benetti, S. and Pastorello, A. and Harutyunyan, A. 2011, A&A, 527, L6

Perlmutter, S. and Aldering, G. and Goldhaber, G. and Knop, R. A. and Nugent, P. and Castro, P. G. and Deustua, S. and Fabbro, S. and Goobar, A. and Groom, D. E. and Hook, I. M. and Kim, A. G. and Kim, M. Y. and Lee, J. C. and Nunes, N. J. and Pain, R. and Pennypacker, C. R. and Quimby, R. and Lidman, C. and Ellis, R. S. and Irwin, M. and McMahon, R. G. and Ruiz-Lapuente, P. and Walton, N. and Schaefer, B. and Boyle, B. J. and Filippenko, A. V. and Matheson, T. and Fruchter, A. S. and Panagia, N. and Newberg, H. J. M. and Couch, W. J. and Supernova Cosmology Project. 1999, ApJ, 517, 565

Phillips, M. M. 1993, ApJ, 413, L105

Podsiadlowski, P. 1992, PASP, 104, 717

Quimby, R. M. and Kulkarni, S. R. and Kasliwal, M. M. and Gal-Yam, A. and Arcavi, I. and Sullivan, M. and Nugent, P. and Thomas, R. and Howell, D. A. and Nakar, E. and Bildsten, L. and Theissen, C. and Law, N. M. and Dekany, R. and Rahmer, G. and Hale, D. and Smith, R. and Ofek, E. O. and Zolkower, J. and Velur, V. and Walters, R. and Henning, J. and Bui, K. and McKenna, D. and Poznanski, D. and Cenko, S. B. and Levitan, D. 2011, Nature, 474, 487

Reynolds, S. P. and Borkowski, K. J. and Green, D. A. and Hwang, U. and Harrus, I. and Petre, R. 2008, ApJ, 680, L41

Riess, A. G. and Filippenko, A. V. and Challis, P. and Clocchiatti, A. and Diercks, A. and Garnavich, P. M. and Gilliland, R. L. and Hogan, C. J. and Jha, S. and

Kirshner, R. P. and Leibundgut, B. and Phillips, M. M. and Reiss, D. and Schmidt, B. P. and Schommer, R. A. and Smith, R. C. and Spyromilio, J. and Stubbs, C. and Suntzeff, N. B. and Tonry, J. 1998, AJ, 116, 1009

Ruiz-Lapuente, P. and Comeron, F. and Méndez, J. and Canal, R. and Smartt, S. J. and Filippenko, A. V. and Kurucz, R. L. and Chornock, R. and Foley, R. J. and Stanishev, V. and Ibata, R. 2004, Nature, 431, 1069

Scalzo, R. A. and Aldering, G. and Antilogus, P. and Aragon, C. and Bailey, S. and Baltay, C. and Bongard, S. and Buton, C. and Childress, M. and Chotard, N. and Copin, Y. and Fakhouri, H. K. and Gal-Yam, A. and Gangler, E. and Hoyer, S. and Kasliwal, M. and Loken, S. and Nugent, P. and Pain, R. and Pécontal, E. and Pereira, R. and Perlmutter, S. and Rabinowitz, D. and Rau, A. and Rigaudier, G. and Runge, K. and Smadja, G. and Tao, C. and Thomas, R. C. and Weaver, B. and Wu, C. 2010, ApJ, 713, 1073

Schaefer, B. E. and Pagnotta, A. 2012, Nature, 481, 164

Schmitz, M. F. and Gaskell, C. M. 1988, in Supernova 1987A in the Large Magellanic Cloud, ed. M. Kafatos & A. G. Michalitsianos, 112–115

Shapiro, P. R. and Sutherland, P. G. 1982, ApJ, 263, 902

Shappee, B. J. and Kochanek, C. S. and Stanek, K. Z. 2013, ApJ, 765, 150

Silverman, J. M. and Ganeshalingam, M. and Li, W. and Filippenko, A. V. and Miller, A. A. and Poznanski, D. 2011, MNRAS, 410, 585

Smartt, S. J. 2009, ARA&A, 47, 63

Stephenson, F. R. and Green, D. A. 2002, Historical supernovae and their remnants, by F. Richard Stephenson and David A. Green. International series in astronomy and astrophysics, vol. 5. Oxford: Clarendon Press, 2002, ISBN 0198507666, 5

Sullivan, M. and Le Borgne, D. and Pritchet, C. J. and Hodsman, A. and Neill, J. D. and Howell, D. A. and Carlberg, R. G. and Astier, P. and Aubourg, E. and Balam, D. and Basa, S. and Conley, A. and Fabbro, S. and Fouchez, D. and Guy, J. and Hook, I. and Pain, R. and Palanque-Delabrouille, N. and Perrett, K. and Regnault, N. and Rich, J. and Taillet, R. and Baumont, S. and Bronder, J. and Ellis, R. S. and Filiol, M. and Lusset, V. and Perlmutter, S. and Ripoche, P. and Tao, C. 2006, ApJ, 648, 868

Taddia, F. and Stritzinger, M. D. and Sollerman, J. and Phillips, M. M. and Anderson, J. P. and Ergon, M. and Folatelli, G. and Fransson, C. and Freedman, W. and Hamuy, M. and Morrell, N. and Pastorello, A. and Persson, S. E. and Gonzalez, S. 2012, A&A, 537, A140

Thorstensen, J. R. and Fesen, R. A. and van den Bergh, S. 2001, AJ, 122, 297

Utrobin, V. P. and Chugai, N. N. 2011, A&A, 532, A100

Wang, L. and Wheeler, J. C. 2008, ARA&A, 46, 433

Wang, L. and Wheeler, J. C. and Höflich, P. and Khokhlov, A. and Baade, D. and Branch, D. and Challis, P. and Filippenko, A. V. and Fransson, C. and Garnavich, P. and Kirshner, R. P. and Lundqvist, P. and McCray, R. and Panagia, N. and Pun, C. S. J. and Phillips, M. M. and Sonneborn, G. and Suntzeff, N. B. 2002, ApJ, 579, 671

Webbink, R. F. 1984, ApJ, 277, 355

Wheeler, J. C. and Maund, J. R. and Couch, S. M. 2008, ApJ, 677, 1091

Wheeler, J. C. and Piran, T. and Weinberg, S. 1990, Supernovae. Proceedings.

Wheeler, J. C. and Yi, I. and Höflich, P. and Wang, L. 2000, ApJ, 537, 810

Whelan, J. and Iben, Jr., I. 1973, ApJ, 186, 1007

Willingale, R. and Bleeker, J. A. M. and van der Heyden, K. J. and Kaastra, J. S. and Vink, J. 2002, A&A, 381, 1039

Wilson, J. R. 1985, in Numerical Astrophysics, ed. J. M. Centrella, J. M. Leblanc, & R. L. Bowers, 422

Wongwathanarat, A. and Janka, H.-T. and Mueller, E. 2012, ArXiv e-prints, 1210.8148

Woosley, S. E. 1991, Supernovae. Proceedings.

——. 1997, ApJ, 476, 801

Woosley, S. E. and Blinnikov, S. and Heger, A. 2007, Nature, 450, 390

Young, T. R. and Branch, D. 1988, Nature, 333, 305

Chapter 3

Introduction to Scattered Light Echoes

In February of 1901, amateur astronomer Thomas David Anderson discovered Nova Persei 1901 (GK Persei), a cataclysmic variable star rivaling the brightness of Vega a day after its discovery. Later that year, both George Ritchey and Charles Dillon Perrine independently observed an apparently moving nebulosity around Nova Persei 1901 (Ritchey, 1901b,a; Perrine, 1901). The apparent proper motion of the nebulosity was the largest in the Universe to date (Perrine, 1901), and was superluminal for reasonable distance estimates. It was Kapteyn (1902) who first correctly interpreted the moving nebulosity as moving *illumination* of stationary dust. However, it was not until Couderc (1939) that the details and geometry of this phenomenon were worked out. Nova Persei 1901 was the first observation of a *scattered light echo.*

The presence of dust in the region surrounding a SN (or any varying source) allows for outburst light that would not otherwise arrive at Earth to be scattered off of dust towards the observer. Due to the longer path length and fixed speed of light, c, this scattered light will arrive at Earth at a delayed time $t_{obs} > t_0$, where t_0 is the time the direct light was first observed. This phenomenon of observing light from an outburst event at some delayed time describes a scattered light echo. In principle, the source of a LE can be any transient or variable astronomical source that produces variations in brightness. It is the brightness above the static flux output of a source that is relevant for scattered LEs. The focus of this thesis is LEs from SNe, where the static flux output is essentially zero.

3.1 Geometry

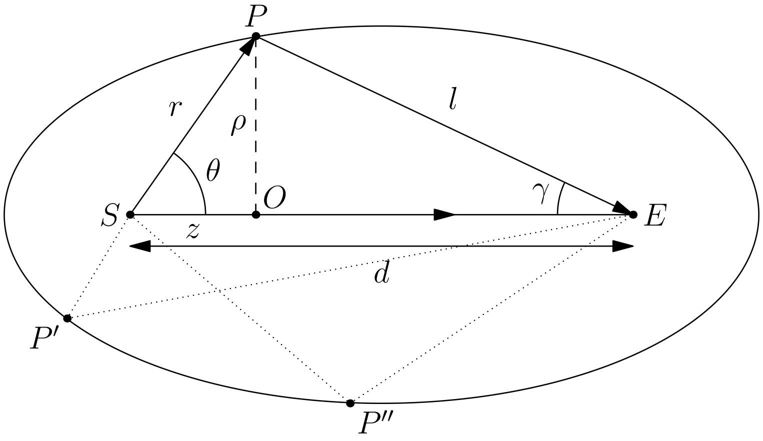

Figure 3.1: Two-dimensional representation of a scattered LE occurring at point P, due to a source event, S, and scattering towards Earth, E. For any given delay time, t, after the direct $S : E$ light has reached Earth, a LE could potentially be observed at any point (e.g., P, P', P'') on an ellipse with the source and Earth at the foci. In three dimensions the scattering surface is an ellipsoid. Notation partially adapted from Falla et al. (2003).

The power of scattered LEs as useful tools in astronomy is primarily due to the simplicity of the geometry in the problem. As mentioned above, this geometry was first established by Couderc (1939) and we summarize it here, reproducing the formalism of Tylenda (2004). Figure 3.1 shows the geometry of a LE due to dust at point P, a distance r from the source, S. The echo is at a distance l from Earth, E, and the source is a distance d away from Earth. z is the line of sight distance from the source to the echo, while ρ is the projected distance as seen on the sky. θ and γ are the angles formed from the line of sight, from the source to the echo and from the Earth to the echo, respectively. For simplicity, we consider the scenario in two dimensions.

Consider the two light paths, $S : E$ and $S : P : E$. For the former, an observer at Earth detects the outburst light from the source directly at time t_0. For the latter, a LE is observed at time t_{obs}, corresponding to a delay time $t = t_{obs} - t_0$. At any given time after t_0, a LE could be observed anywhere in the sky provided that the additional length of the $S : P : E$ light path corresponds to the delay time t. This iso-delay surface is an ellipse (ellipsoid in three dimensions) with the source and the Earth at the foci as depicted in Figure 3.1.

With the geometry laid out, we see that the scattered light has traveled an additional path length

$$ct = [r + l] - [d]. \tag{3.1}$$

Figure 3.1 is not to scale and in practice, $z << d$ ($\gamma \lesssim 8°$ for the the closest galactic LEs discussed in this thesis). That is, $l \simeq (d - z)$ and so $ct = r - z$. Squaring both sides and rearranging we get

$$r^2 + z^2 - 2rz = c^2t^2. \tag{3.2}$$

We can now take advantage of the fact that $r^2 = z^2 + \rho^2$ based on Figure 3.1 and $r = ct + z$, to rewrite as

$$\rho^2 = 2zct + c^2t^2, \tag{3.3}$$

which can be rewritten as

$$z = \frac{\rho^2}{2ct} - \frac{ct}{2}. \tag{3.4}$$

Equation 3.4 is referred to as *the light echo equation.* The power of the geometry of

LEs is illustrated in this equation, where $\rho = (d - z)\tan\gamma$ and so the exact distance, z, of the scattering dust in front of or behind the SN along the line of sight can be established with two observables: the time since the outburst, ct, and the angular separation of the LE, γ, if the distance to the source is known. However, even if the distance is not known, Equation 3.4 establishes exact *relative* distances between LEs from the same source with only these two observables. The applications of this are discussed in Section 3.7.

3.2 Apparent Motion

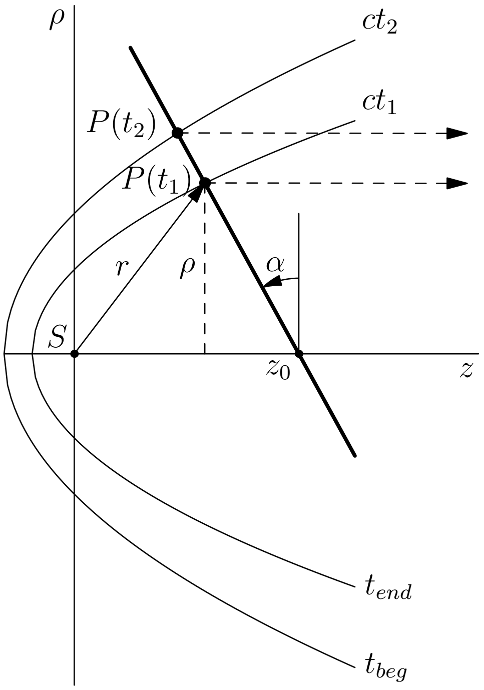

Figure 3.2: Illustrating the LE iso-delay ellipsoid approximated as a parabola (paraboloid in three dimensions) with the source event at the focus, as described by the LE equation (Equation 3.4). For increasing time t_{obs} and therefore increasing delay time t, the iso-delay parabola increases in size on the sky. LEs therefore have an apparent motion, $\dot{\rho}$, on the sky that can be observed. The thick line represents an inclined sheet of dust (inclination angle α), such that LEs are observed at $P(t_1)$ and $P(t_2)$.

As time increases so does the delay time, t, such that the iso-delay LE ellipsoid expands on the sky as a function of time. We illustrate the expansion in Figure 3.2, where two iso-delay parabolas are shown for times t_1 and t_2 such that the additional distances travelled are ct_1 and ct_2, with $ct_2 > ct_1$. A LE can only exist when there is a sufficient density of scattering dust. Therefore, with increasing time, the LE follows the scattering dust. LEs can be used to map the dust, as described in Section 3.7.1. Figure 3.2 outlines this scenario, where LEs occurring at $P(t_1)$ and $P(t_1)$ follow the inclined sheet of scattering dust.

The apparent motion, $\dot{\rho}$, of a LE on the sky is dependent on the orientation of the scattering dust. This is highlighted in Figure 3.3, where different scattering dust inclinations correspond to different apparent motions. Note that inclination, α, as defined here and throughout this thesis corresponds to the angle from the positive ρ axis to the negative z axis. Inclination is measured by monitoring the apparent motion of a LE over several epochs, as described in Section 4.9.1.

As described in Tylenda (2004) and in Section 4.9.1 below, Equation 3.3 can be generalized to the case of an inclined dust sheet as in Figure 3.2. If we define $z = z_0 - a\rho$, where $a = \tan\alpha$, then

$$\rho = -act \pm \sqrt{(1+a^2)(ct)^2 + 2z_0ct}. \tag{3.5}$$

The appearance and evolution of scattered LEs is now clear: Sheets of scattering dust, regardless of inclination, result in the appearance of circular rings of radius $\rho = \sqrt{(1+a^2)(ct)^2 + 2z_0ct}$, with the centre of the rings offset by $\rho_{offset} = -act$. The thickness on the sky of the rings, $\Delta\rho$, is dependent on the duration of the source outburst and is the subject of Chapter 4.

The apparent motion of the LE ring on the sky can be found via taking the time

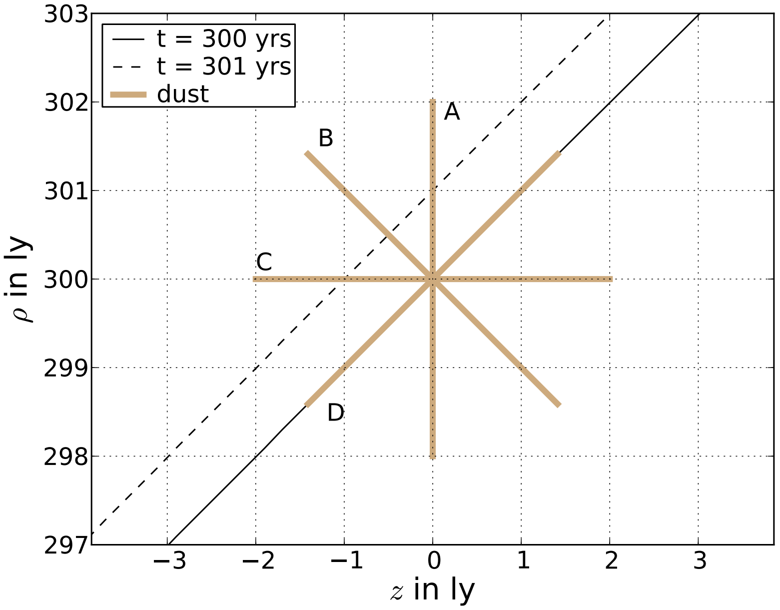

Figure 3.3: Solid and dashed lines show closeups of iso-delay parabolas (as in Figure 3.2) for delay times of 300 and 301 years, respectively. Four dust orientations are shown, A, B, C, D, having inclinations $\alpha = 0°, 45°, 90°, 135°$, respectively. Apparent motions for LEs due to scattering dust A, B, C, D are $\dot{\rho} = 1.0c, 0.5c, 0.0c, \infty$, respectively. Dust inclinations of $-45° < \alpha < 0°$ correspond to superluminal motion $\dot{\rho} > c$. Figure appears as Figure 4 in Rest et al. (2012b), reproduced with permission.

derivative of Equation 3.5:

$$\dot{\rho} = c \times \Big[-a \pm \frac{(1+a^2)(ct) + z_0}{\sqrt{(1+a^2)(ct)^2 + 2z_0 ct}} \Big], \tag{3.6}$$

which is often superluminal. It should be noted that Equation 3.6 represents the projected apparent motion of a patch of LE monitored on the sky. This is different than the physical expansion rate of the LE ring diameter on the sky, which is always $\geq c$. Complete rings are rarely observed. Typical apparent motions discussed in this thesis are $2''\mathrm{yr}^{-1} - 6''\mathrm{yr}^{-1}$ (SN 1987A LEs) and $\sim 30''\mathrm{yr}^{-1}$ (Cas A LEs), both describing superluminal motion. No information is traveling greater than c, however, since a LE is simply the illumination of stationary scattering dust that appears as a proper motion on the sky.

Due to their apparent motion, LEs can be discovered through difference imaging. Multiple observations of the same pointing on the sky are taken with epochs separated by several months. Examples of such difference images are given in Figure 5.1 (SN 1987A) and Figure 6.2 (Cas A). The LE imaging discussed in this thesis was reduced using the ESSENCE/SuperMACHO data reduction and differencing pipeline *photpipe* (Rest et al., 2005a; Garg et al., 2007; Miknaitis et al., 2007).

3.3 Light Echoes as Distance Indicators

The angular separation, γ, from a LE to its source can be measured precisely. The small angle approximation (valid for observed LEs) gives $\gamma = \rho/(d-z)$. The simplest geometry (mathematically, not physically), is a thin, spherical dust shell surrounding the source,

$$\gamma_{sphere} = \frac{\sqrt{2rct-(ct)^2}}{d}, \tag{3.7}$$

where r denotes the radius of the spherical dust distribution (Tylenda, 2004). In the case of a sheet of dust as described above,

$$\gamma_{sheet} = \frac{-act \pm \sqrt{(1+a^2)(ct)^2 + 2z_0ct}}{d}, \tag{3.8}$$

which simplifies to $\gamma_{sheet} = ct/d$ in the special case that $a = z_0 = 0$. In principle, the distance to the source can be extracted by monitoring γ as a function of time and fitting for (d, r) or (d, a, z_0) in Equations 3.7 and 3.8, respectively (e.g. van Loon et al., 2004; Crause et al., 2005; Ortiz et al., 2010). However, large systematic uncertainties can result depending on the degeneracy-breaking assumptions being made about the scattering dust geometry or the outburst timing.

Sparks (1994, 1996) described the potential of polarizations measurements to obtain accurate distance measurements with minimal assumptions. Maximum polarization occurs for scattering angles of 90° in normal scattering conditions (Draine, 2003), which corresponds to the simplified case of $\gamma = ct/d$. Therefore if multiple LEs are observed behind and in front of the source, the angular distance to the LE corresponding to maximum polarization gives the distance to the source, $d = ct/\gamma$, if the delay time is known. Systematic uncertainties associated with the scattering dust and maximum polarization angle are typically $< 10\%$ (e.g. Sparks et al., 2008).

3.4 Light Echo Profiles

The source event of a LE is treated as a light pulse of duration δt_{SN} (typically months to several years for SNe). In order to distinguish echo light from the light received directly, we require the delay time, t, to be sufficiently larger than δt_{SN}. With this in mind, the two iso-delay surfaces of Figure 3.2 can be interpreted in two ways. In the first interpretation $\Delta t = t_2 - t_1 >> \delta t_{SN}$, and the iso-delay surfaces represent two unique surfaces on the sky where a LE of the source event can be observed at $P(t_1)$ and $P(t_2)$. In the scenario where $\Delta t \simeq \delta t_{SN}$, however, the two surfaces correspond to the beginning and end of the source event light curve. Since the beginning of the outburst corresponds to a longer delay time, the end of the outburst appears closest to the source.

The flux profile of a LE as a function of ρ, the projected distance from the source event, is a *light echo profile* and is the subject of intensive inquiry in Chapter 4 and is tested thoroughly in Chapter 5. Figure 3.4 shows an example LE profile from SN 1987A, where the reversed lightcurve shape is clearly seen in the data. In theory, an observed LE profile is the original lightcurve of the source event projected onto the sky. In practice, however, the flux profile is more complicated and the consequences of such effects is a dominant theme of this thesis. These complications

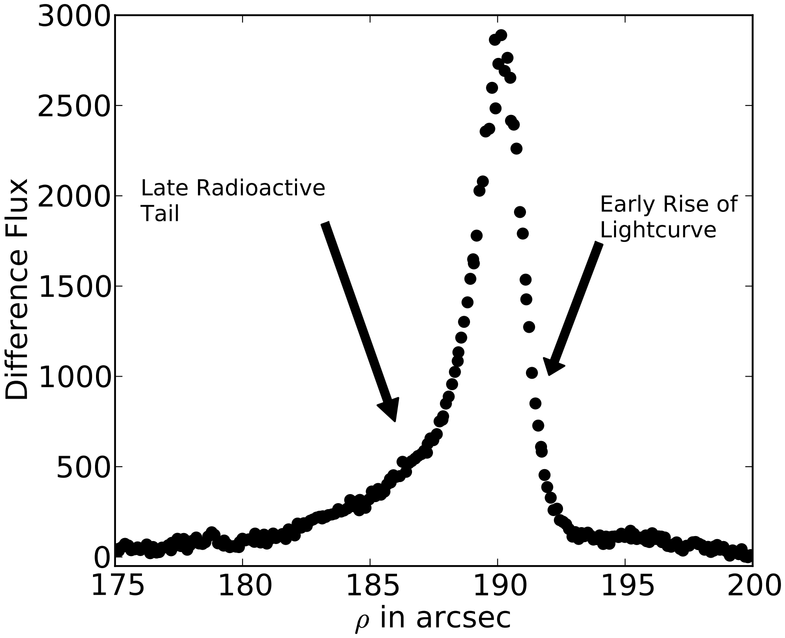

Figure 3.4: Example LE profile of SN 1987A LE. The overall shape of the reversed SN lightcurve can be seen in the profile: the late-epoch radioactive tail of the lightcurve at small ρ values followed by the shorter early rise of the lightcurve at larger ρ values after the LE peak.

can be summarized as follows:

1. The projected lightcurve of the source event is stretched or compressed on the sky depending on the inclination of the scattering dust.
2. In practice, the scattering dust has an associated thickness ($0.03 - 1.00$ ly for Galactic Cas A LEs; $0.5 - 5.5$ ly for LMC SN 1987A LEs), implying multiple epochs from the source lightcurve can contribute to a single line of sight.
3. The flux profile is further convolved due to the effects of astronomical seeing (increased point spread functions due to the atmosphere).

In Chapter 4 we describe and test a method for taking into account the above complications to model LE profiles.

3.5 Dust Scattering and Light Echo Surface Brightness

In the above description of scattered LEs and throughout this thesis, we assume that only one scattering event occurs. Such an assumption is known as the *single-scattering approximation*. Under such circumstances the surface brightness of a LE can be derived (e.g. Dwek, 1983; Chevalier, 1986; Schaefer, 1987; Sparks, 1994; Xu et al., 1994; Sugerman, 2003; Sugerman et al., 2005; Patat, 2005; Rest et al., 2012b). We reproduce the formalism of Sugerman (2003), also used in Rest et al. (2012b). The integrated scattering function, $S_X(\lambda, \mu)$, describes the wavelength-dependent scattering efficiency of a dust grain of type X and may be defined as

$$S_X(\lambda, \mu) = \int Q_{SC,X}(\lambda, a)\sigma_g \Phi_X(\mu, \lambda, a) f_X(a) da, \tag{3.9}$$

where $\mu = \cos\theta$, a is the radius of the dust grain, $Q_{SC,X}(\lambda, a)$ is the grain scattering efficiency for grain type X, and σ_g is the grain cross-section given by $\sigma_g = \pi a^2$. Φ_X is the phase function from Henyey & Greenstein (1941):

$$\Phi_X(\mu, \lambda, a) = \frac{1 - g_X^2(\lambda, a)}{[1 + g_X^2(\lambda, a) - 2g_X(\lambda, a)\mu]^{2/3}}, \tag{3.10}$$

where $g_x(\lambda, a)$ denotes the degree of forward scattering for a grain of type X, with $g = 0$ corresponding to isotropic scattering. As reviewed in Rest et al. (2011b), X may denote silicon dust grains, carbonaceous dust grains with a neutral polycyclic aromatic hydrocarbon component, or carbonaceous dust grains with an ionized polycyclic aromatic hydrocarbon. In Equation 3.9, $f_X(a)$ denotes the grain size distribution for grain type X, and is

$$f(a) \equiv \frac{1}{n_H} \frac{dn_{gr}}{da} \tag{3.11}$$

from Weingartner & Draine (2001), where $n_{gr}(a)$ denotes the number density of grains smaller than size a and n_H is the number density of hydrogen nuclei. Values for $Q_{SC,X}(\lambda, a)$, $g_X(\lambda, a)$, and $f_X(a)$ can be determined using the models of Weingartner & Draine (2001) and Li & Draine (2001) as described in detail in Rest et al. (2012b). Summing $S_X(\lambda, \mu)$ over the different grain types gives the total integrated scattering function, $S(\lambda, \mu)$. For the typical SN 1987A LEs discussed in this thesis, where $\theta \sim 20°$, the scattering efficiency is roughly triple at 4000Å compared to 8000Å (Rest et al., 2012b). The observed efficiency deviates considerably from the strictly Rayleigh scattering limit where $S \propto \lambda^{-4}$. The effect of scattering efficiency is important when comparing LE spectra to historical SN spectra, and is therefore taken into account in the LE spectroscopy work of Chapter 5.

With the integrated scattering efficiency known, the surface brightness flux, f_{SB}, of scattered light can be derived as

$$f_{SB}(\lambda, t, \phi) = F(\lambda) n_H(\mathbf{r}) \frac{c\Delta z}{4\pi r \rho \Delta\rho} S(\lambda, \mu) \tag{3.12}$$

from Sugerman (2003), where $F(\lambda)$ is the lightcurve-weighted integrated flux from the source event, Δz is the LE thickness along the line of sight, and $\Delta\rho$ is the LE thickness projected on the sky. In Chapers 5 and 6 we use a Gaussian dust density distribution when modelling our LE flux profiles on the sky. For the SN 1987A LEs in Chapter 5, the surface brightness varies from 19.3 mag arcsec^{-2} to $\sim$ 24 mag arcsec^{-2} in the "VR" filter ($\lambda_c = 625$ nm, $\Delta\lambda = 220$ nm). For Cas A LEs discussed in Chapter 6, the LEs are fainter with surface brightness from $\sim$ 22 mag arcsec^{-2} to $\sim$ 24 mag arcsec^{-2} in the R filter ($\lambda_c = 651$ nm, $\Delta\lambda = 151$ nm).

As previously stated, the above framework relies on the single-scattering approximation. The impact of multiple-scatterings can be seen in the work by Chevalier (1986) and Patat (2005), where it was shown that the single-scattering approximation is sound for dust optical depths $\tau_d \lesssim 0.3$. For the LEs considered in this thesis, this criterion is valid both with respect to the line of sight optical depth and the optical depth through the LE scattering material itself, as derived by Romaniello et al. (2005).

3.6 Light Echo Spectroscopy

A major focus of this thesis is spectroscopy of scattered LEs, which takes advantage of the partially preserved spectral energy distribution (SED) of the scattered source event. A spectroscopic slit can be placed on a scattered LE after discovery, allowing the source event to be viewed via spectroscopy hundreds of years after it has occurred. Astronomers can therefore overcome one of their biggest challenges: time. The transition between SNe and their corresponding SNR-phases is not well understood due to the timescales involved. SN 1987A represents a rare instance where astronomers are currently witnessing this transition and evolution phase. LE spectroscopy provides a direct causal connection between the spectroscopic properties of a SN explosion and the properties of its bona fide remnant stage.

Here and throughout this thesis we are referring to the tool of *targeted* LE spectroscopy on resolved LEs. The LEs are resolved such that the SNR-to-LE projected distance on the sky, ρ, is sufficiently large that the direct line of sight observation is distinct from the LE observation. Secondly, "targeted" implies a motivation to actively seek out these LEs and point the telescope at the position of the LE rather than at the position of the source, and to use these LEs as a means of understanding the source event. However, LE spectroscopy can also refer to the situation where the LE and the source are unresolved on the sky. An example of unresolved LEs is shown in Figure 3.5, where typical nebular spectra of SN 1991T and SN 1998bu at 1 yr after explosion abruptly change to resemble maximum light spectra at 2 yr after explosion. The presence of a LE in the 2 yr spectra was confirmed for SN 1991T and SN 1998bu by successful modelling with time-integrated (i.e. LE) spectra by Schmidt et al. (1994) and Cappellaro et al. (2001), respectively. Patat (2005) computed that

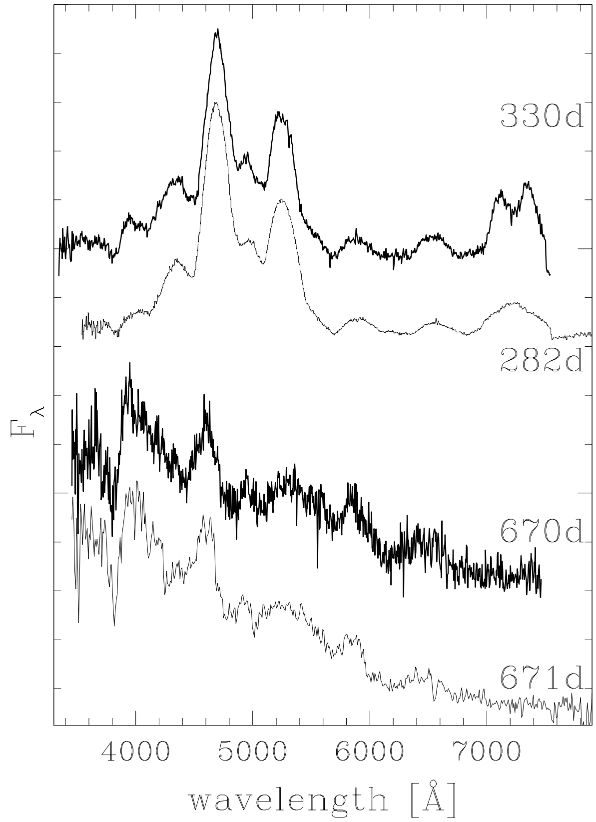

Figure 3.5: From Cappellaro et al. (2001), showing direct line of sight spectra of SN 1998bu (thick lines) and SN 1991T (thin lines) at roughly 1 yr and 2 yr after explosion. At 1 yr both SNe show evidence of typical nebular spectra with strong emission features. At 2 yr broad P Cygni features in spectra are more typical of maximum light features, indicating the presence of an unresolved LE. Figure from Cappellaro et al. (2001), reproduced here with permission.

for Type Ia SNe with dust densities on the order of 1 cm^{-3} along the line sight, unresolved LEs can occur $\sim$ 10 mag fainter than the peak SN brightness. The unresolved LEs typically appear after 2-3 yr once the original declining outburst has faded sufficiently. Recognizing and taking into the effects of unresolved LEs on SN lightcurves and spectra is particularly important when using Type Ia SNe as standard candles in cosmology (Patat et al., 2006).

Unlike unresolved LE spectroscopy, which is often used to correct and regain the original source outburst, the purpose of targeted LE spectroscopy in this thesis is to directly observe the source event in a new manner: either for the first time (as in Cas A) or from multiple perspectives (as in Cas A and SN 1987A). The work on LE profiles presented in Chapters 4 and 5 is a requirement for correctly interpreting the observed source signal from a LE.

The primary purpose of Chapter 4 is to remove assumptions and attempt to calculate the LE spectrum of a source directly from its observed LE profile on the sky. As discussed in Section 3.4, there are multiple effects that contribute to the shape of an observed LE profile. Since LE spectroscopy is performed by placing a spectroscopic slit onto the LE profile, these same effects play a large role in interpreting LE spectra. For example, if a LE profile is stretched or compressed on the sky due to the inclination of the scattering dust, a typical $1''$ wide spectroscopic slit will "pick out" a narrower or wider range of epochs in the explosion, respectively. Similarly, a typical LE profile such as in Figure 3.4 is $10'' - 12''$ wide, therefore the location of a $1''$ wide slit with respect to the LE peak can bias the spectrum towards earlier or later epochs of the SN lightcurve. The following effects play a role in determining the relative contributions of each epoch in the resulting LE spectrum:

1. The inclination of the scattering dust.
2. The width (i.e. depth along the line of sight) of the scattering dust.
3. The width of the slit.
4. The position of the centre of the slit with respect to the peak of the LE profile.
5. The tilt of the slit with respect to the orientation of the LE.
6. The angular point-spread function at time of spectroscopy.

Each of the above effects are taken into consideration in the model presented in Chapter 4. If the relative contributions can be determined, the only remaining unknown in the observed LE is the original source function: the SN lightcurve. For SN 1987A in Chapter 5 we know the SN lightcurve precisely, making the LEs of SN 1987A an excellent testing site for LE models. For Cas A in Chapter 6, the approximately 330-year-old SN lightcurve is not known. Instead, multiple template lightcurves and spectra from previously observed SNe of different types are used to determine the best match to the observed LE spectrum. Using this technique Krause et al. (2008a) and Krause et al. (2008b) were able to determine unambiguously that the Cas A and Tycho SNe were of Type IIb and Type Ia, respectively.

3D Spectroscopy LE spectroscopy also offers the ability to search for asymmetries in the original source event and is the primary science technique demonstrated in Chapters 5 and 6. Figure 3.6 illustrates the technique for the Cas A LEs discovered by Rest et al. (2005b), where each LE corresponds to a unique line of sight with which the SN photosphere can be spectroscopically observed. Unlike the methods of observing SN asymmetries discussed in Section 2.6, 3D LE spectroscopy is an entirely direct asymmetry probe whereby photons emitted from different regions of the photosphere may be spectroscopically observed.

3.6.1 LE Spectroscopy in Practice

Due to the nature of queue observing on large 8m-class telescopes, target locations for LE slit placement must typically be defined weeks before observations take place. For Galactic LEs such as Cas A, a two-week period corresponds to an apparent proper motion of $> 1''$. In Section 5.3.2.2 we show the effect of a $1''$ slit offset from the LE peak, highlighting the necessity of taking into account this slit offset when interpreting LE spectroscopy. A successful LE spectroscopy campaign should be accompanied by sufficient imaging such that the current apparent motion of the LE can be used to *predict* the LE location at time of spectroscopy to minimize slit offset. Imaging is also used to observe the LE profile such that it can be modelled to extract the properties

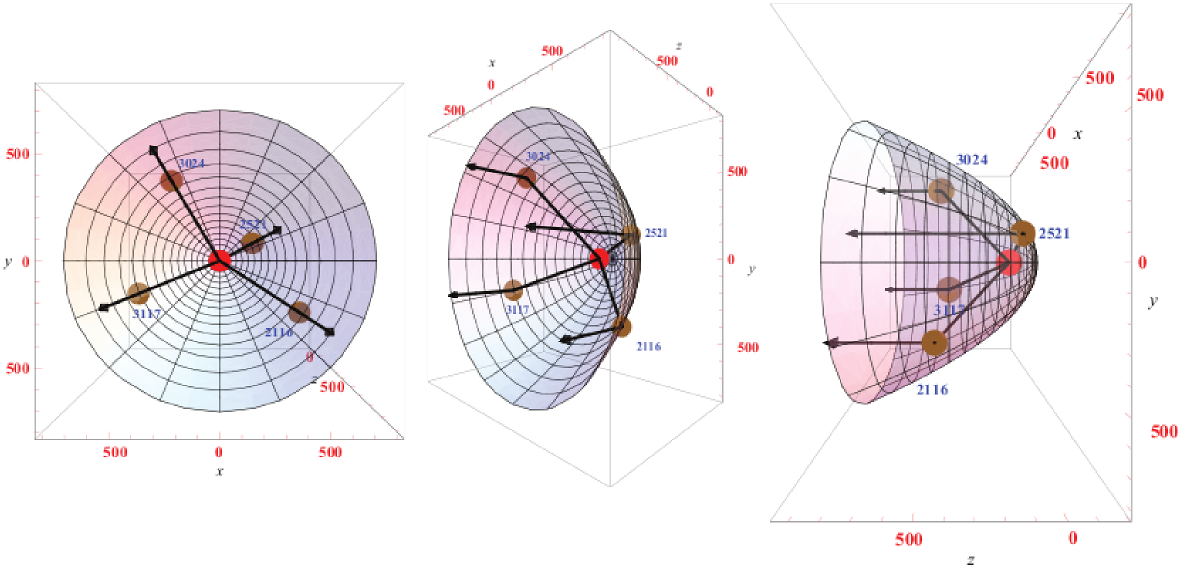

Figure 3.6: Illustration of Cas A LEs showing how they can be used to probe the SN explosion for asymmetries. Cas A is shown in red, with the four brown dots showing the location of the LEs discovered by Rest et al. (2005b). Also shown is the intersection of the LEs with the iso-delay ellipsoidal surface as described in Section 3.1. Figure appears as Figure 7 in Rest et al. (2012b), reproduced with permission.

of the scattering dust.

An example of the actual data used in this thesis is shown in Figure 3.7. The LE spectra contain faint, broad high-velocity absorption and emission flux from the SN explosion. However, the LE spectra also contain much brighter narrow non-SN emission features from the sky background, in addition to image artifacts caused by cosmic rays, CCD charge traps and CCD chip gaps. It is the underlying diffuse flux associated with the SN that is the scientifically useful data for this thesis.

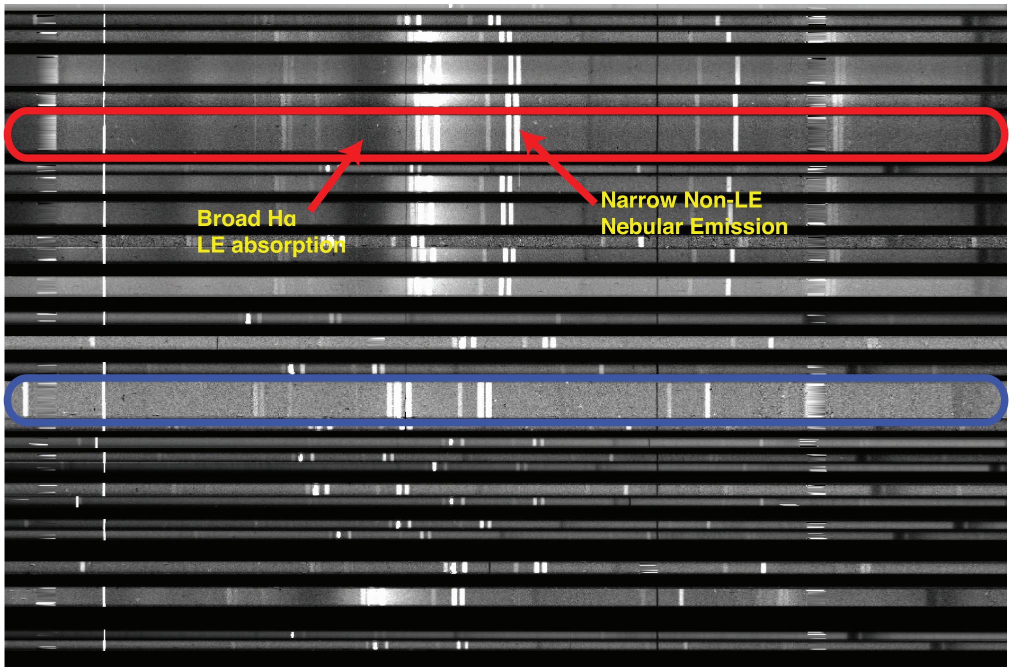

Figure 3.7: Partially reduced Gemini two-dimensional multi-object spectroscopy image from SN 1987A data presented in Chapter 5. The lower spectrum highlighted in blue is a background sky spectrum, showing only narrow nebular emission lines not associated with the SN. The upper spectrum highlighted in red is a LE spectrum, where diffuse broad absorption and emission flux associated with the high-velocity SN can be seen over the underlying nebular emission.

3.7 Previous Light Echo Applications in Astronomy

The field of scattered LEs has evolved tremendously since the geometric details of Nova Persei 1901's LE were first established by Couderc (1939). We briefly summarize the major observational developments in the field in this section. Table 3.1 summarizes the known objects to have observational evidence for scattered LEs from their sources. This list encompasses all known scattered LEs to date (27), highlighting how rare these objects actually are.

Table 3.1. List of known sources with evidence for scattered light echoes, partially adapted from material in Sugerman (2003) and Rest et al. (2012b).

Object	Source Type	References
Nova Persei 1901[a]	Cataclysmic variable	Ritchey (1901b,a); Perrine (1901)
Nova Sagittarii 1936	Cataclysmic variable	Swope (1940)
Nova Cygni 1975	Cataclysmic variable	Bode & Evans (1985)
OH 231.8+4.2	Mira variable	Kastner et al. (1992, 1998)
V838 Mon	Eruptive variable	Bond et al. (2003)
RS Pup	Cepheid variable	Westerlund (1961); Havlen (1972)
S CrA	T Tauri star	Ortiz et al. (2010)
R CrA	Herbig Ae/Be star	Ortiz et al. (2010)
SN 1980K	SN IIL	Sugerman et al. (2012)
SN 1987A[a]	SN II	Crotts (1988); Suntzeff et al. (1988)
SN 1991T	SN Ia	Schmidt et al. (1994); Sparks et al. (1999)
SN 1993J	SN Ib	Sugerman & Crotts (2002); Liu et al. (2003)
SN 1995E	SN Ia	Quinn et al. (2006)
SN 1998bu	SN Ia	Garnavich et al. (2001); Cappellaro et al. (2001)
SN 2002hh	SN IIP	Welch et al. (2007); Otsuka et al. (2012)
SN 2003gd	SN IIP	Sugerman (2005); Van Dyk et al. (2006); Otsuka et al. (2012)
SN 2004et	SN IIP	Otsuka et al. (2012)
SN 2006X	SN Ia	Wang et al. (2008); Crotts & Yourdon (2008)
SN 2006bc	SN II	Gallagher et al. (2012); Otsuka et al. (2012)
SN 2006gy	SN IIn	Miller et al. (2010)
SN 2007it	SN IIP	Andrews et al. (2011)
SNR 0519-69.0	SN Ia	Rest et al. (2005b)
SNR 0509-67.5[a]	SN Ia	Rest et al. (2005b)
SNR N103B	SN Unknown	Rest et al. (2005b)
Cas A[a]	SN IIb	Rest et al. (2007, 2008b); Krause et al. (2008a)
Tycho[a]	SN Ia	Rest et al. (2007, 2008b); Krause et al. (2008b)
η **Car**[a]	Eruptive variable	Rest et al. (2012a)

[a] Targeted spectroscopy of scattered LEs exists.

3.7.1 Mapping Interstellar and Circumstellar Material

As previously stated, the simple geometry of LEs allows the exact determination of 3-dimensional dust locations surrounding the source, with only the distance affecting the uncertainty since the delay-time and angular separation are usually known to very good precision. Relative 3-dimensional dust locations are immune to this uncertainty. LEs are therefore excellent probes of circumstellar and interstellar material surrounding eruptive environments.

The vast quantity of resolved LEs around SN 1987A has allowed its dusty environment to be mapped in detail. The circumstellar material was mapped to provide insight into the mass-loss history of the progenitor system (Crotts & Kunkel, 1991; Crotts et al., 1995; Crotts & Heathcote, 2000; Sugerman et al., 2005; Sugerman, 2005), while the interstellar material was also mapped to identify SN 1987A's local environment within the LMC (Xu et al., 1994, 1995; Xu & Crotts, 1999).

Tylenda (2004) and Tylenda & Kamiński (2012) studied the material around V838 Mon using scattered LEs from its 2002 major outburst. Beautiful images of the LE were captured by Hubble Space Telescope (Bond et al., 2003; Bond, 2007), shown in Figure 3.8. Ortiz et al. (2010) discovered LEs around the young T Tauri star S CrA. They found the apparent motion of the LEs were best fit with an incomplete spherical shell or an inclined torus model for the scattering dust, concentrated within 10 000 AU from the star. They note the dust structure may be an analogue to the Solar System Oort cloud. Most recently, Sugerman et al. (2012) modelled the LEs of SN 1980K to find circumstellar material in a thin shell $14-15$ ly from the progenitor.

3.7.2 Distance Indicators

Based on its LEs, Crause et al. (2005) used the parameter fitting method described above to obtain a distance to V838 Mon $d = 8.9 \pm 1.6$ kpc and $d = 12.0 \pm 6.5$ kpc using spherical and sheet models for the scattering dust, respectively. Sparks et al. (2008) greatly improved this measurement by using polarization data to obtain $d =$

Figure 3.8: False-coloured Hubble Space Telescope image of light echoes from V838 Mon's 2002 giant eruption. Image courtesy of NASA and STScI.

6.1 ± 0.6 kpc.

Kervella et al. (2008) claimed a distance $d = 1992 \pm 28$ pc to the Cepheid RS Pup based on its LEs. However, Bond & Sparks (2009) identified flawed assumptions about the scattering dust geometry, invalidating the result. Ortiz et al. (2010) used a similar method to derive a distance to S CrA of $d = 128 \pm 16$ pc based on its LEs. But again, assumptions were made by the authors about the dust geometry as highlighted in Rest et al. (2012b).

3.7.3 Targeted LE spectroscopy

The first LE spectrum was of the apparently moving nebulosity of Nova Persei 1901 taken by Perrine (1903). With his 35-hour LE spectrum, Perrine was able to note that the LE spectrum was most similar to spectra of Nova Persei 1901 taken in early 1901 near maximum brightness, rather than spectra at later epochs. This spectrum would be the first observational evidence that the scattered LE interpretation of Kapteyn (1902) was indeed correct.

Another LE spectrum would not be taken for over 80 years, until the discovery of LEs from SN 1987A. Both Gouiffes et al. (1988) and Suntzeff et al. (1988) obtained spectra of SN 1987A's outer LE ring. Both groups confirmed that the LE spectra resembled a maximum light spectrum, and went on to show that time-integration effects appeared in the spectra. Smith et al. (2003) performed spectroscopy of η Carinae's Homunculus Nebula at multiple positions to observe the outflow from different latitudes. However, it should be noted that this is spectroscopy of a reflection nebula rather than a scattered LE as traditionally defined.

The first ancient SN to be typed by a LE spectrum corresponded to SNR 0509-675 in the LMC, and was found to be an overluminous Type Ia by Rest et al. (2008a). The Galactic SNe that caused the Cas A and Tycho remnants were spectroscopically typed as Type IIb and Type Ia by Krause et al. (2008a) and Krause et al. (2008a), respectively. 3D LE spectroscopy was performed by Sinnott et al. (2013) and Rest et al. (2011a) on SN 1987A and Cas A, respectively, and is reproduced in this thesis as Chapters 5 and 6. Rest et al. (2012a) performed LE spectroscopy for the first time on a luminous blue variable by obtaining a spectrum of η Car's 19^{th}-century "Great Eruption."

3.7.4 Additional Astronomical Time-Delay Events

Other applications exist in astronomy where similar time-delay effects pay a key role, even if they are not the subject of this thesis. All of these additional tools use time-delay effects to overcome spatial or temporal resolutions that are unattainable by other means.

Infrared Echoes Instead of scattering directly, the source outburst may heat the surrounding dust resulting in infrared emission at longer wavelengths. For examples of infrared LEs from SN sources, see Dwek (1983); Krause et al. (2005); Kotak et al. (2009); Besel & Krause (2012); Vogt et al. (2012).

Recombination Echoes Emission can also be due to recombination lines from source photons which are absorbed by the scattering dust. A famous example of a recombination echo is the illumination of SN 1987A's circumstellar rings. Panagia et al. (1991) determined a geometrical distance to the LMC of $d = 50.1 \pm 3.1$ kpc using time-delay effects of the gaseous emission from the inner ring.

Reverberation Mapping Time-delay effects occur in the broad-line region of AGN. In the analogy to scattered LEs, the "source" is the fluctuating continuum emission due to the AGN, while the "echo" is the emission line response due to the fluctuating continuum. By monitoring the continuum and the emission as a function of time, the structure and geometry of the broad-line region can be probed (Blandford & McKee, 1982; Peterson, 1993).

Ionization Echoes The recently discovered ionized gas cloud "Hanny's Voorwerp" has been interpreted as a quasar LE in IC 2497 by Lintott et al. (2009). Additional observations agree with the interpretation of an ionization echo (Rampadarath et al., 2010; Keel et al., 2012b), and additional similar objects have now been detected (Keel et al., 2012a; Schirmer et al., 2013). This has resulted in a new class of galaxies: "green bean" galaxies (Schirmer et al., 2013), named due to their shared colour to "green pea" galaxies (Cardamone et al., 2009). It is thought these extremely rare "green bean" galaxies harbour echoes from previous AGN activity. In that scenario, the width of the echo will relate to the duration of time the quasar was active. Quasar LEs can therefore act as impresive probes of the time-scales of AGN life-cycles on the order of the light-crossing time of the galaxy ($\sim 10^4 - 10^5$ yr) (Schirmer et al., 2013).

Bibliography

Andrews, J. E. and Sugerman, B. E. K. and Clayton, G. C. and Gallagher, J. S. and Barlow, M. J. and Clem, J. and Ercolano, B. and Fabbri, J. and Meixner, M. and Otsuka, M. and Welch, D. L. and Wesson, R. 2011, ApJ, 731, 47

Besel, M.-A. and Krause, O. 2012, A&A, 541, L3

Blandford, R. D. and McKee, C. F. 1982, ApJ, 255, 419

Bode, M. F. and Evans, A. 1985, A&A, 151, 452

Bond, H. E. 2007, in Astronomical Society of the Pacific Conference Series, Vol. 363, The Nature of V838 Mon and its Light Echo, ed. R. L. M. Corradi & U. Munari, 130–+

Bond, H. E. and Henden, A. and Levay, Z. G. and Panagia, N. and Sparks, W. B. and Starrfield, S. and Wagner, R. M. and Corradi, R. L. M. and Munari, U. 2003, Nature, 422, 405

Bond, H. E. and Sparks, W. B. 2009, A&A, 495, 371

Cappellaro, E. and Patat, F. and Mazzali, P. A. and Benetti, S. and Danziger, J. I. and Pastorello, A. and Rizzi, L. and Salvo, M. and Turatto, M. 2001, ApJ, 549, L215

Cardamone, C. and Schawinski, K. and Sarzi, M. and Bamford, S. P. and Bennert, N. and Urry, C. M. and Lintott, C. and Keel, W. C. and Parejko, J. and Nichol, R. C. and Thomas, D. and Andreescu, D. and Murray, P. and Raddick, M. J. and Slosar, A. and Szalay, A. and Vandenberg, J. 2009, MNRAS, 399, 1191

Chevalier, R. A. 1986, ApJ, 308, 225

Couderc, P. 1939, Annales d'Astrophysique, 2, 271

Crause, L. A. and Lawson, W. A. and Menzies, J. W. and Marang, F. 2005, MNRAS, 358, 1352

Crotts, A. P. S. 1988, ApJ, 333, L51

Crotts, A. P. S. and Heathcote, S. R. 2000, ApJ, 528, 426

Crotts, A. P. S. and Kunkel, W. E. 1991, ApJ, 366, L73

Crotts, A. P. S. and Kunkel, W. E. and Heathcote, S. R. 1995, ApJ, 438, 724

Crotts, A. P. S. and Yourdon, D. 2008, ApJ, 689, 1186

Draine, B. T. 2003, ARA&A, 41, 241

Dwek, E. 1983, ApJ, 274, 175

Falla, D. F. and Floyd, M. J. and Potter, A. G. 2003, European Journal of Physics, 24, 197

Gallagher, J. S. and Sugerman, B. E. K. and Clayton, G. C. and Andrews, J. E. and Clem, J. and Barlow, M. J. and Ercolano, B. and Fabbri, J. and Otsuka, M. and Wesson, R. and Meixner, M. 2012, ApJ, 753, 109

Garg, A. and Stubbs, C. W. and Challis, P. and Wood-Vasey, W. M. and Blondin, S. and Huber, M. E. and Cook, K. and Nikolaev, S. and Rest, A. and Smith, R. C. and Olsen, K. and Suntzeff, N. B. and Aguilera, C. and Prieto, J. L. and Becker, A.

and Miceli, A. and Miknaitis, G. and Clocchiatti, A. and Minniti, D. and Morelli, L. and Welch, D. L. 2007, AJ, 133, 403

Garnavich, P. M. and Kirshner, R. P. and Challis, P. and Jha, S. and Branch, D. and Chevalier, R. and Filippenko, A. V. and Li, W. and Fransson, C. and Lundqvist, P. and McCray, R. and Panagia, N. and Phillips, M. M. and Pun, C. S. J. and Sonneborn, G. and Schmidt, B. P. and Suntzeff, N. B. and Wheeler, J. C. and Supernova INtensive Study (SINS) Collaboration. 2001, in Bulletin of the American Astronomical Society, Vol. 33, American Astronomical Society Meeting Abstracts, 1370

Gouiffes, C. and Rosa, M. and Melnick, J. and Danziger, I. J. and Remy, M. and Santini, C. and Sauvageot, J. L. and Jakobsen, P. and Ruiz, M. T. 1988, A&A, 198, L9

Havlen, R. J. 1972, A&A, 16, 252

Henyey, L. G. and Greenstein, J. L. 1941, ApJ, 93, 70

Kapteyn, J. C. 1902, Astronomische Nachrichten, 157, 201

Kastner, J. H. and Weintraub, D. A. and Merrill, K. M. and Gatley, I. 1998, AJ, 116, 1412

Kastner, J. H. and Weintraub, D. A. and Zuckerman, B. and Becklin, E. E. and McLean, I. and Gatley, I. 1992, ApJ, 398, 552

Keel, W. C. and Chojnowski, S. D. and Bennert, V. N. and Schawinski, K. and Lintott, C. J. and Lynn, S. and Pancoast, A. and Harris, C. and Nierenberg, A. M. and Sonnenfeld, A. and Proctor, R. 2012a, MNRAS, 420, 878

Keel, W. C. and Lintott, C. J. and Schawinski, K. and Bennert, V. N. and Thomas, D. and Manning, A. and Chojnowski, S. D. and van Arkel, H. and Lynn, S. 2012b, AJ, 144, 66

Kervella, P. and Mérand, A. and Szabados, L. and Fouqué, P. and Bersier, D. and Pompei, E. and Perrin, G. 2008, A&A, 480, 167

Kotak, R. and Meikle, W. P. S. and Farrah, D. and Gerardy, C. L. and Foley, R. J. and Van Dyk, S. D. and Fransson, C. and Lundqvist, P. and Sollerman, J. and Fesen, R. and Filippenko, A. V. and Mattila, S. and Silverman, J. M. and Andersen, A. C. and Höflich, P. A. and Pozzo, M. and Wheeler, J. C. 2009, ApJ, 704, 306

Krause, O. and Birkmann, S. M. and Usuda, T. and Hattori, T. and Goto, M. and Rieke, G. H. and Misselt, K. A. 2008a, Science, 320, 1195

Krause, O. and Rieke, G. H. and Birkmann, S. M. and Le Floc'h, E. and Gordon, K. D. and Egami, E. and Bieging, J. and Hughes, J. P. and Young, E. T. and Hinz, J. L. and Quanz, S. P. and Hines, D. C. 2005, Science, 308, 1604

Krause, O. and Tanaka, M. and Usuda, T. and Hattori, T. and Goto, M. and Birkmann, S. and Nomoto, K. 2008b, Nature, 456, 617

Li, A. and Draine, B. T. 2001, ApJ, 554, 778

Lintott, C. J. and Schawinski, K. and Keel, W. and van Arkel, H. and Bennert, N. and Edmondson, E. and Thomas, D. and Smith, D. J. B. and Herbert, P. D. and Jarvis, M. J. and Virani, S. and Andreescu, D. and Bamford, S. P. and Land, K. and Murray, P. and Nichol, R. C. and Raddick, M. J. and Slosar, A. and Szalay, A. and Vandenberg, J. 2009, MNRAS, 399, 129

Liu, J.-F. and Bregman, J. N. and Seitzer, P. 2003, ApJ, 582, 919

Miknaitis, G. and Pignata, G. and Rest, A. and Wood-Vasey, W. M. and Blondin, S. and Challis, P. and Smith, R. C. and Stubbs, C. W. and Suntzeff, N. B. and Foley, R. J. and Matheson, T. and Tonry, J. L. and Aguilera, C. and Blackman, J. W. and Becker, A. C. and Clocchiatti, A. and Covarrubias, R. and Davis, T. M. and Filippenko, A. V. and Garg, A. and Garnavich, P. M. and Hicken, M. and

Jha, S. and Krisciunas, K. and Kirshner, R. P. and Leibundgut, B. and Li, W. and Miceli, A. and Narayan, G. and Prieto, J. L. and Riess, A. G. and Salvo, M. E. and Schmidt, B. P. and Sollerman, J. and Spyromilio, J. and Zenteno, A. 2007, ApJ, 666, 674

Miller, A. A. and Smith, N. and Li, W. and Bloom, J. S. and Chornock, R. and Filippenko, A. V. and Prochaska, J. X. 2010, AJ, 139, 2218

Ortiz, J. L. and Sugerman, B. E. K. and de La Cueva, I. and Santos-Sanz, P. and Duffard, R. and Gil-Hutton, R. and Melita, M. and Morales, N. 2010, A&A, 519, A7+

Otsuka, M. and Meixner, M. and Panagia, N. and Fabbri, J. and Barlow, M. J. and Clayton, G. C. and Gallagher, J. S. and Sugerman, B. E. K. and Wesson, R. and Andrews, J. E. and Ercolano, B. and Welch, D. 2012, ApJ, 744, 26

Panagia, N. and Gilmozzi, R. and Macchetto, F. and Adorf, H.-M. and Kirshner, R. P. 1991, ApJ, 380, L23

Patat, F. 2005, MNRAS, 357, 1161

Patat, F. and Benetti, S. and Cappellaro, E. and Turatto, M. 2006, MNRAS, 369, 1949

Perrine, C. D. 1901, ApJ, 14, 359

——. 1903, ApJ, 17, 310

Peterson, B. M. 1993, PASP, 105, 247

Quinn, J. L. and Garnavich, P. M. and Li, W. and Panagia, N. and Riess, A. and Schmidt, B. P. and Della Valle, M. 2006, ApJ, 652, 512

Rampadarath, H. and Garrett, M. A. and Józsa, G. I. G. and Muxlow, T. and Oosterloo, T. A. and Paragi, Z. and Beswick, R. and van Arkel, H. and Keel, W. C. and Schawinski, K. 2010, A&A, 517, L8

Rest, A. and Becker, A. C. and Bergmann, M. and Blondin, S. and Challis, P. and Clocchiatti, A. and Cook, K. H. and Damke, G. and Garg, A. and Huber, M. E. and Lanning, H. and Matheson, T. and Minniti, D. and Morelli, L. and Nikolaev, S. and Olsen, K. and Oasterle, L. and Pignata, G. and Prieto, J. and Smith, R. C. and Stubbs, C. and Suntzeff, N. B. and Welch, D. L. and Wood-Vasey, W. M. and Zenteno, A. 2007, in Bulletin of the American Astronomical Society, Vol. 38, Bulletin of the American Astronomical Society, 935

Rest, A. and Foley, R. J. and Sinnott, B. and Welch, D. L. and Badenes, C. and Filippenko, A. V. and Bergmann, M. and Bhatti, W. A. and Blondin, S. and Challis, P. and Damke, G. and Finley, H. and Huber, M. E. and Kasen, D. and Kirshner, R. P. and Matheson, T. and Mazzali, P. and Minniti, D. and Nakajima, R. and Narayan, G. and Olsen, K. and Sauer, D. and Smith, R. C. and Suntzeff, N. B. 2011a, ApJ, 732, 3

Rest, A. and Matheson, T. and Blondin, S. and Bergmann, M. and Welch, D. L. and Suntzeff, N. B. and Smith, R. C. and Olsen, K. and Prieto, J. L. and Garg, A. and Challis, P. and Stubbs, C. and Hicken, M. and Modjaz, M. and Wood-Vasey, W. M. and Zenteno, A. and Damke, G. and Newman, A. and Huber, M. and Cook, K. H. and Nikolaev, S. and Becker, A. C. and Miceli, A. and Covarrubias, R. and Morelli, L. and Pignata, G. and Clocchiatti, A. and Minniti, D. and Foley, R. J. 2008a, ApJ, 680, 1137

Rest, A. and Prieto, J. L. and Walborn, N. R. and Smith, N. and Bianco, F. B. and Chornock, R. and Welch, D. L. and Howell, D. A. and Huber, M. E. and Foley, R. J. and Fong, W. and Sinnott, B. and Bond, H. E. and Smith, R. C. and Toledo, I. and Minniti, D. and Mandel, K. 2012a, Nature, 482, 375

Rest, A. and Sinnott, B. and Welch, D. L. 2012b, Proceedings of the Astronomical Society of Australia, 29, 466

Rest, A. and Sinnott, B. and Welch, D. L. and Foley, R. J. and Narayan, G. and Mandel, K. and Huber, M. E. and Blondin, S. 2011b, ApJ, 732, 2

Rest, A. and Stubbs, C. and Becker, A. C. and Miknaitis, G. A. and Miceli, A. and Covarrubias, R. and Hawley, S. L. and Smith, R. C. and Suntzeff, N. B. and Olsen, K. and Prieto, J. L. and Hiriart, R. and Welch, D. L. and Cook, K. H. and Nikolaev, S. and Huber, M. and Prochtor, G. and Clocchiatti, A. and Minniti, D. and Garg, A. and Challis, P. and Keller, S. C. and Schmidt, B. P. 2005a, ApJ, 634, 1103

Rest, A. and Suntzeff, N. B. and Olsen, K. and Prieto, J. L. and Smith, R. C. and Welch, D. L. and Becker, A. and Bergmann, M. and Clocchiatti, A. and Cook, K. and Garg, A. and Huber, M. and Miknaitis, G. and Minniti, D. and Nikolaev, S. and Stubbs, C. 2005b, Nature, 438, 1132

Rest, A. and Welch, D. L. and Suntzeff, N. B. and Oaster, L. and Lanning, H. and Olsen, K. and Smith, R. C. and Becker, A. C. and Bergmann, M. and Challis, P. and Clocchiatti, A. and Cook, K. H. and Damke, G. and Garg, A. and Huber, M. E. and Matheson, T. and Minniti, D. and Prieto, J. L. and Wood-Vasey, W. M. 2008b, ApJ, 681, L81

Ritchey, G. W. 1901a, ApJ, 14, 293

——. 1901b, ApJ, 14, 167

Romaniello, M. and Patat, F. and Panagia, N. and Sparks, W. B. and Gilmozzi, R. and Spyromilio, J. 2005, ApJ, 629, 250

Schaefer, B. E. 1987, ApJ, 323, L47

Schirmer, M. and Diaz, R. and Holhjem, K. and Levenson, N. A. and Winge, C. 2013, ApJ, 763, 60

Schmidt, B. P. and Kirshner, R. P. and Leibundgut, B. and Wells, L. A. and Porter, A. C. and Ruiz-Lapuente, P. and Challis, P. and Filippenko, A. V. 1994, ApJ, 434, L19

Sinnott, B. and Welch, D. L. and Rest, A. and Sutherland, P. G. and Bergmann, M. 2013, ApJ, 767, 45

Smith, N. and Davidson, K. and Gull, T. R. and Ishibashi, K. and Hillier, D. J. 2003, ApJ, 586, 432

Sparks, W. B. 1994, ApJ, 433, 19

——. 1996, ApJ, 470, 195

Sparks, W. B. and Bond, H. E. and Cracraft, M. and Levay, Z. and Crause, L. A. and Dopita, M. A. and Henden, A. A. and Munari, U. and Panagia, N. and Starrfield, S. G. and Sugerman, B. E. and Wagner, R. M. and White, R. L. 2008, AJ, 135, 605

Sparks, W. B. and Macchetto, F. and Panagia, N. and Boffi, F. R. and Branch, D. and Hazen, M. L. and della Valle, M. 1999, ApJ, 523, 585

Sugerman, B. E. K. 2003, AJ, 126, 1939

——. 2005, ApJ, 632, L17

Sugerman, B. E. K. and Andrews, J. E. and Barlow, M. J. and Clayton, G. C. and Ercolano, B. and Ghavamian, P. and Kennicutt, Jr., R. C. and Krause, O. and Meixner, M. and Otsuka, M. 2012, ApJ, 749, 170

Sugerman, B. E. K. and Crotts, A. P. S. 2002, ApJ, 581, L97

Sugerman, B. E. K. and Crotts, A. P. S. and Kunkel, W. E. and Heathcote, S. R. and Lawrence, S. S. 2005, ApJS, 159, 60

Suntzeff, N. B. and Heathcote, S. and Weller, W. G. and Caldwell, N. and Huchra, J. P. 1988, Nature, 334, 135

Swope, H. H. 1940, Harvard College Observatory Bulletin, 913, 11

Tylenda, R. 2004, A&A, 414, 223

Tylenda, R. and Kamiński, T. 2012, A&A, 548, A23

Van Dyk, S. D. and Li, W. and Filippenko, A. V. 2006, PASP, 118, 351

van Loon, J. T. and Evans, A. and Rushton, M. T. and Smalley, B. 2004, A&A, 427, 193

Vogt, F. P. A. and Besel, M.-A. and Krause, O. and Dullemond, C. P. 2012, ApJ, 750, 155

Wang, X. and Li, W. and Filippenko, A. V. and Foley, R. J. and Smith, N. and Wang, L. 2008, ApJ, 677, 1060

Weingartner, J. C. and Draine, B. T. 2001, ApJ, 548, 296

Welch, D. L. and Clayton, G. C. and Campbell, A. and Barlow, M. J. and Sugerman, B. E. K. and Meixner, M. and Bank, S. H. R. 2007, ApJ, 669, 525

Westerlund, B. 1961, PASP, 73, 72

Xu, J. and Crotts, A. P. S. 1999, ApJ, 511, 262

Xu, J. and Crotts, A. P. S. and Kunkel, W. E. 1994, ApJ, 435, 274

——. 1995, ApJ, 451, 806

Chapter 4

On the Interpretation of Supernova Light Echo Profiles and Spectra

This chapter incorporates a reformatted article previously published in The Astrophysical Journal, originally appearing as:

"Rest, A., Sinnott, B., Welch, D. L., Foley, R. J., Narayan, G., Mandel, K., Huber, M. E., and Blondin, S. The Astrophysical Journal, **732**, 2 (2011)."

4.1 Introduction

The first light echoes (LEs) were discovered around Nova Persei 1901 (Ritchey, 1901a,b, 1902; Kapteyn, 1902). Since then, LEs (whereby we mean a simple scattering echo rather than fluorescence or dust re-radiation) have been seen in the Galactic Nova Sagittarii 1936 (Swope, 1940) and the eruptive variable V838 Monocerotis (e.g., Bond et al., 2003). LEs have also been observed from extragalactic supernovae (SNe), with SN 1987A (Kunkel et al., 1987) being the most famous case (Crotts, 1988; Suntzeff et al., 1988; Bond et al., 1990; Xu et al., 1995; Sugerman et al., 2005a,b; Newman

& Rest, 2006), but also including SNe 1991T (Schmidt et al., 1994; Sparks et al., 1999), 1993J (Sugerman & Crotts, 2002; Liu et al., 2003), 1995E (Quinn et al., 2006), 1998bu (Cappellaro et al., 2001), 2002hh (Meikle et al., 2006; Welch, 2007), 2003gd (Sugerman, 2005; Van Dyk et al., 2006), and 2006X (Wang et al., 2008).

The suggestion that historical SNe might be studied by their scattered LEs was first made by Zwicky (1940) and attempted by van den Bergh (1965, 1966). The first LEs of centuries-old SNe were discovered in the Large Magellanic Cloud (LMC) (Rest et al., 2005b). They found three LE complexes associated with three small and therefore relatively young SN remnants (SNRs) in the LMC which were subsequently dated as being between 400–1000 years old using the LMC distance and LE feature positions and apparent motions (Rest et al., 2005b). These findings provided the extraordinary opportunity to study the spectrum of the SN light that reached Earth hundreds of years ago and had never been recorded visually or by modern scientific instrumentation. A spectrum of one of the LEs associated with SNR 0509-675 revealed that the reflected LE light came from a high-luminosity SN Ia (Rest et al., 2008a), similar to SN 1991T (Filippenko et al., 1992; Phillips et al., 1992) and SN 1999aa (Garavini et al., 2004) — the first time that an ancient SNe was classified using its LE spectrum. Analysis of *ASCA* X-ray data of SNR 0509-675 led Hughes et al. (1995) to suggest that this SNR likely came from a SN Ia. Recent analysis of its *Chandra* X-ray spectra by Badenes et al. (2008) also supported the classification of this object as a high-luminosity SN Ia.

The interpretation of LEs, however, is fraught with subtleties. Krause et al. (2005), for example, identified moving Cas A features (called "infrared echoes" or "IR echoes") using mid-IR imaging from the *Spitzer Space Telescope.* IR echoes are the result of dust absorbing the outburst light, warming and re-radiating at longer wavelengths. The main scientific conclusion of Krause et al. (2005) was that most of the IR echoes were caused by a series of recent X-ray outbursts from the compact object in the Cas A SNR based on their apparent motions. However, the analysis was flawed because it did not account for the fact that the apparent motion strongly depends on the inclination of the scattering dust filament (Dwek & Arendt, 2008; Rest et al., 2011). Dwek & Arendt (2008) also showed that X-ray flares are not energetic enough to be the source of these IR echoes, but that instead the LEs must have been generated by an intense and short burst of EUV-UV radiation associated with the break out of the shock through the surface of the Cas A progenitor star. Therefore, the most likely source of all LEs associated with Cas A, both infrared and scattered, is the Cas A SN explosion itself. The need to properly analyze the growing collection of LE spectra is what motivated the present work.

The first scattered LEs of Galactic SNe associated with Tycho's SN and the Cas A SN were discovered by Rest et al. (2007, 2008b). Contemporaneously, Krause et al. (2008) obtained a spectrum of a scattered optical LE spatially coincident with one of the Cas A IR echoes, and identified the Cas A SN to be of Type IIb. Because Rest et al. (2008b) discovered several LEs with multiple position angles relative to the SNRs, there is a new opportunity for observational SN research — the ability to measure the spectrum of the same SN from several different directions. At any given instant after the SN light has reached an observer by the direct path, an ellipsoidal surface exists where scattered light from the SN may reach the observer, whose arrival to the observer is delayed by the additional path length. Interstellar dust concentrations must lie at one or more locations on the ellipsoid for the scattered LE to be detectable. Since each LE is at a unique position on the ellipsoid, each LE has a unique line of sight to the SN. Therefore, the scattered spectral light can provide spectral information on the asymmetry of the SN photosphere. In the limiting case of dust on the ellipsoid opposite the observer, the spectrum of the scattered LE carries the signature of conditions on the SN hemisphere usually hidden from the observer. As the time since the explosion increases, the scattering ellipsoid surface expands and may intersect additional dust concentrations. We present a framework on how to interpret observed LE spectra depending on the scattering dust properties, seeing, and spectrograph slit width and position.

In this paper, we examine the pitfalls of previous analyses, suggest improvements for future studies, and present the application of our methods to data. In Section 4.2, we describe how the properties of the scattering dust can cause significant differences to observed LE spectra, and show a specific example of how this has been overlooked in the past. In Section 4.3, we quantify how observed LE spectra depend on potential differences in dust characteristics (thickness and inclination), as well as observational characteristics (seeing and spectroscopic slit size and orientation). We then apply this framework to observations of Cas A (Section 4.4) and SN 1987A (Section 4.5). In Section 4.6, we discuss how differences in the dust and observing conditions can effect an analysis of LE spectra and suggest future applications of LE observations. We conclude in Section 4.7.

4.2 A Case Study: The Krause et al. (2008) Cas A Light Echo Spectrum

A common assumption is that an observed LE spectrum is equivalent to the light-curve weighted integration of the spectra at individual epochs (e.g., Rest et al., 2008a; Krause et al., 2008). However, Figure 4.1 illustrates how slit width, dust filament width and inclination significantly influence the observed LE spectrum. We consider a LE from a 300-year-old event 10,000 light years away that lasts 150 days (yellow shaded area), with a rising and declining arm of 30 and 120 days, respectively. The peak of the event is indicated with the red line. We place the origin of our coordinate system ρ, z at the source event. The z-axis is the distance of the dust to the source event along the line of sight. The ρ-axis is in the plane of the sky from the source event to the LE position. The quadratic relation between the parameters z, ρ, and the time since explosion t is described by the well-known LE equation (Couderc, 1939) (see Section 4.9.1 for details).

The scattering dust filament (brown shaded area) is located at $(\rho, z) = (300, 0)$ ly with an inclination of $\alpha = 0°$ where α is the angle with respect to the plane of the sky (see Equation 4.3). The dust width is 0.02 ly, 0.2 ly, and 0.6 ly from left to right, respectively. The rightmost panel of Figure 4.1 shows the flux of the LE that we would observe with these dust filaments versus ρ. We denote these as the LE profiles, which essentially are cuts through the LE along the axis pointing toward the source event. In order to be able to directly compare the LE profiles to the dust and LE pulse geometry, we show the flux and ρ as the x- and y-axis, respectively. Note that for very thin dust filaments like the one with $\sigma_d = 0.02$ ly, the LE profile is the the projected light curve.

A spectroscopic slit with a width of $1''$ is indicated with the gray shaded area. In the leftmost panel, the dust filament has a dust width of 0.02 ly (0.006 pc). Only light that is in the intersection of the event pulse, dust, and slit (indicated with the thick black rectangle) contributes to the observed spectra. In this case, only 20% of the event (30 out of 150 days, indicated by the dashed blue lines) contribute to the spectrum. The second panel from the left shows the same example, but this time the dust filament has a width of 0.2 ly (0.06 pc), and ∼51% of the event pulse (77 out of 150 days) contributes to the spectrum. Only if the dust width is at least 0.6 ly (0.18 pc) thick (third panel from the left), the full event contributes to the spectrum.

This clearly demonstrates that the observed LE spectrum is not necessarily the full light-curve weighted integrated spectrum when the scattering dust filament is sufficiently thin. The effect of a thin filament of dust on the interpretation of a LE spectrum is best appreciated by considering the difference in persistence of spectral features at early and late time. Naively, one might expect that the faintness of a SN at late times would not result in spectral features from those phases contributing to the integrated spectrum in a significant way. However, in the late nebular phases, most of the flux is typically concentrated in very few lines. The top panel of Figure 4.2 portrays the spectra of SN 1993J, the very well-observed and prototypical example

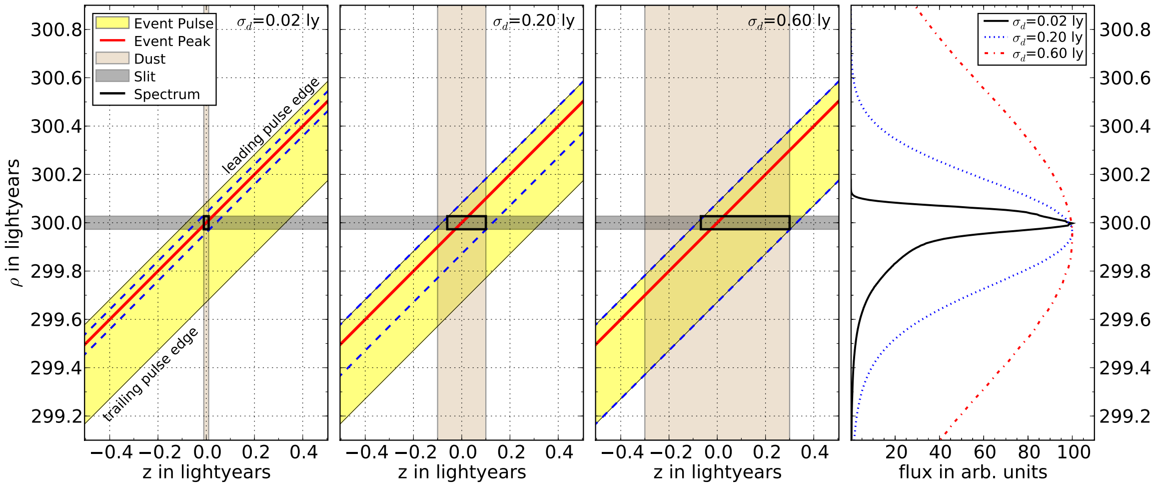

Figure 4.1: Illustration of how the dust filament width, σ_d, influences the observed LE spectrum. The yellow shaded area indicates a 300-year-old SN event that lasts 150 days, with a rising and declining arm of 30 and 120 days, respectively. The peak is indicated with a red line. The scattering dust filament (light grey shaded region) is located in the plane of the sky crossing the event position ($z = 0.0$ ly), with an inclination of $\alpha = 0°$. The dust width is 0.02 ly, 0.2 ly, and 0.6 ly from left to right, respectively, and the left panel shows the respective LE profiles. A spectroscopic slit with a width of $1''$ is indicated with the dark gray shaded area. Only light that is within the intersection of the event pulse, dust, and slit (indicated with the thick black rectangle) contributes to the observed spectrum. The blue dashed lines indicate which part of the light pulse is probed by the spectrum.

of the SN IIb class (e.g., Filippenko et al., 1993; Richmond et al., 1994; Filippenko et al., 1994; Matheson et al., 2000), at 6, 39, 88, and 205 days after peak brightness from the bottom to the top, respectively (Jeffery et al., 1994; Barbon et al., 1995; Fransson et al., 2005). During the late phases, a significant fraction of flux is radiated in the [O I] $\lambda\lambda$6300, 6364 doublet, which completely dominates the spectra for times later than 200 days. The bottom panel shows the light-curve weighted integrated spectra of SN 1993J with different integration limits. The integration limits of these spectra are from 20 days before peak brightness to P_{max}, where P_{max} ranges from 5 to 300 days after peak brightness from the bottom to the top. The most significant difference between the integrated spectra with early and late integration limits is the emergence of the [O I] doublet. We use the SN 1993J lightcurve from Richmond et al. (1996) as weights for the integration.

SNe IIb are not unique in this regard. The nebular spectra of all SNe are dominated by strong emission lines. Specifically, SNe Ia have strong [Fe II] and [Fe III] lines, SNe Ib/c have strong [O I], [Mg I], Ca II, and [Ca II] lines, and SNe II have strong hydrogen Balmer lines. See Filippenko (1997) for a review of SN spectroscopy.

The perils of not properly accounting for differences in dust filament thickness are clear — the strength of features in observed LE spectra can be significantly altered by the width of the scattering dust on the sky.

In Figure 4.2, we display the LE spectrum of Cas A by Krause et al. (2008) in red. This spectrum has a weak [O I] doublet, consistent with the integrated spectra of SN 1993J, but *only if integrated until ∼80 days after peak brightness.* The full integrated spectra of SN 1993J have a much stronger [O I] feature. If the LE spectrum is the full light-curve weighted integrated spectrum of Cas A, then Cas A and SN 1993J have a significant difference at wavelengths near the [O I] feature. The alternative is that the LE spectrum does not contain light from the late-time portion of the SN light curve, i.e., the weighting function is truncated at late times.

In their comparison to the observed Cas A LE, Krause et al. (2008) also used an

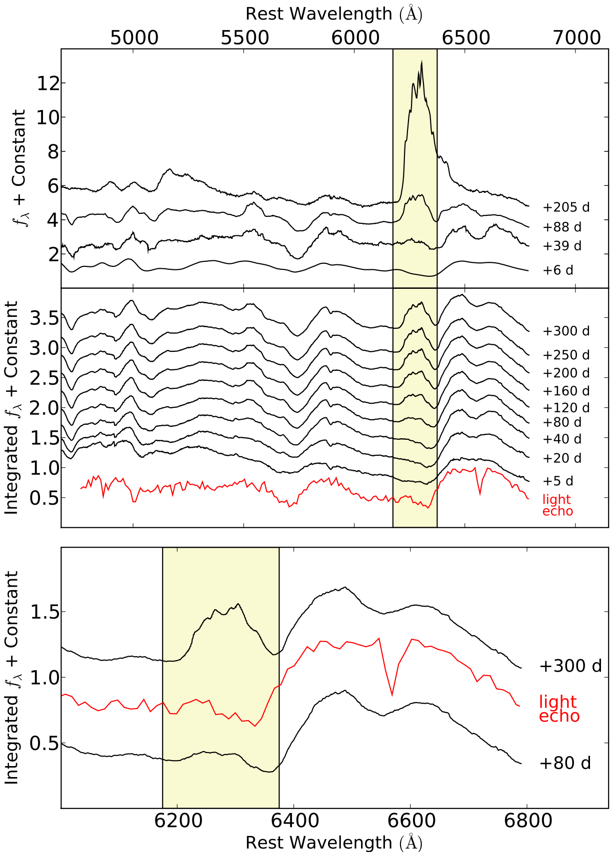

Figure 4.2: *Top panel:* Spectra of SN 1993J at +6, +39, +88, and +205 days relative to peak brightness from the bottom to the top, respectively. During the late phases ($\gtrsim$ 40 days after peak), a significant fraction of flux is emitted in the [O I] $\lambda\lambda$6300, 6364 doublet, which dominates the spectra after ~200 days. The [O I] doublet is indicated by the yellow-shaded region. *Middle panel:* light-curve weighted integrated spectra of SN 1993J. The integration limits of these spectra are from −20 days relative to peak brightness to $P_{\rm max}$, where $P_{\rm max}$ ranges from +5 to +300 days from the bottom to the top. The most significant difference between the integrated spectra with early and late integration limits is the emergence of the [O I] doublet. The Cas A LE spectrum of Krause et al. (2008) is shown in red, which does not show a prominent [O I] doublet feature. *Bottom panel:* light-curve weighted integrated spectra of SN 1993J in the wavelength region near the [O I] doublet and Hα features. The integrated spectra have integration limits of +80 days and +300 days are compared to the Cas A LE spectrum of Krause et al. (2008, red curve). The integrated SN 1993J spectrum with the +80 day integration limit is a better fit to the [O I] doublet in the observed Cas A spectrum.

integrated SN 1993J spectrum — but only integrated to 83 days after peak brightness. This seemingly prudent choice was not explained in the text, but presumably they found this integration time to yield the best comparison. However, this analysis leaves an open question: Was the Cas A SN different from SN 1993J in this regard or are the differences due to the properties of the scattering dust? In the following sections, we attempt to answer this question and its more general counterpart for all LEs.

4.3 Light Echo Profile Modeling

In Appendix 4.9.1, we derive that the observed LE profile shape, P, strongly depends on the dust thickness, dust inclination, and seeing. We also show that this may have a significant impact on the observed LE spectra (see Appendix 4.9.2 and 4.9.3). Here we investigate the magnitude of each of these effects on observed LE spectra.

For this analysis, we examine a toy model of a LE that, despite its simplicity in some respects, appears to be representative of actual LE situations. The toy model is a LE from a 300-year-old event 10,000 ly from the observer. For the event light curve, we choose a “sail” shape, with the peak at phase 0.0 years and then decreasing to zero flux at a phase of 0.3 years and -0.1 years (see the dotted curves in the right-hand panel of Figures 4.3 through 4.7 for a representation of this light curve), sharing the characteristic short rise and long decline of a SN light curve. The scattering dust filament intercepts the LE paraboloid at $(\rho_0, z_0) = (300, 0)$ ly. For the dust model, we use a dust filament that is locally planar and perpendicular to the (ρ, z) plane, with a boxcar width profile. In the following subsections, we vary the properties of a single parameter while holding the others constant. We are therefore able to determine the effects of each parameter on the observed LE and its spectrum.

4.3.1 Dust Thickness

As described above, the dust thickness can significantly alter the LE spectrum. Using our toy model, we can quantify this effect.

Figure 4.3 presents LE profiles, window functions, and effective light curves for the toy model with different dust widths. The left column shows the LE profiles for each dust thickness. The x-axis is $\Delta\rho = \rho - \rho_0$, where (ρ_0, z_0) is the position where the dust intersects with the LE paraboloid at phase 0.0 years of the event. We choose a dust filament inclination of $\alpha = 45°$, since it is perpendicular to the LE paraboloid and thus most representative of typical inclinations. Centering a $1.0''$ spectroscopic slit on the peak of the LE profile, we calculate the associated window function (middle column) and effective light curves (right column), which are simply the light curve convolved with the window function. The different rows show different dust widths.

There are two distinct regimes where a modest change in the dust width has little effect on the effective light curve or integrated spectrum. The first one is shown in the top panels, where the dust width is so thin that the observed LE profile is effectively the projected initial light curve (corresponding to the left panel of Figure 4.1). The other limit is a very thick dust sheet (corresponding to the right panel of Figure 4.1).

In the former case (top row of Figure 4.3), changing the dust width from $\sigma_d = 0.001$ ly to $\sigma_d = 0.01$ ly only marginally modifies the effective light curve. Centering a spectroscopic slit on the LE profile results in a box-car window function, and the effective light curve is truncated to the region near maximum brightness. In the latter case (bottom row of Figure 4.3), the dust width is large enough that the LE profile is dominated by the dust width. The LE profile has a flat top, and only the edges are impacted by the original light curve profile. Centering a spectroscopic slit on the LE profile results in very wide window functions, and the effective light curve is essentially the same as original light curve (see the right panel of Figure 4.1 for an illustration).

As we show in Sections 4.4 and 4.5, our observations of LEs have been a mixture of

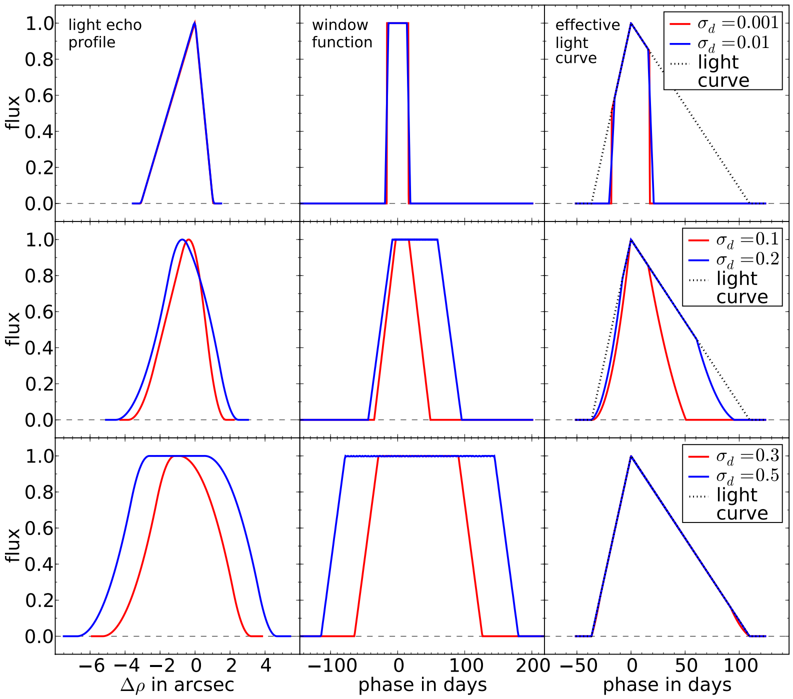

Figure 4.3: Modeled LE profiles (left column), window functions (middle column), and effective light curves (right column) for our toy model as a function of dust width. All models in all rows have the same parameters except for the dust width; the separation into three rows is only for clarity. $\Delta\rho$ is with respect to the position where the dust intersects the light pulse. The toy model is a 300-year-old event with a "sail" shape as described in the text. The scattering dust filament intersects the event pulse paraboloid at $z = 0.0$, and has an inclination of $\alpha = 45°$.

both regimes. The middle row of Figure 4.3 shows the light curves, window functions, and effective light curves for dust widths of $\sigma_d = 0.1$ ly (0.03 pc) and $\sigma_d = 0.2$ ly (0.06 pc). The effective light curve is still heavily weighted to the time near maximum[1], but with increasing dust width the effective light curve slowly transitions to the full light curve.

4.3.2 Dust Inclination

The dust inclination has a large effect on the LE profile. This is simply a projection effect; as the dust sheet rotates, the projection of the light curve on the sky can change significantly. Turning to our toy model, we quantify this effect.

We fix the dust width to $\sigma_d = 0.1$ ly. Figure 4.4 shows modeled LE profiles, window functions, and effective light curves for several examples that only differ by the inclination of the scattering dust filament. As expected, we find that the filament inclination has a profound impact on the LE profile width. For inclinations close to 90° (see $\alpha = 70°$ in the top row of Figure 4.4), the dust filament is aligned along the line of sight, while the light curve projected into ρ space is compressed. Consequently, the window function has large wings, and the effective light curve is very similar to the full light curve. However, for inclination angles corresponding to dust sheets close to the tangent plane of the LE paraboloid (for $z_0 = 0.0$ ly is $-45°$), the LE profile subtends a larger angle on the sky (see $\alpha = -30°$ in bottom row of Figure 4.4). As a result, a spectroscopic slit will cover a very small portion of the light curve, and the window function is approximately a box car with a small width.

It is clear that the determining the dust inclination is very important, but fortunately it is straightforward to do so from the observations in cases where the location of the SN and date of outburst are known. In Appendix 4.9.5 and in more detail in Rest et al. (in prep.), we derive the dust inclination from the apparent motion of the

---

[1] In this example, with increasing dust width, the peak of the LE profile moves away from $\Delta\rho$ towards the negative direction. This is caused by using a box-car profile for the dust width profile. This effect is minimized if the dust width profile is peaked (e.g., if it is a Gaussian).

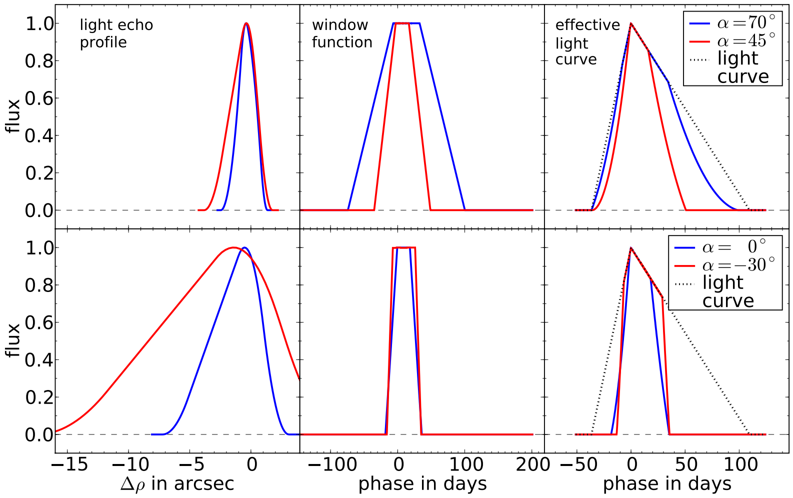

Figure 4.4: Same as Figure 4.3, but for varying dust filament inclinations, α, and constant dust width. The width of the dust filament is $\sigma_d = 0.1$ ly. Note that the LE profile gets "stretched" when the inclination of the dust filament approaches the tangential angle of the LE ellipsoid, which is $\alpha = -45°$ for $z = 0$ ly.

LE in difference images, and discuss its sources of uncertainty. We discuss the impact the dust inclination has on the possibility of sampling the spectra within different age intervals for the same SN, as well as the possibility of constraining the SN light curve shape in Section 4.6.2 and 4.6.3, respectively.

4.3.3 Point-Spread Function Size

Observations of resolved sources must always account for the point-spread function (PSF). LEs are no exception since degradation of an image by a large PSF will not only smear the LE across the sky, but will also smear the LE in *time*. Again, we turn to our toy model, and vary the PSF to determine its effect on the interpretation of LEs.

Figure 4.5 shows our toy model with dust inclination of $\alpha = 45°$. We examine a Gaussian PSF with four different full-widths at half-maximum (FWHMs): $0.0''$ (corresponding to a δ function PSF), $0.4''$, $1''$, and $2''$. Each row of Figure 4.5 represents a different dust thickness, with the top, middle, and bottom rows corresponding to

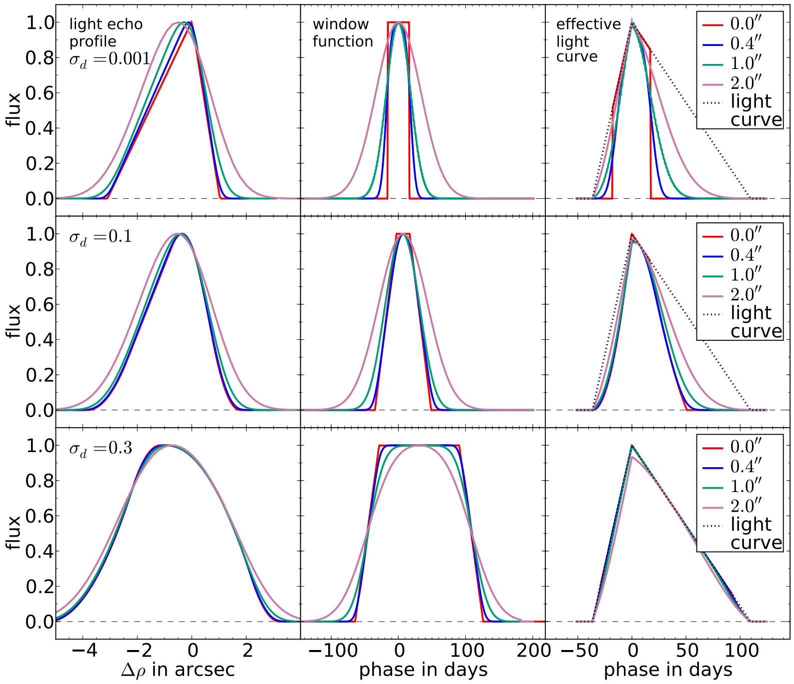

Figure 4.5: Same model as in Figure 4.3, but with varying the dust filament width and seeing. The dust width presented are $\sigma_d = 0.001$ ly (top row), $\sigma_d = 0.1$ ly (middle row), and $\sigma_d = 0.3$ ly (bottom row). Seeing of 0.0″, 0.4″, 1.0″, and 2.0″ is indicated with red, blue, yellow, and green lines, respectively.

$\sigma_d = 0.001$, 0.1, and 0.3 ly, respectively. For small dust widths ($\lesssim 0.1$ ly), and thus thin LE profiles, the effective light curve depends significantly on the seeing. However, for larger dust widths, the seeing has very little effect on the effective light curve. This insight provides guidance for prioritizing targets for spectroscopic follow-up observations based on the conditions at the telescope.

4.3.4 Slit Offset

Thus far, we have assumed for our toy model that the spectroscopic slit was centered on the peak of the LE profile. However, LEs are usually both very faint and extended. Additionally, their apparent motion on the sky makes perfect alignment of a spectroscopic slit unlikely - especially when there is a significant delay between the time of mask preparation and observations. Figure 4.6 shows the effect of having

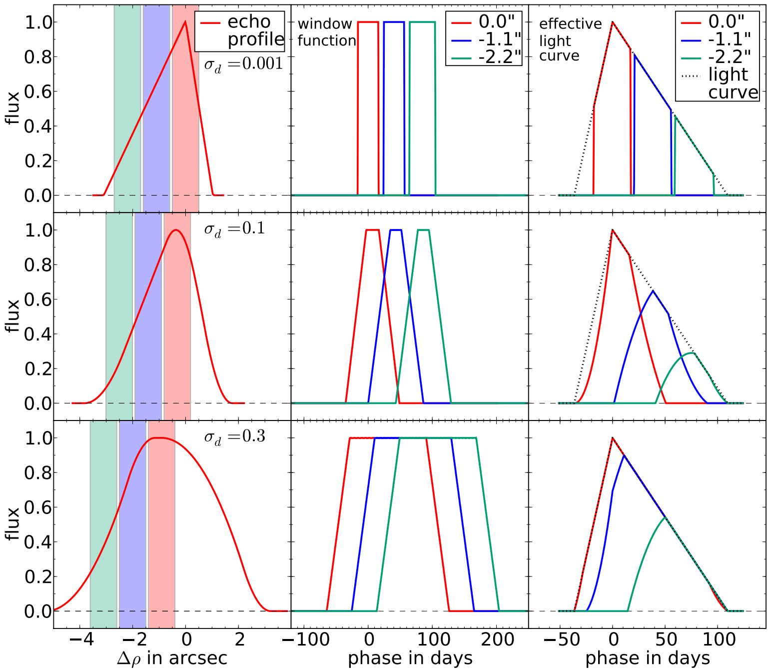

Figure 4.6: Same as Figure 4.3, but with slits that are offset by $0.0''$, $-1.1''$, and $-2.2''$ from the peak of the LE profile. The $1''$ slits are indicated with the shaded areas in the left column.

the slit offset from the LE profile peak. As before, we choose a representative dust inclination of $\alpha = 45°$, and the three rows, from top-to-bottom, correspond to dust widths of $\sigma_d = 0.001$, 0.1, and 0.3 ly, respectively. The red, blue, and green shaded areas indicate $1''$ slits with $0.0''$, $-1.1''$, and $-2.2''$ offsets from the peak, respectively. Clearly a $1''$ offset has a significant impact on the effective light curve for all but the thickest dust widths (but even in that case, it could still result in a significant difference if the spectroscopic features in the outburst spectra are changing rapidly with time). Figure 4.7 shows the same scenario as Figure 4.6, but with the addition of a $1''$ PSF to the model.

Figure 4.8 illustrates the application of this model to a “real world” set of conditions. We define a coordinate system $(\Delta\rho, u)$, where as before $\Delta\rho = \rho - \rho_0$, and u is orthogonal to the ρ-axis through $\Delta\rho = 0.0$ in the plane of the sky. For a dust filament that is locally planar and perpendicular to the (ρ, z) plane, i.e. parallel to

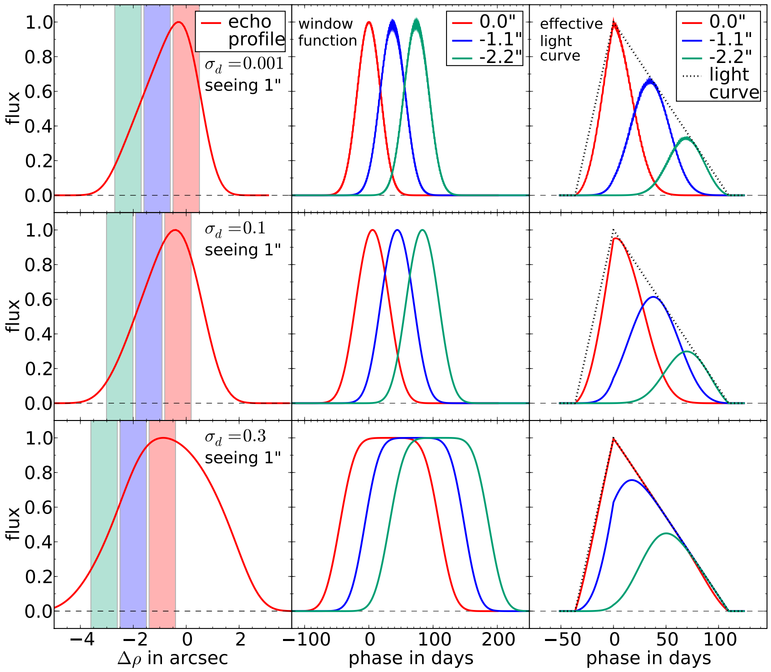

Figure 4.7: Same as Figure 4.6 but in 1″ seeing.

u, the LE is aligned with the u axis. However, if it is tilted with respect to u by an angle of δ_1, then the LE will also be tilted by the same angle (see gray shaded area in illustration). We consider a slit (red box in Figure 4.8) that is misaligned with the LE by an angle δ_2, and also offset along the ρ axis by Δs.

In this situation, we can recover the proper LE window functions. To do so, we can split the slit into multiple subslits, (in this example, we show this with the horizontal dotted lines). For each of these subslits, we determine the LE profile, calculate the offset of the subslit to the LE using δ_2 and Δs as described in Appendix 4.9.3, and determine the window function for each subslit. The total window function for the full slit is then the flux-weighted average of the subslit window functions.

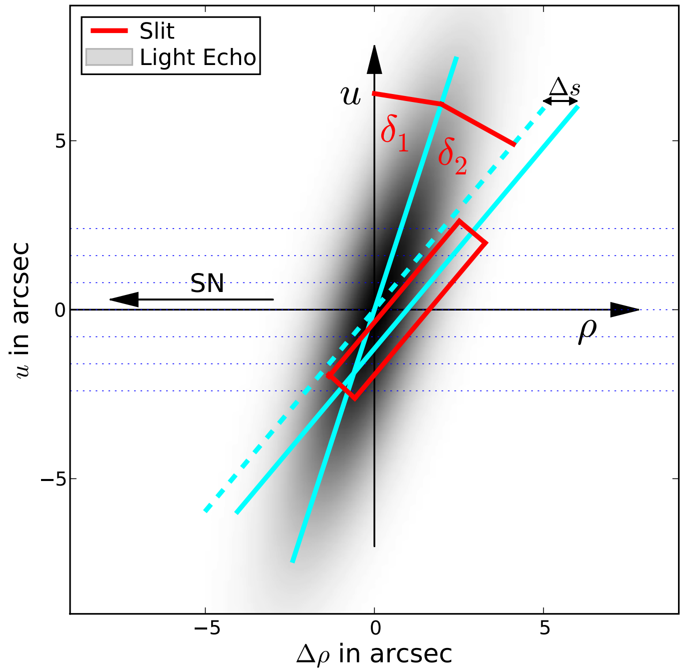

Figure 4.8: Toy model of a LE and spectroscopic slit configuration where the slit is misaligned both in angle and offset relative to the LE. The LE is indicated with the shaded area. We define a coordinate system (ρ, u) in the plane of the sky centered at the LE, where the ρ axis is in the direction to the source event, and u is perpendicular to ρ, with the positive direction along positive position angle of LE-SNR. The LE is along the u axis if the dust filament is perpendicular to the (ρ, z) plane. In this example he angle δ_1 between the LE and the u-axis is 18°, and the angle δ_2 between slit and LE is 22°. Six subslits of width $0.8''$ are indicated with the blue dotted lines. The offset Δs is $1.0''$.

4.4 Cas A Light Echoes

4.4.1 Observations

As a case study, we investigate LEs discovered in a multi-season campaign beginning in October 2006 on the Mayall 4 m telescope at Kitt Peak National Observatory (Rest et al., 2008b). The MOSAIC imager on the Mayall 4 m telescope, which operates at the f/3.1 prime focus at an effective focal ratio of f/2.9, was used with the Bernstein "*VR*" broad filter ($\lambda_c = 595$ nm, $\delta\lambda = 212$ nm; NOAO Code k1040). The imaging data was kernel- and flux-matched, aligned, subtracted, and masked using the SMSN pipeline (Rest et al., 2005a; Garg et al., 2007; Miknaitis et al., 2007). We investigate the three Cas A SN light echoes LE2116, LE2523, and LE3923, for which we presented spectra in Rest et al. (2010). Figure 4.9 shows the difference images and the slit position for these three LEs, and Table 6.1 lists the positions, lengths, and position angles for each slit. LE2116 was previously reported by Rest et al. (2008b), whereas LE2521 and LE3923 were discovered on 2009 September 14 and 16, respectively. For the analysis of LE2116, we use images from 2009 September 14, while we use the discovery images for LE2521 and LE3923.

4.4.2 Cas A Light Echo Template Spectra

There are several LEs associated with the Cas A SN. Here we examine three LEs for which we have spectra. Their profiles are shown in Figure 4.10. To fit the LE profiles,

Table 4.1. Positions, lengths, and position angles for each Cas A slit.

LE	Telescope	RA (J2000)	Dec (J2000)	PA SNR-LE (°)	Seeing[a] (″)	Width[a] (″)	Length[a] (″)	PA[a] (°)
LE2116	Keck	23:02:27.10	+56:54:23.4	237.83	0.81	1.5	2.69	0.0
LE2521	Keck	23:12:03.86	+59:34:59.3	299.11	0.79	1.5	4.32	41.0
LE3923	Keck	00:21:04.97	+61:15:37.3	65.08	0.89	1.5	7.72	0.0

[a] Parameters for spectroscopic slit

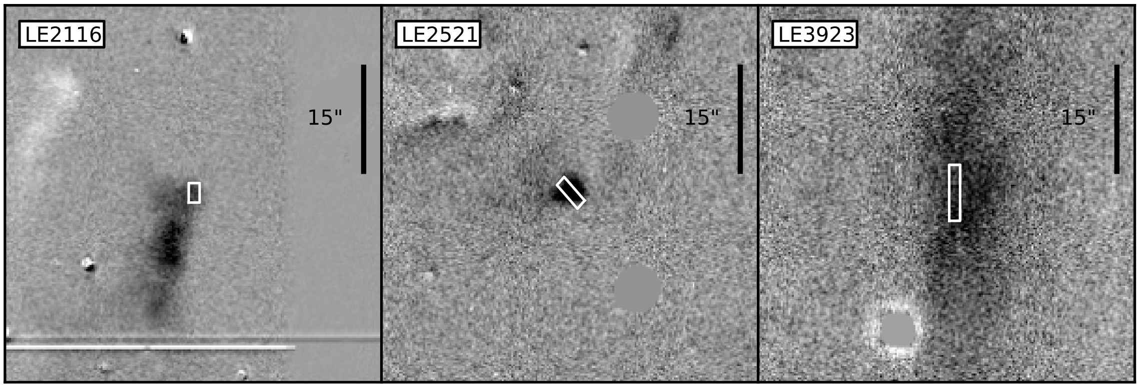

Figure 4.9: Difference image cutouts for LE2116, LE2521, and LE3923 from left to right, respectively. For all image stamps north is up and east is left. Excess flux in the first and second epoch is white and black, respectively. The position and size of the spectroscopic slit is indicated by the white rectangle.

we numerically solve the model defined by Equation 4.14 for the observed data. To do this, we assume that the explosion occurred in the year 1681 ± 19 (Fesen et al., 2006), determine the scattering dust coordinates ρ_0 and z_0 by using Equation 4.1 with the measured angular separation between the LE and the SNR, and we determine the dust inclination from the apparent motion of the LEs (this process is defined in Appendix 4.9.5 and described in more detail by Rest et al., in prep.). The remaining free model parameters are the LE profile peak height and position and the dust filament width, which has physical implications. For the three LEs presented above, we display their best fit model profiles in Figure 4.10.

To numerically fit the model parameters, we determine the best fitting profile by calculating the reduced χ^2 for a 3-dimensional grid of the three fit parameters. For each parameter, we marginalize over the other parameters to obtain the best-fitting value. The initial step sizes of the parameter grid are often too large for a proper marginalization. To ensure a proper determination of the parameters, we iterate this process three times adjusting the grid spacing, guided by the fitted parameters and their uncertainties from the previous iteration. In all but the lowest signal-to-noise ratio cases, the probability density functions have a well-behaved Gaussian shape.

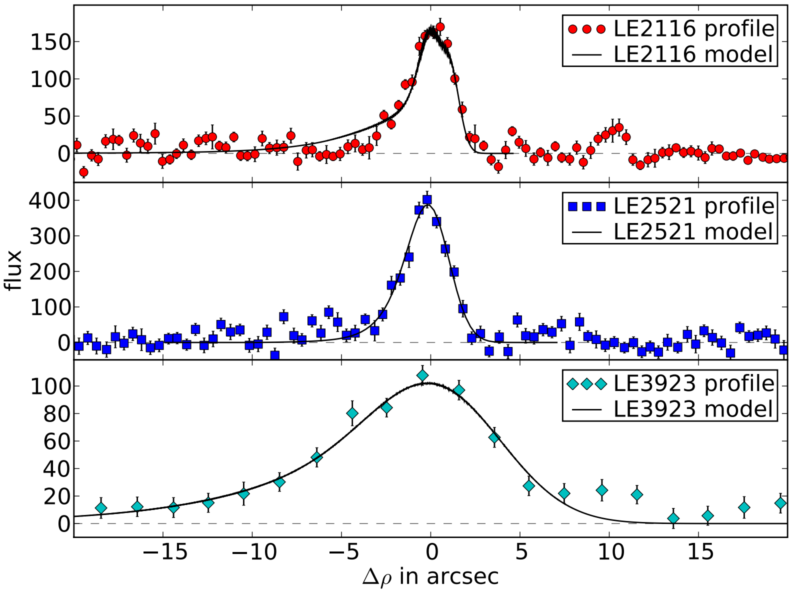

Figure 4.10: LE profiles for LE2116, LE2521, and LE3923 from top to bottom, respectively. The model fit is indicated with the black lines.

Table 4.2. Input and fitted parameters of the Cas A light echo profiles.

LE	Image UT Date	Seeing ($''$)	α ($^\circ$)	δ_1 ($^\circ$)	δ_2 ($^\circ$)	$\Delta\rho_{\mathrm{offset}}$ ($''$)	ρ_0 (ly)	z_0 (ly)	σ_d (ly)	SB (mag)	$\sigma_{s,\mathrm{eff}}$ ($''$)
LE2116	20090914	0.97	9(5)	7.80	−39.97	−0.42	627.9561(18)	437.11	0.031(10)	22.82(02)	1.77
LE2521	20090914	1.13	54(5)	−10.98	−0.91	−0.01	317.9613(23)	−9.89	0.093(04)	21.83(02)	1.53
LE3923	20090916	1.65	7(5)	10.44	−35.36	−0.35	1203.904(76)	2045.38	0.614(53)	23.35(04)	1.65

Note. — All the values are for the subslits with $u = 0.5$.

Figure 4.11 shows as examples the marginal probability density functions (PDFs) for the peak position and dust width of the LE2521 LE profile at $u = 0.5''$.

Table 4.2 shows the input and fitted parameters of these three LE profiles. These profiles are for subslits with $u = 0.5''$, i.e., close to the center of the spectroscopic slit. The definition of the (ρ, u) coordinate system and how it relates to the LE and the subslits is explained in detail in Section 4.3.4, Appendix 4.9.3 and Figure 4.8. LE2116 and LE2521 have profiles with a similar width. The profile of LE3923, however, has a significantly larger width. Note that the model fits the data very well.

Figure 4.12 shows the fitted LE peak position ρ_0, dust width σ_d, and peak surface

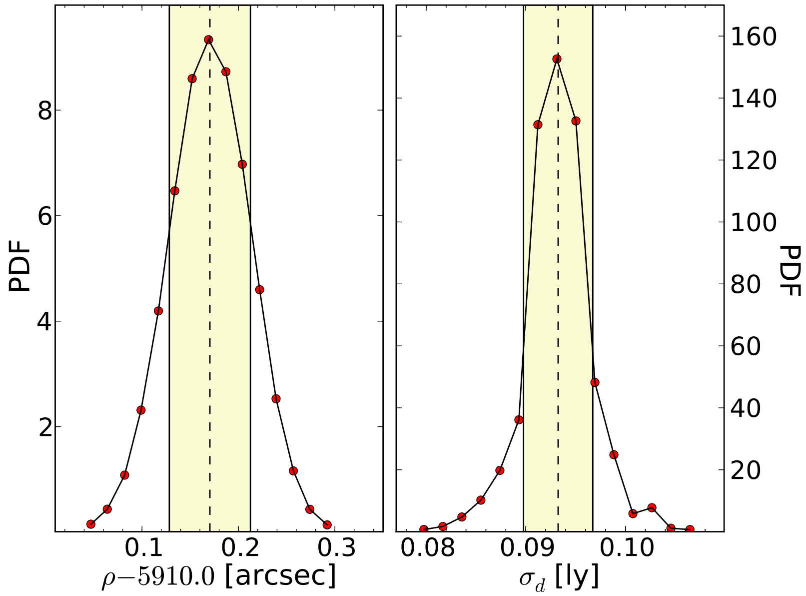

Figure 4.11: Probability density functions (PDFs) for the peak position (left) and dust width (right) of LE2521 at $u = 0.5''$. The most likely value is indicated with a dashed line, and the yellow shaded region indicates the 1-σ interval.

brightness *SB* for all subslits of each of the three LEs. Panels A–C show ρ_0 for the three LEs, with the spectroscopic slit overplotted (black solid lines). The dashed line indicates a straight line fit to the subslits that are within the spectroscopic slit. Even though there is some structure in the ρ_0 versus u relation, locally the LE position can be approximated very well with a straight line. Panel D shows the dust width σ_d. The dust width of LE3923 is nearly constant over $20''$ and is an order of magnitude larger than the dust width of the other two LEs. The dust width for LE2116 decreases and then increases over only $\sim 2''$. The width decreases to $\sigma_d = 0.03$ ly for $u \geq 0.5$, making this portion of the LE2116 filament the thinnest yet observed. We discuss potential scientific opportunities for a LE with such a thin dust width in Section 4.6.3. Panel E shows the surface brightness. LE2521 has a surface brightness brighter than 21 mag/arcsec^{-2} and is the brightest Cas A LE yet reported. However, it is spatially small. On the other hand, LE3923 is relatively faint, but its large size makes spectroscopy productive.

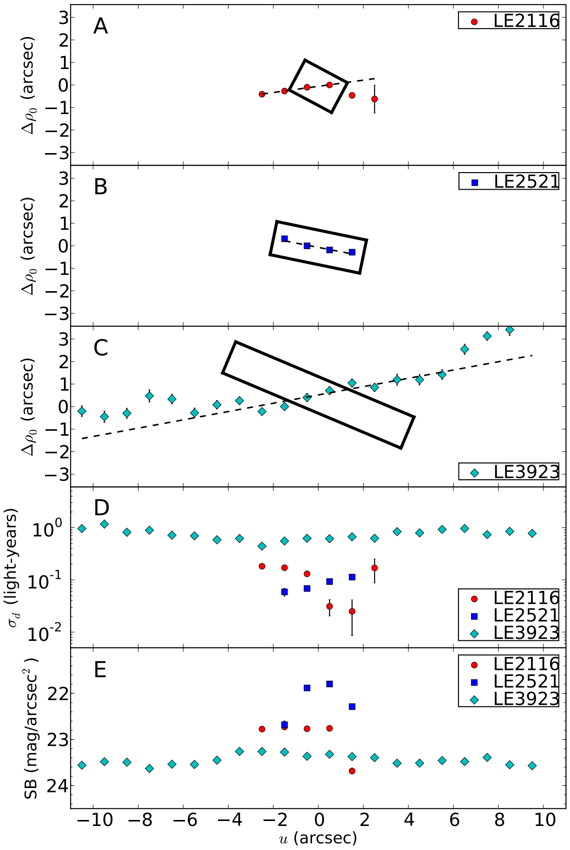

Figure 4.12: Panel A, B, and C show the positions of the LE profile peaks for the different subslits for LE2116, LE2521, and LE3923, respectively. $\Delta\rho_0(u)$ is defined as $\rho_0(u) - \rho_0(0)$, and u is orthogonal to the ρ-axis through $\rho_0(0)$. Red, blue, and cyan symbols indicate LE2116, LE2521, and LE3923, respectively. Panel D shows the fitted dust widths, σ_d, and Panel E shows the surface brightnesses.

For the spectra presented by Rest et al. (2010), the profile fits had not been completed when slit masks were designed. As a result, the alignment between the LEs and the slit were not optimal. In particular, there is a large misalignment in angle for LE3923; however, that LE has a large profile (FWHM $\approx 10''$; see bottom panel of Figure 4.10) and therefore an offset at the 1–2$''$ scale does not decrease the total amount of flux by a significant amount. However, it does affect the observed spectra since the window function and effective light curves strongly depend on these offsets.

For each LE, we calculate the window function by fitting the observed LE profile with the numerical model as described above. The spectroscopic slit is applied to the fitted LE profile using Equations 4.15–4.18 as described in Appendix 4.9.2. It is important to note that now the seeing from the spectroscopic observation is used instead of the seeing from the image used to determine the LE profile. For each slit, the weighted average of all subslits is calculated using Equations 4.20 – 4.23 in Appendix 4.9.3.

The top panel of Figure 4.13 shows the window functions for the three LEs for which we have spectra. The middle panel shows the SN 1993J light curve and the effective light curves for each LE (using the LE profiles and assuming that their light curves are the same as SN 1993J).

Even though LE2521 and LE2116 have comparable dust widths, the dust inclination for LE2521 is significantly larger, resulting in a wider window function than LE2116. This also causes the projected SN light-curve shape to be "squashed." LE3923 has a similar inclination to that of LE2116, but its scattering dust is thicker, also leading to a wider window function. Note that the three window functions, and therefore also the effective light curves (see middle panel in Figure 4.13), have significantly dropped off after 100 days past maximum. However, the decline time of SN is significantly longer, and consequently the contribution of spectra with phases ≥ 100 days is cut off - a fact illustrated in the bottom panel of Figure 4.13, which

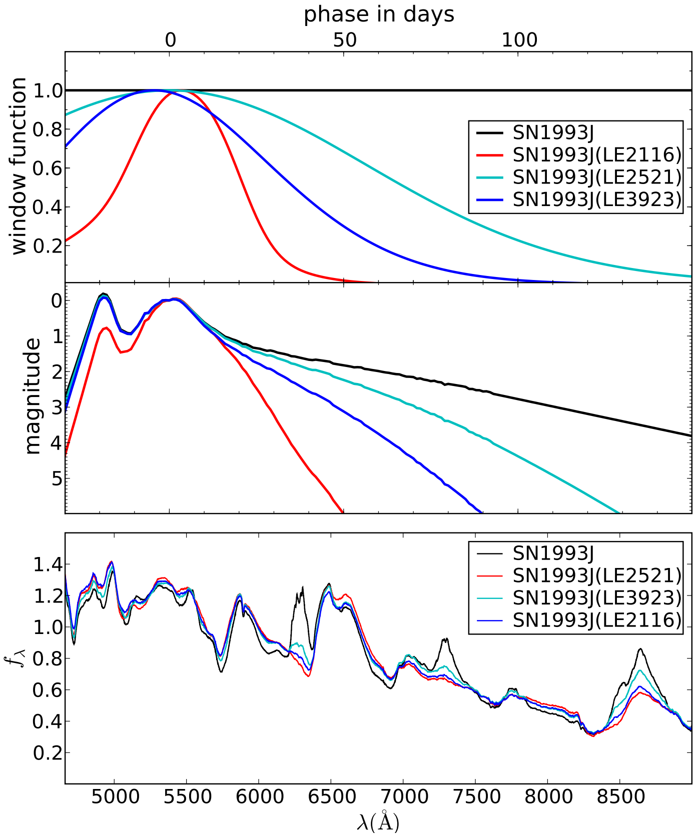

Figure 4.13: *Top:* window function for the different LEs. *Middle:* effective light curves of SN 1993J for the LEs. The unmodified light curve of SN 1993J is shown in black. *Bottom:* integrated SN 1993J spectra, where the integration is weighted by the respective effective light curve. Red, cyan, and blue curves represent LE2116, LE2521, and LE3923, respectively. The black spectrum is weighted by the original, unmodified SN 1993J light curve. The differences in the spectra are mainly due to the strong [O I] $\lambda\lambda$6300, 6363, [Ca II] $\lambda\lambda$7291, 7324, and Ca II NIR triplet features in the late-phase spectra.

shows the integrated spectra for SN 1993J. The late type spectra of SN IIb like SN 1993J are dominated by [O I] $\lambda\lambda$6300, 6363, [Ca II] $\lambda\lambda$7291, 7324, and the Ca II NIR triplet. Note that the black spectrum, which is weighted by the original, unmodified light curve, is much stronger at the position of these lines compared to the other spectra, which are integrated using the effective light curves. We conclude that a perfectly symmetrical SN observed at different position angles might be erroneously interpreted as asymmetrical if scattering dust properties, seeing, and slit width are not taken into account.

4.4.3 Light Echo Spectra: Systematics

We have shown in Section 4.3 with simulated light curves and dust filaments how the LE spectra are influenced by the dust properties and observing conditions, and in Section 4.4.2 we have applied this to the real-world example of the Cas A LEs. In this section, we investigate how changing these properties impacts the LE spectra. We start with the fit to the Cas A LE profiles of LE2521 described in Section 4.4.2, and create a window function, effective light curve, and LE spectrum using using the spectroscopic and photometric library of SN 1993J as a template. We then vary dust width, dust inclination, and seeing while keeping all other parameters fixed.

Figure 4.14 shows the effective light curves (left panels) and integrated SN 1993J spectra (right panels). In the top panel, we vary the dust width, σ_d. We find that, consistent with the simulations in Section 4.3, the nebular [O I] and [Ca II] lines in the integrated spectra have a strong dependence on the dust width. For $\sigma_d \lesssim 0.1$ ly, the [O I] and [Ca II] emission lines are weak, whereas for larger values the integrated spectrum quickly approaches the limit of the integrated spectrum without any window function applied with strong [O I] and [Ca II] emission lines. We find similar results for the dust inclination: the difference between the integrated spectra is small and the [O I] and [Ca II] lines are weak for $\alpha \lesssim 60°$, but then rapidly approaches the integrated spectrum without any window function applied for α close to 90°. We find

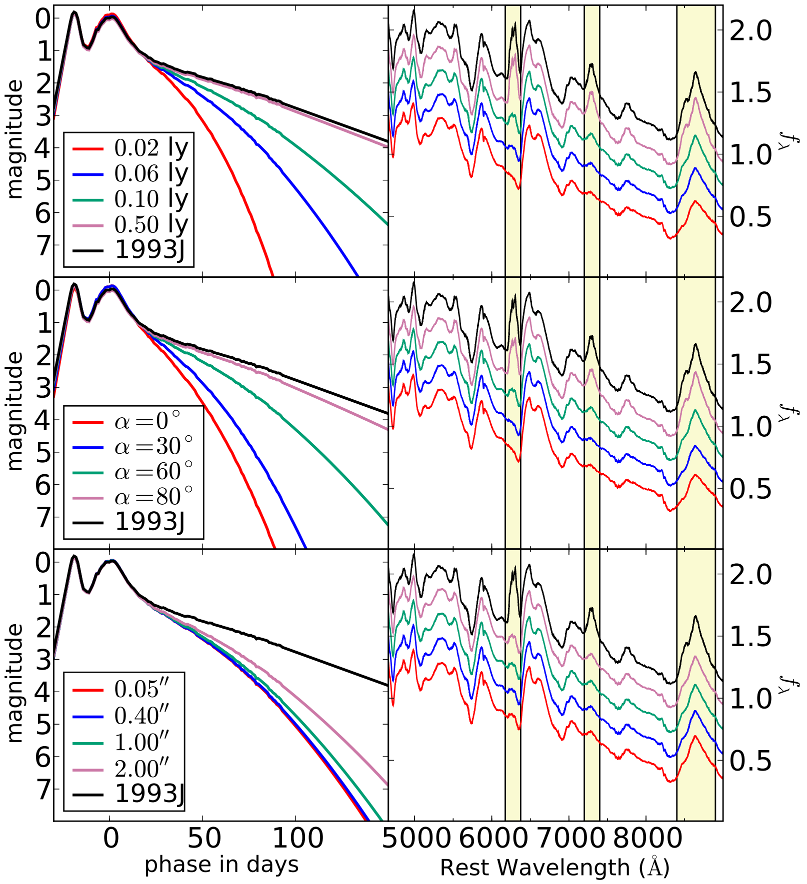

Figure 4.14: Effective light curves and integrated SN 1993J spectra varying the dust width, σ_d (top row), the dust inclination, α (middle row), and the seeing (bottom row) for LE2521. For a given row, only one parameter varies, with the other parameters are set by the fit described above and shown in Figure 4.10. The black line indicates the original SN 1993J light curve and the corresponding integrated spectra.

that the seeing (bottom panel) only has a very strong impact on the observed LE spectrum if the dust width is very small as discussed in Section 4.6.2 and 4.6.3.

We also investigate how uncertainties in the dust inclination impact the derived integrated spectra template. To do this, we fixed the dust inclination from 0° to 80°for LE2521, and fit the LE profile. Figure 4.15 shows the fitted dust width, σ_d, with respect to the input dust inclination, α. Three examples of the fitted LE profiles are shown in the top panel of Figure 4.16. The bottom panels show the corresponding effective light curves (left) and integrated spectrum (right).

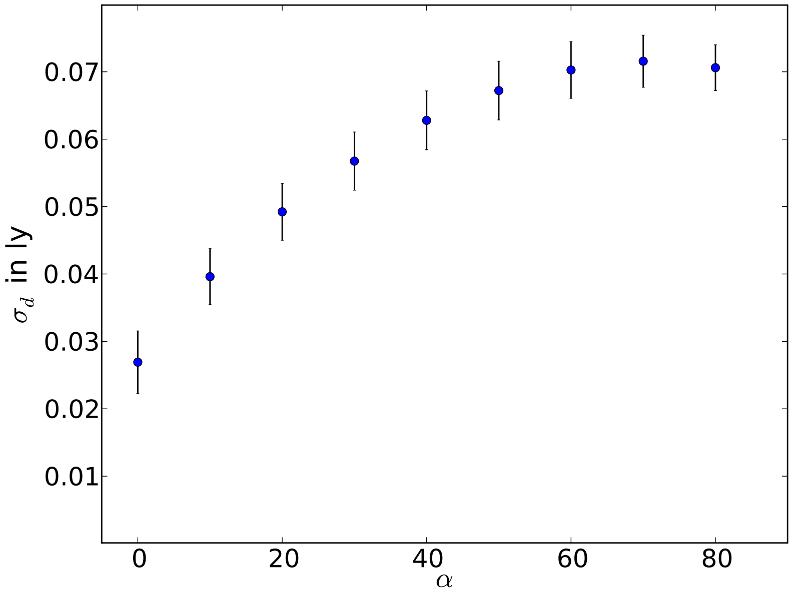

Figure 4.15: Fitted dust width, σ_d, for the LE2521 LE profile for different input dust inclination, α.

Note that while the LE profile fit is very good in all cases, the effective light curves are different, and thus the integrated spectra differ significantly in [O I] and [Ca II] line strengths. The reason for these differences is the degeneracy between the dust inclination and the dust width. For decreasing dust inclination (i.e., the dust inclination gets closer to the tangential of the LE paraboloid), the projected light curve is “stretched.” This effect can be nullified by decreasing the dust width, resulting in a similar fit to the LE profile with significantly different parameters (see Figure 4.15).

For inclinations close to 90°, the LE profile is dominated by the dust profile and not by the projected light-curve profile. Such a situation manifests itself in a LE profile that is symmetrical (see green line in top panel of Figure 4.16) in contrast to the asymmetrical LE profile shape (see red line in top panel of Figure 4.16) that still reveals indications of the original light curve. Similarly, the fitted σ_d is essentially constant for $\alpha \approx 90°$.

The tests in this section have shown that an incorrect dust inclination can sys-

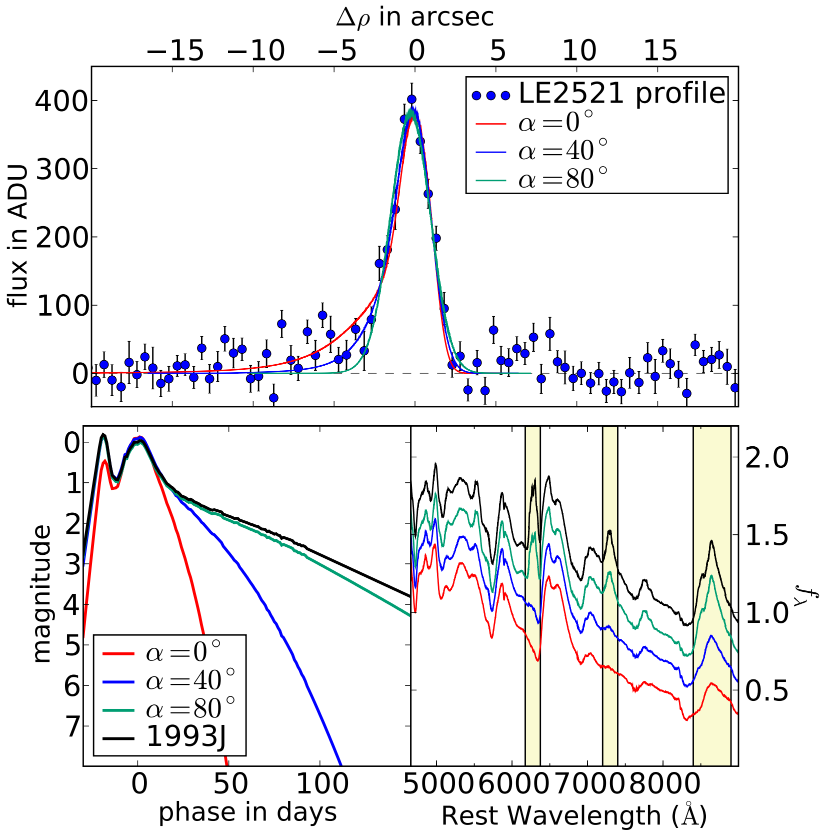

Figure 4.16: *Top:* LE2521 profile and model fits for varying inclination angles, α. *Bottom:* Effective light curves (left) and the corresponding integrated spectra (right). The black line indicates the original SN 1993J light curve and the corresponding integrated spectra.

tematically bias the interpretation of SN properties from LE spectra. We discuss the sources of uncertainty in the determination of the inclination in Appendix 4.9.5.

4.5 SN 1987A Light Echoes

4.5.1 Observations

Beginning in 2001, the SuperMACHO Project microlensing survey employed the CTIO 4 m Blanco telescope with its 8K × 8K MOSAIC imager (plus its atmospheric dispersion corrector) to monitor the central portion of the LMC every other night for 5 seasons (September through December). The images were taken through our custom "*VR*" filter ($\lambda_c = 625$ nm, $\delta\lambda = 220$ nm; NOAO Code c6027). SN 1987A and its LEs are in field sm77, which was observed with exposure times between 150 and 200 seconds. We have continued monitoring this field since the survey ended. The difference imaging reduction process was identical to the KPNO Cas A imaging.

4.5.2 Profile Modeling

The ring-shaped LEs associated with SN 1987A have previously been studied in great detail, mapping the dust structure surrounding the SN (e.g., Sugerman et al., 2005b). Unlike historical SNe, a complete spectral and photometric history of the SN is available for SN 1987A. This historical database allows an observed LE spectrum to be modeled unambiguously against a spherically symmetric model for the explosion. In addition, the high signal-to-noise ratio of the SN 1987A LEs make them ideal for our tests.

We consider an example LE from SN 1987A corresponding to a unique position angle on the sky. The spectrum associated with this LE was taken using the Gemini Multi-Object Spectrograph (GMOS; Hook et al., 2004) on Gemini-South, using the R400 grating. The spectroscopic slit was $1.0''$ wide and $2.16''$ long, with the slit tilted

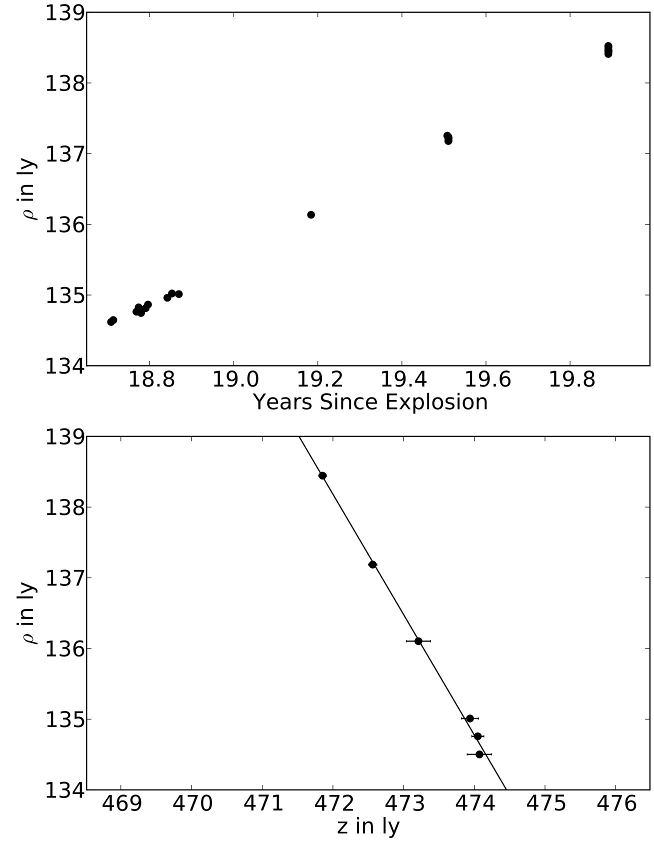

Figure 4.17: *Top:* Apparent motion of a single position angle of the LE system of SN 1987A. The uniform motion of the LE on the sky indicates a unique inclination for the dust structure. The superluminal motion of the LE is 4.09 ± 0.02 ″/year. *Bottom:* The above (ρ, t) data is binned when observations are taken within 10 days of each other, and converted to the (z, ρ) plane using equation 4.1. The resulting fit (solid line) gives an inclination of $\alpha = 30.4 \pm 0.8°$.

to be tangential to the observed LE ring. The upper panel of Figure 4.17 shows the apparent motion of the LE monitored over more than a year. The motion on the sky is constant on such time scales (4.09 ± 0.02 ″/year), indicating constant inclination of the dust structure. To determine the angle of inclination, α, we translate (ρ, t) into (z, ρ) as described in Appendix 4.9.5, resulting in a dust inclination of $\alpha = 30.4 \pm 0.8°$ (see lower panel of Figure 4.17).

A high signal-to-noise ratio difference image is used to model the effect of the dust on the spectroscopic slit. Input parameters are the inclination ($\alpha = 30.4°$), observed

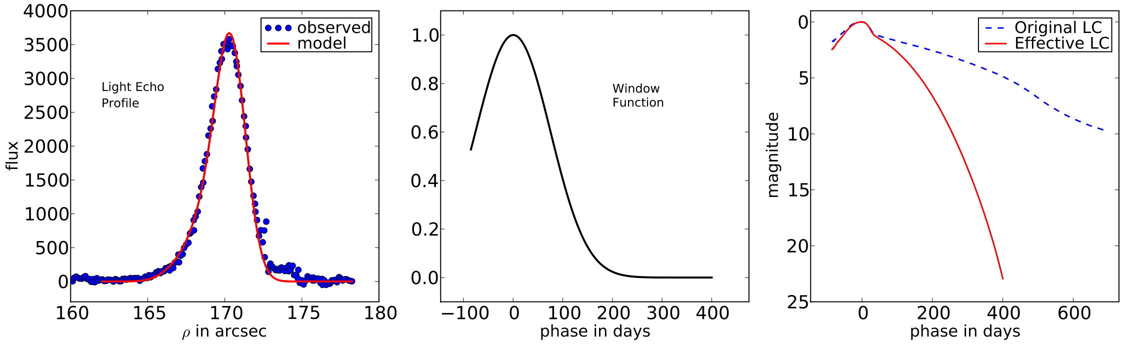

Figure 4.18: *Left:* observed profile for the SN 1987A LE, with the best-fit model profile over-plotted. *Middle:* resulting window function associated with the 1.0″ wide spectroscopic slit. *Right:* effective light curve from the model compared with the original light curve of SN 1987A.

seeing for the image (1.22″), and delay time since explosion ($ct = 19.9$ years). The photometric data of SN 1987A (Hamuy et al., 1988; Suntzeff et al., 1988; Hamuy & Suntzeff, 1990) are used to model the LE profile observed on the sky, with the best-fitting model shown in the left panel of Figure 4.18. The dust structure model is able to recreate the observed LE profile exceedingly well. The window function and resulting effective light curve associated with the spectroscopic slit (convolved to the seeing at time of spectroscopy) are shown in the middle and right panels of Figure 4.18, respectively. The average dust width associated with the spectroscopic slit is $\sigma_d = 4.26 \pm 0.06$ ly (1.31 ± 0.02 pc). We note that at the inclination and dust widths observed here, the model is less sensitive to uncertainties in α. Testing of the model shows that at such inclinations, uncertainties in α on the order of 5° have little impact on the window function and resulting integrated spectrum (see Section 4.3.2).

The impact of the scattering dust is clear when fitting the model to the observed spectrum. To integrate the spectral history of SN 1987A we take advantage of the extensive spectral database from SAAO and CTIO observations after the explosion (Menzies et al., 1987; Catchpole et al., 1987, 1988; Whitelock et al., 1988; Catchpole et al., 1989; Whitelock et al., 1989; Phillips et al., 1988, 1990). Figure 4.19 shows the observed LE spectrum (black), the model spectrum (red), and the full light-curve integrated spectrum (blue dashed). Note that the observed LE spectrum includes strong nebular emission lines that are not associated with the SN. Both the model spectrum and the full light-curve weighted integrated spectrum show a good fit for features blueward of 5500 Å. However, the lower panel of Figure 4.19 shows that the spectrum redward of 5500 Å, and in particular the Hα feature, are best fit by the spectrum corresponding to the best-fit LE profile model. From Figure 4.18, it is clear that the strength of the Hα feature in the integrated spectrum is highly dependent on the window function. At late times, the spectra of SN 1987A are dominated by strong Hα emission. The excellent fit to the LE spectrum of SN 1987A validates our method of determining the effective light curve from the LE profile.

4.5.3 Impact of Dust Parameters on Observed Spectrum

Similar to the analysis performed in Section 4.4.3, we vary the three free parameters of our model to determine their impact on the observed LE spectrum for SN 1987A. Figure 4.20 shows the effective light curves (left column) and integrated SN 1987A spectra (right column). The top, middle, and bottom rows show the model varying the dust width (σ_d), dust inclination (α), and seeing, respectively, while holding the other parameters constant. To emphasize the differences in the integrated spectra, the figure focuses on the Hα feature. The advantage of the SN 1987A observations over those of Cas A is that there is a complete linking between the LE and the final integrated spectrum via observation, since we have a priori knowledge of the SN creating the observed LE profile.

The dependence on the integrated spectra of SN 1987A are similar to that of SN 1993J (see Figure 4.14), where increasing the dust width, inclination, or seeing all share the result of stretching the weight function closer to the $wf = 1$ case, resulting in an effective light curve approaching that of the original SN 1987A light curve. Figure 4.20 allows us to rank the impact of the dust parameters on the observed LE spectrum. Seeing has the least significance on the spectrum, although we note

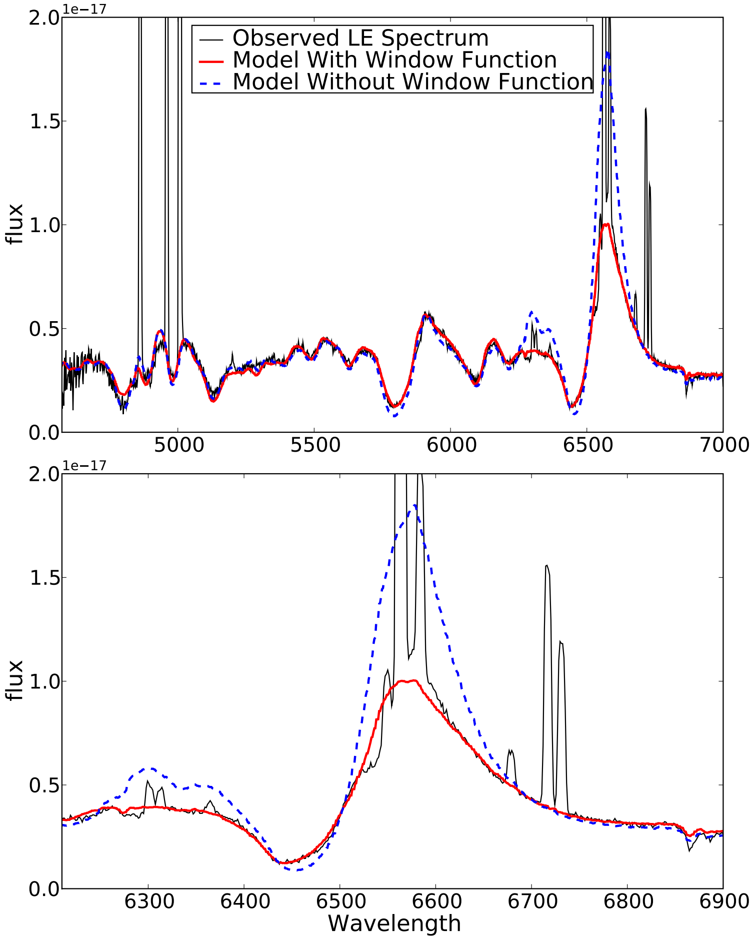

Figure 4.19: *Top:* Observed LE spectrum of SN 1987A (black) with the best-fit model (using the window function from Figure 4.18) integrated spectrum (red) and the full light-curve weighted integrated spectrum (blue). *Bottom:* Detail of the spectra near the Hα feature. Note that the narrow lines dominating the emission peak of the profile are strong nebular emission lines, and are not associated with the SN. The best-fit model integrated spectrum fits the observed LE spectrum well in this region, while the full light-curve weighted integrated spectrum is a poor fit.

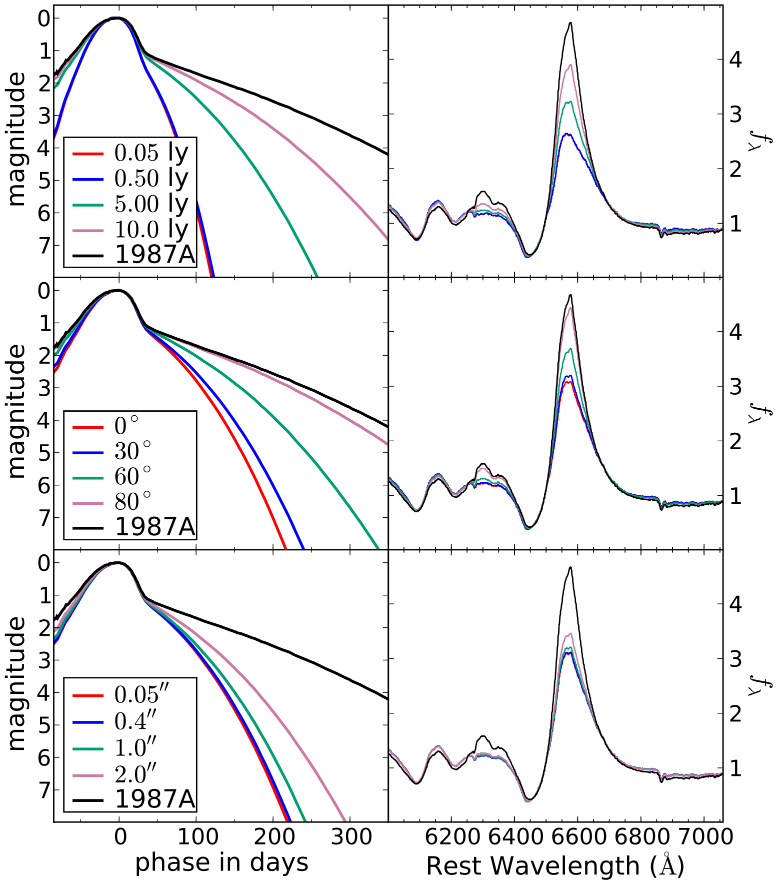

Figure 4.20: Effective light curves (left column) and integrated spectra (right column) for SN 1987A, varying the dust width, σ_d (top row), the dust inclination, α (middle row), and the seeing (bottom row). For a given row, only one parameter varies, with the other parameters are set by the fit described above and shown in Figure 4.18.

that poor image quality should still be taken into account. Dust inclination has a large effect, although the sensitivity is small if the dust is close to perpendicular to the observer. The dust width has the greatest impact on the spectrum, which is particularly noteworthy since this quantity has been ignored until now. For SN 1987A, the Hα peak height increases by about 20% if the dust thickness is 10 ly instead of 5 ly, indicating a sensitivity that exceeds that of the other parameters.

Figure 4.20, as well as the SN 1987A spectrum presented in Section 4.5.2, clearly show the danger in interpreting spectroscopic data from LEs without proper modeling. Any interpretation of LE spectra based on relative line strengths must be accompanied by a careful analysis of the dust properties associated with the LE.

4.6 Discussion

In the previous sections, we have presented the LE model, the dependency of the model on various parameters, and have applied that model to multiple real-world cases. In this section, we discuss how we can use our new understanding of LEs and the scattering dust to perform additional observations that will provide new insight into historical SNe.

4.6.1 Verification of Model Parameters And Systematic Biases

The analysis of SN 1987A LEs has the added benefit that the validity of our dust models and their impact on the observed LE profiles and spectra can be tested, since the spectrophotometric evolution of the SN itself has been monitored extensively. We show in Section 4.5 and in more detail in Sinnott et al. (2011) that the observed LE profile, apparent motion, and spectra can all be brought in excellent accordance with what is predicted using the SN 1987A spectrophotometric library and our dust model locally parameterized as a planar filament with a Gaussian density profile.

This shows that at least in the case of SN 1987A, the Gaussian dust model is a good approximation of the true dust profile.

In general, dust structures are filamentary in nature, which is easily visible in its effect on the shapes of LEs, which often show twists and furcations. However, on the few arcsecond scale, most of the shape and profiles of LEs change slowly over months and even years. For example, the dust width, σ_d, for LE3923 and LE2521 is nearly constant over $20''$ (see second panel from the bottom in Figure 4.12) and smoothly increasing, respectively. In order to account for small changes in the dust parameters, we split the slit into $1''$ sections and fit the dust parameters separately for each of these sections.

If there are significant deviations from the Gaussian dust density model (e.g., if there is substructure in the density on small scales), the window function can potentially be biased, which in turn, can cause spectral differences that would be interpreted as intrinsic to the SN. We can test and guard against these systematic biases: LEs often come in "groups"; i.e., there are often several distinct LEs separated by tens of arcseconds for LEs of Galactic SNe. The scattering dust filaments likely belong to the same dust structure, but are tens of light years apart. Therefore any substructure in these filaments is uncorrelated. For LEs of the same source event only tens or hundred of arcseconds apart, the physical properties of the source event are the same. An upper limit on the systematic bias can be set by the differences in the observed spectra which are not accounted for by the differences in fitted dust parameters. In all data obtained by our team, we have not found any evidence that there are significant biases in our analysis due to substructure in the dust or deviation from the dust model. This is particularly important for the two novel methods that we describe in the next two sections.

If LEs from two different SNe are reflected off the same dust, then the dust thickness measured from our method should be the same for both sets of LEs. Such a scenario is a direct test of the model fits. Fortunately, this situation occurs for LEs from Cas A and Tycho, and a comparison of the derived values will be presented in a future work. Since this situation was discovered in a relatively small and low filling factor survey, it is reasonable to expect other such regions of the sky exist where dust is at the intersection of two historical SN LE ellipsoids.

4.6.2 Temporally Resolving Light Echo Spectra

One of the most exciting opportunities LEs present is to use them to *temporally resolve* the SN spectrum: If a slit is aligned perpendicular to a LE profile instead of parallel, different parts of the slit probe different epochs of the SN light curve.

As an example, we imagine a SN LE where the SN is a carbon copy of SN 1993J, the dust filament is at $z = 400$ ly with an inclination of 0° and a width of 0.02 ly. With a *Hubble Space Telescope*-like (*HST*) PSF FWHM of $0.05''$, the projected light curve would have minimal distortion. If a spectrum is taken with the slit perpendicular to the LE arc (i.e., parallel to the line from the LE to the SNR) with $0.05''$ seeing, then the spatially resolved spectrum (i.e., moving along the axis perpendicular to the wavelength direction) corresponds to a temporally resolved spectrum. The left panel of Figure 4.21 shows the effective light curves for this situation if spectra are extracted from $1''$ long parts of the slit. The offset from the peak of the LE are $1.0''$, $0.0''$, and $-1.0''$ along the ρ-axis. The right panel shows the corresponding integrated spectra. The three spectra show clear differences, in particular the spectra with $\Delta\rho_{\mathrm{offset}} = 1.0$ is very blue since it is dominated by the first peak of the light curve.

Aligning the slit perpendicular to the LE can significantly reduce the amount of light within the slit, and therefore, this method is best applied to the brightest LEs. To maximize the temporal resolution of the LE spectra, the LE should have the following properties:

1. The dust filament is very thin— on the order of 0.01 ly.
2. The inclination is close to the LE ellipsoid tangential. This “stretches” the

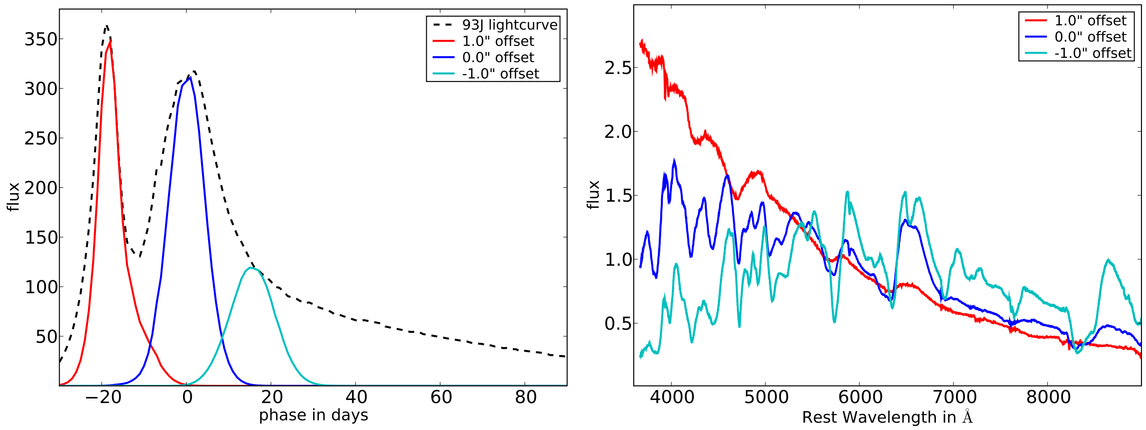

Figure 4.21: *Left:* Effective light curves for LE2116 with a 1″ slit and offsets, $\Delta\rho_{\text{offset}}$, of $-1.0''$, $0.0''$, and $1.0''$ shown in red, blue, and cyan, respectively. *Right:* Integrated spectra corresponding to the effective light curves in the left panel.

projected light curve along the ρ-axis.

3. The LE is bright.

4. The PSF of the spectroscopic observation is small.

Even though there are no known Galactic LEs that fulfill all of these criteria, we note that the existing surveys are far from complete. Additionally, even in non-ideal conditions, some temporal information could be obtained. The ability to temporally resolve the SN spectra will allow us to follow the evolution of the explosion, specifically measure velocity gradients of spectral features, and potentially probing the abundances of elements in the ejecta.

4.6.3 Constraining Supernova Light-Curve Shapes

Under similar circumstances needed to temporally resolve the LE spectra (see Section 4.6.2), we will also be able to *spatially resolve* the temporal characteristics of the source event light curve. The most important requirements are that the dust width has to be thin, the inclination close to the LE ellipsoid tangential, and the PSF needs to be significantly smaller than the width of the LE profile. Note that in contrast to temporally resolving the LE spectra, constraining the LE shape can be done with LEs that have a significantly lower signal-to-noise ratio.

Unfortunately, there is a degeneracy between the dust width and the light curve parameters (e.g., peak width and height; peak ratio if double-peaked) which can be broken if different areas of the LE have different dust widths. Since the light curve must be the same for all LEs in a given direction, any difference in the shape must be from the dust. If this degeneracy cannot be broken, LEs can still provide interesting constraints. First, the light curve can only be broadened by the dust, so any profile will provide some constraint on the light-curve shape. Additionally, by comparing the profile to known SN light curves, the properties of the SN can be further constrained.

The light-curve shape of a SN can give important insights into the nature of the SN explosion. SNe Ia, for example, show a clear relationship between the width of their light curves and their intrinsic brightness (e.g., Phillips, 1993). Another example is if the shock break-out of a core-collapse SN is resolved in the light curve, which would provide a measurement (or strict constraints) on the radius of the progenitor star. We will discuss this in more detail in the following paragraphs.

After the gravitational collapse of the core of a massive star, the core bounces, sending a shock wave out through the outer layers of the star, exploding the star (Woosley & Weaver, 1986). When the shock wave reaches the surface of the star, a flash (at optical wavelengths, it has a thermal spectrum) is generated that decays over hours to days (Colgate, 1974; Klein & Chevalier, 1978). This has been seen for SNe IIP (Gezari et al., 2008; Schawinski et al., 2008), but was best observed recently with SN Ib 2008D (Soderberg et al., 2008; Modjaz et al., 2009). As the stellar envelope cools, the optical emission fades away. This subsequent fading was first detected in SN 1987A (e.g., Woosley et al., 1987; Hamuy et al., 1988), which had a shock break-out cooling phase that was unusually long. This cooling phase has been detected for a handful of other SNe, notably SN 1993J (e.g., Richmond et al., 1994), a SN IIb similar to Cas A.

The duration, luminosity, and SED of the shock break-out phase depends on a handful of parameters such as the presence of a stellar wind and the ejecta mass (Matzner & McKee, 1999), but is most dependent on the progenitor radius (Calzavara & Matzner, 2004). The peak brightness of the subsequent fading is dependent on the ejecta mass, kinetic energy, and progenitor radius, while the timescale for the fading is proportional to both the radius of the photosphere and its temperature (Waxman et al., 2007). One caveat is that interaction of the shock with shells of material outside the star can produce prompt emission similar to a shock breakout.

The disadvantage of using LEs to observe the shock break-out is that if the resolution of the image is poor or the dust thickness is too large, it is impossible to distinguish between a shock break-out, subsequent fading, and normal radioactive-decay powered SN light curve, and a somewhat broader radioactive-decay powered SN light curve. For Cas A, where we might expect to see a shock break-out, we are unable to separate the light curve into multiple components in ground-based images with moderate seeing ($< 1''$). However, as shown in Figure 4.22, if the dust thickness is sufficiently small, we should detect a luminous shock break-out with the resolution of *HST*, if it exists. This will allow us to constrain the radius of the progenitor and its mass loss history, linking the physical properties of a star with its SNR.

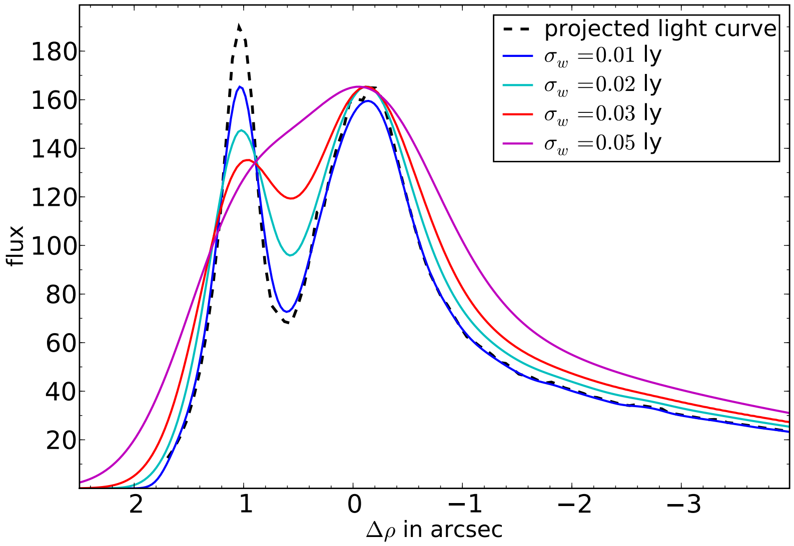

Figure 4.22: Simulated LE profiles of SN 1993J assuming different scattering dust widths. The scattering dust filament for the simulations is at $z = 400$ ly with an inclination of 0°, and the PSF FWHM is $0.05''$, similar to what can be expected from space-based imaging. The black dashed line is the projected SN 1993J light curve.

4.7 Conclusions

In recent years, LEs of SNe have offered the rare opportunity to spectroscopically classify the SN type hundreds of years after the light of the explosion first reached the Earth (e.g., Rest et al., 2008a). Recently, we have obtained the first spectroscopic observations of a historical SN from different lines of sight using LEs (Rest et al., 2010). These observations provide the unique opportunity to examine a SN from different directions, with the light for each LE coming from slightly different hemispheres of the SN. In this paper, we have demonstrated that to properly separate differences in the observed LE spectra caused by intrinsic asymmetries in the SN from those caused by scattering dust, seeing, and spectroscopic slit position, it is necessary to properly model the latter.

Throughout this paper, we have shown how to both determine the properties of the scattering dust and their influence, as well as that of the PSF and spectroscopic slit position, on the observed LE spectra. We found that the dust width and inclination are the dominant factors, especially when the dust filament is thin. These two factors can be degenerate with respect to the LE profile shape; therefore, it is essential to determine the dust filament inclination independently using the LE proper motion from images taken at two (or more) epochs. The slit width and its misalignment with the major axis of the LE are is also a significant factor. The image PSF smears out the observed LE and thus also impacts the observed LE spectrum. Taking all of these factors into account, we found that the observed LE spectrum is not the light-curve weighted integration of the spectra at all epochs, but rather the integration of the spectra weighted by an effective light curve. This effective light curve is the original light curve convolved with a window function, and it is different for every LE location. In general, the most significant difference between the effective light curves and the original light curve was that later epochs tend to be truncated in the effective light curves.

We used fits to the LE profiles of Cas A and SN 1987A to test the consistency and veracity of our model. We fit the model to the observed LE profiles, where the three free parameters were the LE profile peak height, LE position, and – physically most important – the dust filament width. The model reproduced the observed LE profiles very well, and we found that it was possible to determine all factors influencing the observed LE spectrum *a priori* just from images, without using the observed spectrum.

We constructed window functions and effective light curves for the Cas A LEs using SN 1993J as a template. We found a much better match of the SN 1993J spectra template to the observed Cas A LE spectrum if we used the effective light curve instead of the real light curve for weighting. The most significant difference was in the late-phase emission lines [O I] $\lambda\lambda$6300, 6363, [Ca II] $\lambda\lambda$7291, 7324, and the Ca II NIR triplet, consistent with our expectation from the model. Although we do not have access to the Krause et al. (2008) images, we find that their Cas A spectrum is consistent with an integrated spectrum weighted with a light curve truncated at

80 days. Our expectation is that the majority of differences between the Cas A LE spectrum and the full light-curve weighted SN 1993J spectrum are due to scattering dust properties.

We also constructed a window function and effective light curve for a SN 1987A LE which constitutes a special test case since the light curve and spectral data of the SN are available. With this data, we constructed a LE spectrum from the original SN and compared it to the observed LE spectrum. We found that the constructed LE spectrum correctly predicted the line strength of the Hα line, while a simple integration weighted by the light curve was a poor fit.

We presented several additional investigations that can be attempted with LEs in the near future. Two of these studies, temporally resolved spectra and spatially resolved light curves, require thin dust filaments. Until now, the assumption of thick scattering dust prevented such studies.

4.8 Acknowledgements

We thank J. Menzies for providing the spectral database of SN 1987A obtained from SAAO. AR was partially supported by the Goldberg Fellowship Program. AR thanks Jeremiah Murphy for stimulating discussions. Supernova research at Harvard College Observatory is supported in part by NSF grant AST-0907903. Based on observations obtained at the Gemini Observatory (program ID GS-2006B-Q-41), which is operated by the Association of Universities for Research in Astronomy, Inc., under a cooperative agreement with the US National Science Foundation on behalf of the Gemini partnership: the NSF (United States), the Science and Technology Facilities Council (United Kingdom), the National Research Council (Canada), CONICYT (Chile), the Australian Research Council (Australia), Ministério da Ciência e Tecnologia (Brazil) and Ministerio de Ciencia, Tecnología e Innovación Productiva (Argentina). NOAO is operated by AURA under cooperative agreement with the NSF.

4.9 Appendix

4.9.1 Light Echo Profiles

The LE equation (Couderc, 1939),

$$z = \frac{\rho^2}{2ct} - \frac{ct}{2}, \tag{4.1}$$

relates the depth coordinate, z, the LE-SN distance projected along the line-of-sight, to the LE distance ρ perpendicular to the line of sight, and the time t since the initial (undelayed) arrival of SN photons. Then the distance r from the scattering dust to the source event is $r^2 = \rho^2 + z^2$, and ρ is

$$\rho = (D - z)\sin\gamma, \tag{4.2}$$

where D is the distance from the observer to the source event, and γ is the angular separation between the source event and the scattering dust, which yields the three-dimensional position of the dust associated with the arclet.

Tylenda (2004) elegantly derives the apparent expansion of a LE ring caused by a thin plane-parallel sheet of dust. In a very similar manner, we derive how the dust filament inclination influences the observed LE profile. Because of the symmetry around the z-axis, we define our coordinate system so that the dust sheet is normal in the (ρ, z) plane. This allows us to do all our calculations in the two-dimensional (ρ, z) space. We define the dust sheet as

$$z = z_d - a\rho, \tag{4.3}$$

where $a = \tan\alpha$. We define α as the angle of the dust sheet with respect to the ρ axis, where positive angles go from the positive ρ axis towards the negative z axis. The dust sheet intersects with the z axis at $z = z_d$. The two intersections of the dust sheet with the reflection paraboloid defined in Equation 4.1 are then

$$\rho_{\pm}(t, z_d, a) = -act \pm \xi, \text{ where} \tag{4.4}$$

$$\xi = \sqrt{(1+a^2)\,(ct)^2 + 2z_0 ct}. \tag{4.5}$$

Now consider a LE caused by a source event with a peak at t_0 at an angular separation γ from the source. Assuming a distance D to the source event, we can then calculate the position of the scattering dust (ρ_0, z_0) using Equation 4.1 and 4.2. The dust sheet defined in Equation 4.3 goes through (ρ_0, z_0) if

$$z_d = z_0 + a\rho_0. \tag{4.6}$$

There are two special dust inclinations. We denote the inclination angle of the dust sheet tangential and orthogonal to the LE ellipse as $\alpha_{\|}$ and $\alpha_{\perp}$, respectively. Then the slopes of the dust sheets are $a_{\|} = \tan\alpha_{\|}$, and $a_{\perp} = \tan\alpha_{\perp}$, and we can calculate them as

$$a_{\|} = -\left(1 + \frac{2z_0}{ct}\right)^{1/2} = -\frac{\rho_0}{ct}; \tag{4.7}$$

$$a_{\perp} = -a_{\|}^{-1} = \left(1 + \frac{2z_0}{ct}\right)^{-1/2} = \frac{ct}{\rho_0}. \tag{4.8}$$

The intersection of the dust sheet with the LE ellipsoid is then at

$$\rho_0 = \begin{cases} 0 & \text{for } \alpha = 90^\circ \\ \rho_+ & \text{for } a > a_{\|} \\ \rho_- & \text{for } a < a_{\|} \end{cases}. \tag{4.9}$$

Now consider a dust sheet with a finite width defined by a density $D(\Delta r)$, and a light curve $f_{\text{source}}(\Delta t)$, where Δr is the distance orthogonal to the dust sheet, and

$\Delta t = t - t_0$ (see Section 4.9.4 for a more detailed description of the dust model $D(\Delta r)$). The flux from the source event at time t is reflected by the part of the dust sheet at a distance Δr to the center of the dust sheet, and makes a relative contribution to the LE signal of

$$f_{\mathrm{LE}} = D(\Delta r) f_{\mathrm{source}}(\Delta t) \tag{4.10}$$

at the position

$$\rho_{\mathrm{LE}} = \begin{cases} \rho_+(t_0 + \Delta t, z_d + \Delta r/\cos\alpha, a) & \text{if } \rho_0 = \rho_+ \\ \rho_-(t_0 + \Delta t, z_d + \Delta r/\cos\alpha, a) & \text{if } \rho_0 = \rho_- \end{cases}. \tag{4.11}$$

The reason for choosing $+$ and $-$ is based on the choice made for ρ_0. For all practical purposes, Δr and Δt are small, and therefore the sign should be the same. Exceptions are $\alpha \approx 0.0$ and $a \approx a_{\parallel}$. We define

$$\Delta\rho = \rho_{\mathrm{LE}} - \rho_0. \tag{4.12}$$

By examining the relative contribution for all values of Δr and Δt and using Equation 4.10 – 4.12, we can calculate a cumulative grid of fluxes, $F'_{\mathrm{LE}}(\Delta t, \Delta\rho)$.

The model must now account for seeing. We describe the data PSF as a Gaussian with a FWHM of x arcsec and Gaussian width of $\sigma_{\mathrm{PSF}} = x/(2\sqrt{2\ln(2)}) \approx x/2.35$. Then the cumulative grid of fluxes convolved with the seeing is

$$F_{\mathrm{LE}}(\Delta t, \Delta\rho) = \sum_{\Delta\rho'} F'_{\mathrm{LE}}(\Delta t, \Delta\rho') \frac{1}{\sqrt{2\pi\sigma^2_{\mathrm{PSF}}}} \exp\left(\frac{(\Delta\rho - \Delta\rho')^2}{2\sigma^2_{\mathrm{PSF}}}\right). \tag{4.13}$$

Integrating over Δt returns the LE flux profile with respect to ρ:

$$P_{\mathrm{LE}}(\Delta\rho) = \int F_{\mathrm{LE}}(\Delta t, \Delta\rho)\mathrm{d}t. \tag{4.14}$$

4.9.2 Dependence of the Light Echo Spectrum on Light Echo Profile

We now examine the LE flux for a spectroscopic observation. Consider a slit positioned at ρ_s with a effective width of $\sigma_{s,\text{eff}}$. The reason that this is the effective slit width and its relation to the real, physical slit width σ_s is explained below in Appendix 4.9.3. We define the offset between the slit and the LE measured parallel to the ρ axis as $\Delta\rho_{\text{offset}} = \rho_s - \rho_0$. The slit then subtends from

$$\Delta\rho_{\text{min}} = \Delta\rho_{\text{offset}} - \sigma_{s,\text{eff}}/2 \text{ to} \tag{4.15}$$

$$\Delta\rho_{\text{max}} = \Delta\rho_{\text{offset}} + \sigma_{s,\text{eff}}/2. \tag{4.16}$$

We can then calculate the relative contribution, $H(\Delta t)$, of the source event at time Δt to the spectra with

$$H(\Delta t) = \int_{\Delta\rho_{\text{min}}}^{\Delta\rho_{\text{max}}} F_{\text{LE}}(\Delta t, \Delta\rho)\text{d}\Delta\rho. \tag{4.17}$$

$H(\Delta t)$ is also the effective light curve. We define the window function $w(\Delta t)$ as the fractional difference between the effective light curve and the real light curve,

$$w(\Delta t) = f_{\text{source}}(\Delta t)/H(\Delta t). \tag{4.18}$$

The observed LE spectrum $S_{\text{LE}}(\lambda)$ is then

$$S_{\text{LE}}(\lambda) = \int S(\lambda, \Delta t)H(\Delta t)\text{d}\Delta t, \tag{4.19}$$

where $S(\lambda, \Delta t)$ is the spectrum of the source event at the given phase Δt.

4.9.3 Dependence of the Light Echo Spectrum on Slit Position

The position and inclination of the slit with respect to the LE has a major impact on the observed spectrum. We illustrate this in Figure 4.8. We define a coordinate system (ρ, u), where u is orthogonal to ρ through $\Delta\rho = 0.0$ in the plane of the sky. For a dust filament that is locally planar and perpendicular to the (ρ, z) plane (i.e., parallel to u), the LE is aligned with the u axis. However, if it is tilted with respect to u by an angle of δ_1, then the LE will also be tilted by the same angle (see gray shaded area in Figure 4.8).

Now consider a slit (red box in Figure 4.8) that is misaligned with the LE by an angle δ_2, and also offset along the ρ axis by Δs. We split the slit into subslits, indicated with the dotted blue lines in Figure 4.8. For each of these subslits, we determine the LE profile in Figure 4.8. The offset $\Delta\rho_{\mathrm{offset},i}$ of the subslit i centered at u_i to the LE is

$$\Delta\rho_{\mathrm{offset},i} = u_i \sin(\delta_2) + \Delta s, \tag{4.20}$$

where δ_2 is the angle between the slit and the LE, and Δs is the offset of the center of the slit to the LE (see Figure 4.8). The effective slit width $\sigma_{s,\mathrm{eff}}$ depends on the physical slit width σ_s and is

$$\sigma_{s,\mathrm{eff}} = \sigma_s / \cos(\delta_2). \tag{4.21}$$

The effective light curve H_i and window function w_i for each subslit i can be calculated plugging $\Delta\rho_{\mathrm{offset},i}$ into Equation 4.15 and 4.16. The total window function w_{slit} for the full slit is then the weighted average of the subslit window functions, where the weight is the flux f_w that falls into the subslit is

$$f_{w,i} = \int_{\Delta\rho_{\min}}^{\Delta\rho_{\max}} P_{\mathrm{LE}}(\Delta\rho)\mathrm{d}\Delta\rho \text{ with} \tag{4.22}$$

$$w_{\mathrm{slit}} = \frac{\sum_i w_i f_{w,i}^{-2}}{\sum_i f_{w,i}^{-2}}. \tag{4.23}$$

The integrated spectrum can then be calculated by using w_{slit} in Equations 4.18 and 4.19.

4.9.4 Dust Model

For simplicity in our simulations, we choose a box-car dust density profile $D(\Delta r)$. A more realistic density profile is a Gaussian, and therefore when fitting observed LE profiles we use a profile

$$D(\Delta r) = \frac{c}{\sqrt{2\pi\sigma_d^2}} \exp\left(\frac{\Delta r^2}{2\sigma_d^2}\right), \tag{4.24}$$

where σ_d is the width of the Gaussian, and c is a normalization factor. Note that the physical dust density profile width $\sigma_{d,\mathrm{phys}}$ is different from the nominal fitted σ_d if $\delta_1 \neq 0$. They are related through

$$\sigma_{d,\mathrm{phys}} = \sigma_d \cos(\delta_1). \tag{4.25}$$

4.9.5 Dust Filament Inclination

We refer the reader to a more thorough and detailed discussion about the apparent motion and its dependence on the dust filament inclination by Rest et al. (in prep.). However, we present an initial treatment of the process here. We define the dust filament inclination α as

$$\alpha = \tan^{-1}\left(-\frac{z(t_2) - z(t_1)}{\rho(t_2) - \rho(t_1)}\right) \tag{4.26}$$

with $t_2 > t_1$, and with z calculated from Equation 4.1 for a measured ρ and given t. Note that a dust filament in the plane of the sky has $\alpha = 0^\circ$, and dust filaments tilted away from the observer have positive α. If more than two epochs are available, fitting a straight line through (ρ, z) increases the accuracy of α.

There are several sources that can introduce errors into the measurement of the dust inclination, specifically:

- Poisson uncertainty in the apparent motion of the LE, especially for the fainter LEs
- A small number of epochs
- Intrinsic differences in the filament inclination with ρ

The first two mainly increase the Poisson noise in the inclination. The last one, however, is the most significant one since it can introduce systematic uncertainties. If the dust filament has additional substructure, such as twisted dust on small scales, then the inclination of the scattering dust changes on small scales and a correct constraint on the dust inclination at the time of spectroscopy can only be done if there are several epochs close to the time of the spectroscopy.

Bibliography

Badenes, C. and Hughes, J. P. and Cassam-Chenaï, G. and Bravo, E. 2008, ApJ, 680, 1149

Barbon, R. and Benetti, S. and Cappellaro, E. and Patat, F. and Turatto, M. and Iijima, T. 1995, A&AS, 110, 513

Bond, H. E. and Gilmozzi, R. and Meakes, M. G. and Panagia, N. 1990, ApJ, 354, L49

Bond, H. E. and Henden, A. and Levay, Z. G. and Panagia, N. and Sparks, W. B. and Starrfield, S. and Wagner, R. M. and Corradi, R. L. M. and Munari, U. 2003, Nature, 422, 405

Calzavara, A. J. and Matzner, C. D. 2004, MNRAS, 351, 694

Cappellaro, E. and Patat, F. and Mazzali, P. A. and Benetti, S. and Danziger, J. I. and Pastorello, A. and Rizzi, L. and Salvo, M. and Turatto, M. 2001, ApJ, 549, L215

Catchpole, R. M. and Menzies, J. W. and Monk, A. S. and Wargau, W. F. and Pollaco, D. and Carter, B. S. and Whitelock, P. A. and Marang, F. and Laney, C. D. and Balona, L. A. and Feast, M. W. and Lloyd Evans, T. H. H. and Sekiguchi, K.

and Laing, J. D. and Kilkenny, D. M. and Spencer Jones, J. and Roberts, G. and Cousins, A. W. J. and van Vuuren, G. and Winkler, H. 1987, MNRAS, 229, 15P

Catchpole, R. M. and Whitelock, P. A. and Feast, M. W. and Menzies, J. M. and Glass, I. S. and Marang, F. and Laing, J. D. and Spencer Jones, J. H. and Roberts, G. and Balona, L. A. and Carter, B. S. and Laney, C. D. and Evans, L. T. and Sekiguchi, K. and Hutchinson, G. G. and Maddison, R. and Albinson, J. and Evans, A. and Allen, F. A. and Winkler, H. and Fairall, A. and Corbally, C. and Davies, J. K. and Parker, Q. A. 1988, MNRAS, 231, 75P

Catchpole, R. M. and Whitelock, P. A. and Menzies, J. W. and Feast, M. W. and Marang, F. and Sekiguchi, K. and van Wyk, F. and Roberts, G. and Balona, L. A. and Egan, J. M. and Carter, B. S. and Laney, C. D. and Laing, J. D. and Spencer Jones, J. H. and Glass, I. S. and Winkler, H. and Fairall, A. P. and Lloyd Evans, T. H. H. and Cropper, M. S. and Shenton, M. and Hill, P. W. and Payne, P. and Jones, K. N. and Wargau, W. and Mason, K. O. and Jeffery, C. S. and Hellier, C. and Parker, Q. A. and Chini, R. and James, P. A. and Doyle, J. G. and Butler, C. J. and Bromage, G. 1989, MNRAS, 237, 55P

Colgate, S. A. 1974, ApJ, 187, 333

Couderc, P. 1939, Annales d'Astrophysique, 2, 271

Crotts, A. 1988, IAU Circ., 4561, 4

Dwek, E. and Arendt, R. G. 2008, ApJ, 685, 976

Fesen, R. A. and Hammell, M. C. and Morse, J. and Chevalier, R. A. and Borkowski, K. J. and Dopita, M. A. and Gerardy, C. L. and Lawrence, S. S. and Raymond, J. C. and van den Bergh, S. 2006, ApJ, 645, 283

Filippenko, A. V. 1997, ARA&A, 35, 309

Filippenko, A. V. and Matheson, T. and Barth, A. J. 1994, AJ, 108, 2220

Filippenko, A. V. and Matheson, T. and Ho, L. C. 1993, ApJ, 415, L103

Filippenko, A. V. and Richmond, M. W. and Matheson, T. and Shields, J. C. and Burbidge, E. M. and Cohen, R. D. and Dickinson, M. and Malkan, M. A. and Nelson, B. and Pietz, J. and Schlegel, D. and Schmeer, P. and Spinrad, H. and Steidel, C. C. and Tran, H. D. and Wren, W. 1992, ApJ, 384, L15

Fransson, C. and Challis, P. M. and Chevalier, R. A. and Filippenko, A. V. and Kirshner, R. P. and Kozma, C. and Leonard, D. C. and Matheson, T. and Baron, E. and Garnavich, P. and Jha, S. and Leibundgut, B. and Lundqvist, P. and Pun, C. S. J. and Wang, L. and Wheeler, J. C. 2005, ApJ, 622, 991

Garavini, G. and Folatelli, G. and Goobar, A. and Nobili, S. and Aldering, G. and Amadon, A. and Amanullah, R. and Astier, P. and Balland, C. and Blanc, G. and Burns, M. S. and Conley, A. and Dahlén, T. and Deustua, S. E. and Ellis, R. and Fabbro, S. and Fan, X. and Frye, B. and Gates, E. L. and Gibbons, R. and Goldhaber, G. and Goldman, B. and Groom, D. E. and Haissinski, J. and Hardin, D. and Hook, I. M. and Howell, D. A. and Kasen, D. and Kent, S. and Kim, A. G. and Knop, R. A. and Lee, B. C. and Lidman, C. and Mendez, J. and Miller, G. J. and Moniez, M. and Mourão, A. and Newberg, H. and Nugent, P. E. and Pain, R. and Perdereau, O. and Perlmutter, S. and Prasad, V. and Quimby, R. and Raux, J. and Regnault, N. and Rich, J. and Richards, G. T. and Ruiz-Lapuente, P. and Sainton, G. and Schaefer, B. E. and Schahmaneche, K. and Smith, E. and Spadafora, A. L. and Stanishev, V. and Walton, N. A. and Wang, L. and Wood-Vasey, W. M. 2004, AJ, 128, 387

Garg, A. and Stubbs, C. W. and Challis, P. and Wood-Vasey, W. M. and Blondin, S. and Huber, M. E. and Cook, K. and Nikolaev, S. and Rest, A. and Smith, R. C. and Olsen, K. and Suntzeff, N. B. and Aguilera, C. and Prieto, J. L. and Becker, A. and Miceli, A. and Miknaitis, G. and Clocchiatti, A. and Minniti, D. and Morelli, L. and Welch, D. L. 2007, AJ, 133, 403

Gezari, S. and Dessart, L. and Basa, S. and Martin, D. C. and Neill, J. D. and Woosley, S. E. and Hillier, D. J. and Bazin, G. and Forster, K. and Friedman, P. G. and Le Du, J. and Mazure, A. and Morrissey, P. and Neff, S. G. and Schiminovich, D. and Wyder, T. K. 2008, ApJ, 683, L131

Hamuy, M. and Suntzeff, N. B. 1990, AJ, 99, 1146

Hamuy, M. and Suntzeff, N. B. and Gonzalez, R. and Martin, G. 1988, AJ, 95, 63

Hook, I. M. and Jørgensen, I. and Allington-Smith, J. R. and Davies, R. L. and Metcalfe, N. and Murowinski, R. G. and Crampton, D. 2004, PASP, 116, 425

Hughes, J. P. and Hayashi, I. and Helfand, D. and Hwang, U. and Itoh, M. and Kirshner, R. and Koyama, K. and Markert, T. and Tsunemi, H. and Woo, J. 1995, ApJ, 444, L81

Jeffery, D. J. and Kirshner, R. P. and Challis, P. M. and Pun, C. S. J. and Filippenko, A. V. and Matheson, T. and Branch, D. and Chevalier, R. A. and Fransson, C. and Panagia, N. and Wagoner, R. V. and Wheeler, J. C. and Clocchiatti, A. 1994, ApJ, 421, L27

Kapteyn, J. C. 1902, Astronomische Nachrichten, 157, 201

Klein, R. I. and Chevalier, R. A. 1978, ApJ, 223, L109

Krause, O. and Birkmann, S. M. and Usuda, T. and Hattori, T. and Goto, M. and Rieke, G. H. and Misselt, K. A. 2008, Science, 320, 1195

Krause, O. and Rieke, G. H. and Birkmann, S. M. and Le Floc'h, E. and Gordon, K. D. and Egami, E. and Bieging, J. and Hughes, J. P. and Young, E. T. and Hinz, J. L. and Quanz, S. P. and Hines, D. C. 2005, Science, 308, 1604

Kunkel, W. and Madore, B. and Shelton, I. and Duhalde, O. and Bateson, F. M. and Jones, A. and Moreno, B. and Walker, S. and Garradd, G. and Warner, B. and Menzies, J. 1987, IAU Circ., 4316, 1

Liu, J.-F. and Bregman, J. N. and Seitzer, P. 2003, ApJ, 582, 919

Matheson, T. and Filippenko, A. V. and Ho, L. C. and Barth, A. J. and Leonard, D. C. 2000, AJ, 120, 1499

Matzner, C. D. and McKee, C. F. 1999, ApJ, 510, 379

Meikle, W. P. S. and Mattila, S. and Gerardy, C. L. and Kotak, R. and Pozzo, M. and van Dyk, S. D. and Farrah, D. and Fesen, R. A. and Filippenko, A. V. and Fransson, C. and Lundqvist, P. and Sollerman, J. and Wheeler, J. C. 2006, ApJ, 649, 332

Menzies, J. W. and Catchpole, R. M. and van Vuuren, G. and Winkler, H. and Laney, C. D. and Whitelock, P. A. and Cousins, A. W. J. and Carter, B. S. and Marang, F. and Lloyd Evans, T. H. H. and Roberts, G. and Kilkenny, D. and Spencer Jones, J. and Sekiguchi, K. and Fairall, A. P. and Wolstencroft, R. D. 1987, MNRAS, 227, 39P

Miknaitis, G. and Pignata, G. and Rest, A. and Wood-Vasey, W. M. and Blondin, S. and Challis, P. and Smith, R. C. and Stubbs, C. W. and Suntzeff, N. B. and Foley, R. J. and Matheson, T. and Tonry, J. L. and Aguilera, C. and Blackman, J. W. and Becker, A. C. and Clocchiatti, A. and Covarrubias, R. and Davis, T. M. and Filippenko, A. V. and Garg, A. and Garnavich, P. M. and Hicken, M. and Jha, S. and Krisciunas, K. and Kirshner, R. P. and Leibundgut, B. and Li, W. and Miceli, A. and Narayan, G. and Prieto, J. L. and Riess, A. G. and Salvo, M. E. and Schmidt, B. P. and Sollerman, J. and Spyromilio, J. and Zenteno, A. 2007, ApJ, 666

Modjaz, M. and Li, W. and Butler, N. and Chornock, R. and Perley, D. and Blondin, S. and Bloom, J. S. and Filippenko, A. V. and Kirshner, R. P. and Kocevski, D. and Poznanski, D. and Hicken, M. and Foley, R. J. and Stringfellow, G. S. and Berlind, P. and Barrado y Navascues, D. and Blake, C. H. and Bouy, H. and Brown, W. R.

and Challis, P. and Chen, H. and de Vries, W. H. and Dufour, P. and Falco, E. and Friedman, A. and Ganeshalingam, M. and Garnavich, P. and Holden, B. and Illingworth, G. and Lee, N. and Liebert, J. and Marion, G. H. and Olivier, S. S. and Prochaska, J. X. and Silverman, J. M. and Smith, N. and Starr, D. and Steele, T. N. and Stockton, A. and Williams, G. G. and Wood-Vasey, W. M. 2009, ApJ, 702, 226

Newman, A. B. and Rest, A. 2006, PASP, 118, 1484

Phillips, M. M. 1993, ApJ, 413, L105

Phillips, M. M. and Hamuy, M. and Heathcote, S. R. and Suntzeff, N. B. and Kirhakos, S. 1990, AJ, 99, 1133

Phillips, M. M. and Heathcote, S. R. and Hamuy, M. and Navarrete, M. 1988, AJ, 95, 1087

Phillips, M. M. and Wells, L. A. and Suntzeff, N. B. and Hamuy, M. and Leibundgut, B. and Kirshner, R. P. and Foltz, C. B. 1992, AJ, 103, 1632

Quinn, J. L. and Garnavich, P. M. and Li, W. and Panagia, N. and Riess, A. and Schmidt, B. P. and Della Valle, M. 2006, ApJ, 652, 512

Rest, A. and Becker, A. C. and Bergmann, M. and Blondin, S. and Challis, P. and Clocchiatti, A. and Cook, K. H. and Damke, G. and Garg, A. and Huber, M. E. and Lanning, H. and Matheson, T. and Minniti, D. and Morelli, L. and Nikolaev, S. and Olsen, K. and Oasterle, L. and Pignata, G. and Prieto, J. and Smith, R. C. and Stubbs, C. and Suntzeff, N. B. and Welch, D. L. and Wood-Vasey, W. M. and Zenteno, A. 2007, in Bulletin of the American Astronomical Society, Vol. 38, 935

Rest, A. and Foley, R. J. and Sinnott, B. and Welch, D. L. and Badenes, C. and Filippenko, A. V. and Bergmann, M. and Bhatti, W. A. and Blondin, S. and Challis, P. and Damke, G. and Finley, H. and Huber, M. E. and Kasen, D. and

Kirshner, R. P. and Matheson, T. and Mazzali, P. and Minniti, D. and Nakajima, R. and Narayan, G. and Olsen, K. and Sauer, D. and Smith, R. C. and Suntzeff, N. B. 2010, ArXiv e-prints, 1003.5660

Rest, A. and Matheson, T. and Blondin, S. and Bergmann, M. and Welch, D. L. and Suntzeff, N. B. and Smith, R. C. and Olsen, K. and Prieto, J. L. and Garg, A. and Challis, P. and Stubbs, C. and Hicken, M. and Modjaz, M. and Wood-Vasey, W. M. and Zenteno, A. and Damke, G. and Newman, A. and Huber, M. and Cook, K. H. and Nikolaev, S. and Becker, A. C. and Miceli, A. and Covarrubias, R. and Morelli, L. and Pignata, G. and Clocchiatti, A. and Minniti, D. and Foley, R. J. 2008a, ApJ, 680, 1137

Rest, A. and Sinnott, B. and Welch, D. L. 2011, in prep.

Rest, A. and Stubbs, C. and Becker, A. C. and Miknaitis, G. A. and Miceli, A. and Covarrubias, R. and Hawley, S. L. and Smith, R. C. and Suntzeff, N. B. and Olsen, K. and Prieto, J. L. and Hiriart, R. and Welch, D. L. and Cook, K. H. and Nikolaev, S. and Huber, M. and Prochtor, G. and Clocchiatti, A. and Minniti, D. and Garg, A. and Challis, P. and Keller, S. C. and Schmidt, B. P. 2005a, ApJ, 634, 1103

Rest, A. and Suntzeff, N. B. and Olsen, K. and Prieto, J. L. and Smith, R. C. and Welch, D. L. and Becker, A. and Bergmann, M. and Clocchiatti, A. and Cook, K. and Garg, A. and Huber, M. and Miknaitis, G. and Minniti, D. and Nikolaev, S. and Stubbs, C. 2005b, Nature, 438, 1132

Rest, A. and Welch, D. L. and Suntzeff, N. B. and Oaster, L. and Lanning, H. and Olsen, K. and Smith, R. C. and Becker, A. C. and Bergmann, M. and Challis, P. and Clocchiatti, A. and Cook, K. H. and Damke, G. and Garg, A. and Huber, M. E. and Matheson, T. and Minniti, D. and Prieto, J. L. and Wood-Vasey, W. M. 2008b, ApJ, 681, L81

Richmond, M. W. and Treffers, R. R. and Filippenko, A. V. and Paik, Y. 1996, AJ, 112, 732

Richmond, M. W. and Treffers, R. R. and Filippenko, A. V. and Paik, Y. and Leibundgut, B. and Schulman, E. and Cox, C. V. 1994, AJ, 107, 1022

Ritchey, G. W. 1901a, ApJ, 14, 293

——. 1901b, ApJ, 14, 167

——. 1902, ApJ, 15, 129

Schawinski, K. and Justham, S. and Wolf, C. and Podsiadlowski, P. and Sullivan, M. and Steenbrugge, K. C. and Bell, T. and Röser, H.-J. and Walker, E. S. and Astier, P. and Balam, D. and Balland, C. and Carlberg, R. and Conley, A. and Fouchez, D. and Guy, J. and Hardin, D. and Hook, I. and Howell, D. A. and Pain, R. and Perrett, K. and Pritchet, C. and Regnault, N. and Yi, S. K. 2008, Science, 321, 223

Schmidt, B. P. and Kirshner, R. P. and Leibundgut, B. and Wells, L. A. and Porter, A. C. and Ruiz-Lapuente, P. and Challis, P. and Filippenko, A. V. 1994, ApJ, 434, L19

Sinnott, B. and Welch, D. and Rest, A. and Matheson, T. and Blondin, S. and Bergmann, M. and Suntzeff, N. B. and Smith, R. C. and Olsen, K. and Prieto, J. L. and Garg, A. and Challis, P. and Stubbs, C. and Hicken, M. and Modjaz, M. and Wood-Vasey, W. M. and Zenteno, A. and Damke, G. and Newman, A. and Huber, M. and Cook, K. H. and Nikolaev, S. and Becker, A. C. and Miceli, A. and Covarrubias, R. and Morelli, L. and Pignata, G. and Clocchiatti, A. and Minniti, D. and Foley, R. J. 2011, in prep.

Soderberg, A. M. and Berger, E. and Page, K. L. and Schady, P. and Parrent, J. and Pooley, D. and Wang, X.-Y. and Ofek, E. O. and Cucchiara, A. and Rau, A. and Waxman, E. and Simon, J. D. and Bock, D. C.-J. and Milne, P. A. and Page, M. J.

and Barentine, J. C. and Barthelmy, S. D. and Beardmore, A. P. and Bietenholz, M. F. and Brown, P. and Burrows, A. and Burrows, D. N. and Byrngelson, G. and Cenko, S. B. and Chandra, P. and Cummings, J. R. and Fox, D. B. and Gal-Yam, A. and Gehrels, N. and Immler, S. and Kasliwal, M. and Kong, A. K. H. and Krimm, H. A. and Kulkarni, S. R. and Maccarone, T. J. and Mészáros, P. and Nakar, E. and O'Brien, P. T. and Overzier, R. A. and de Pasquale, M. and Racusin, J. and Rea, N. and York, D. G. 2008, Nature, 453, 469

Sparks, W. B. and Macchetto, F. and Panagia, N. and Boffi, F. R. and Branch, D. and Hazen, M. L. and della Valle, M. 1999, ApJ, 523, 585

Sugerman, B. E. K. 2005, ApJ, 632, L17

Sugerman, B. E. K. and Crotts, A. P. S. 2002, ApJ, 581, L97

Sugerman, B. E. K. and Crotts, A. P. S. and Kunkel, W. E. and Heathcote, S. R. and Lawrence, S. S. 2005a, ApJ, 627, 888

——. 2005b, ApJS, 159, 60

Suntzeff, N. B. and Heathcote, S. and Weller, W. G. and Caldwell, N. and Huchra, J. P. 1988, Nature, 334, 135

Swope, H. H. 1940, Harvard College Observatory Bulletin, 913, 11

Tylenda, R. 2004, A&A, 414, 223

van den Bergh, S. 1965, PASP, 77, 269

——. 1966, PASP, 78, 74

Van Dyk, S. D. and Li, W. and Filippenko, A. V. 2006, PASP, 118, 351

Wang, X. and Li, W. and Filippenko, A. V. and Foley, R. J. and Smith, N. and Wang, L. 2008, ApJ, 677, 1060

Waxman, E. and Mészáros, P. and Campana, S. 2007, ApJ, 667, 351

Welch, D. L. 2007, ApJ, 669, 525

Whitelock, P. A. and Catchpole, R. M. and Menzies, J. W. and Feast, M. W. and Woosley, S. E. and Allen, D. and van Wyk, F. and Marang, F. and Laney, C. D. and Winkler, H. and Sekiguchi, K. and Balona, L. A. and Carter, B. S. and Spencer Jones, J. H. and Laing, J. D. and Evans, T. L. and Fairall, A. P. and Buckley, D. A. H. and Glass, I. S. and Penston, M. V. and da Costa, L. N. and Bell, S. A. and Hellier, C. and Shara, M. and Moffat, A. F. J. 1989, MNRAS, 240, 7P

Whitelock, P. A. and Catchpole, R. M. and Menziez, J. W. and Feast, M. W. and Winkler, H. and Marang, F. and Glass, I. S. and Balona, L. A. and Egan, J. and Carter, B. S. and Roberts, G. and Sekiguchi, K. and Laney, C. D. and Lloyd Evans, T. and Laing, J. D. and Spencer Jones, J. and Fernley, J. and James, P. and Fairall, A. P. and Monk, A. S. and van Wyk, F. 1988, MNRAS, 234, 5P

Woosley, S. E. and Pinto, P. A. and Martin, P. G. and Weaver, T. A. 1987, ApJ, 318, 664

Woosley, S. E. and Weaver, T. A. 1986, ARA&A, 24, 205

Xu, J. and Crotts, A. P. S. and Kunkel, W. E. 1995, ApJ, 451, 806

Zwicky, F. 1940, Reviews of Modern Physics, 12, 66

Chapter 5

Asymmetry in the Outburst of SN 1987A Detected Using Light Echo Spectroscopy

This chapter incorporates a reformatted article previously published in The Astrophysical Journal, originally appearing as:

"Sinnott, B., Welch, D. L., Rest, A., Sutherland P. G., and Bergmann, M. The Astrophysical Journal, **767**, 45 (2013)."

5.1 Introduction

A light echo (LE) occurs when outburst light from an event is scattered by circumstellar or interstellar dust into the line of sight of the observer. LE imaging has long been used as a powerful tool for studying the three-dimensional dust structure surrounding supernovae (SNe) (Crotts, 1988; Xu et al., 1995; Sugerman et al., 2005; Kim et al., 2008). In 1988, spectra of the inner and outer LE rings of SN 1987A confirmed the resemblance to a maximum-light spectrum (Gouiffes et al., 1988; Suntzeff et al., 1988b). More recently, however, this technique of targeted LE spectroscopy has been used on historical SNe to identify the spectral type of the original outburst. After the serendipitous discovery of LEs from ancient SNe in the Large Magellanic Cloud (LMC) during the SuperMACHO project by Rest et al. (2005b), follow-up spectroscopy by Rest et al. (2008a) identified the type of SN responsible for the remnant SNR 0509-675. The spectral types of the Cas A and Tycho SNe have also been identified using this method of targeted LE spectroscopy (Rest et al., 2008b; Krause et al., 2008a,b). Rest et al. (2011a) used LE spectroscopy to detect asymmetries in the outburst of the Cas A SN, while Rest et al. (2012a) recently obtained LE spectroscopy from the "Great Eruption" of η Carinae. We refer the reader to Rest et al. (2012b) for a review of LE spectroscopy emphasizing these more recent results. Given the acceleration of the field of LE spectroscopy in recent years, a detailed study of spectra of the well-known LE system of SN 1987A can provide a foundation for future studies, as well as provide new insight into the explosion of SN 1987A.

In the case of historical LEs, one has to use the photometric and spectroscopic history of a different SN to model the LE spectrum (see, e.g. Rest et al., 2011a, where the Cas A outburst is modeled with the lightcurve and spectra of SN 1993J and SN 2003bg). For SN 1987A, however, the exact spectral and photometric history of the LE source is known with high-precision, allowing observed LE spectra to be compared unambiguously to an isotropic scenario. In addition to acting as a test bed for LE spectroscopy theories, the near-circular LE rings of SN 1987A allow the original outburst to be probed for asymmetries in an entirely direct way. Different position angles (PAs) on the LE system probe different viewing angles from which we can view the time-integrated spectrum of the original event.

Observations as well as theoretical simulations indicate that core-collapse SNe are asymmetric in nature. Polarization measurements show deviations from spherical symmetry in all core-collapse SN with sufficient data (Wang & Wheeler, 2008), while recent simulations in two and three spatial dimensions show large deviations from symmetry (e.g., Hammer et al., 2010; Gawryszczak et al., 2010; Müller et al., 2012). Coupled with the fact that state of the art spherically symmetric core-collapse simulations in one spatial dimension fail at producing an explosion for $> 10\mathrm{M}_{\odot}$ projenitors (Burrows, 2012), multi-dimensional physics such as the standing accretion shock instability (SASI; Blondin et al., 2003) may play a key role in understanding the explosion mechanism. As a new method for observing asymmetries, LE spectroscopy of SNe may be able to provide new insight into the origin of SN asymmetries and their relation to the core-collapse explosion mechanism.

SN 1987A was a peculiar Type II SN with a blue supergiant progenitor located in the LMC (see, e.g., Arnett et al., 1989, and references therein for a review of SN 1987A and its progenitor). SN 1987A was known to be an asymmetric SN. Early polarization measurements (e.g., Jeffery, 1987; Bailey, 1988; Cropper et al., 1988) and an elongated initial speckle image (Papaliolios et al., 1989) suggested a non-spherical event. Fine structure in the Hα line (the "Bochum event") at 20-100 days after the explosion as well as redshifted emission lines at more than 150 days after explosion provide strong evidence for radial-mixing of heavy elements into the upper envelope (Hanuschik & Dachs, 1987; Phillips & Heathcote, 1989; Spyromilio et al., 1990). Updated models of the bolometric lightcurve at early epochs also require radial-mixing of ^{56}Ni (Shigeyama & Nomoto, 1990; Utrobin, 2004). Direct HST imaging by Wang et al. (2002) showed an elongated remnant ejecta, claimed to be bipolar and showing evidence for a jet-induced explosion. Recent integral field spectroscopy of the ejecta by Kjær et al. (2010) showed a prolate structure for the ejecta oriented in the plane of the equatorial ring, arguing against a jet-induced explosion.

Here we present detailed imaging and spectroscopy of the SN 1987A LE system. We infer the relative contributions of the different epochs of the SN to the observed LE spectrum by modeling images of the LE, as demonstrated by Rest et al. (2011b). We fit the observed LE spectra and use specific examples to illustrate the models ability to correctly interpret the observations. We then use the LE spectra to probe for asymmetries in the explosion of SN 1987A and compare to previous observations of asymmetry.

5.2 Observations and Reductions

5.2.1 Imaging

Imaging of the SN 1987A LE system was performed under the SuperMACHO Project microlensing survey (Rest et al., 2005a) using the CTIO 4m Blanco telescope. The survey monitored the central portion of the LMC for five seasons beginning in 2001 using the 8K × 8K MOSAIC imager (plus atmospheric dispersion corrector) with the custom "VR" filter ($\lambda_c = 625$ nm, $\delta\lambda = 220$ nm). Exposure times were between 150 and 200 s. We have continued to monitor the field containing SN 1987A and its LEs (field sm77) since the survey ended. Data reduction and difference images were performed using the ESSENCE/SuperMACHO pipeline *photpipe* (Rest et al., 2005a; Garg et al., 2007; Miknaitis et al., 2007). A stacked and mosaiced difference image of the LE system is shown in Figure 5.1. The near-circular rings illuminate three general dust structures: a smaller structure ~ 85 pc in front of SN 1987A, only visible in the south; a near-complete ring at ~ 185 pc and brightest in the north-east; as well as a larger and fainter near-circular illumination at ~ 400 pc in front of the SNR. All three of these structures have been mapped previously in detail by Xu et al. (1995) and can be referred to as three "sheets" of ISM dust roughly in the plane of the sky. However, it is important to note that the LE flux observed in Figure 5.1 is due to dense filamentary structure within the general "sheets" of ISM dust. The physical properties of the scattering dust filaments (inclination and thickness) can vary greatly within what appears to be a uniform "sheet" of dust. This distinction is important to make when modeling the LE photometry and spectroscopy.

5.2.2 Gemini Spectroscopy

We obtained multi-object optical spectroscopy (MOS) for five fields of the SN 1987A echo system in the 2006B term, using the R400 grating and GG455 blocking filter on the Gemini Multi-Object Spectrograph (GMOS) on Gemini-South. SuperMACHO or GMOS preimages were differenced with previous SuperMACHO images to establish the precise location of the echo system, allowing the design of GMOS masks. The locations of five MOS fields and the 14 1.0″wide LE slitlets are shown in Figure 5.1.

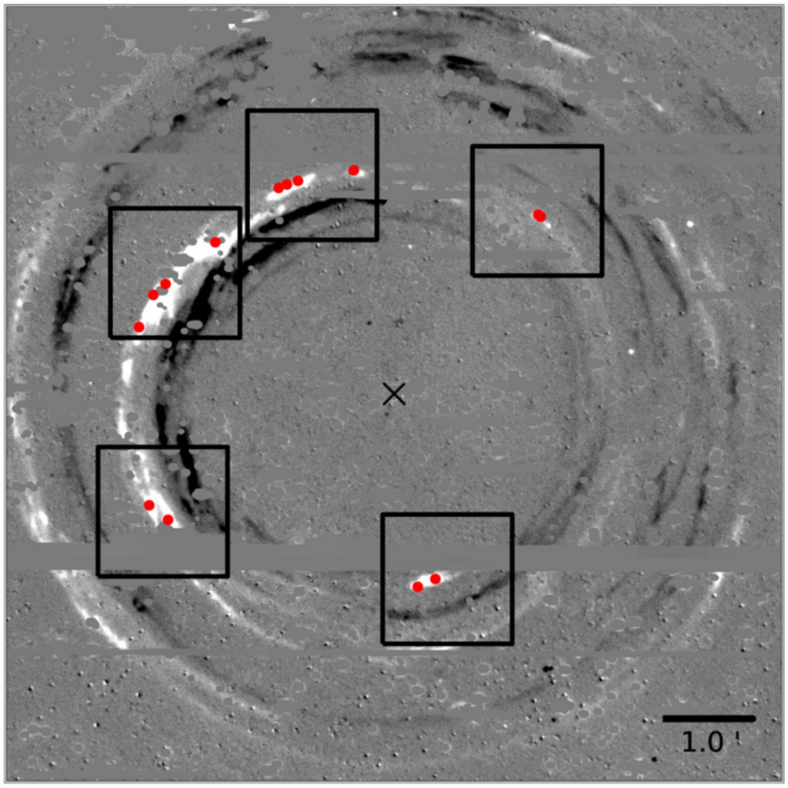

Figure 5.1: Mosaiced SuperMACHO difference image of August 2006 and January 2002 epochs of the SN 1987A LE system. The locations of the 14 GMOS slits appear in red, while the black cross indicates the location of SNR. Slitlets are not to scale. The black squares collect LEs which were observed in the same MOS field. North is up and east is to the left.

The nod and shuffle mode of GMOS was used to best isolate the diffuse LE signal from the nebular sky background. To ensure clear sky in the offset position, the telescope was nodded off-source several degrees every 225 s. On-source integration times for the brightest echo fields were 30 minutes, and 90 minutes for the fainter, more diffuse echoes. During each night of observations, flat field and CuAr spectral calibration images were taken before or after the science images. We also acquired dark images with the same nod and shuffle parameters used during integration. These specialized dark images allow features associated with charge-traps in the GMOS CCDs to be masked out during reduction.

The observations result in LE spectra from SN 1987A with a spectral range of 4500-8500 Å, contaminated by strong emission lines from the nebular region, as well as any stellar continuum entering the slitlets. The P Cygni Hα line seen in the spectra is further degraded due to six strong nebular emission lines ([NII] λ6548, Hα λ6563, [NII] λ6585, HeI λ6678, [SiII] λ6717, [SiII] λ6731). Signal from the emission peak of the P Cygni Hα line is therefore lost to nebular emission, and this region of the profile cannot be interpreted with confidence. In particular, the location and flux of the emission peak cannot be determined without interpolations which we found introduced large uncertainties.

The nebular contamination can be greatly reduced since the LE system is expanding superluminally on the sky (as seen in Figure 5.1). We therefore have the unique opportunity in astronomy to observe only the background sky signal at the *same location on the sky* as the initial sky+object observation. Sky-only observations were taken in the 2009A and 2009B semesters for the five MOS fields. The spectroscopy was carried out using the same GMOS configuration as the previous sky+object 2006B observations, with 30 minutes on-source integration times in nod and shuffle mode. The spectrophotometric standard star LTT 3864 was observed during the 2009A observations.

5.2.3 Spectra Reduction

All spectra were reduced using IRAF[1] and the Gemini IRAF package, with bias subtraction and trimming done on each CCD individually. Science images were dark subtracted using the special nod and shuffle darks, with each CCD being cleaned of cosmic rays using the Laplacian rejection algorithm LACOSMIC (van Dokkum, 2001). Nod and shuffle sky subtraction was performed on each science exposure using the *gnsskysub* task. Individual slitlets were automatically cut from the wavelength calibrations frames, however this procedure required manual tweaking to achieve the best cutting possible. A wavelength solution was found for each slitlet in the calibration frame. Science frames were flattened, CCDs mosaiced together, and slitlets cut from the images. The wavelength solution for each slitlet was then applied to the corresponding science spectrum in two dimensions. Since the LE signal is so weak, determining an extraction aperture is very difficult. Instead, we collapsed the entirety of each slitlet to one dimension using a block average.

No suitable spectrophotometric standard star was observed during the 2006B observing semester, nor did a suitable standard star matching our unique instrument configuration exist in the data archive nearby temporally. However, the spectrophotometric standard LTT 3864 was observed during the 2009A observations. We therefore used the 2009A standard to perform the flux calibration for all of the 2006 and 2009 spectra. While this leads to large errors in absolute flux calibration, our analysis is independent of absolute flux levels. Instead, the purpose of the flux calibration used here is to remove the effect of CCD sensitivity from the spectra, which is relatively stable in time. A LE spectrum is a weighted average of many epochs from the outburst. Determining the continuum of such a spectrum is therefore difficult, and the alternative analysis procedure of removing the continuum from all of our spectra would have had a larger error than that of the flux calibration.

---

[1] IRAF is distributed by the National Optical Astronomy Observatory, which is operated by the Association of Universities for Research in Astronomy, Inc., under cooperative agreement with the National Science Foundation.

The sky-only spectra from 2009 were subtracted in one dimension from the 2006 LE spectra for each MOS slit. This procedure was performed interactively, adjusting the scale and wavelength of the sky spectrum in small increments using the IRAF task *skytweak* to minimize sky subtraction residuals in the final spectra. Since we focus our science analysis on the Hα line, we performed the sky subtraction such that the subtraction residuals in the P Cygni profile of Hα were minimized. All spectra were Doppler-corrected, adopting a LMC radial velocity of 286.5 km s^{-1}(Meaburn et al., 1995).

5.3 Analysis

5.3.1 Light Echo Spectra

The upper panel of Figure 5.2 shows a reduced LE spectrum from the 2006 observations along with the underlying sky-only nebular spectrum from 2009. The high-velocity P Cygni profiles including Hα resemble a Type II SN spectrum at maximum light, confirming the LE spectra probe the original outburst light of SN 1987A. Strong, narrow nebular lines not associated with the SN outburst dominate the spectrum around 5000Å and the Hα line at 6563Å. The result of performing difference spectroscopy is shown in the lower panel of Figure 5.2, where the sky-only signal has been subtracted from the 2006 echo spectrum. Flux from the emission component of the Hα line is recovered that was initially lost to nebular contamination. In the majority of our spectra we are able to resolve the Hα emission peak without loss due to the nebular lines.

5.3.2 Modeled Isotropic Spectrum

To search for asymmetries in SN 1987A using spectroscopy of its LEs, we need to first consider what defines asymmetry in observed spectra. As shown in Rest et al. (2011b),

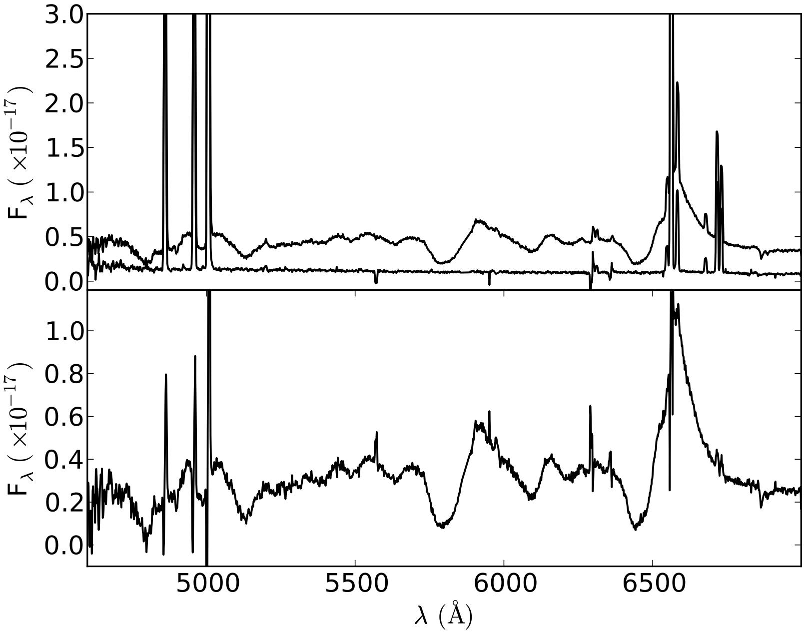

Figure 5.2: Upper Panel: Example LE+sky spectrum from 2006 shown with the corresponding sky-only nebular spectrum from 2009. Lower Panel: The result of difference spectroscopy, showing the LE-only spectrum along with remaining nebular residuals from the subtraction. The strength of the Hα emission peak can now be estimated in the difference spectrum.

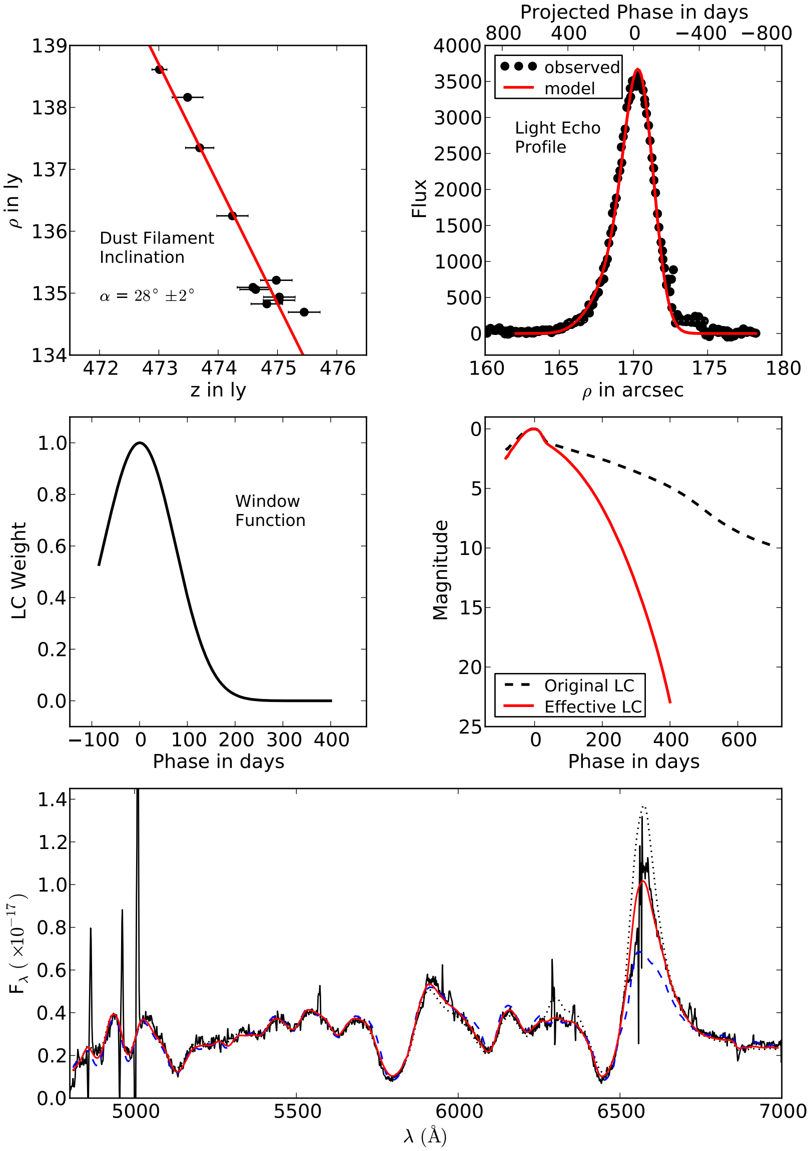

Figure 5.3: Summary of modeling procedure for each LE spectrum. The inclination of the dust filament is measured (upper left panel), allowing the shape of the LE profile to be modeled to determine the dust width (upper right panel). The properties of the slit determine the window function containing the relative contribution from each epoch (middle left panel), which when multiplied by the original lightcurve gives the effective lightcurve for this observation (middle right panel). We integrate the historical spectra of SN 1987A, flux-weighted with the effective lightcurve, and take into account wavelength-dependent scattering and reddening to obtain a fit between the LE model and the observed spectrum (lower panel). The lower panel plot shows the model LE fit (solid red) along with the attempted fit with the maximum light spectrum of SN 1987A (dashed blue) and the full lightcurve-integrated spectrum (dotted black).

multiple LE spectra from the same transient source, with differing line strength ratios, does not necessarily imply an asymmetry in the outburst light. An observed LE spectrum will depend strongly on the physical properties of the scattering dust as well as the instrument configuration and seeing conditions at time of observation. Specifically, the dominant epochs of the original outburst probed by a LE spectrum can change with the above properties. Relative comparisons of LE spectra can therefore easily lead to false-detections of asymmetry if the above factors are not taken into consideration. Each LE spectrum should instead be compared to a single isotropic spectrum modeled for each observation. We define our isotropic model spectrum as the original outburst of SN 1987A, as it would have been spectroscopically observed if scattered by dust corresponding to the observed LE. This provides a direct probe of asymmetry since differences between observed and model spectra represent deviations from the historically observed outburst of SN 1987A.

A LE observed on the sky has a flux profile (flux versus ρ, where ρ is the distance on the sky from the SNR, see upper right panel of Figure 5.3) that is the projected lightcurve of the source event stretched or compressed depending on the inclination of the scattering dust. The width of the scattering dust and the point spread function (PSF) further distort the observed LE. The dust inclination is measured through imaging the LE at multiple epochs and can be measured prior to spectroscopy. The PSF is also known, allowing the width of the scattering dust filament to be determined through fitting the LE flux profile.

The inclination, α, is obtained by monitoring the apparent motion of the LE on the sky. Positive values of α correspond to scattering dust sheets tilted out of the plane of the sky, from the positive ρ axis toward the negative z axis, where z is the distance in front of the remnant. Using the SuperMACHO database of difference images around SN 1987A, we are able to monitor the apparent motion of the echo system over seven years from 2002 to 2008. For each difference image and each slit location in Figure 5.1, we measure the one dimensional profile of the difference flux as a function of distance away from the SNR, ρ. Carefully monitoring the superluminal apparent motion in this way allows us to determine the inclination of the scattering dust for each slit location, as described in Rest et al. (2011b) (see, e.g., upper left panel of Figure 5.3). We find the apparent motion (and therefore inclination) is typically stable over a one year period. We find typical uncertainties in the inclination are less than 5° for our 14 dust locations. Rest et al. (2011b) showed that, for the case of SN 1987A, changes in inclination on the order of 10° do not alter the final modeled spectrum in a significant way. With the inclination known, the photometric history of SN 1987A (Hamuy et al., 1988; Suntzeff et al., 1988a; Hamuy & Suntzeff, 1990) can be used to model the one dimensional flux profile and determine the best-fitting scattering dust width. The upper right panel of Figure 5.3 shows an example fit to the LE profile.

The above procedure determines the properties of the scattering dust for each LE location. We also take into account the location, orientation, and size of the spectroscopic slit to compute a window function that is unique to each LE observation (see, e.g., middle left panel of Figure 5.3). This window function is the relative contribution from each epoch of the lightcurve when observed through the slit. The slit offset, $\Delta\rho$, measures the offset between the peak of the LE profile and the location of the slit on the sky. This is an important parameter, as it shifts the window function in time, systematically probing later or early epochs in the spectrum if the slit is positioned closer or further away from the SNR, respectively.

Multiplying the window function with the original lightcurve of SN 1987A, we determine an *effective lightcurve* corresponding to each observed LE spectrum (see, e.g., middle right panel of Figure 5.3). The isotropic model spectrum is then the integration of the historical spectra of SN 1987A weighted with the effective lightcurve. We refer the reader to Rest et al. (2011b) where our model is described in detail with SN 1987A examples. To integrate the historical spectra of SN 1987A, we use the integration method described in Rest et al. (2008a), with the spectral database from

SAAO and CTIO observations (Menzies et al., 1987; Catchpole et al., 1987, 1988; Whitelock et al., 1988; Catchpole et al., 1989; Whitelock et al., 1989; Caldwell et al., 1993; Phillips et al., 1988, 1990).

The wavelength-dependent effect of scattering by dust grains is taken into account when fitting the isotropic model to our observed LE spectra. We calculate the integrated scattering function for each LE (i.e. scattering angle) using the method described in Rest et al. (2012b), using the *"LMC avg"* carbonaceous-silicate grain model of Weingartner & Draine (2001). We then fit the model spectrum to the observed LE spectrum (see, e.g., lower panel of Figure 5.3) varying three parameters: the reddening (E(B-V) assuming $R_v = 3.2$), a normalization constant, and a small flux offset (to account for small errors in sky subtraction).

Figure 5.3 summarizes the modeling procedure outlined above and in Rest et al. (2011b) that occurs for each LE spectrum. The lower panel shows the final isotropic model spectrum in red, which fits the features in the observed LE spectrum very well. To highlight the importance of the modeling procedure, we also attempt to fit the LE spectrum with a spectrum of SN 1987A near maximum light (dashed blue line), and an integrated spectrum obtained by flux-weighting with the original lightcurve of SN 1987A (dotted black line). The maximum light spectrum cannot reproduce the strength of the observed Hα emission. Conversely, the full lightcurve-integrated spectrum has an excess in Hα emission and a lower Hα velocity in the absorption minimum. Only by integrating using the modeled window function (solid red line) are we able to obtain a good fit to the Hα profile. Below we highlight the importance of the LE modeling by considering two scenarios.

5.3.2.1 Dust-Dominated Scenario

Both the physical properties of the scattering dust as well as the configuration of the observation affect the observed LE spectrum. Here we highlight the effect of the scattering dust. Table 5.1 shows the observed inclinations and best-fitting dust widths for the 14 LE locations shown in Figure 5.1. Figure 5.4 shows two examples of observed flux profiles, corresponding to the two LEs in Figure 5.1 at PA $\sim 115°$, LE113 and LE117. Note the numbers in the names of the LEs correspond to the PA of the LE with respect to the SNR. Both LEs are at essentially the same PA along the echo system, so probe the same viewing angle onto the SN. However, as shown in Figure 5.1 the two slits are placed on physically distinct dust filaments. The bright filament in LE113 is 53 ly closer to the observer along the line of sight than the bright LE117 filament, while both are 3 ly thick. The observed widths and shapes of the LE profiles in Figure 5.4 are also different, with LE113 having a larger width on the sky and a more symmetric shape. This is explained entirely by the $\sim 50°$ difference in the inclinations of the two dust filaments. The highly inclined dust filament for LE113 is within $\sim 15°$ of the tangential to the scattering ellipsoid and compresses the lightcurve on the sky, causing the LE113 profile to resemble a point-like source with a broad, symmetric profile. The lower inclination of the LE117 dust filament preserves the shape of the lightcurve with a broad increase in flux at small ρ values (the long decay of the SN lightcurve) and a sharp decrease in flux at large ρ values (the short rise of the SN lightcurve). It should be noted that the LE113 profile in the left panel of Figure 5.4 shows dust substructure to the left of the main LE peak. The additional contribution from the secondary peak is weak pre-maximum flux and we found the effect on the Hα emission strength in the integrated spectra to be $< 4\%$. However, we do take substructure in the dust into account in the extreme case of LE186 as shown in Section 5.3.3.1 below. The effect of dust substructure is considered more formally in the Appendix.

The modeled isotropic spectra are shown in Figure 5.5, with the upper left panel showing the observed LE spectrum for the LE117 slit (black), the corresponding LE117 model (thin red), and the non-matching LE113 model (thick cyan) derived using the larger inclination. Since the dust inclination of LE113 compresses the lightcurve on the sky, a much larger range of epochs span the width of the slit resulting in a wide window function compared to the LE117 slit (Table 5.1 lists the approximate range of epochs probed by each LE). The LE113 model therefore has an excess of Hα emission from the inclusion of late-time nebular epochs. The LE117 model is able to correctly match the observed LE117 Hα strength. The lower panel of Figure 5.5 shows the same LE113 model with the corresponding LE113 observed LE spectrum, showing good agreement. The fact that two distinct LEs with differing line strengths and differing dust properties show the same result – that the observed LE spectra from this viewing angle can be modeled with an isotropic historical spectrum – shows the interpretation of LE spectroscopy described here and in detail in Rest et al. (2011b) is correct.

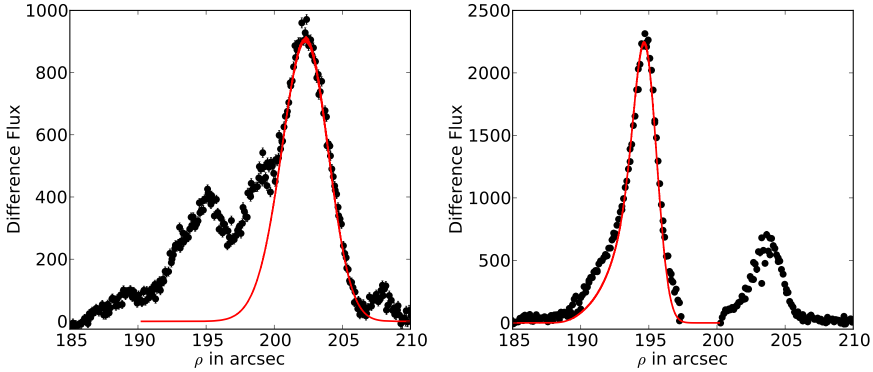

Figure 5.4: Observed LE profiles and corresponding best-fit models (red line) for LE113 (left) and LE117 (right). The larger width and symmetric shape of the LE113 profile on the sky is due to the dust filament being inclined ∼ 50° closer to the tangential to the line-of-sight than the LE117 dust filament, compressing the entire lightcurve on the sky and resulting in a more symmetric point-like LE profile.

5.3.2.2 Observation-Dominated Scenario

Here we consider a scenario where the properties of the observation (specifically the slit location) are the dominant factors in two very different observed LE spectra that have similar viewing angles onto the photosphere. Figure 5.6 shows the LE profiles of LE053 and LE066, corresponding to the slits at PA∼ 60° in Figure 5.1. The gray shaded region indicates the location of the slit for both profiles. The slit of LE066

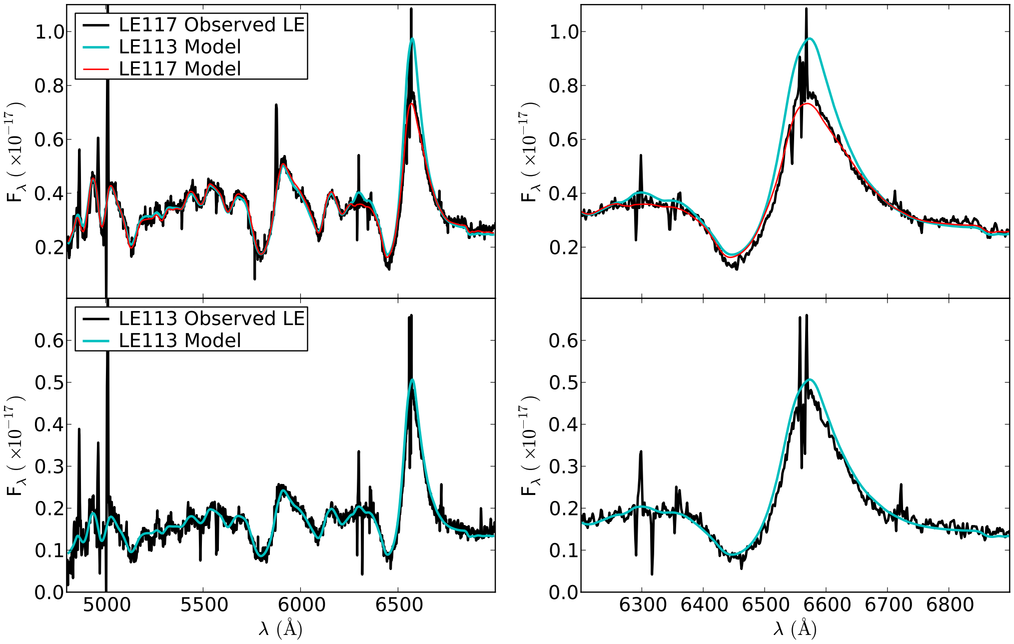

Figure 5.5: The upper left panel shows the observed LE spectrum of LE117 with its corresponding isotropic model, along with the incorrect model of the nearby dust filament LE113. Only the matching LE117 model can fit the observed LE spectrum, while the lower left panel shows the LE113 observed LE spectrum can be fit with its corresponding model. The right panels show enlargements of the Hα profile in both cases.

Table 5.1. Summary of SN 1987A light echo observations and scattering dust properties.

LE ID[a]	PA[b] (°)	z_0[c] (ly)	θ[d] (°)	α[e] (°)	σ_d[f] (ly)	$\Delta\rho_{\mathrm{offset}}$[g] ($''$)	Epochs[h] (days)
LE016	15.8	428.91	17.1	22 ± 6	4.49 ± 0.03	-0.35	0-180
LE029	29.2	473.13	16.3	28 ± 2	4.49 ± 0.03	-0.19	5-200
LE032	31.8	483.02	16.2	-46 ± 2	2.71 ± 0.05	-0.27	30-180
LE034	33.9	486.53	16.1	-16 ± 2	3.37 ± 0.15	+0.26	0-140
LE053	53.0	505.05	15.8	38 ± 7	5.26 ± 0.03	-0.18	0-215
LE066	66.3	590.39	14.7	11 ± 2	4.50 ± 0.55	+1.05	0-80
LE069	69.3	624.64	14.3	66.8 ± 0.2	1.80 ± 0.07	+0.57	0-110
LE076	76.4	648.50	14.0	11 ± 4	0.60 ± 0.22	-0.08	40-135
LE113	112.5	671.04	13.8	79 ± 1	3.06 ± 0.09	-0.39	0-330
LE117	116.8	618.40	14.3	33 ± 5	3.10 ± 0.39	-0.14	35-155
LE180	180.2	289.69	20.7	-49 ± 2	4.53 ± 0.06	+0.73	0-290
LE186	185.6	270.34	21.3	70 ± 3	3.52 ± 0.18	-1.00	0-420
LE325	325.3	369.67	18.4	-6 ± 11	1.13 ± 0.16	+0.18	20-120
LE326	326.1	370.33	18.4	15 ± 3	2.24 ± 0.51	+0.21	0-130

[a] Naming convention corresponds to position angle of LE slit with respect to SNR.

[b] Position angle of the scattering dust with respect to the SNR.

[c] Distance along line of sight from SNR to scattering dust.

[d] Scattering angle.

[e] Inclination of scattering dust with respect to the plane of the sky. α increases from the positive ρ axis towards the negative z axis.

[f] Average best-fitting width of scattering dust sheet over the length of the spectroscopic slit.

[g] Offset between center of slit and peak LE flux, where positive values indicate slit further from SNR than peak echo flux.

[h] Approximate range of epochs probed by the LE. Corresponds to epochs in window function in which the relative contribution contribution is $>$ 50% (prior to flux-weighting) in the LE integration.

was placed $\sim 1''$ farther away from the SNR than the peak of the LE. This was unintentional since the location of the LE peak may not be very well known when making the MOS masks. The offset results in very different observed LE spectra for the two profiles, as shown in Figure 5.7. When compared to the observed LE spectra of Figure 5.5 and LE053 in Figure 5.7, the spectrum of LE066 looks more like an early-time spectrum with a lower Hα emission-to-absorption ratio and a higher temperature continuum. Since the slit is centered on the pre-maximum light portion of the LE profile, LE066 does not probe epochs > 100 days after maximum light, while LE053 probes epochs out to ~ 300 days after maximum light. As in the previous example, both model isotropic spectra are good fits to their observed LE spectra. However, the model of LE053 has a lower Hα absorption velocity and a larger Hα emission-to-absorption ratio, making it a poor fit to the LE066 observed LE spectrum.

The above dust- and observation-dominated examples highlight the danger in comparing LE spectra without sufficient modeling. Without the corresponding models for the LE053 and LE066 observed spectra, one might make a false-detection of asymmetry: the LE066 spectrum has a larger Hα velocity and excess in emission compared to the LE053 spectrum. If the two LEs occurred at opposite PAs this asymmetry claim would be even more tempting to make.

5.3.3 Evidence for Asymmetry in SN 1987A

Each PA on the LE system of SN 1987A represents a distinct viewing angle with which to view the original outburst. LEs originating to the north of SN 1987A probe outburst light originating mainly from the northern portion of the photosphere. Therefore, by observing the LEs as a function of increasing PA, we are able to view the outburst of SN 1987A as a function of north to south lines of sight. The scattering angles probed by the LE ring are listed in Table 5.1 and lead to typical opening angles of $\sim 35^\circ - 40^\circ$.

Observed LE spectra and corresponding dust-modeled isotropic spectra are plotted

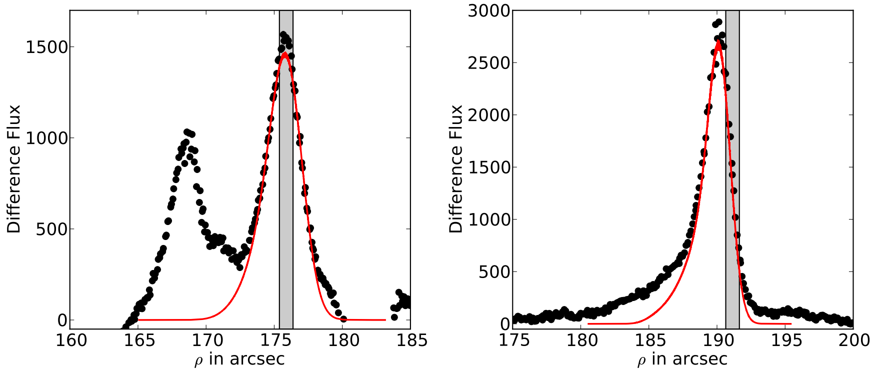

Figure 5.6: Observed LE profiles and corresponding best-fit models (red line) for LE053 (left) and LE066 (right). The grey shaded regions indicate the location of the spectroscopic slit. The slit offset from the LE peak in the LE066 LE produces an observed spectrum that is heavily weighted towards the earlier epochs of the outburst.

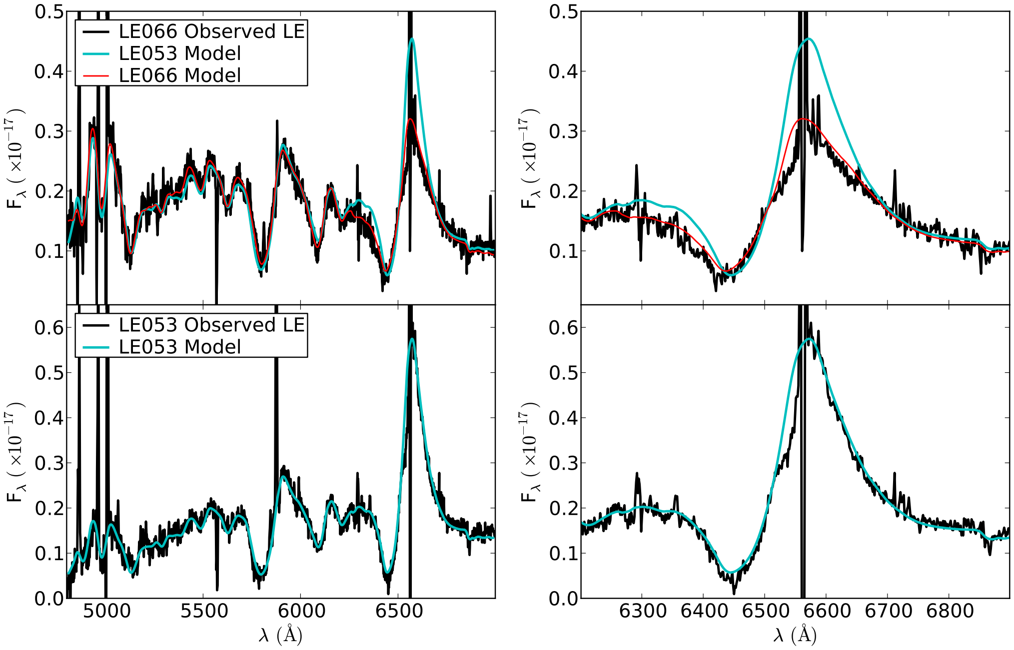

Figure 5.7: The upper left panel shows the observed LE spectrum of LE066 with its corresponding isotropic model, along with the incorrect model of the nearby dust filament LE053. Only the higher velocity LE066 early-epoch model is a good fit for the observed LE spectrum. The lower left panel shows the LE053 observed LE spectrum which probes later epochs of the explosion. The lower velocity and larger Hα emission-to-absorption ratio of the LE053 model is a good fit to the observed spectrum. The right panels show enlargements of the Hα profile in both cases.

as a function of PA in Figures 5.8-5.12, with each figure representing a field as shown in Figure 5.1. Figure 5.8 corresponds to the most northern field. As previously mentioned, we should avoid searching for differences between observed LE spectra. Instead, deviations in asymmetry are defined by deviations from the dust-modeled isotropic spectrum (red line) for each line of sight. A deviation from the model then describes a deviation from the appropriate weighted set of outburst spectra of SN 1987A as it was historically observed along the direct line of sight.

5.3.3.1 Hα Profiles

Figures 5.8-5.12 show that most features and line strengths observed in the optical LE spectra can be fit with the isotropic historical spectrum of SN 1987A, without the need to invoke asymmetry in the outburst. However, the fine-structure and strength of the Hα λ6563 line show deviations from symmetry as a function of PA (i.e. viewing angle onto the SN).

Figure 5.13 shows a closeup of the Hα profiles of seven unique viewing angles as a function of increasing PA from top to bottom (the geometry of the viewing angles is shown in Figure 5.14). The most northern line of sight LE, LE016, shows a strong blue knee in the profile at ~ -2000 km s^{-1}in addition to a strong excess of emission that is redshifted from the rest wavelength by $\sim +800$ km s^{-1}(and by $\sim +500$ km s^{-1}compared to the historical spectrum). The most southern LE, LE186, has a PA almost directly opposite that of LE016. Its Hα profile (second from bottom in Figure 5.13) shows a red knee in the fine-structure at $\sim +2200$ km s^{-1}and an excess in emission shifted towards the blue by ~ -500 km s^{-1}(and by ~ -1000 km s^{-1}compared to the historical spectrum). The qualitative difference in the Hα profile shape between the two extreme viewing angles, LE016 and LE186, is shown in Figure 5.15. This figure does not take into account the effects of the LE observations on the integrated spectra and so cannot be used as a direct comparison between the viewing angles. However, it does qualitatively describe the asymmetry in the fine-structure between

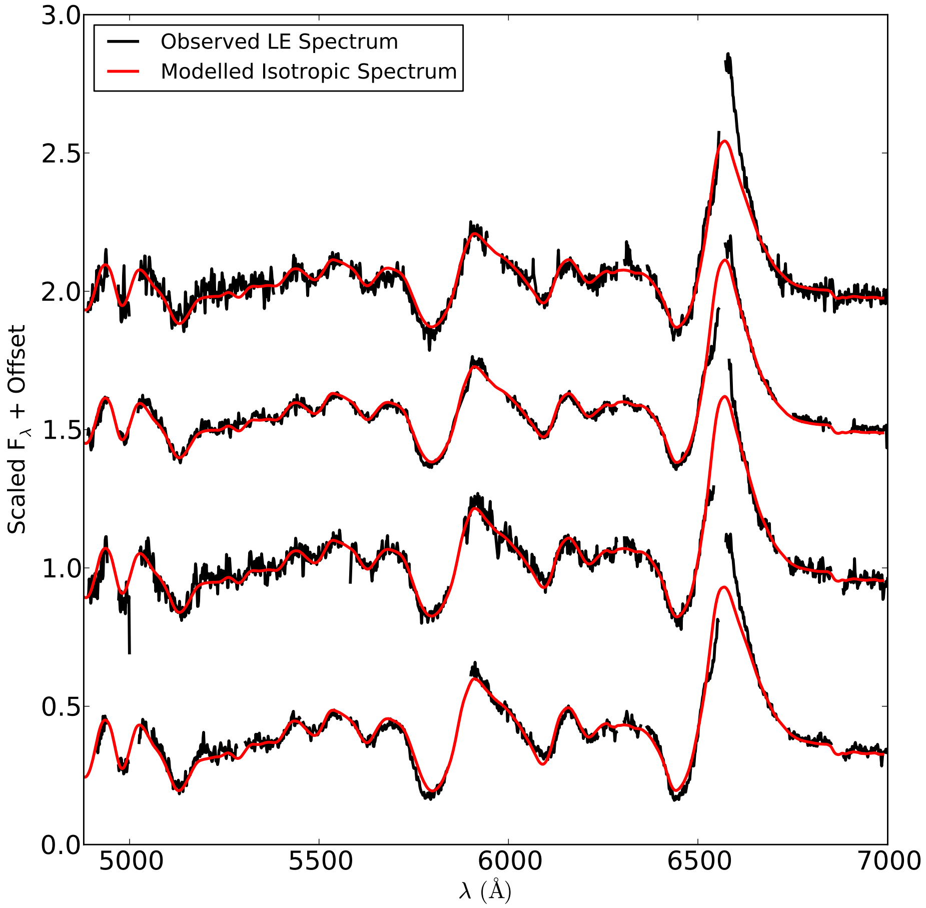

Figure 5.8: Observed LE spectra with corresponding modeled isotropic spectra for field at PA $\sim 30°$ in Figure 5.1. Spectra are plotted from top to bottom as a function of increasing position angle as shown in Figure 5.1: LE016, LE029, LE032, LE034. Gaps in the observed spectra correspond to areas contaminated by sky-subtraction residuals.

the two viewing angles.

The two asymmetries in the Hα profile (summarized in Figure 5.15) are the fine-structure, with a blue knee in the northern profiles and a red knee in the southern profile, as well as an excess of Hα emission that is redshifted in the north and blueshifted in the south. Both of these asymmetries appear to be physical for a number of reasons. The excess in Hα emission as well as the blue knee feature smoothly diminish

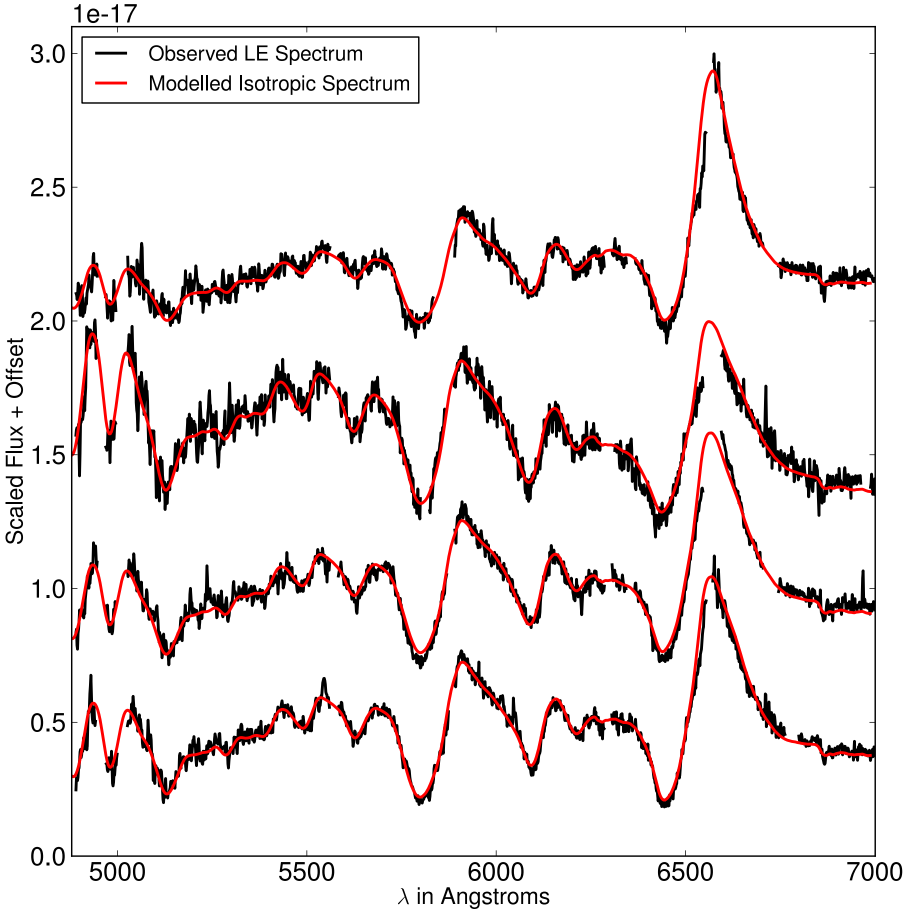

Figure 5.9: Observed LE spectra with corresponding modeled isotropic spectra for field at PA ∼ 65° in Figure 5.1. Spectra are plotted from top to bottom as a function of increasing position angle as shown in Figure 5.1: LE053, LE066, LE069, LE076. Gaps in the observed spectra correspond to areas contaminated by sky-subtraction residuals.

in Figure 5.13 as PA is increased. At PA ∼ 110° in the south-east quadrant, both the Hα strength and fine-structure from LEs LE113 and LE117 can be fit with the historical model spectrum of SN 1987A. The fact that both Hα asymmetries (fine-structure and redshifted emission) smoothly diminish as a function of viewing angle from north to south in the eastern half of the LE ring is strong evidence that these asymmetries are physical.

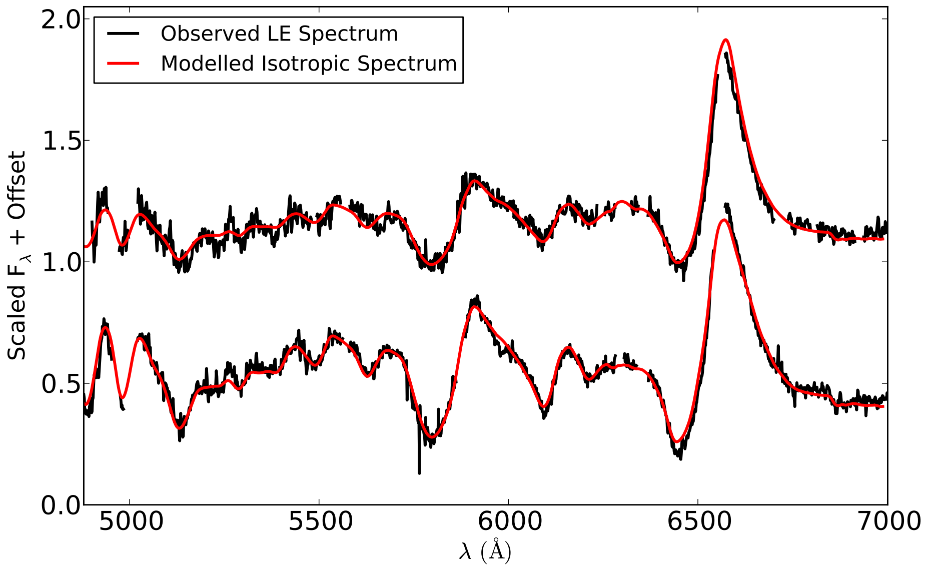

Figure 5.10: Observed LE spectra with corresponding modeled isotropic spectra for field at PA ∼ 115° in Figure 5.1. Spectra are plotted from top to bottom as a function of increasing position angle as shown in Figure 5.1: LE113, LE117. Gaps in the observed spectra correspond to areas contaminated by sky-subtraction residuals.

This fine-structure in the Hα profile is similar to the "Bochum event" (named after the 61 cm Bochum telescope at La Silla, Chile) originally observed in SN 1987A (Hanuschik & Dachs, 1987; Phillips & Heathcote, 1989), where blue and red satellite emission features were observed 20-100 days after explosion. Figure 5.16 shows the Hα profile of a CTIO spectrum taken 34 days after explosion (Phillips et al., 1988). The blue and red emission satellites are similar to the blue and red knees observed in the LE016 and LE186 LE spectra, respectively. It is tempting to compare the Hα fine-structure observed in Figure 5.16 directly with the fine-structure observed in the LE profiles. *However, LE spectra represent an integration of many epochs of signal and cannot be compared directly to a single epoch spectrum.* Although the "Bochum event" is prominent in Figure 5.16, there is no evidence for fine-structure in any of the isotropic model spectra in Figure 5.13. That is, the "Bochum event" does not survive the smoothing effect when the historical spectra of SN 1987A are integrated.

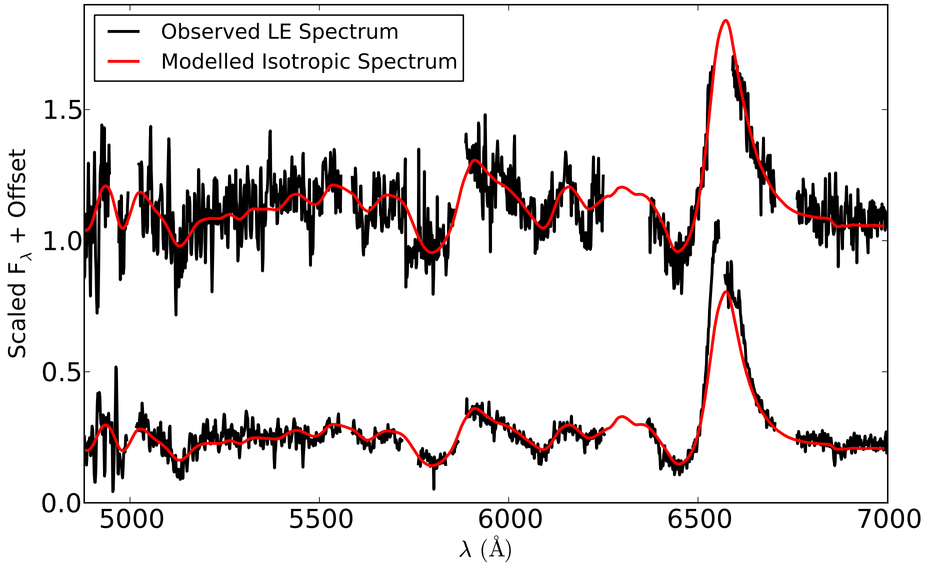

Figure 5.11: Observed LE spectra with corresponding modeled isotropic spectra for field at PA ∼ 185° in Figure 5.1. Spectra are plotted from top to bottom as a function of increasing position angle as shown in Figure 5.1: LE180, LE186. Gaps in the observed spectra correspond to areas contaminated by sky-subtraction residuals. LE180 (upper spectrum) represents an example where our LE fitting algorithms fail to extract meaningful results due to the complexity and low signal-to-noise of both the spectrum and the LE flux profile.

This can be seen in the lower panel of Figure 5.3, where the fine-structure from the "Bochum event" is faintly visible in the maximum light spectrum, but entirely nonexistent in the integrated model spectra. The fact that fine-structure similar to the "Bochum event" is present in the observed LE spectra is evidence for underlying fine-structure that is much stronger than that originally observed for SN 1987A. In general, small deviations from symmetry observed in a LE spectrum must represent very large deviations from symmetry in the underlying outburst in order to remain after the integrating effect of the LE phenomenon. This is an important aspect of all LE spectroscopy work that is rarely emphasized.

The excess emission in the north and south from profiles LE016 and LE186, respectively, cannot be explained within uncertainties. To obtain the largest temporal

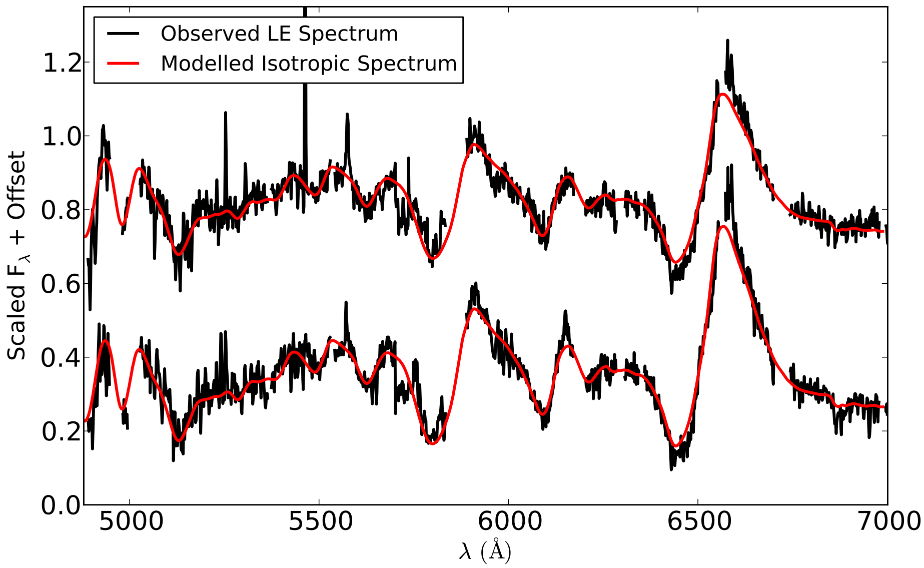

Figure 5.12: Observed LE spectra with corresponding modeled isotropic spectra for field at PA ~ 325° in Figure 5.1. Spectra are plotted from top to bottom as a function of increasing position angle as shown in Figure 5.1: LE325, LE326. Gaps in the observed spectra correspond to areas contaminated by sky-subtraction residuals.

coverage we used both CTIO and SAAO spectra when integrating the model spectrum. There exists known systematic differences between the datasets of the original observations from the two locations (Hamuy et al., 1990). Using the two data sets individually in our analysis pipeline can lead to differences in the Hα strength by $5\% - 10\%$ in our models, but cannot account for the $30\% - 40\%$ excess observed in the LE016 and LE186 spectra. We also stress that our analysis is based on relative flux comparisons only.

The LE profile on the sky for LE016 is very similar to that shown in Figure 5.3. Since it is a single peak, the theoretical maximum amount of Hα emission in the model would correspond to integrating the historical spectra with the full lightcurve of SN 1987A out to $t = t_{now}$, rather than an effective lightcurve that is truncated by a window function (i.e. having an infinitely thick dust sheet). However, even this unphysical limit cannot reproduce the Hα emission-to-absorption ratio that is seen in

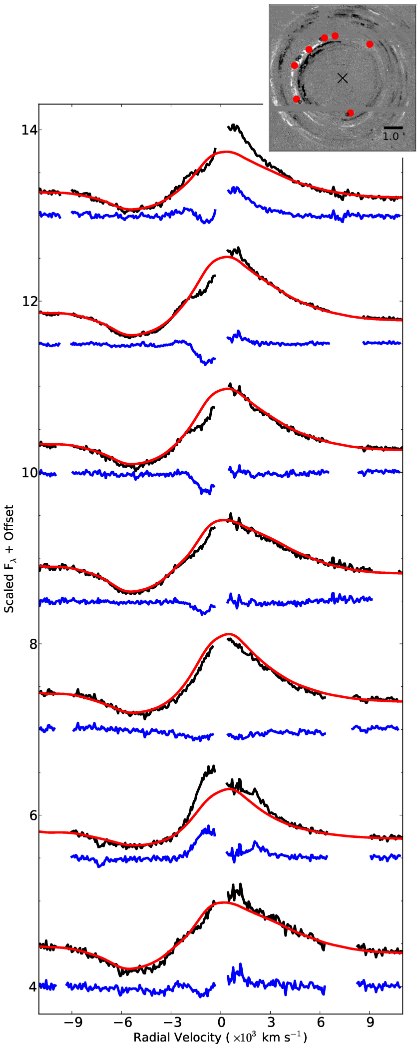

Figure 5.13: Closeup of observed Hα profiles (black) and corresponding dust-modeled isotropic spectra (red), as a function of PA for seven viewing angles. The top Hα profile corresponds to the most northern slit in the upper right legend, and the profiles increase in PA from top to bottom: LE016, LE029, LE053, LE076, LE113, LE186, LE326. LE naming convention corresponds to PA of LE with respect to SNR. Residuals between the observed LE spectra and the dust-modeled isotropic spectra are plotted in blue below each profile. To prevent guiding the eye, the portions of the Hα profile containing residuals from sky subtraction have been masked out. The most northern profile, LE016, has an excess in redshifted Hα emission and a blue knee at ~ -2000 km s^{-1}are observed. At almost opposite PA (LE0186, second from bottom), the opposite asymmetry is observed in the Hα profile: an excess in blueshifted emission and a red knee at $\sim +2200$ km s^{-1}. Both asymmetry features diminish as a function of viewing angle away from the north. Portions of the observed Hα peak contaminated by sky-subtraction residuals have been removed to prevent guiding the eye. No smoothing has been applied to any of the spectra.

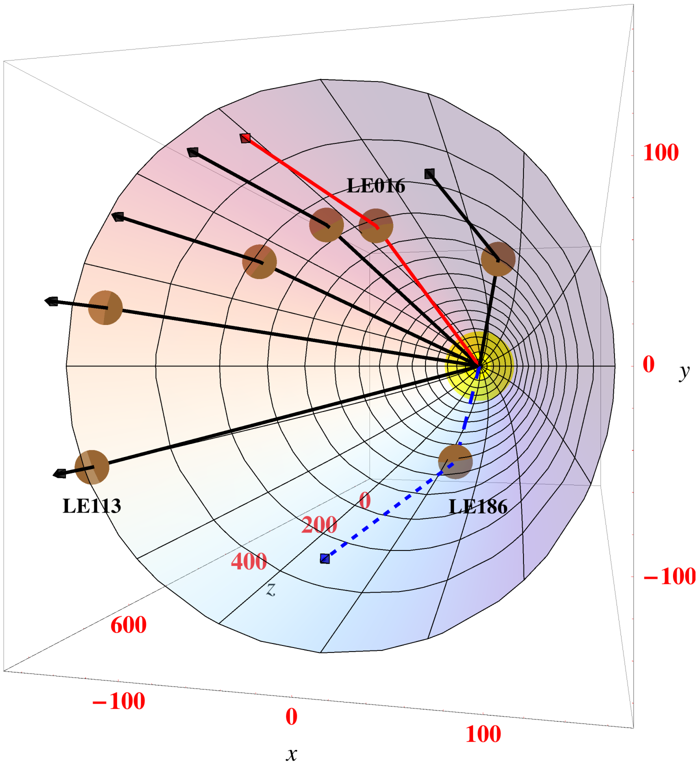

Figure 5.14: 3D locations of the scattering dust for the seven LEs from Figure 5.13. Highlighted in solid red and dashed blue are the extreme viewing angles corresponding to LE016 and LE186. North is towards the positive y axis, east is towards the negative x axis, and z is the distance in front of the SN. All units are in light years.

the observed LE profile of LE016. The LE profile on the sky and the slit location for LE186, which has two closely spaced filaments, are shown in Figure 5.17. Since the slit was placed on the first peak, there will be late-time nebular emission entering the slit from the second peak at larger ρ. In such a case, it is possible to obtain a larger emission-to-absorption ratio. However, we have taken this into account by modeling both LE peaks and determining the relative contributions from each peak entering the slits. This effect, discussed in more detail in the Appendix, cannot account for the excess in emission in LE186. We also stress that the apparent lack of any Hα emission excess in LE180 is due to limitations in our LE fitting algorithrims when dealing with such low signal-to-noise data. LE180 is discussed in more detail in the Appendix. It should be noted, however, that LE180 appears to show the same fine-structure in

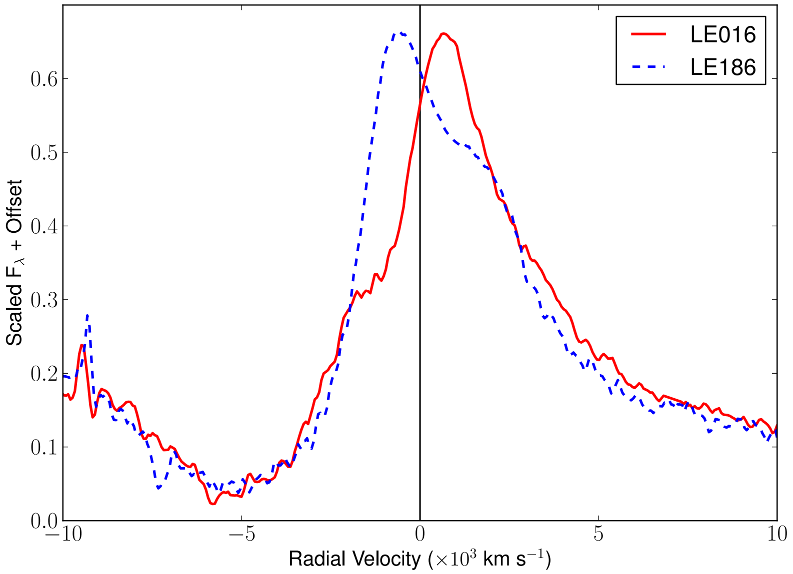

Figure 5.15: Observed Hα lines from LE016 and LE186. Emission peaks have been interpolated with high-order polynomials. Spectra are scaled and offset for comparison purposes, as well as smoothed with a boxcar of 3 pixels. Although this plot does not take into account the important differences in LE time-integrations between the spectra, it highlights the overall difference in fine-structure in the two LE spectra from opposite PAs. Observing Hα profiles with opposite asymmetry structure at opposite PAs is surprising considering the opening angle between the two LEs is $< 40°$.

Hα (blueshifted emission peak and red knee) despite the low signal of the spectrum.

The opening angles probed by the LE lines of sight are < 45 deg. The fact that large asymmetries are seen in the observed integrated LE spectra for relatively small changes in viewing angle is evidence for a strong asymmetry in the explosion.

5.3.3.2 Additional Evidence of Asymmetry

Although the Hα profile shows the strongest asymmetry signature that is dependent on viewing angle, we note here two additional possible sources of asymmetry from the LE spectra: a velocity shift in the Fe II λ5018 line that appears to be correlated with the Hα asymmetry, and an unidentified feature near 5265Å present in only one direction.

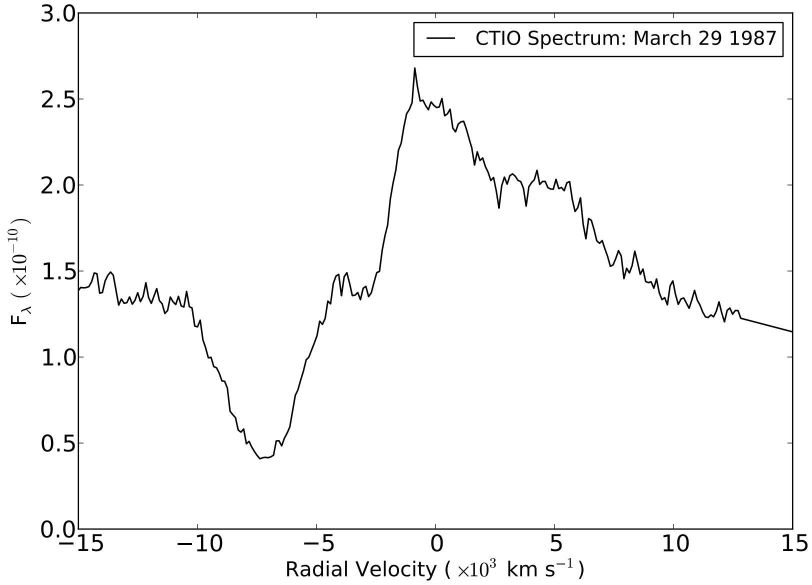

Figure 5.16: Historical CTIO Hα profile from Phillips et al. (1988) of SN 1987A taken on March 29, 1987, 34 days after explosion. The fine-structure, showing blue and red features at $\sim \pm3500$ km s^{-1}, defines the "Bochum event" which was observed 20-100 days after explosion. Evidence for this fine structure is not present after the historical spectra are integrated with the LE scattering model (red lines in Figure 5.13). Hα fine structure observed in the LE spectra in Figure 5.13 must therefore require stronger line profile asymmetry than the original "Bochum event" or the asymmetry must last for much longer than originally observed for SN 1987A.

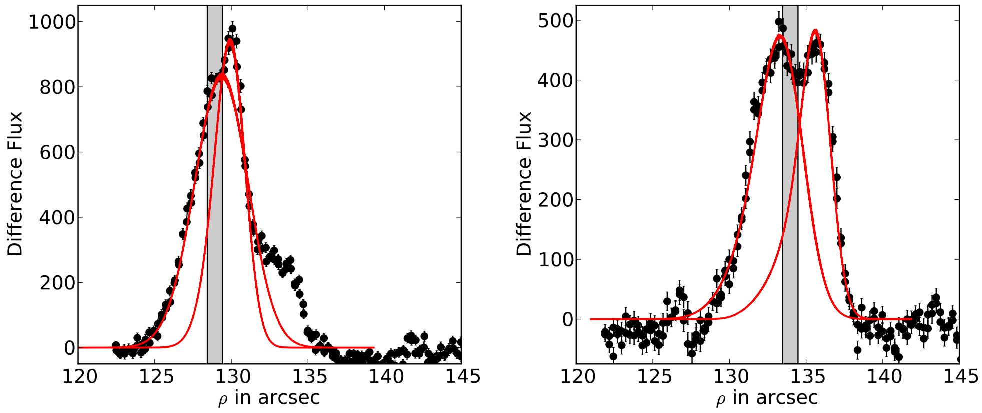

Figure 5.17: LEFT: Observed LE profile on the sky for the southern LE186. Overplotted in red are models for two scattering dust filaments which both contribute signal to the slit (plotted as the shaded region). Although the narrow filament at larger ρ contributes late-time epochs to the spectrum, allowing for a larger emission-to-absorption ratio, the excess emission in the LE186 Hα profile in Figure 5.13 cannot be modeled with the historical spectra of SN 1987A. See Appendix for full consideration. RIGHT: Observed LE profile of LE180. See Appendix for full consideration on why the LE fitting algorithm does not provide meaningful results in this complex case.

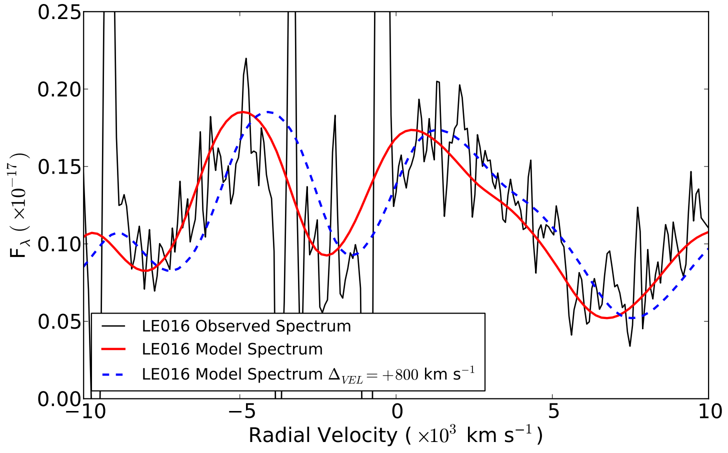

Figure 5.18: Observed Fe II λ5018 line in LE016 most-northern LE spectrum. The isotropic dust-modeled spectrum is over-plotted (solid red line), along with the same isotropic spectrum shifted 800 km s^{-1}to the red (dashed blue line), corresponding to the best fit to the peak location of the λ5018 line and of similar magnitude to the velocity shift observed in the Hα profile. Note that the velocity-shifted model spectrum is a better fit to the observed LE spectrum, indicating that the Hα velocity asymmetry may be correlated with the velocity of the Fe II λ5018 line.

Figure 5.18 plots the Fe II $\lambda5018$ line for the observed LE spectra of LE016 (black), the asymmetric northern viewing angle. The dust-modeled isotropic spectrum is plotted as solid red. We also plot in dashed blue the same isotropic spectrum redshifted by +800 km s^{-1}, which gives the best fit to the emission peak of the Fe II $\lambda5018$ line (determined by eye). The redshifted spectrum is a better fit to the line and is consistent with the $600 - 800$ km s^{-1}redshift observed in the Hα line for the same viewing angle. As with the Hα line asymmetry, the magnitude of the best-fitting redshift for the Fe II $\lambda5018$ line decreases as a function of viewing angle away from the LE016 line of sight. For the case of LE186, the line is weak and heavily contaminated from sky residuals. Although it has the most blueward Fe II $\lambda5018$ line of all observed LE spectra, it is unclear if the line is actually blueshifted with respect to the isotropic model or to zero. The structure is complicated since this line is part of a blend of the Fe II $\lambda\lambda4924$, 5018, 5169 features.

Figure 5.19 shows an unidentified feature near 5265Å in the observed LE spectra for both "equatorial" (i.e. perpendicular to maximum asymmetry axes 16°/186°) lines of sight at PA $\sim 115°$. Many LE spectra have signal-to-noise ratios higher than the lower spectrum of Figure 5.19, however there is no evidence for the feature in any other line of sight. The fact that the feature is broader in the LE117 (lower) spectrum is consistent with that LE probing a narrower range of early, high-velocity epochs as described in Section 5.3.2.1. Considering this wavelength region is populated with many line blends and the fact that the spectra represent a time-integration, it is currently unclear if the feature is due to differences in chemical or velocity properties at this viewing angle.

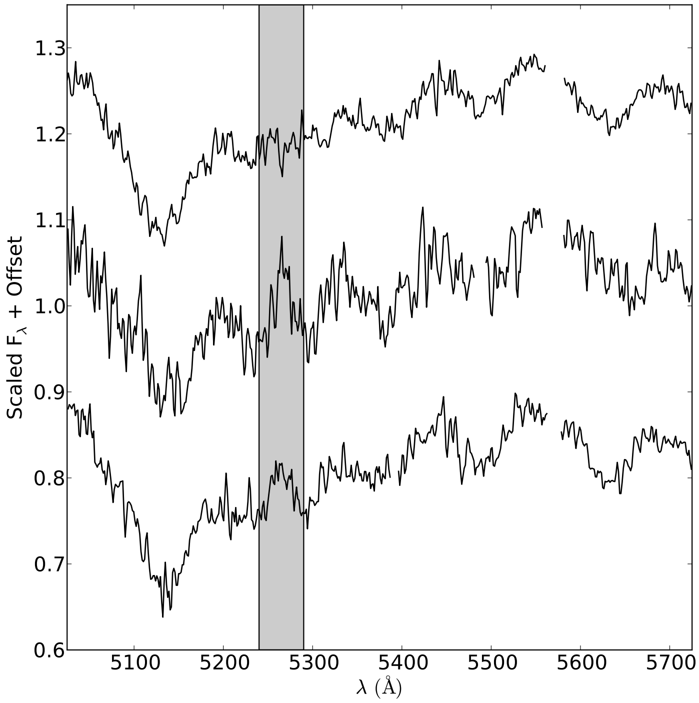

Figure 5.19: Observed LE spectrum for LE016 (top) compared with the two "equatorial" LE locations (LE113 and LE117, middle and lower, respectively) shown at PA ∼ 115° in Figure 5.1. Both spectra show an unidentified feature near 5265Å that is not present in any other viewing angle. The fact that the line appears broader in the upper spectrum is consistent with that LE probing a narrower range of early, high-velocity epochs compared to the lower spectrum as described in Section 5.3.2.1.

5.4 Discussion

Ignoring the smaller knee-like fine-structure, the Hα profiles of the LE016 and LE186 viewing angles in Figure 5.15 argue strongly for a one-sided asymmetry in SN 1987A. An overabundance of ^{56}Ni in the southern far hemisphere would create an excess in nonthermal excitation of hydrogen. This results in an excess in redshifted emission for the northern LE016 viewing angle. If the overabundance of ^{56}Ni is inclined close to the plane of the sky (within 21°), the overexcitation would occur in the near hemisphere with respect to the LE186 line of sight, explaining the blueshifted Hα emission in LE186. The question remains if the asymmetry summarized in Figure 5.15 is strictly a result of this one-sided asymmetry plus time-integration effects, or if an additional asymmetry is the cause of the blue and red knee in the fine-structure of Hα in LE016 and LE186, respectively.

The "Bochum event" (Figure 5.16) has previously been interpreted as an asymmetric distribution of ^{56}Ni (e.g., Lucy, 1988; Hanuschik & Thimm, 1990; Chugai, 1991a). Although both blue and red emission features are observed in Figure 5.16, the blue emission feature was only additionally observed in Hβ (Hanuschik & Thimm, 1990) while the redshifted emission feature was also observed in infrared hydrogen lines (Larson et al., 1987) and [Fe II] lines (Haas et al., 1990). Chugai (1991a) proposed a two-sided ^{56}Ni asymmetry: (1) a dominant ^{56}Ni cloud in the far hemisphere producing the red emission fine-structure and the redshifted emission peak at later epochs, and (2) a smaller, higher velocity ^{56}Ni cloud in the near hemisphere producing the blue fine-structure. However, instead of invoking a smaller ^{56}Ni cloud in the near hemisphere, the more recent explanation for the blue fine-structure is a non-monotonic Sobolev optical depth, $\tau(v)$, for Hα with a minimum near $v \approx 5000$ km s^{-1} (Chugai, 1991b; Utrobin et al., 1995; Wang et al., 2002; Utrobin & Chugai, 2002, 2005). This interpretation does not require breaking spherical symmetry to explain the blue fine-structure. Although Utrobin & Chugai (2005) favor this scenario, their model cannot successfully produce the optical depth minimum at the required strength. The smooth transition of the Hα profiles in PA from LE016 to LE117 in Figure 5.13 shows that the blue fine structure is dependent on viewing angle. As such, *some form* of deviation from spherical symmetry must be the root of the blue fine-structure in the LE Hα profiles and presumably directly correlated to the blue fine-structure observed in the "Bochum event."

The "Bochum event" was observed on days 20-100, while the redshift in lines of hydrogen and other elements was observed after ~ 150 days. For each LE spectrum, Table 5.1 lists the approximate range of epochs that contribute to the LE spectrum at greater than the 50% level. This relative contribution is based on the window function generated for each LE (Figure 5.3), prior to any flux-weighted integration. While the temporal resolution in the LEs is not capable of distinguishing between photospheric and nebular epochs, we can compare LEs with different degrees of nebular emission. It is therefore interesting to note that *both* the fine-structure and the velocity shift of the Hα line appear to be more dominantly a function of viewing angle rather than a function of epoch. LE066 probes the first ~ 80 days of the explosion only, but does not show fine-structure in Hα considerably different than the nearby LEs probing much later epochs. The fact that the blue fine-structure feature is also present in the early-epoch LE066 spectrum almost certainly links this feature to an exaggerated version of the original "Bochum event."

Since the Hα P Cygni line is a blend with Ba II λ6497, it is possible an asymmetry in the Ba II line is causing the observed blue fine-structure in the LE spectra. However, Utrobin et al. (1995) determined that the inclusion of the Ba II line was not sufficient to explain the blue emission in the "Bochum event." Additionally, unlike Hα, the Ba II λ6142 line appears to be fit well with the isotropic model in the LE spectra.

A two-sided ^{56}Ni model such as Chugai (1991a) could explain the Hα LE observations. A smaller high-velocity cloud blueshifted in the north causing the blue and red fine-structure in the north and south viewing angles, respectively. And a larger cloud redshifted in the south causing the red- and blue-shifted excess in the emission observed in the north and south viewing angles, respectively. The larger cloud could also be responsible for the Fe II asymmetry shown in Figure 5.18. The original observations of SN 1987A provided strong evidence for the large cloud being in the far hemisphere as previously stated. This is apparent in the isotropic model spectrum of LE186, where the time-integrated emission peak of Hα is shifted to the red. LE186 probes a larger range of epochs in the explosion (out to ~ 400 days), so the redshift and integrated line profile asymmetry is most apparent in the LE186 isotropic model. The observed LE spectrum, however, shows a small blueshift with respect to zero velocity, implying the overabundance is inclined within 21° of the plane of the sky in the southern far hemisphere. If the cloud was $\sim 20°$ from the plane of the sky, the radial velocities would be a factor of $1.7 - 1.9$ larger in the north and south viewing angles, more easily altering the Hα profile shape of the integrated LE spectra.

Figure 5.15 highlights the Hα emission peak redshifted and blueshifted with respect to zero velocity in the northern (LE016) and southern (LE186) viewing angles, respectively. With respect to the isotropic model of SN 1987A, the absolute velocity shift of the Hα peak is twice as large in the south (-1000 km s^{-1}in LE186 compared to $+500$ km s^{-1}in LE016). This is surprising considering both LEs have nearly equal $\sim 20°$ north and south lines of sight onto the photosphere. However, LE186 probes over twice the range of epochs in the original explosion compared to LE016. The velocity shift is most likely more apparent at these later nebular epochs as previously discussed, potentially accounting for the larger velocity shift for LE186.

In addition to SN 1987A, a velocity shift in the Hα peak or a Bochum-like event has also been observed for the Type IIP SNe SN 1999em, SN 2000cb, SN 2004dj, and SN 2006ov, as well as the Type II SN 2006bc (Elmhamdi et al., 2003; Kleiser et al., 2011; Chugai et al., 2005; Chornock et al., 2010; Gallagher et al., 2012). The Hα profiles of SN 2004dj are strikingly similar to that of the LE186 profile in Figure 5.15. Although LE spectra cannot be compared directly with instantaneous spectra, it appears the Hα lines from Chugai et al. (2005) would resemble that of LE186 after being smoothed by time-integration. Chugai et al. (2005) were able to successfully model the SN 2004dj Hα fine-structure using an asymmetric bipolar ^{56}Ni distribution, including a spherical component with two cylindrical components. They modeled the observer viewing a dominant jet 30° off-axis, resulting in a larger blueshifted emission peak with a smaller redshifted feature in the profiles of Hα . This describes the LE186 LE profile in Figure 5.15, suggesting a bipolar ^{56}Ni distribution as a possible explanation. Since at the opposite PA, LE016, we see the opposite set of features in Figure 5.15, the two LE viewing angles would have to be looking towards opposite ends of the bipolar distribution in the model of Chugai et al. (2005). Since the viewing angles only differ by $\sim 40°$, this would put strict constraints on the orientation of the bipolar distribution. This is, however, consistent with the dominant ^{56}Ni component being aligned within $\sim 20°$ to the plane of the sky, as previously suggested.

As noted in the introduction, one of the benefits of LE spectroscopy is it allows the signatures of the explosion in the first few hundred days to be compared directly with the state of the remnant. The PA of the symmetry axis of the elongated ejecta was measured to be $14° \pm 5°$ using HST imaging (Wang et al., 2002) and $15° \pm 0.9°$ using IFU spectra (Kjær et al., 2010). This PA corresponds to LE016, where we see the maximum deviation from symmetry in Hα in the northern hemisphere. Kjær et al. (2010) found the present-day ejecta to be blueshifted in the north and redshifted in the south, inclined out of the plane of the sky by $\sim 25°$. The bipolar ^{56}Ni distribution proposed above to explain the LE observations is therefore aligned with the roughly 25 year-old ejecta both in PA and inclination out of the sky. The inner ring of circumstellar material is inclined 49° out of the plane of the sky, blueshifted in the north (Sugerman et al., 2005). The outer circumstellar rings are similarly inclined, presumably related to the rotation axis of the progenitor. The elongated ejecta and ^{56}Ni distribution probed by the LE observations are therefore aligned approximately

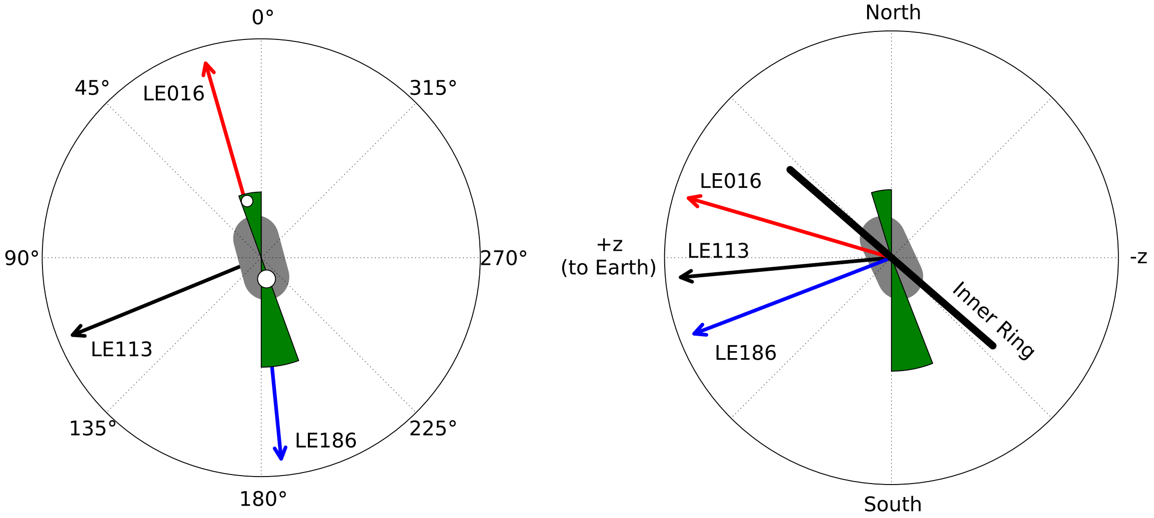

Figure 5.20: LEFT: PAs on the sky of the three dominant LE viewing angles LE016, LE113 and LE186. The central grey region denotes the orientation on the sky of the elongated remnant ejecta (PA = 16°) from Kjær et al. (2010). The green wedges illustrate the proposed two-sided distribution of ^{56}Ni, most dominant in the southern hemisphere. White circles illustrate the locations of the two mystery spots as identified by Nisenson & Papaliolios (1999), with radius proportional to relative brightness in magnitudes of the two sources. Only the *relative* distance from the center of the SNR to the mystery spots is to scale in the image. RIGHT: Schematic with viewing angle perpendicular to Earth's line of sight. The inclination of the inner circumstellar ring is shown along with the proposed two-sided distribution of ^{56}Ni in green. Note that the green wedges are to highlight the proposed geometry (not absolute velocity) of the ^{56}Ni asymmetry probed by the LE spectra, illustrating that the southern overabundance is most dominant.

in plane with the equatorial ring, as opposed to sharing a symmetry axis as initially proposed by Wang et al. (2002). This disfavors the axially symmetric jet-induced explosion model for SN 1987A proposed by Wang et al. (2002). We illustrate the proposed asymmetry with a schematic in Figure 5.20, highlighting the overabundance of ^{56}Ni close to the plane of the sky and redshifted in the southern hemisphere.

The "mystery spot" of SN 1987A was a bright source observed in speckle interferometry measurements 30, 38, and 50 days after the explosion, separated by only 60 mas from the SN (Nisenson et al., 1987; Meikle et al., 1987), and appearing at PA=194° ± 2°. Nisenson & Papaliolios (1999) reprocessed this data, and identified *two* mystery spots in the data: (1) the original bright source at PA=194° ± 3° separated by 60 ± 8 mas from the SNR, and (2) a fainter source at PA=14° ± 3° separated by 160 ± 8 mas from the SNR. In order to be associated with the SN, they claimed the mystery spots must be at relativistic speeds with the northern spot blueshifted. A satisfactory explanation of the mystery spot (or spots) has yet to appear, a fact which is often forgotten. Figure 5.20 highlights the location of the mystery spots of Nisenson & Papaliolios (1999) with respect to our LEs. Since the PAs for the LE Hα spectra showing maximum asymmetry (16°/186°) match the mystery spot PAs to within 10°, future modeling of the LE lines may aid in an explanation of the mystery spots.

If in fact the blue fine-structure of the "Bochum event" is due to an asymmetrical ^{56}Ni feature in the northern hemisphere, as the LE spectra here suggest, ^{56}Ni is transported to even higher velocities than previously considered. The blue feature emerges after 20 days at a radial velocity of -5000 km s^{-1} in the Hα profile. Since the blue fine-structure is most dominant in LE016 at a scattering angle of 17°, the lower limit of the absolute velocity of the ^{56}Ni cloud in the near hemisphere is 5200 km s^{-1}, a velocity difficult to explain in current neutrino-driven explosion models. Absolute velocities of > 7000 km s^{-1} are required if the cloud is inclined within 45° to the plane of the sky and upwards of 10000 km s^{-1} if within 30°. Assuming the dominant southern ^{56}Ni overabundance (and change in Hα peak velocity) is correlated to the red emission feature observed in the "Bochum event" requires absolute velocities of ~ 10000 km s^{-1} for that feature for an inclination of 20° out of the plane of the sky. For the case of SN 2000cb, Utrobin & Chugai (2011) required radial mixing ^{56}Ni to velocities of 8400 km s^{-1} to reproduce the observed lightcurve of SN 2000cb, although it was a more energetic Type IIP than SN 1987A. Therefore, these unrealistically high velocities of ^{56}Ni for current neutrino-powered core-collapse explosion models require us to step back and view the asymmetries in Figure 5.15 at their most basic level: a non-spherical excitation structure in the early ejecta. Dessart & Hillier (2011) demonstrated that the P Cygni line profiles from non-spherical Type II ejecta can be altered significantly depending on viewing angle. Only future modeling of the LE spectra, taking into account the effects of time-integration, will allow the ejecta geometry to be determined or further constrained.

5.5 Conclusions

We have obtained optical spectra from the LE system of SN 1987A, allowing time-integrated spectra of the first few hundred days of the original explosion to be viewed from multiple lines of sight. We have modeled the LE spectra using the original photometry and spectroscopy of SN 1987A using the model of Rest et al. (2011b). Using specific examples we have showed the model correctly interprets LE flux profiles and spectra when both scattering dust properties and observational properties are taken into consideration.

Each PA on the LE system represents a unique viewing angle onto the photosphere which can be spectroscopically compared to the isotropic spectrum calculated from the original outburst of SN 1987A. The LE spectra show evidence for asymmetry, demonstrating the technique of targeted LE spectroscopy as a useful probe for observing SN asymmetries. The observed asymmetries can be summarized as follows:

1. Fine-structure in the Hα line stronger than the original "Bochum event" is observed most strongly at PAs 16° and 186°, with the Hα profiles showing opposite asymmetry features in the north and south viewing angles.

2. At PA 16° we observed an excess in redshifted Hα emission and a blueshifted knee. At PA 186° we observed an excess of blueshifted Hα emission and a red knee. This fine-structure diminishes slowly as the PA increases from 16° to $16°+90°$, with the LEs perpendicular to the symmetry axis showing no evidence for asymmetry.

3. At PA 16° we observe a velocity shift in the Fe II λ5018 line of the same magnitude and direction as the velocity shift in the Hα emission peak at the same viewing angle. As with the Hα fine-structure, this velocity shift appears to diminish as PA increases from 16°.

4. At PA $\sim$ 115° (roughly perpendicular to symmetry axis defined by 16°/186° viewing angles) we observed an unidentified feature near λ5265Å not observed in any other viewing angle.

This symmetry axis defined by the 16°/186° viewing angles is in excellent agreement with the current axis of symmetry in the ejecta geometry, the initial polarization and speckle observations, as well as the location of the "mystery spot." The Hα lines at PAs 16° and 186° are very similar to the Hα lines observed in SN 2004dj and modeled as a two-sided ^{56}Ni distribution by Chugai et al. (2005). This same model could describe a two-sided ejection of ^{56}Ni in SN 1987A as probed by the LE Hα lines. The ^{56}Ni is blueshifted in the north and redshifted in the south, with the dominant overabundance of ^{56}Ni being inclined $\sim$ 20° from the plane of the sky. The indication that high-velocity ^{56}Ni is not correlated with the inner ring and presumed rotation axis may indicate that the explosion mechanism is independent of rotation. While these observations argue for a two-sided distribution of high-velocity ^{56}Ni, at their most basic level they probe unequal source functions of the Hα line at different viewing angles. Only future modeling of the LE spectra will be able to constrain the early ejecta geometry with confidence.

5.6 Acknowledgements

We thank John Menzies for organizing and providing the original SAAO spectra of SN 1987A. We also thank the anonymous referee for very useful comments. BPS thanks Rollin Thomas and Tomasz Plewa for helpful discussion. DLW acknowledges support from the Natural Sciences and Engineering Research Council of Canada (NSERC). SuperMACHO was supported by the HST grant GO-10583 and GO-10903. Based on observations obtained at the Gemini Observatory (Program IDs GS-2006B-Q-41, GS-2009A-Q-7, and GS-2009B-Q-22), which is operated by the Association of Universities for Research in Astronomy, Inc., under a cooperative agreement with the NSF on behalf of the Gemini partnership: the National Science Foundation (United States), the National Research Council (Canada), CONICYT (Chile), the Australian Research Council (Australia), Ministério da Ciência, Tecnologia e Inovação (Brazil) and Ministerio de Ciencia, Tecnología e Innovación Productiva (Argentina).

5.7 Appendix

5.7.1 Effect of Dust Substructure in LE Profiles

For the observed LE profiles presented in this work, 11/14 show no strong evidence for dust substructure within the profile. These LE profiles can be modeled with one dust sheet effectively. However, LE113, LE180, and LE186 all show significant substructure in the their profiles (Figures 5.4 and 5.17) and we seek to quantify the effect this can have on the observed LE spectrum. Figures 5.21-5.23 show the observed LE profiles and the effect of dust substructure on the window functions and effective lightcurves. Figure 5.24 shows the differences in Hα strengths obtained with and without including the effect of the secondary dust structure.

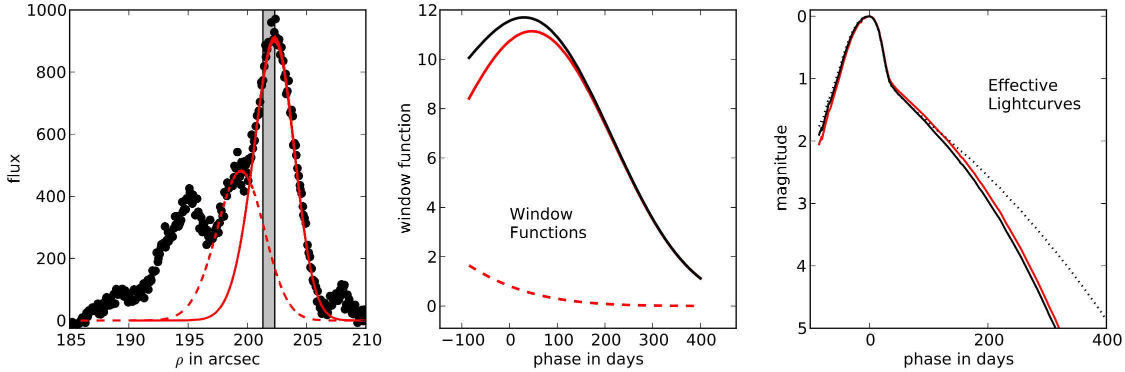

Figure 5.21: LEFT: LE113 observed LE profile (black points) with the best fit to the primary dust sheet (solid red line), as well as the best fit to the secondary dust sheet (dashed red line). The location of the slit is shown with the grey region. MIDDLE: Window functions for the primary (solid red line) and secondary (dashed red line) dust sheets, as well as the total window function (solid black line). RIGHT: Effective lightcurves for the primary dust sheet (solid red line), the total effective lightcurve from both dust sheets (solid black line), and the original lightcurve of SN 1987A (dotted line). The effect of the secondary dust sheet is minimal in this case.

As shown in Figure 5.24, the effect of the secondary substructure on the resulting Hα profile is minimal for LE113 ($< 4\%$ difference in strength of emission peak), primarily because the flux contribution from the wing of the LE profile is so small. For LE186, including the secondary LE profile decreases the Hα emission peak by 11%. Note, however, that because of the significant offset of the slit from the primary peak, the Hα emission for LE186 is in excess of the full lightcurve-weighted integration of SN 1987A. For the case of LE180, the secondary peak significantly alters the window function and subsequent Hα line, increasing the emission strength by $\sim 40\%$.

5.7.2 The Excess of Hα Emission in LE186

The observed LE spectra and isotropic models for LE180 and LE186 in Figure 5.11 show two different results. LE186 shows a clear, high signal-to-noise excess in Hα emission over the isotropic dust-modeled spectrum. LE180, probing essentially the same view-

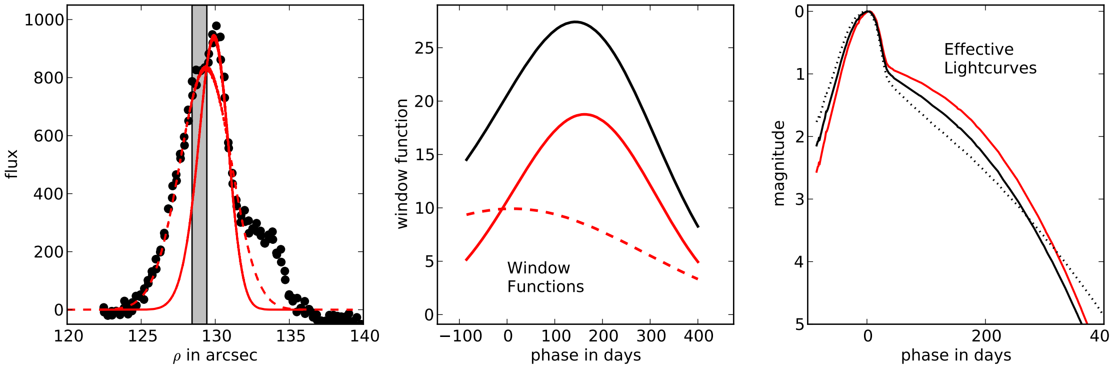

Figure 5.22: LEFT: LE186 observed LE profile (black points) with the best fit to the primary dust sheet (solid red line), as well as the best fit to the secondary dust sheet (dashed red line). The location of the slit is shown with the grey region. MIDDLE: Window functions for the primary (solid red line) and secondary (dashed red line) dust sheets, as well as the total window function (solid black line). RIGHT: Effective lightcurves for the primary dust sheet (solid red line), the total effective lightcurve from both dust sheets (solid black line), and the original lightcurve of SN 1987A (dotted line). Without the secondary peak, the effective lightcurve is significantly biased towards later times due to the location of the slit. The secondary peak contributes flux from early epochs, reducing the late-epoch biased produced by the slit.

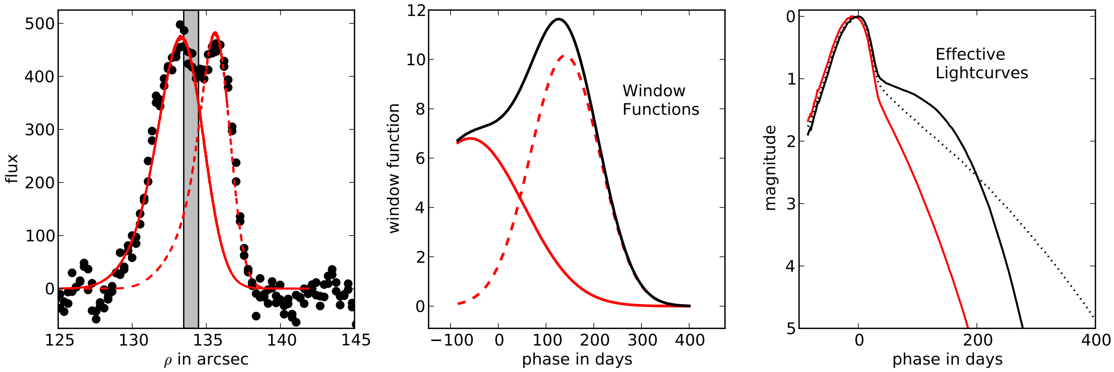

Figure 5.23: LEFT: LE180 observed LE profile (black points) with the best fit to the primary dust sheet (solid red line), as well as the best fit to the secondary dust sheet (dashed red line). The location of the slit is shown with the grey region. MIDDLE: Window functions for the primary (solid red line) and secondary (dashed red line) dust sheets, as well as the total window function (solid black line). RIGHT: Effective lightcurves for the primary dust sheet (solid red line), the total effective lightcurve from both dust sheets (solid black line), and the original lightcurve of SN 1987A (dotted line). Here the two dust sheets create LE substructure with nearly equal amounts of flux. The window function in this case is significantly shifted to later times due to the presence of the secondary peak at larger values of ρ.

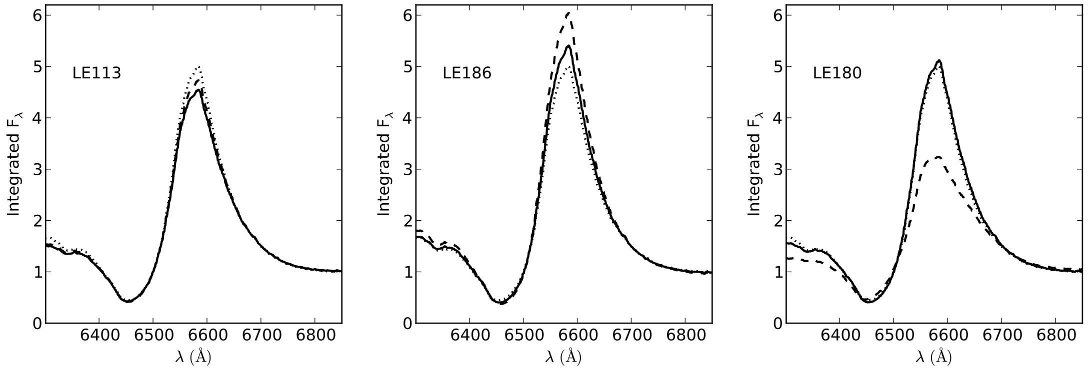

Figure 5.24: Resulting Hα profiles obtained by integrating the historical spectra of SN 1987A with the effective lightcurves in Figures 5.21-5.23 for LE113 (left panel), LE186 (middle panel), and LE180 (right panel). For each panel, the solid and dashed lines are from integrations of the total and primary-only effective lightcurves. The dotted line is Hα profile obtained by integrating the actual lightcurve of SN 1987A with no window function truncating the integration.

ing angle onto the photosphere, does not show such an excess in the Hα profile. In addition to the much lower signal-to-noise of LE180, we can use arguments based on the above dust substructure analysis to show that the excess emission observed in LE186 is physical.

As shown in the middle panel of Figure 5.24, the effect of the secondary LE peak in the LE186 profile is to *reduce* the emission peak of Hα . The maximum amount of Hα emission for LE186 therefore occurs when no secondary substructure is included. Since this gives an excess of only $\sim 10\%$, even this scenario is not able to account for the $\sim 30\%$ excess in Hα in the observed LE186 spectrum.

For the case of LE180, the effect of the substructure is to *increase* the Hα emission peak substantially ($\sim 40\%$ using the profile fits in Figure 5.23). Unlike the case of LE186, where the LE profile fits are well constrained within the data, the fits to the LE180 profile in Figure 5.23 are an example of a situation where our profile fitting algorithms cannot extract meaningful results due to the intrinsic complexity and low signal-to-noise ratio. It is most likely the case the secondary substructure in the LE180 profile is actually much wider than shown in Figure 5.23, which would result in more late-epoch contribution from the secondary peak and more emission in Hα .

Bibliography

Arnett, W. D. and Bahcall, J. N. and Kirshner, R. P. and Woosley, S. E. 1989, ARA&A, 27, 629

Bailey, J. 1988, Proceedings of the Astronomical Society of Australia, 7, 405

Blondin, J. M. and Mezzacappa, A. and DeMarino, C. 2003, ApJ, 584, 971

Burrows, A. 2012, ArXiv e-prints, 1210.4921

Caldwell, J. A. R. and Menzies, J. W. and Banfield, R. M. and Catchpole, R. M. and Whitelock, P. A. and Feast, M. W. and Lloyd Evans, T. H. H. and Sekiguchi, K. and Zijlstra, A. and Allen, D. A. and Bell, S. A. and Blades, J. C. and Buckley, D. A. H. and Byrne, P. B. and Callanan, P. and Collins, C. and Cumming, R. J. and O'Donoghue, D. and Fairall, A. P. and Freeman, F. F. and Holmgren, D. and Jones, K. and Latham, D. W. and Maddox, S. and Meadows, V. S. and Meikle, W. P. S. and Mittaz, J. P. D. and Monk, A. and Penny, A. J. and Pollacco, D. and Slawson, R. D. and Soltynski, M. G. and Spyromilio, J. and Stirpe, G. M. and Stobie, R. S. and Willmer, C. 1993, MNRAS, 262, 313

Catchpole, R. M. and Menzies, J. W. and Monk, A. S. and Wargau, W. F. and Pollaco, D. and Carter, B. S. and Whitelock, P. A. and Marang, F. and Laney, C. D. and Balona, L. A. and Feast, M. W. and Lloyd Evans, T. H. H. and Sekiguchi, K.

and Laing, J. D. and Kilkenny, D. M. and Spencer Jones, J. and Roberts, G. and Cousins, A. W. J. and van Vuuren, G. and Winkler, H. 1987, MNRAS, 229, 15P

Catchpole, R. M. and Whitelock, P. A. and Feast, M. W. and Menzies, J. M. and Glass, I. S. and Marang, F. and Laing, J. D. and Spencer Jones, J. H. and Roberts, G. and Balona, L. A. and Carter, B. S. and Laney, C. D. and Evans, L. T. and Sekiguchi, K. and Hutchinson, G. G. and Maddison, R. and Albinson, J. and Evans, A. and Allen, F. A. and Winkler, H. and Fairall, A. and Corbally, C. and Davies, J. K. and Parker, Q. A. 1988, MNRAS, 231, 75P

Catchpole, R. M. and Whitelock, P. A. and Menzies, J. W. and Feast, M. W. and Marang, F. and Sekiguchi, K. and van Wyk, F. and Roberts, G. and Balona, L. A. and Egan, J. M. and Carter, B. S. and Laney, C. D. and Laing, J. D. and Spencer Jones, J. H. and Glass, I. S. and Winkler, H. and Fairall, A. P. and Lloyd Evans, T. H. H. and Cropper, M. S. and Shenton, M. and Hill, P. W. and Payne, P. and Jones, K. N. and Wargau, W. and Mason, K. O. and Jeffery, C. S. and Hellier, C. and Parker, Q. A. and Chini, R. and James, P. A. and Doyle, J. G. and Butler, C. J. and Bromage, G. 1989, MNRAS, 237, 55P

Chornock, R. and Filippenko, A. V. and Li, W. and Silverman, J. M. 2010, ApJ, 713, 1363

Chugai, N. N. 1991a, Soviet Astronomy, 35, 171

——. 1991b, Soviet Astronomy Letters, 17, 400

Chugai, N. N. and Fabrika, S. N. and Sholukhova, O. N. and Goranskij, V. P. and Abolmasov, P. K. and Vlasyuk, V. V. 2005, Astronomy Letters, 31, 792

Cropper, M. and Bailey, J. and McCowage, J. and Cannon, R. D. and Couch, W. J. 1988, MNRAS, 231, 695

Crotts, A. P. S. 1988, ApJ, 333, L51

Dessart, L. and Hillier, D. J. 2011, MNRAS, 415, 3497

Elmhamdi, A. and Danziger, I. J. and Chugai, N. and Pastorello, A. and Turatto, M. and Cappellaro, E. and Altavilla, G. and Benetti, S. and Patat, F. and Salvo, M. 2003, MNRAS, 338, 939

Gallagher, J. S. and Sugerman, B. E. K. and Clayton, G. C. and Andrews, J. E. and Clem, J. and Barlow, M. J. and Ercolano, B. and Fabbri, J. and Otsuka, M. and Wesson, R. and Meixner, M. 2012, ApJ, 753, 109

Garg, A. and Stubbs, C. W. and Challis, P. and Wood-Vasey, W. M. and Blondin, S. and Huber, M. E. and Cook, K. and Nikolaev, S. and Rest, A. and Smith, R. C. and Olsen, K. and Suntzeff, N. B. and Aguilera, C. and Prieto, J. L. and Becker, A. and Miceli, A. and Miknaitis, G. and Clocchiatti, A. and Minniti, D. and Morelli, L. and Welch, D. L. 2007, AJ, 133, 403

Gawryszczak, A. and Guzman, J. and Plewa, T. and Kifonidis, K. 2010, A&A, 521, A38

Gouiffes, C. and Rosa, M. and Melnick, J. and Danziger, I. J. and Remy, M. and Santini, C. and Sauvageot, J. L. and Jakobsen, P. and Ruiz, M. T. 1988, A&A, 198, L9

Haas, M. R. and Erickson, E. F. and Lord, S. D. and Hollenbach, D. J. and Colgan, S. W. J. and Burton, M. G. 1990, ApJ, 360, 257

Hammer, N. J. and Janka, H.-T. and Müller, E. 2010, ApJ, 714, 1371

Hamuy, M. and Suntzeff, N. B. 1990, AJ, 99, 1146

Hamuy, M. and Suntzeff, N. B. and Bravo, J. and Phillips, M. M. 1990, PASP, 102, 888

Hamuy, M. and Suntzeff, N. B. and Gonzalez, R. and Martin, G. 1988, AJ, 95, 63

Hanuschik, R. W. and Dachs, J. 1987, A&A, 182, L29

Hanuschik, R. W. and Thimm, G. J. 1990, A&A, 231, 77

Jeffery, D. J. 1987, Nature, 329, 419

Kim, Y. and Rieke, G. H. and Krause, O. and Misselt, K. and Indebetouw, R. and Johnson, K. E. 2008, ApJ, 678, 287

Kjær, K. and Leibundgut, B. and Fransson, C. and Jerkstrand, A. and Spyromilio, J. 2010, A&A, 517, A51

Kleiser, I. K. W. and Poznanski, D. and Kasen, D. and Young, T. R. and Chornock, R. and Filippenko, A. V. and Challis, P. and Ganeshalingam, M. and Kirshner, R. P. and Li, W. and Matheson, T. and Nugent, P. E. and Silverman, J. M. 2011, MNRAS, 415, 372

Krause, O. and Birkmann, S. M. and Usuda, T. and Hattori, T. and Goto, M. and Rieke, G. H. and Misselt, K. A. 2008a, Science, 320, 1195

Krause, O. and Tanaka, M. and Usuda, T. and Hattori, T. and Goto, M. and Birkmann, S. and Nomoto, K. 2008b, Nature, 456, 617

Larson, H. P. and Drapatz, S. and Mumma, M. J. and Weaver, H. A. 1987, in European Southern Observatory Conference and Workshop Proceedings, Vol. 26, European Southern Observatory Conference and Workshop Proceedings, ed. I. J. Danziger, 147–151

Lucy, L. B. 1988, in Supernova 1987A in the Large Magellanic Cloud, ed. M. Kafatos & A. G. Michalitsianos, 323–334

Meaburn, J. and Bryce, M. and Holloway, A. J. 1995, A&A, 299, L1

Meikle, W. P. S. and Matcher, S. J. and Morgan, B. L. 1987, Nature, 329, 608

Menzies, J. W. and Catchpole, R. M. and van Vuuren, G. and Winkler, H. and Laney, C. D. and Whitelock, P. A. and Cousins, A. W. J. and Carter, B. S. and Marang, F. and Lloyd Evans, T. H. H. and Roberts, G. and Kilkenny, D. and Spencer Jones, J. and Sekiguchi, K. and Fairall, A. P. and Wolstencroft, R. D. 1987, MNRAS, 227, 39P

Miknaitis, G. and Pignata, G. and Rest, A. and Wood-Vasey, W. M. and Blondin, S. and Challis, P. and Smith, R. C. and Stubbs, C. W. and Suntzeff, N. B. and Foley, R. J. and Matheson, T. and Tonry, J. L. and Aguilera, C. and Blackman, J. W. and Becker, A. C. and Clocchiatti, A. and Covarrubias, R. and Davis, T. M. and Filippenko, A. V. and Garg, A. and Garnavich, P. M. and Hicken, M. and Jha, S. and Krisciunas, K. and Kirshner, R. P. and Leibundgut, B. and Li, W. and Miceli, A. and Narayan, G. and Prieto, J. L. and Riess, A. G. and Salvo, M. E. and Schmidt, B. P. and Sollerman, J. and Spyromilio, J. and Zenteno, A. 2007, ApJ, 666, 674

Müller, B. and Janka, H.-T. and Marek, A. 2012, ApJ, 756, 84

Nisenson, P. and Papaliolios, C. 1999, ApJ, 518, L29

Nisenson, P. and Papaliolios, C. and Karovska, M. and Noyes, R. 1987, ApJ, 320, L15

Papaliolios, C. and Krasovska, M. and Koechlin, L. and Nisenson, P. and Standley, C. 1989, Nature, 338, 565

Phillips, M. M. and Hamuy, M. and Heathcote, S. R. and Suntzeff, N. B. and Kirhakos, S. 1990, AJ, 99, 1133

Phillips, M. M. and Heathcote, S. R. 1989, PASP, 101, 137

Phillips, M. M. and Heathcote, S. R. and Hamuy, M. and Navarrete, M. 1988, AJ, 95, 1087

Rest, A. and Foley, R. J. and Sinnott, B. and Welch, D. L. and Badenes, C. and Filippenko, A. V. and Bergmann, M. and Bhatti, W. A. and Blondin, S. and Challis, P. and Damke, G. and Finley, H. and Huber, M. E. and Kasen, D. and Kirshner, R. P. and Matheson, T. and Mazzali, P. and Minniti, D. and Nakajima, R. and Narayan, G. and Olsen, K. and Sauer, D. and Smith, R. C. and Suntzeff, N. B. 2011a, ApJ, 732, 3

Rest, A. and Matheson, T. and Blondin, S. and Bergmann, M. and Welch, D. L. and Suntzeff, N. B. and Smith, R. C. and Olsen, K. and Prieto, J. L. and Garg, A. and Challis, P. and Stubbs, C. and Hicken, M. and Modjaz, M. and Wood-Vasey, W. M. and Zenteno, A. and Damke, G. and Newman, A. and Huber, M. and Cook, K. H. and Nikolaev, S. and Becker, A. C. and Miceli, A. and Covarrubias, R. and Morelli, L. and Pignata, G. and Clocchiatti, A. and Minniti, D. and Foley, R. J. 2008a, ApJ, 680, 1137

Rest, A. and Prieto, J. L. and Walborn, N. R. and Smith, N. and Bianco, F. B. and Chornock, R. and Welch, D. L. and Howell, D. A. and Huber, M. E. and Foley, R. J. and Fong, W. and Sinnott, B. and Bond, H. E. and Smith, R. C. and Toledo, I. and Minniti, D. and Mandel, K. 2012a, Nature, 482, 375

Rest, A. and Sinnott, B. and Welch, D. L. 2012b, Proceedings of the Astronomical Society of Australia, 29, 466

Rest, A. and Sinnott, B. and Welch, D. L. and Foley, R. J. and Narayan, G. and Mandel, K. and Huber, M. E. and Blondin, S. 2011b, ApJ, 732, 2

Rest, A. and Stubbs, C. and Becker, A. C. and Miknaitis, G. A. and Miceli, A. and Covarrubias, R. and Hawley, S. L. and Smith, R. C. and Suntzeff, N. B. and Olsen, K. and Prieto, J. L. and Hiriart, R. and Welch, D. L. and Cook, K. H. and Nikolaev, S. and Huber, M. and Prochtor, G. and Clocchiatti, A. and Minniti, D. and Garg, A. and Challis, P. and Keller, S. C. and Schmidt, B. P. 2005a, ApJ, 634, 1103

Rest, A. and Suntzeff, N. B. and Olsen, K. and Prieto, J. L. and Smith, R. C. and Welch, D. L. and Becker, A. and Bergmann, M. and Clocchiatti, A. and Cook, K. and Garg, A. and Huber, M. and Miknaitis, G. and Minniti, D. and Nikolaev, S. and Stubbs, C. 2005b, Nature, 438, 1132

Rest, A. and Welch, D. L. and Suntzeff, N. B. and Oaster, L. and Lanning, H. and Olsen, K. and Smith, R. C. and Becker, A. C. and Bergmann, M. and Challis, P. and Clocchiatti, A. and Cook, K. H. and Damke, G. and Garg, A. and Huber, M. E. and Matheson, T. and Minniti, D. and Prieto, J. L. and Wood-Vasey, W. M. 2008b, ApJ, 681, L81

Shigeyama, T. and Nomoto, K. 1990, ApJ, 360, 242

Spyromilio, J. and Meikle, W. P. S. and Allen, D. A. 1990, MNRAS, 242, 669

Sugerman, B. E. K. and Crotts, A. P. S. and Kunkel, W. E. and Heathcote, S. R. and Lawrence, S. S. 2005, ApJS, 159, 60

Suntzeff, N. B. and Hamuy, M. and Martin, G. and Gomez, A. and Gonzalez, R. 1988a, AJ, 96, 1864

Suntzeff, N. B. and Heathcote, S. and Weller, W. G. and Caldwell, N. and Huchra, J. P. 1988b, Nature, 334, 135

Utrobin, V. P. 2004, Astronomy Letters, 30, 293

Utrobin, V. P. and Chugai, N. N. 2002, Astronomy Letters, 28, 386

——. 2005, A&A, 441, 271

——. 2011, A&A, 532, A100

Utrobin, V. P. and Chugai, N. N. and Andronova, A. A. 1995, A&A, 295, 129

van Dokkum, P. G. 2001, PASP, 113, 1420

Wang, L. and Wheeler, J. C. 2008, ARA&A, 46, 433

Wang, L. and Wheeler, J. C. and Höflich, P. and Khokhlov, A. and Baade, D. and Branch, D. and Challis, P. and Filippenko, A. V. and Fransson, C. and Garnavich, P. and Kirshner, R. P. and Lundqvist, P. and McCray, R. and Panagia, N. and Pun, C. S. J. and Phillips, M. M. and Sonneborn, G. and Suntzeff, N. B. 2002, ApJ, 579, 671

Weingartner, J. C. and Draine, B. T. 2001, ApJ, 548, 296

Whitelock, P. A. and Catchpole, R. M. and Menzies, J. W. and Feast, M. W. and Woosley, S. E. and Allen, D. and van Wyk, F. and Marang, F. and Laney, C. D. and Winkler, H. and Sekiguchi, K. and Balona, L. A. and Carter, B. S. and Spencer Jones, J. H. and Laing, J. D. and Evans, T. L. and Fairall, A. P. and Buckley, D. A. H. and Glass, I. S. and Penston, M. V. and da Costa, L. N. and Bell, S. A. and Hellier, C. and Shara, M. and Moffat, A. F. J. 1989, MNRAS, 240, 7P

Whitelock, P. A. and Catchpole, R. M. and Menziez, J. W. and Feast, M. W. and Winkler, H. and Marang, F. and Glass, I. S. and Balona, L. A. and Egan, J. and Carter, B. S. and Roberts, G. and Sekiguchi, K. and Laney, C. D. and Lloyd Evans, T. and Laing, J. D. and Spencer Jones, J. and Fernley, J. and James, P. and Fairall, A. P. and Monk, A. S. and van Wyk, F. 1988, MNRAS, 234, 5P

Xu, J. and Crotts, A. P. S. and Kunkel, W. E. 1995, ApJ, 451, 806

Chapter 6

Direct Confirmation of the Asymmetry of the Cas A Supernova with Light Echoes

This chapter incorporates a reformatted article previously published in The Astrophysical Journal, originally appearing as:

"Rest, A., Foley, R. J., Sinnott, B., Welch, D. L., Badenes, C., Filippenko, A. V., Bergmann, M., Bhatti, W. A., Blondin, S., Challis, P., Damke, G., Finley, H., Huber, M. E., Kasen, D., Kirshner, R. P., Matheson, T., Mazzali, P., Minniti, D., Nakajima, R., Narayan, G., Olsen, K., Sauer, D., Smith, R. C., and Suntzeff, N. B. The Astrophysical Journal, **732**, 3 (2011)."

6.1 Introduction

Light echoes (LEs) are the scattered light of a transient event that reflects off dust in the interstellar medium. The extra path length of the two-segment trajectory results in LE light arriving at an observer significantly later than the undelayed photons. Such circumstances provide exciting scientific opportunities that are extremely rare in astronomy — specifically, to observe historical events with modern instrumentation and to examine the same event from different lines of sight (LoS). We have previously employed LEs to take advantage of the time delay, identifying systems of such LEs associated with several-hundred-year old supernova (SN) remnants (SNRs) in the Large Magellanic Cloud and subsequently spectroscopically classifying the supernovae (SNe; Rest et al., 2005b, 2008a). Our work represented the first time that the spectral classification of SN light was definitively linked with a SNR. The analysis of the X-ray spectrum of that SNR by Badenes et al. (2008) provided confirmation of both its classification (Type Ia) and subclass (high luminosity). Clearly, LE spectroscopy is a powerful technique for understanding the nature of SNe in the Milky Way and Local Group galaxies.

Cas A is the brightest extrasolar radio source in the sky (Ryle & Smith, 1948) and the youngest (age ∼330 yr) Milky Way core-collapse SNR (Stephenson & Green, 2002). Its distance is approximately 3.4 kpc. Dynamical measurements of the SNR indicate that the explosion occurred in year 1681 ± 19 (Fesen et al., 2006a); we adopt this date for age calculations in this paper. A single historical account of a sighting in 1680 by Flamsteed is attributed to the Cas A SN (Ashworth, 1980), although this has been disputed (Kamper, 1980). Cas A is the youngest of the certain historical CC SNe and is thus an excellent target for LE studies.

Krause et al. (2005) identified a few moving Cas A features (called "infrared echoes") using infrared (IR) images from the *Spitzer Space Telescope*, the result of dust absorbing the SN light, warming up, and reradiating light at longer wavelengths. Their main scientific conclusion, that most if not all of these IR echoes were caused by a series of recent X-ray outbursts from the compact object in the Cas A SNR, was incorrect because they did not take into account that the apparent motion strongly depends on the inclination of the scattering dust filament (Dwek & Arendt, 2008;

Rest et al., 2011). Rather, the echoes must have been generated by an intense and short burst of ultraviolet (UV) radiation associated with the breakout of the SN shock through the surface of the progenitor star of Cas A (Dwek & Arendt, 2008).

The first scattered LEs of Galactic SNe associated with Tycho's SN and the Cas A SN were discovered by Rest et al. (2007, 2008b). Contemporaneously, Krause et al. (2008) obtained a spectrum of a scattered optical light echo spatially coincident with one of the Cas A IR echoes, and identified the Cas A SN to be of Type IIb from its similarity to the spectrum of SN 1993J, the very well-observed and prototypical example of the SN IIb class (e.g., Filippenko et al., 1993; Richmond et al., 1994; Filippenko et al., 1994; Matheson et al., 2000).

The discovery and spectroscopic follow-up observations of different LEs from the same SN allow us to benefit from the unique advantages of LEs — their ability to probe the SN from significantly different directions. The only time this technique has been applied previously was by Smith et al. (2001, 2003), who used spectra of the reflection nebula of η Carinae to observe its central star from different directions. Dust concentrations scattering SN light lie at numerous different position angles and at different radial distances from the observer. This is illustrated in Figure 6.1, which shows the Cas A SNR (red dots), the scattering dust (brown dots), and the light paths. We denote the light echoes as LE2116, LE2521, and LE3923, where the number represents the ID of the grid tile of the search area in this region of the sky. LE2521 and LE3923 are newly discovered and LE2116 was discovered by Rest et al. (2008b). The scattering dust of LE3923 is more than 2000 ly in front of Cas A, much farther than any other scattering dust; thus, we show only part of its light path.

The study of a single SN from different LoS is particularly relevant for the Cas A SNR. With observations of the LEs shown in Figure 6.1, we are positioned to *directly* measure the symmetry of a core-collapse SN, and compare it to the structure of the remnant. The thermal X-ray emission as well as the optical emission of the Cas A SNR is very inhomogeneous, with large Fe-rich and Si-rich outflows being spa-

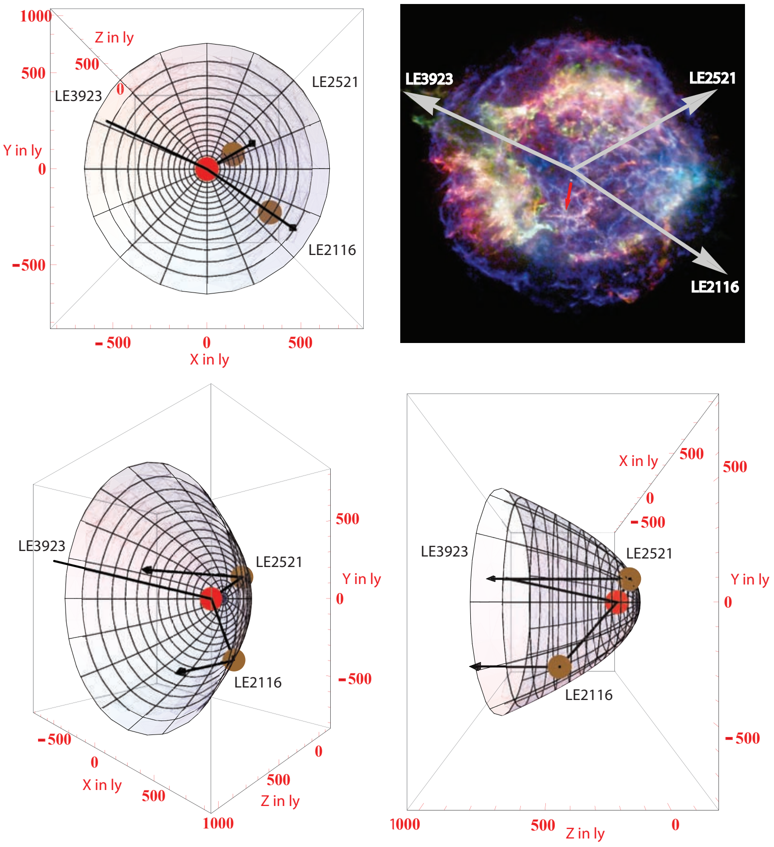

Figure 6.1: North is toward the positive-y axis (up), east is toward the negative-x axis (left), and the positive-z axis points toward the observer with the origin at the SNR. The SN to LE cone apex distance, in light years, is half the interval of time since the SN explosion. The red and brown circles indicate the SN and scattering dust, respectively. The black lines show the path of the light scattering from the LE-producing dust concentrations. The scattering dust of LE3923 is more than 2000 ly in front of Cas A, much farther than any other scattering dust; thus, we show only part of the light path, and do not include its dust location. The top-left panel shows an *Chandra* X-ray image (Hwang et al., 2004), with the projected light path from SN to scattering dust overplotted (gray arrows). The red arrow indicates the X-ray compact object and its apparent motion. In this false-color image, red corresponds to low-energy X-rays around the Fe L complex (∼1 keV and below), green to mid-energy X-rays around the Si K blend (∼2 keV), and blue to high-energy X-rays in the 4–6 keV continuum band between the Ca K and Fe K blends.

tially distinct, indicating that the SN explosion was asymmetric (Hughes et al., 2000; Hwang et al., 2004; Fesen et al., 2006a). The nature of these outflows and their individual relevance to the SN explosion is still debated (Burrows et al., 2005; Wheeler et al., 2008; DeLaney et al., 2010). Tananbaum (1999) detected in *Chandra* images a compact X-ray source $7''$ from the Cas A SNR center; it is an excellent candidate for being the neutron star produced by the SN explosion (Tananbaum, 1999; Fesen et al., 2006b). The position angle of the X-ray source is off by only $\sim 30^\circ$ from the position angle of the southeast Fe-rich structure (Wheeler et al., 2008), and has a projected apparent motion of 350 km s^{-1}. In §6.2 of this paper, we report two new LE complexes associated with Cas A, and we show optical spectra of these LEs as well as one of the previously known LEs. With these data we are able to view three distinct directions, where each dust concentration probes different hemispheres of the SN photosphere. In Rest et al. (2010) we have introduced an innovative technique for modeling both astrophysical (dust inclination, scattering, and reddening) and observational (seeing and slit width) effects to measure the light-curve weighted window function which is the determining factor for the relative time-weighting of the observed (integrated) LE spectrum. We apply this technique in §6.3 to similar well-observed SNe to produce appropriate comparison spectra. Such spectra are necessary to compare the Cas A spectra to other SNe as well as to compare the LE spectra to each other. We show that the Cas A SN was indeed very similar to the prototypical Type IIb SN 1993J, as claimed by Krause et al. (2008). In §6.4 we demonstrate that, despite the excellent agreement between the Cas A spectra and SN 1993J, one LE has a systematically higher ejecta velocity than either SN 1993J *or the other LEs*, revealing that Cas A was an intrinsically asymmetric explosion; observers from different directions would have viewed a "different" SN spectroscopically. In this section we also discuss the implications of our finding for both other historical SNe and for core-collapse SNe and their explosions.

6.2 Observations & Reductions

6.2.1 Imaging

We reobserved LEs discovered in a campaign of several observing runs on the Mayall 4 m telescope at Kitt Peak National Observatory (KPNO) starting in 2006 (Rest et al., 2008b). As described in that paper, the Mosaic imager, which operates at the $f/3.1$ prime focus at an effective focal ratio of $f/2.9$, was used with the Bernstein VR broad-band filter (k1040) which has a central wavelength of 5945 Å and a full width at half-maximum intensity (FWHM) of 2120 Å. The images were kernel- and flux-matched, aligned, subtracted, and masked using the SMSN pipeline (Rest et al., 2005a; Garg et al., 2007; Miknaitis et al., 2007). LE2116 had been previously discovered and reported (Rest et al., 2008b), whereas LE2521 and LE3923 are light echoes discovered on 2009 September 14 and 16, respectively (UT dates are used throughout this paper).

Figure 6.2 shows the LEs and the adopted spectroscopic slit positions. For the LE2116 mask design, we used images from KPNO obtained on 2009 September 14, ~1 week before the spectroscopy was obtained. Note that we had a third slit in the high surface brightness region between slits A and B. Unfortunately, the LE filled the entire slit, making proper sky subtraction impossible. Sky subtraction using the sky observed in other slits produced inaccurate spectra with large residuals near the sky lines. As a result, we have not included the spectra from this slit in our analysis. For LE3923, we used images obtained at the Apache Point Observatory 3.5 m telescope on 2009 October 16 with the SPIcam[1] CCD imager in the SDSS-r' filter and processed in a similar manner with the SMSN pipeline. Since the apparent motion of the LEs is $\sim 30''$ per year, we measured the apparent motion and adjusted the slit position accordingly. These position adjustments amounted to $\sim 1''$. LE2521 was sufficiently compact and bright that long-slit spectroscopy was favored over masks. A summary of the spectroscopic and geometric parameters is given in Tables 6.1 and 6.2, respectively.

---

[1] http://www.apo.nmsu.edu/arc35m/Instruments/SPICAM/.

Table 6.1. Summary of spectroscopic observations of and scattering dust properties of Cas A light echoes.

LE	Telescope	R.A. (J2000)	decl. (J2000)	PA SNR-LE (°)	UT Date[a]	Seeing[a] (″)	ID[a]	Width[a] (″)	Length[a] (″)	PA[a] (°)	UT Mask[b]
2116	Keck	23:02:27.10	+56:54:23.4	237.79	20090922	0.81	A	1.5	2.69	0.0	20090914
2116	Keck	23:02:27.67	+56:54:07.7	237.79	20090922	0.81	B	1.5	3.59	0.0	20090914
2521	Keck	23:12:03.86	+59:34:59.3	299.10	20090922	0.79	···	1.5	4.32	41.0	···
2521	MMT	23:12:03.88	+59:34:59.2	299.10	20090921	0.70	···	1.0	4.20	30.0	···
3923	Keck	00:21:04.97	+61:15:37.3	65.08	20091023	0.89	···	1.5	7.72	0.0	20091016

[a] Parameters for spectroscopic slit.

[b] UT date of image used for mask design.

For the light-echo profile fits described in §6.3, we used the deep images in good seeing from 2009 September 14–16.

6.2.2 Spectroscopy

We obtained spectra of the LEs with the Low Resolution Imaging Spectrometer (LRIS; Oke et al., 1995) on the 10 m Keck I telescope and with the Blue Channel spectrograph (Schmidt et al., 1989) on the 6.5 m MMT (see Table 6.1). For the LRIS observations, slit masks were designed to maximize the efficiency of the telescope time. Standard CCD processing and spectrum extraction were performed with IRAF[2]. The data were extracted using the optimal algorithm of Horne (1986). Low-order polynomial fits to calibration-lamp spectra were used to establish the wavelength scale, and small adjustments derived from night-sky lines in the object frames were applied. We employed our own IDL routines to flux calibrate the data and remove telluric lines using the well-exposed continua of spectrophotometric standard stars (Wade & Horne, 1988; Matheson et al., 2000; Foley et al., 2003). For LE2116, we combine slits A and B using weights of 0.9 and 0.1, respectively. We present our LE spectra in §6.4.

---

[2] IRAF: the Image Reduction and Analysis Facility is distributed by the National Optical Astronomy Observatory, which is operated by the Association of Universities for Research in Astronomy (AURA), Inc., under cooperative agreement with the National Science Foundation (NSF).

Table 6.2. Physical sizes and locations of Cas A light echoes.

LE	δ^{a} (°)	ρ^{b} (ly)	x^{c} (ly)	y^{c} (ly)	z^{c} (ly)
2116	3.376	628	531	-335	437
2521	1.642	318	278	155	-10
3923	7.587	1204	-1092	507	2045

[a] Angular distance between SNR and LE.

[b] Distance between SNR and LE in the plane of the sky ($\rho^2 = x^2 + y^2$).

[c] Coordinates x,y, and z of the LE with origin at the SNR. The positive x and y axis are in the plane of the sky toward West and North, respectively. The positive z axis is along the line of sight from the SNR toward the observer. We assume a distance to the Cas A SNR of 3.4 kpc and 1681 AD as the time of explosion.

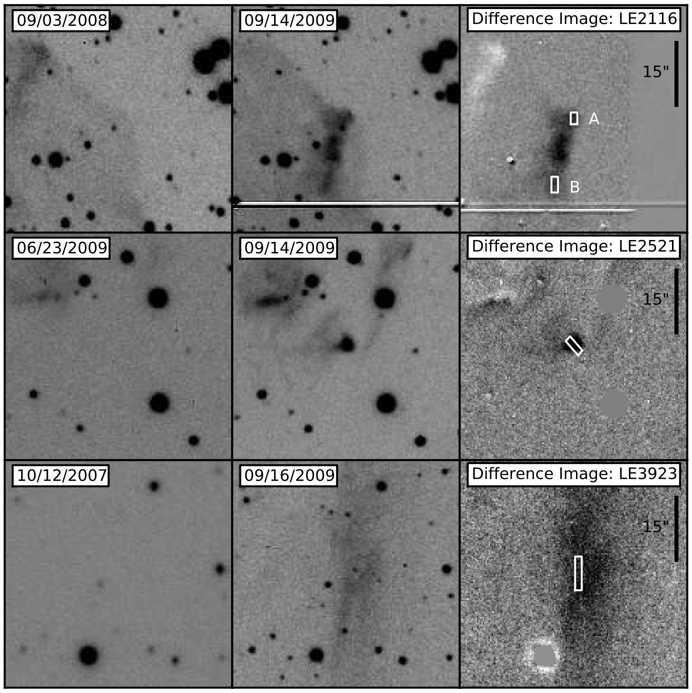

Figure 6.2: Image stamps of the LE discovery images and slit positions for spectroscopy for the three LE complexes LE2116, LE2521, and LE3923 (along horizontal panels). Left vertical panels are the reference template image at an earlier epoch (on the date shown in the box at top). Middle vertical panels are the image fields at a later epoch, centered here on the LE position. Right vertical panels are the difference images of the respective recent image and the earlier reference template to isolate the transient flux of the LE. For all image stamps north is up and east is to the left. The position and size of the slit used for spectroscopy is indicated by the rectangular overlay.

6.3 Generating Comparison Spectra

We have recently determined that modeling the dust-filament properties (e.g., the dust width) is required to accurately model LE spectra (Rest et al., 2010). All previous studies have neglected this aspect. Because the dust filament that reflects the LE has a nonzero size, it translates into a window function over the time domain as the SN light traverses over it. If this window function is narrower than the SN light curve, the observed LE spectrum is affected. We find that the observed LE spectrum is a function of dust-filament thickness, dust-filament inclination, seeing, spectrograph slit width, and slit rotation/position with respect to the LE. All of the noninstrumental parameters can be determined with an analysis of the LE in images at different epochs, and an individually modeled spectral template for a given observed LE can be constructed *a priori* without using the actual observed LE spectrum. Rest et al. (2010) describe this process in detail, showing that the observed LE spectrum is the integration of the individual spectra weighted with an effective light curve, which is the product of the light curve with the dust-filament-dependent window function. We emphasize that these window functions are different for every LE location. The top-left panel of Figure 6.3 shows the window functions for the LEs for which we have spectra using the SN 1993J spectral library (Jeffery et al., 1994; Barbon et al., 1995; Fransson et al., 2005) and light curve (Richmond et al., 1996). We refer the reader to Rest et al. (2010) for a detailed description of how the effective light curves are derived. Examples of the fitted parameters are given in Tables 1 and 2 and shown in Figure 12 of Rest et al. (2010)

Even though LE2521 and LE2116 have comparable dust widths, LE2521 has a considerably wider window function than LE2116 since its dust-filament inclination ($\alpha = 54°$) is significantly larger than that of LE2116 ($\alpha = 9°$), causing the projected SN light-curve shape to be “squashed.” LE3923 has an inclination similar to that of LE2116, but its scattering dust is thicker, leading to a wider window function. We note that the dust-filament inclination and width are the two most influential

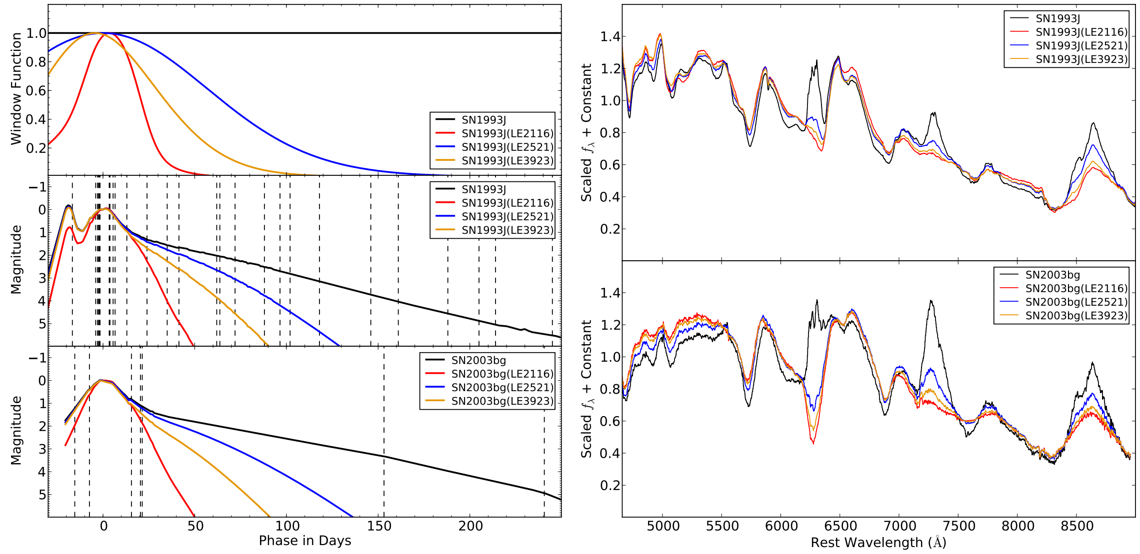

Figure 6.3: Red, cyan, and blue indicate LEs LE2521, LE3923, and LE2116, respectively. *Top left:* window function for each LE. *Middle left:* effective light curves of SN 1993J for each LE. The unmodified light curve of SN 1993J is shown in black. Epochs with spectra are indicated by the dashed lines. *Bottom left:* same as middle left, but for SN 2003bg. *Top right:* integrated SN 1993J spectra, where the integration is weighted by the respective effective light curve. Note that the black spectrum is weighted by the original, unmodified SN 1993J light curve. The differences in the spectra are mainly due to the strong lines of [O I] $\lambda\lambda$6300, 6363, [Ca II] $\lambda\lambda$7291, 7324, and the Ca II NIR triplet in the late-phase spectra. *Bottom right:* same as top right, but for SN 2003bg.

parameters affecting the window function.

The middle-left and bottom-left panels of Figure 6.3 show the effective light curves of SN 1993J and SN 2003bg, respectively. We constructed the effective light curve of SN 2003bg using the spectra and light curve in Hamuy et al. (2009). In general, the rise time of a SN is shorter than 50 days. Since the window functions have, in most cases, FWHM $\geq$ 30 days (see the top-left panel in Figure 6.3), the rising wing of the effective light curves and the real light curve are similar (see the middle-left and bottom-left panels in Figure 6.3), and consequently the impact on the integrated spectra is small. However, the decline time of a SN is significantly longer, and therefore the window function has a much more profound impact at late phases: it cuts off the contribution of spectra with phases ≥ 100 days. Even though the intrinsic brightness of the SN at late phases is much fainter than at peak, these late-phase spectra still significantly contribute to the integrated spectra since they are completely dominated by a few persistent lines. This is illustrated in the top-right and bottom-right panels of Figure 6.3, which show the integrated spectra of SN 1993J and SN 2003bg, respectively. The late-time spectra of SNe IIb such as SN 1993J and SN 2003bg are dominated by [O I] $\lambda\lambda$6300, 6363, [Ca II] $\lambda\lambda$7291, 7324, and the Ca II NIR triplet. Note that the black spectra, which are weighted by the original, unmodified light curve, are much stronger at these lines compared to the other spectra, which are integrated using the effective light curves. This figure clearly illustrates the impact and importance of the effective light curve on the contribution of the late-phase spectra to the observed integrated spectrum.

6.3.1 Integrating and Fitting the Spectral Templates to the Observed LE Spectra

We numerically integrate the spectral templates of SN 1993J (Jeffery et al., 1994; Barbon et al., 1995; Richmond et al., 1996; Fransson et al., 2005), SN 2003bg (Hamuy et al., 2009), and SN 2008ax (Chornock et al., 2010a) by weighting the individual epochs with the light curve as described by Rest et al. (2008a), with the only difference being that the real light curve is replaced with an effective light curve as described in §6.3 and in more detail by Rest et al. (2010).

Several authors have addressed the single-scattering approximation for LEs (e.g., Couderc, 1939; Chevalier, 1986; Emmering & Chevalier, 1989; Sugerman, 2003; Patat, 2005). The total surface brightness depends on parameters such as the intrinsic brightness of the event, dust density and thickness, and others. For our purposes, we only need to consider the parameters that attenuate the spectrum, which are (1) the forward scattering described by the integrated scattering function $S(\lambda, \theta)$ as derived by Sugerman (2003), and (2) the reddening due to the extinction by Galactic dust.

The attenuation by forward scattering can be determined *a priori* using the observed angular separation of the LE from Cas A. The only uncertainties introduced here are due to the assumed age and distance for Cas A. The reddening cannot be determined independently and therefore we fit for it. We fit the template spectra to the observed LE spectra with the only free parameters being the normalization and the reddening. Figure 6.4 compares the LE spectrum of LE2521 (blue line) to various SNe Ib, Ic, and II using the window function for LE2521. SN 1993J and SN 2003bg quite clearly provide the best fit.

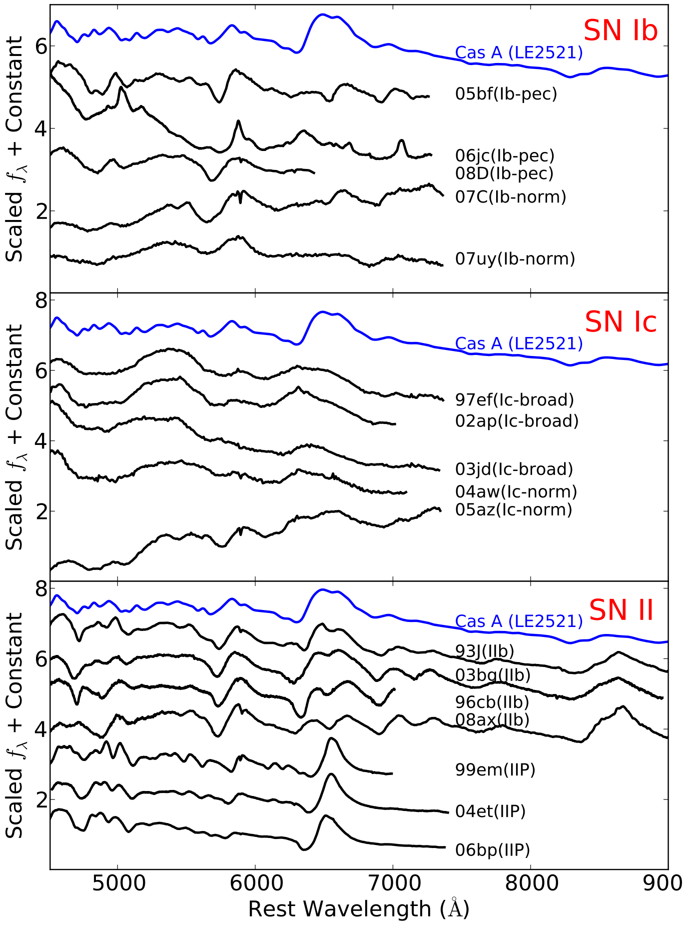

Figure 6.4: The LE spectrum of LE2521 (blue line) compared to various SNe Ib, Ic, and II using the window function shown in Figure 6.3. SN 1993J and SN 2003bg unambiguously give the best fit.

6.4 Comparison of the Cas A Light Echoes

In Figure 6.5, we present four spectra of Cas A LEs, corresponding to three different directions. LE2521 was much brighter than the other LEs, and as a result, its spectrum has a higher signal-to-noise ratio (S/N) than the others. The spectrum of LE3923 has the lowest S/N, but it still displays the same spectral features as the other spectra. All three directions have very similar spectra with the main differences being the continuum shape, which we have shown to be a result of different scattering and reddening for the various directions. The line profiles do exhibit some differences, but as shown in §6.3, different window functions can create significant differences in the spectra.

To properly compare the LEs from different directions, one must make a comparison to another SN, which removes the effect of the window function. Assuming that the window functions are correct, if a LE spectrum is the same as the integrated spectrum of a SN, then the two objects likely looked the same at maximum light (there is obviously some degeneracy between the different epochs within the window function). If the two spectra are different, then either their maximum-light spectra or light curves were likely different; regardless, it is a direct indication that the two objects appeared different along those LoS. Moreover, if one LE matches the integrated spectrum of a particular spectrum, but a LE from a different direction does not, then observers along the two LoS would have seen "different" SNe.

For Cas A, we have compared the LEs to spectra of SNe 1993J, 2003bg, and 2008ax (see Fig. 6.5). These are the best-observed SNe IIb for which we had light curves and a good time series of spectra. As described above, SN 1993J is an iconic SN IIb that was extensively observed (e.g., Filippenko et al., 1993; Richmond et al., 1994; Filippenko et al., 1994; Matheson et al., 2000) and whose progenitor system was identified in pre-explosion images (Podsiadlowski et al., 1993; Aldering et al., 1994), and its binary companion was identified through late-time spectroscopy (Maund et al., 2004). SN 2003bg was a luminous event (both optically and in the radio) with broad

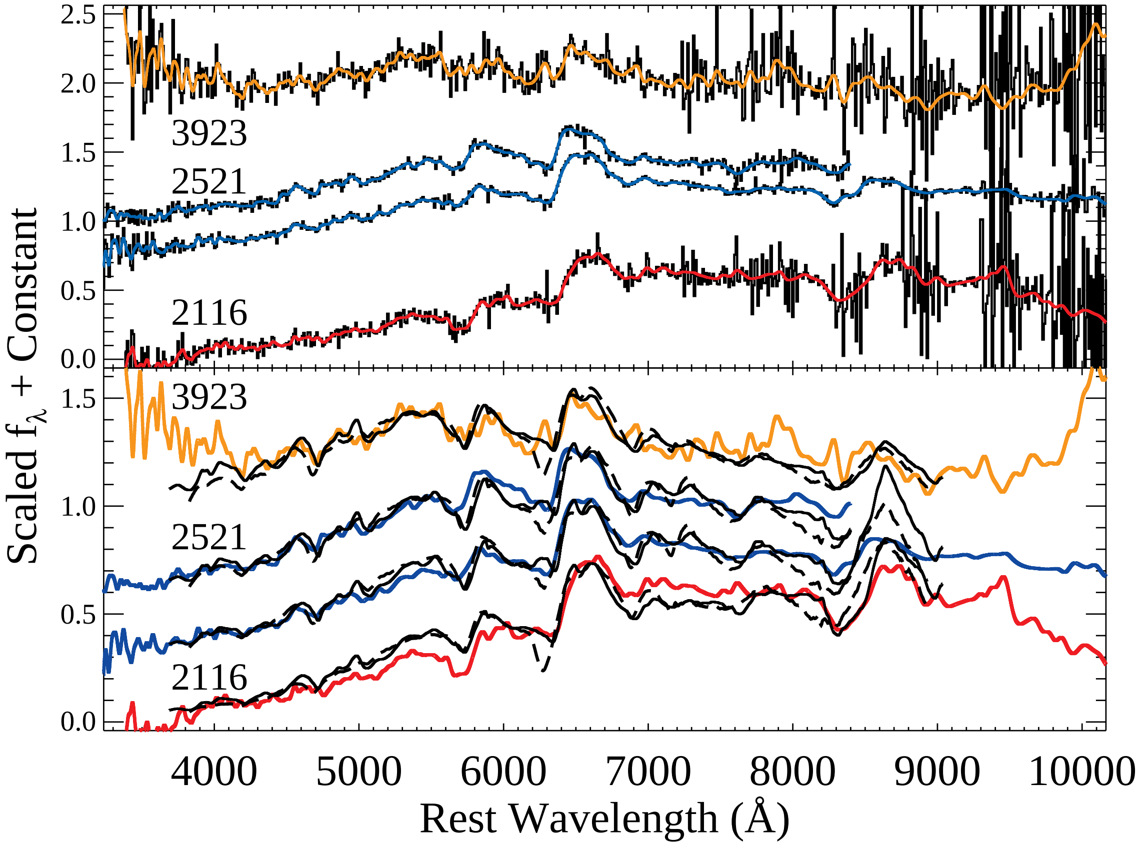

Figure 6.5: *Top panel*: observed LE spectra binned to 10 Å pixel^{-1} (black curves). The colored curves are the variance-weighted smoothed spectra with the red, blue, and orange curves corresponding to LEs LE2116, LE2521, and LE3923, respectively. The LE2521 spectrum with the shorter wavelength range is from the MMT; the remaining spectra are from Keck. *Bottom panel*: variance-weighted smoothed LE spectra (colored curves) compared to their corresponding light-curve weighted integrated SN 1993J (solid black curves) and SN 2003bg spectra (dashed black curves). The LE spectra are equivalent to the spectra in the top panel. The SNe 1993J and 2003bg spectra have been processed to reflect the dust scattering and reddening associated with each LE (see text for details). The spectra of Cas A are very similar to both SNe 1993J and 2003bg from all three directions probed; however, there are some significant differences (see §6.4).

lines at early times (Soderberg et al., 2006; Hamuy et al., 2009; Mazzali et al., 2009). SN 2008ax was discovered hours after explosion, which enabled significant follow-up observations (Pastorello et al., 2008; Roming et al., 2009; Chornock et al., 2010b), including extensive spectropolarimetry (Chornock et al., 2010b) indicating that the outer layers of the ejecta were rather aspherical. Furthermore, its progenitor system was also detected in pre-explosion images (Crockett et al., 2008).

Examining Figure 6.5, it is clear that the LE spectra in all directions are similar to each other. In addition, the LE spectra are similar to spectra of SNe 1993J and 2003bg, indicating that no dramatic differences are seen from the various directions (such as a different spectral classification). SN 2008ax is a worse match to the LEs, having significantly weaker Hα emission than the other objects. Since our spectral series of SN 2008ax (both CfA and published spectra from Chornock et al. 2010b) is not as exhaustive as that of SNe 1993J and 2003bg, we do not know if the differences are intrinsic or the result of incomplete data. Because of the poor match and the differences not necessarily being physical, as well as for clarity, we do not show in Figure 6.5 the comparison spectra generated from SN 2008ax.

Despite all LEs being quite similar, a detailed comparison of the LE line profiles to those of SN 1993J in Figure 6.6 indicates that while two directions (LE2116 and LE3923) are consistent with the line velocities of SN 1993J, one direction (LE2521) has higher-velocity absorption for the He I λ5876 and Hα features. Specifically, the minima of the features are blueshifted by an additional 4000 and 3000 km s^{-1}, respectively. In addition to the blueshifted absorption minima, the entire profile of the features seems to be shifted blueward, including the emission component of the P-Cygni profile. The Ca II NIR triplet may have a slightly larger velocity for LE2521 than in the other directions, but this does not appear to be significant. We estimate that the uncertainties in these lines are small and not significantly more than $\sim$100 km s^{-1}.

Interestingly, the comparison spectra from SN 2003bg show Hα velocities that are larger than those of Cas A for LE2116 and LE3923, but the velocity matches that of Cas A for LE2521. For this direction, the profile shape is also matched. The LE2521 He I velocity (and full profile) appears to be larger than that of SN 2003bg, which

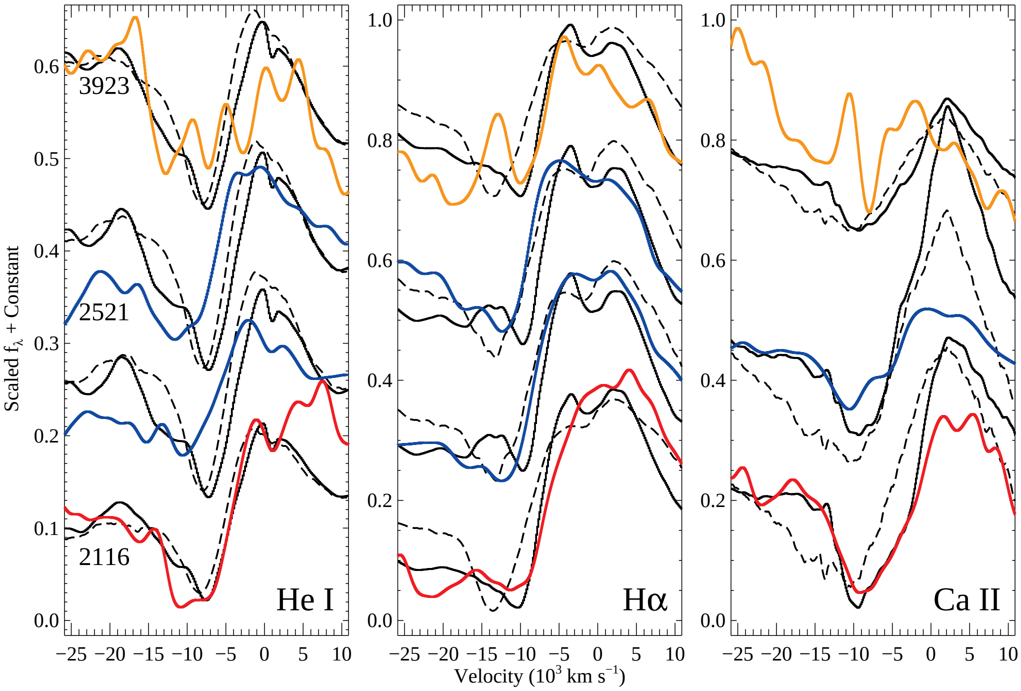

Figure 6.6: Observed LE spectra near the He I λ5876 (left), Hα (middle), and Ca II NIR triplet (right) features, shown on a velocity scale. The red, blue, and orange curves correspond to LEs LE2116, LE2521, and LE3923, respectively (see Fig. 6.5 for details). The top LE2521 spectrum (which is not shown in the right-hand panel) is from the MMT; the remaining spectra are from Keck. The solid and dashed black curves are the corresponding light-curve weighted integrated spectra of SNe 1993J and 2003bg, respectively.

has a similar velocity to that of SN 1993J. This indicates that although SN 2003bg is an excellent match to the Hα feature of LE2521, there are still differences, and SN 2003bg is not a perfect analog. SN 2003bg has a slightly higher velocity for the Ca II NIR triplet than SN 1993J, which makes it more consistent with LE2521, but we reiterate that the difference is not significant.

6.5 Comparison of the Light Echoes to the SNR structure

The structure of the Cas A SNR is very complex — from the large scales, which show spatially distinct Fe-rich and Si-rich regions, to the small scales, which are dominated by many filaments and bright knot-like features in the optical and X-ray bands. Overall, the ejecta emission from the SNR appears very turbulent and inhomogeneous, similar to other remnants of core-collapse SNe (e.g., G292.0+1.8, Park et al., 2007). Hughes et al. (2000) argue that the ejecta have overturned during the explosion, since the Fe-rich material is ahead of the Si-rich material in the southeast (SE; however, see DeLaney et al., 2010). The Si-rich regions in the northeast (NE) and southwest (SW) show structure that was interpreted by Hwang et al. (2004) as indicative of a bipolar jet system. These "jet-like" outflows were also seen by Fesen et al. (2006a) in the *Hubble Space Telescope (HST)* census of fast-moving optical knots of the intermediate-mass elements N II and O II, further supporting this NE–SW bipolar jet interpretation.

While this "jet-counterjet" structure is clearly a directional outflow associated with the ejecta (and not the result of some pre-existing bipolar cavity in the circumstellar medium; e.g., Blondin et al., 1996), it seems that the outflow was not energetic enough to power the entire explosion (Laming et al., 2006). In addition, the projected motion of the compact object detected in the X-rays (Tananbaum, 1999; Fesen et al., 2006b), thought to be the neutron star or black hole created by the explosion, is perpendicular to the NE–SW outflows. Most jet-powered explosion models predict that the neutron-star kick would be roughly aligned with the jet axis. Furthermore, the Fe-rich outflows are concentrated into two regions in the SE and NW (Hughes et al., 2000; Willingale et al., 2002; Dewey et al., 2007), with the SE outflow blueshifted and the NW outflow redshifted (Willingale et al., 2002). This has given rise to a new picture that there is an axis in the Cas A SNR from the SE to the NW at a position angle of ∼125° aligned with the Fe-rich knots. In this model, the Si-rich structures to the NE and SW are only secondary features caused by instability-powered flows from an equatorial torus (Burrows et al., 2005; Wheeler et al., 2008).

In a recent study, DeLaney et al. (2010) used the technique of Doppler imaging to give the most complete and updated three-dimensional (3D) model. This model is derived from IR (*Spitzer*), optical (ground-based and *HST*), and X-ray (*Chandra*) data. DeLaney et al. (2010) used velocity information from specific spectral features to deproject the structure of the SNR along the radial direction perpendicular to the plane of the sky (see their §2, §3, and §4 for details of the data reduction and deprojection techniques). Their work reveals a very complex 3D structure that can be characterized by a spherical component, a tilted "thick disk," and multiple ejecta outflows. In their model, the thick disk is tilted from the plane of the sky at an angle of ∼25° from the E–W axis and ∼30° from the N–S axis. This thick disk contains all the ejecta structures, including the most prominent outflows that show up best in X-ray Fe K emission, but also appear in other datasets. Infrared emission in the [Ar II] and [Ne II] lines often reveals ring-like structures, which are sometimes seen as broken rings, at the base of these outflows. DeLaney et al. (2010) note that these rings appear at the intersection between the thick-disk structures and a roughly spherical reverse shock. Some of the outflows are bipolar, with oppositely directed flows about the expansion center, while others are not. In particular, the blueshifted emission from the Fe-rich outflow in the SE is clearly collimated, but the corresponding redshifted emission in the NW is not.

The 3D analysis by DeLaney et al. (2010) suggests that the Cas A SN explosion was highly asymmetric, with most of the ejecta flattened in a thick disk that is slightly tilted from the plane of the sky and no prominent structures perpendicular to the plane of the sky. It is possible that this might be due to selection effects, at least to some extent, because limb brightening will make structures close to the plane of the sky easier to detect, but given the quality of the individual datasets, it is unlikely that any prominent outflows along the radial direction would have been missed completely by DeLaney et al. (2010).

In Figure 6.7, we superimpose the LoS from our LEs onto three of the [Ar II] and Fe K datasets from DeLaney et al. (2010). The thick disk is apparent in the structure of the SNR as seen from the positive N axis (middle panel of Fig. 6.7), and (to a lesser extent) the positive E axis (right panel of Fig. 6.7). Among our observed LEs, LE2116 and LE3923 are sampling LoS away from this disk, and do not intersect any prominent ejecta structures. The LoS of LE2521, on the other hand, intersects the edge of the large complex of Fe K emission in the NW that is at the edge of the thick disk.

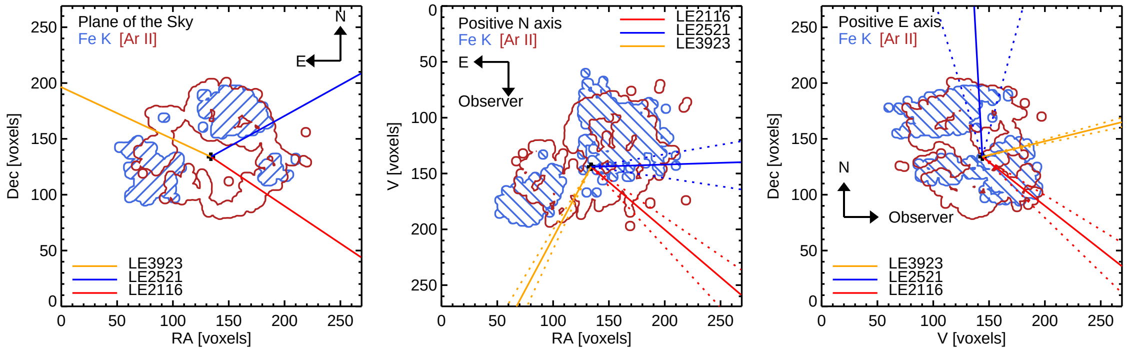

Figure 6.7: Three-dimensional [Ar II] (red) and Fe K (blue) datasets from DeLaney et al. (2010). The datasets are viewed from Earth's perspective (as they appear on the plane of the sky, left panel), from above (from a point along the positive N axis, middle panel), and sideways (from a point along the positive E axis, right panel). The datasets are represented in discrete voxels (volumetric pixels), roughly $0.2''$ on a side (see DeLaney et al., 2010, for details). The expansion center is represented by a black cross in all three panels. The LE directions are shown for the fiducial distance of 3.4 kpc (solid lines), and for reasonable upper and lower limits, respectively 4.0 and 3.0 kpc (dotted lines).

6.6 Discussion

6.6.1 Systematic Effects

To properly assess differences in the LE spectra, we have compared each LE to light-curve and window-function weighted spectra of well-studied SNe. When assessing the similarities of a LE to another SN, this process is straightforward. However, when comparing different LEs by examining their similarities to other SNe, there are potential systematic effects.

6.6.1.1 Window Functions and Comparison Objects

When making integrated comparison spectra, the light curve and spectra of that particular SN are used. If that object is not a perfect analog of Cas A, then different window functions can introduce apparent differences between the LEs. As an extreme example, consider two window functions: one which is a top hat only covering the premaximum portion of the light curve, and another top hat only covering the post-maximum portion of the light curve. If the comparison SN had lower line velocities than Cas A before maximum brightness, but similar line velocities after maximum, the comparison spectra would indicate a difference for the two LEs.

For the LEs presented here, the window functions are not significantly different. In Figure 6.3, we see that the major differences are the contribution of the light curve 50–140 days after maximum brightness. One main source of uncertainty in the window function is caused by the uncertainty in the dust inclination. The dust inclination is derived from the apparent motion. In particular, for faint LEs, the uncertainty in the apparent motion can introduce uncertainties in the inclination of $\sim 5^\circ$ (Rest et al., 2010). We have not yet fully explored all ways to improve how we determine the dust inclination, and we hope that better modeling will further reduce its uncertainty in the future. Another source of uncertainty is caused by imperfections in the light-echo profile modeling and thus the dust width caused by substructure in the dust. This can be tested with the SN 1987A LEs (Kunkel et al., 1987; Crotts, 1988; Suntzeff et al., 1988), since the spectrophotometric evolution of the SN itself has been monitored extensively. We show in Rest et al. (2010) and Sinnott et al. (2011) that the observed LE profile, apparent motion, and spectra can all be brought in excellent accordance with what is predicted using the SN 1987A spectrophotometric library.

Figure 6.3 shows how the window functions change the integrated spectra, including a flat window function, corresponding to the full light-curve weighted integrated spectrum. The most significant differences occur at the positions of nebular emission lines, particularly [O I] $\lambda\lambda$6300, 6363, [Ca II] $\lambda\lambda$7291, 7324, and the Ca II NIR triplet.

The Hα line is most affected by the [O I] feature. For SN 1993J, as [O I] becomes more prominent, it can make the velocity of the minimum of the Hα absorption appear lower, which may affect our interpretation of this feature for Cas A. However, it does not affect the blue edge of the emission feature. For SN 2003bg, the Hα absorption is at a higher velocity, coinciding almost exactly with the peak of the [O I] emission. As a result, the differences in window functions do not dramatically change the apparent velocity of the Hα absorption, but rather just affect its strength.

For both SNe 1993J and 2003bg, the He I feature does not change much with different window functions. There is a noticeable change in the spectra between those with the measured window functions and the full light-curve weighted spectrum. The full light-curve weighted spectrum has a slightly lower velocity for both SNe 1993J and 2003bg.

Although we cannot rule out that the window function has created the differences seen in Cas A, that scenario requires particular tuning. One way this could happen is if Cas A changes from a SN 1993J-like spectrum to a higher-velocity spectrum from about 80 days after maximum, when the window functions for LE2116 and LE3923 are 6 mag below peak, significantly less than the window function of LE2521. In addition, most of the flux at these late phases needs to be in Hα and He I instead of the nebular emission lines, which is physically unlikely for SNe IIb. Then the integrated spectrum of SN 1993J could show a lower velocity than LE2521 while still having the same velocity for the other directions. Additional comparison objects and LE spectra with different window functions should address this potential systematic effect.

6.6.2 Connection to Explosion Models

The LE data alone suggest that Cas A was an asymmetric SN. As outlined in §6.5, this is consistent with observations of the SNR, which indicate the existence of a rich set of multiple outflows (e.g., Hughes et al., 2000; Willingale et al., 2002; Fesen et al., 2006a). The most prominent are bipolar Fe-rich outflows in the SE and NW that are blueshifted and redshifted, respectively. These outflows are approximately (but not exactly) aligned along a single axis through the kinematic center of the SNR (Burrows et al., 2005; Wheeler et al., 2008; DeLaney et al., 2010). The combination of LE and SNR data paint a coherent picture of the SN, and further connect observations to the explosion.

Our detection of blueshifted Hα and He I emission from the direction of the NW outflow (LE2521) is the first direct connection between significantly higher kinetic energy per unit mass in the SN explosion in one direction and outflows observed in the SNR. Additionally, the NW outflow that seems to be associated with LE2521 is in roughly the opposite direction of the apparent motion of a compact X-ray source, which is presumed to be the resulting neutron star (NS). From the position of the NS relative to the kinematic center of the SNR and the age of the SNR, Fesen et al. (2006a) determined that the object is moving at 350 $\mathrm{km\,s^{-1}}$ in the plane of the sky with a position angle of $169° \pm 8.4°$. A simple explanation of both the high-velocity ejecta in the direction of LE2521 and the NS kick direction and velocity is an inherently asymmetric explosion.

Although this alignment could be coincidental, it may provide a key clue to understanding core-collapse SN explosions. In particular, these observations indicate that the explosion mechanism may be directly connected to the observed SN — a nontrivial statement considering the size scales between the core and outer envelope of the star.

One model to give the NS a kick is the ejecta-driven mechanism, in which asymmetry in density before the collapse leads to an asymmetric explosion. This gives the protoneutron star a kick in the opposite direction than the ejecta, as in the rocket effect (Burrows & Hayes, 1996; Fryer, 2004). However, if neutrino-driven kicks help drive the supernova explosion, then the strongest ejecta motion can be in the direction of the NS, and opposite the direction of the neutrinos (Fryer & Kusenko, 2006; Socrates et al., 2005).

Numerical models have shown that large asymmetric instabilities can occur near the core during collapse (e.g., Blondin et al., 2003; Burrows et al., 2007; Marek & Janka, 2009). These instabilities can be imprinted on both the SN ejecta and NS by aligning high-velocity ejecta along the same axis as the NS kick. 3D models have only recently been explored, and the models have not been extended to examine the effects of this mechanism on the composition, density, or velocity structure of the ejecta. Nonetheless, these mechanisms are an example of a possible way to directly connect the NS kick with an asymmetric velocity in the ejecta.

To determine if the alignment of the NS kick and higher-velocity ejecta can be physically explained, we perform a simple calculation using the ejecta-driven model. If we assume that in the direction of the NS's motion the ejecta velocity is the same as in the lower-velocity directions we have measured, and that the momentum of the NS is equal to the excess momentum of the ejecta in the opposite direction, we can measure the mass of ejecta at higher velocity. The velocity difference is ~4000 km s^{-1} for the different LoS. We also assume that $1\mathrm{M}_\odot \leq M_{\mathrm{NS}} \leq 2\mathrm{M}_\odot$. Then we have

$$M_{\mathrm{HV\,ej}} \approx 0.09 \left(\frac{v_{\mathrm{NS}}}{350\,\mathrm{km\,s^{-1}}}\right) \left(\frac{4000\,\mathrm{km\,s^{-1}}}{\Delta v_{\mathrm{HV\,ej}}}\right) M_{\mathrm{NS}}. \tag{6.1}$$

For our assumed NS mass, we find that the amount of material moving at the higher velocity would be $0.09 \lesssim M_{\mathrm{HV\,ej}} \lesssim 0.18\,\mathrm{M}_{\odot}$. This mass estimate assumes that the radial velocity of the NS is zero. Although the radial velocity could be quite large, it is likely of order the transverse velocity, and will not affect our mass estimate by more than a factor of a few. Similarly, we have assumed that the velocity difference in the ejecta is the total velocity difference, but there could be a significant component perpendicular to our line of sight.

Willingale et al. (2003) determined that the Cas A SNR had a total mass of 2.2 $\mathrm{M}_{\odot}$ with $\sim$0.4 $\mathrm{M}_{\odot}$ of fast-moving ejecta having an initial velocity of 15,000 km s^{-1}, consistent with our measured velocity but slightly higher than our estimated mass of high-velocity material. Willingale et al. (2003) claim that ~90% of the kinetic energy of the SN was at the highest velocities, which seems inconsistent with SN explosion models. If the Cas A SN explosion was similar to these models, which expect most of the kinetic energy to be at lower velocities (e.g., $\sim$ 6000 km s^{-1}), then the lower mass estimate for the high-velocity material seems reasonable. This implies a kinetic energy of $\sim 2 \times 10^{50}$ erg located in high-velocity material. The estimate of the kinetic energy of Cas A is $\sim(2\text{–}3)\times10^{51}$ erg (Laming & Hwang, 2003) for an ejected mass of $\sim 2\mathrm{M}_{\odot}$. These values are very similar to those derived for SN 2006aj, the SN Ic associated with the X-ray flash GRB 060218 (e.g., Pian et al., 2006) and which Mazzali et al. (2006) suggested to have been the result of a magnetar event. The analogy with the properties of Cas A and the orientation of the motion of the NS suggests that the Cas A SN may have produced a magnetar. This would justify the higher-than average kinetic energy of Cas A.

A further constraint for explosion models is the different velocities of H, He, and Ca for LE2521 relative to SNe 1993J and 2003bg. SNe 1993J and 2003bg have similar velocities for the Ca II NIR triplet, and both are consistent with that of LE2521. The Hα velocity of SN 2003bg is significantly larger than that of SN 1993J, and is consistent with that of LE2521. However, SNe 1993J and 2003bg have similar velocities for He I, with SN 2003bg having a slightly larger velocity. Conversely, LE2521 has a much larger He I velocity than that of either comparison object.

There are several ways to explain the velocity structure. First, since all spectra appear to have similar velocities for Ca II, it is likely that the feature is forming in a more symmetric region of the ejecta. The small differences between the LEs and the relatively low velocities of the feature suggest that the Ca-emitting region is more central than that of H or He, and that the central region of the ejecta is more symmetric than the outer layers.

There are several explanations for the He I velocity being higher than that of SN 2003bg, which had the same Hα velocity of LE2521. In Cas A the H layer may have been extremely thin (thinner than in either SN 1993J or SN 2003bg), causing the H and He velocities to be coincident. Alternatively, the Cas A He layer may be more mixed into the hydrogen layer than in SN 2003bg, causing He I to have a velocity similar to that of Hα. Finally, the ^{56}Ni distribution may have been different in the two objects, causing a different ionization structure in the outer ejecta.

6.7 Conclusions

We have obtained optical spectra of LEs from three different perspectives of the Cas A SN, effectively probing different regions of the SN photosphere — the first time that this technique has been applied to a SN. The spectra are very similar to each other and are all similar to the prototypical SN IIb 1993J. After accounting for the window function determined by the combination of dust inclination and slit orientation, we are able to precisely compare Cas A to other SNe as well as compare the LEs to each other. From these comparisons, two of the three directions have spectra which are indistinguishable from that of SN 1993J; however, one direction has He I and Hα P-Cygni features that are significantly blueshifted ($\sim$4000 km s^{-1}) relative to SN 1993J and the other two directions, indicating a higher ejecta velocity from Cas A *in that one direction*. This is direct and independent evidence of an asymmetric explosion.

The spectrum for the discrepant LE has an Hα line profile consistent with that of the high-luminosity SN IIb 2003bg, but its He I λ5876 line profile had an even higher velocity than that of SN 2003bg. This may indicate that Cas A had a very thin hydrogen layer, significant ejecta mixing, or different ionization structure in this direction. All LE spectra have Ca II NIR triplet line profiles consistent with each other as well as with those of SNe 1993J and 2003bg. This suggests that the emitting region of the Ca is distributed more spherically than that of the H or He-emitting regions.

Even though there seems to be a "jet-like" structure in the NE corner and a counterjet in the SW corner (Hwang et al., 2004; Fesen et al., 2006a), recent optical and X-ray data from the Cas A SNR indicate that the dominant Cas A SN outflow is in the SE at a position angle of $\sim$115°, slightly tilted toward the observer, and its counterpart approximately on the opposite side (Burrows et al., 2005; Wheeler et al., 2008; DeLaney et al., 2010). Our detection of a blueshift looking into the counter outflow in the NW corner is the first direct, unambiguous, and independent confirmation of this outflow. It is also in excellent agreement with the apparent motion of the compact object, which moves at a position angle of $169° \pm 8.4°$ (Tananbaum, 1999; Fesen et al., 2006b) away from the center of the SNR.

Finally, we note that the existing surveys for LE features in this portion of the Galactic plane are far from complete, and that additional LEs are very likely to be discovered, providing additional perspectives of the SN in three dimensions. The inventory of such features will further illuminate the degree of asymmetry of the SN, but will also serve the purpose of testing the degree of coherence of spectra from similar perspectives. Since the spectrum at a given dust-concentration location is the result of integration over an entire hemisphere of SN photosphere, spectral differences are expected to vary slowly with changes in the perspective angle.

6.8 Acknowledgments

We thank A. Becker, A. Clocchiatti, A. Garg, M. Wood-Vasey, and the referee for useful comments that helped improve the manuscript. We are grateful to B. Jannuzi and H. Schweiker for taking images with the KPNO 4 m telescope prior to the design of the Keck slit masks, to J. M. Silverman for assistance with the Keck observations, and to T. Delaney for giving us access to her manuscript and 3D data for the structure of Cas A before publication. A.R. thanks the Goldberg Fellowship Program for its support. D.W. acknowledges support from the Natural Sciences and Engineering Research Council of Canada (NSERC). C.B. acknowledges the Benoziyo Center for Astrophysics for support at the Weizmann Institute of Science. D.M. is supported by grants from FONDAP CFA 15010003, BASAL CATA PFB-06, and MIDEPLAN MWM P07-021-F. R.P.K is grateful for the support of NSF grant AST-0907903. A.V.F. is grateful for the support of NSF grant AST-0908886, the TABASGO Foundation, and NASA grant GO-11114 from the Space Telescope Science Institute, which is operated by AURA, Inc., under NASA contract NAS 5-26555.

Some of the observations were obtained with the Apache Point Observatory 3.5 m telescope, which is owned and operated by the Astrophysical Research Consortium. Part of the data presented herein were obtained at the W. M. Keck Observatory, which is operated as a scientific partnership among the California Institute of Technology, the University of California, and NASA; the observatory was made possible by the generous financial support of the W. M. Keck Foundation. The authors wish to recognize and acknowledge the very significant cultural role and reverence that the summit of Mauna Kea has always had within the indigenous Hawaiian community; we are most fortunate to have the opportunity to conduct observations from this mountain.

Bibliography

Aldering, G. and Humphreys, R. M. and Richmond, M. 1994, AJ, 107, 662

Ashworth, W. B., Jr. 1980, Journal for the History of Astronomy, 11, 1

Badenes, C. and Hughes, J. P. and Cassam-Chenaï, G. and Bravo, E. 2008, ApJ, 680, 1149

Barbon, R. and Benetti, S. and Cappellaro, E. and Patat, F. and Turatto, M. and Iijima, T. 1995, A&AS, 110, 513

Blondin, J. M. and Lundqvist, P. and Chevalier, R. A. 1996, ApJ, 472, 257

Blondin, J. M. and Mezzacappa, A. and DeMarino, C. 2003, ApJ, 584, 971

Burrows, A. and Hayes, J. 1996, Physical Review Letters, 76, 352

Burrows, A. and Livne, E. and Dessart, L. and Ott, C. D. and Murphy, J. 2007, ApJ, 655, 416

Burrows, A. and Walder, R. and Ott, C. D. and Livne, E. 2005, in Astronomical Society of the Pacific Conference Series, Vol. 332, The Fate of the Most Massive Stars, ed. R. Humphreys & K. Stanek, 350

Chevalier, R. A. 1986, ApJ, 308, 225

Chornock, R. and Filippenko, A. V. and Li, W. and Marion, G. H. and Foley, R. J. and Modjaz, M. and Rafelski, M. and Becker, G. D. and de Vries, W. H. and Garnavich, P. and Jorgenson, R. A. and Lynch, D. K. and Malec, A. L. and Moran, E. C. and Murphy, M. T. and Rudy, R. J. and Russell, R. W. and Silverman, J. M. and Steele, T. N. and Stockton, A. and Wolfe, A. M. and Woodward, C. E. 2010a, ArXiv e-prints, 1001.2775

——. 2010b, ArXiv e-prints, 1001.2775

Couderc, P. 1939, Annales d'Astrophysique, 2, 271

Crockett, R. M. and Eldridge, J. J. and Smartt, S. J. and Pastorello, A. and Gal-Yam, A. and Fox, D. B. and Leonard, D. C. and Kasliwal, M. M. and Mattila, S. and Maund, J. R. and Stephens, A. W. and Danziger, I. J. 2008, MNRAS, 391, L5

Crotts, A. 1988, IAU Circ., 4561, 4

DeLaney, T. and Rudnick, L. and Stage, M. D. and Smith, J. D. and Isensee, K. and Rho, J. and Allen, G. E. and Gomez, H. and Kozasa, T. and Reach, W. T. and Davis, J. E. and Houck, J. C. 2010, ApJ, 725, 2038

Dewey, D. and Delaney, T. and Lazendic, J. S. 2007, in Revista Mexicana de Astronomia y Astrofisica Conference Series, Vol. 30, Revista Mexicana de Astronomia y Astrofisica Conference Series, 84

Dwek, E. and Arendt, R. G. 2008, ApJ, 685, 976

Emmering, R. T. and Chevalier, R. A. 1989, ApJ, 338, 388

Fesen, R. A. and Hammell, M. C. and Morse, J. and Chevalier, R. A. and Borkowski, K. J. and Dopita, M. A. and Gerardy, C. L. and Lawrence, S. S. and Raymond, J. C. and van den Bergh, S. 2006a, ApJ, 645, 283

Fesen, R. A. and Pavlov, G. G. and Sanwal, D. 2006b, ApJ, 636, 848

Filippenko, A. V. and Matheson, T. and Barth, A. J. 1994, AJ, 108, 2220

Filippenko, A. V. and Matheson, T. and Ho, L. C. 1993, ApJ, 415, L103

Foley, R. J. and Papenkova, M. S. and Swift, B. J. and Filippenko, A. V. and Li, W. and Mazzali, P. A. and Chornock, R. and Leonard, D. C. and Van Dyk, S. D. 2003, PASP, 115, 1220

Fransson, C. and Challis, P. M. and Chevalier, R. A. and Filippenko, A. V. and Kirshner, R. P. and Kozma, C. and Leonard, D. C. and Matheson, T. and Baron, E. and Garnavich, P. and Jha, S. and Leibundgut, B. and Lundqvist, P. and Pun, C. S. J. and Wang, L. and Wheeler, J. C. 2005, ApJ, 622, 991

Fryer, C. L. 2004, ApJ, 601, L175

Fryer, C. L. and Kusenko, A. 2006, ApJS, 163, 335

Garg, A. and Stubbs, C. W. and Challis, P. and Wood-Vasey, W. M. and Blondin, S. and Huber, M. E. and Cook, K. and Nikolaev, S. and Rest, A. and Smith, R. C. and Olsen, K. and Suntzeff, N. B. and Aguilera, C. and Prieto, J. L. and Becker, A. and Miceli, A. and Miknaitis, G. and Clocchiatti, A. and Minniti, D. and Morelli, L. and Welch, D. L. 2007, AJ, 133, 403

Hamuy, M. and Deng, J. and Mazzali, P. A. and Morrell, N. I. and Phillips, M. M. and Roth, M. and Gonzalez, S. and Thomas-Osip, J. and Krzeminski, W. and Contreras, C. and Maza, J. and González, L. and Huerta, L. and Folatelli, G. and Chornock, R. and Filippenko, A. V. and Persson, S. E. and Freedman, W. L. and Koviak, K. and Suntzeff, N. B. and Krisciunas, K. 2009, ApJ, 703, 1612

Horne, K. 1986, PASP, 98, 609

Hughes, J. P. and Rakowski, C. E. and Burrows, D. N. and Slane, P. O. 2000, ApJ, 528, L109

Hwang, U. and Laming, J. M. and Badenes, C. and Berendse, F. and Blondin, J. and Cioffi, D. and DeLaney, T. and Dewey, D. and Fesen, R. and Flanagan, K. A. and Fryer, C. L. and Ghavamian, P. and Hughes, J. P. and Morse, J. A. and Plucinsky, P. P. and Petre, R. and Pohl, M. and Rudnick, L. and Sankrit, R. and Slane, P. O. and Smith, R. K. and Vink, J. and Warren, J. S. 2004, ApJ, 615, L117

Jeffery, D. J. and Kirshner, R. P. and Challis, P. M. and Pun, C. S. J. and Filippenko, A. V. and Matheson, T. and Branch, D. and Chevalier, R. A. and Fransson, C. and Panagia, N. and Wagoner, R. V. and Wheeler, J. C. and Clocchiatti, A. 1994, ApJ, 421, L27

Kamper, K. W. 1980, The Observatory, 100, 3

Krause, O. and Birkmann, S. M. and Usuda, T. and Hattori, T. and Goto, M. and Rieke, G. H. and Misselt, K. A. 2008, Science, 320, 1195

Krause, O. and Rieke, G. H. and Birkmann, S. M. and Le Floc'h, E. and Gordon, K. D. and Egami, E. and Bieging, J. and Hughes, J. P. and Young, E. T. and Hinz, J. L. and Quanz, S. P. and Hines, D. C. 2005, Science, 308, 1604

Kunkel, W. and Madore, B. and Shelton, I. and Duhalde, O. and Bateson, F. M. and Jones, A. and Moreno, B. and Walker, S. and Garradd, G. and Warner, B. and Menzies, J. 1987, IAU Circ., 4316, 1

Laming, J. M. and Hwang, U. 2003, ApJ, 597, 347

Laming, J. M. and Hwang, U. and Radics, B. and Lekli, G. and Takács, E. 2006, ApJ, 644, 260

Marek, A. and Janka, H.-T. 2009, ApJ, 694, 664

Matheson, T. and Filippenko, A. V. and Ho, L. C. and Barth, A. J. and Leonard, D. C. 2000, AJ, 120, 1499

Maund, J. R. and Smartt, S. J. and Kudritzki, R. P. and Podsiadlowski, P. and Gilmore, G. F. 2004, Nature, 427, 129

Mazzali, P. A. and Deng, J. and Hamuy, M. and Nomoto, K. 2009, ApJ, 703, 1624

Mazzali, P. A. and Deng, J. and Nomoto, K. and Sauer, D. N. and Pian, E. and Tominaga, N. and Tanaka, M. and Maeda, K. and Filippenko, A. V. 2006, Nature, 442, 1018

Miknaitis, G. and Pignata, G. and Rest, A. and Wood-Vasey, W. M. and Blondin, S. and Challis, P. and Smith, R. C. and Stubbs, C. W. and Suntzeff, N. B. and Foley, R. J. and Matheson, T. and Tonry, J. L. and Aguilera, C. and Blackman, J. W. and Becker, A. C. and Clocchiatti, A. and Covarrubias, R. and Davis, T. M. and Filippenko, A. V. and Garg, A. and Garnavich, P. M. and Hicken, M. and Jha, S. and Krisciunas, K. and Kirshner, R. P. and Leibundgut, B. and Li, W. and Miceli, A. and Narayan, G. and Prieto, J. L. and Riess, A. G. and Salvo, M. E. and Schmidt, B. P. and Sollerman, J. and Spyromilio, J. and Zenteno, A. 2007, ApJ, 666

Oke, J. B. and Cohen, J. G. and Carr, M. and Cromer, J. and Dingizian, A. and Harris, F. H. and Labrecque, S. and Lucinio, R. and Schaal, W. and Epps, H. and Miller, J. 1995, PASP, 107, 375

Park, S. and Hughes, J. P. and Slane, P. O. and Burrows, D. N. and Gaensler, B. M. and Ghavamian, P. 2007, ApJ, 670, L121

Pastorello, A. and Kasliwal, M. M. and Crockett, R. M. and Valenti, S. and Arbour, R. and Itagaki, K. and Kaspi, S. and Gal-Yam, A. and Smartt, S. J. and Griffith, R. and Maguire, K. and Ofek, E. O. and Seymour, N. and Stern, D. and Wiethoff, W. 2008, MNRAS, 389, 955

Patat, F. 2005, MNRAS, 357, 1161

Pian, E. and Mazzali, P. A. and Masetti, N. and Ferrero, P. and Klose, S. and Palazzi, E. and Ramirez-Ruiz, E. and Woosley, S. E. and Kouveliotou, C. and Deng, J. and Filippenko, A. V. and Foley, R. J. and Fynbo, J. P. U. and Kann, D. A. and Li, W. and Hjorth, J. and Nomoto, K. and Patat, F. and Sauer, D. N. and Sollerman, J. and Vreeswijk, P. M. and Guenther, E. W. and Levan, A. and O'Brien, P. and Tanvir, N. R. and Wijers, R. A. M. J. and Dumas, C. and Hainaut, O. and Wong, D. S. and Baade, D. and Wang, L. and Amati, L. and Cappellaro, E. and Castro-Tirado, A. J. and Ellison, S. and Frontera, F. and Fruchter, A. S. and Greiner, J. and Kawabata, K. and Ledoux, C. and Maeda, K. and Møller, P. and Nicastro, L. and Rol, E. and Starling, R. 2006, Nature, 442, 1011

Podsiadlowski, P. and Hsu, J. J. L. and Joss, P. C. and Ross, R. R. 1993, Nature, 364, 509

Rest, A. and Becker, A. C. and Bergmann, M. and Blondin, S. and Challis, P. and Clocchiatti, A. and Cook, K. H. and Damke, G. and Garg, A. and Huber, M. E. and Lanning, H. and Matheson, T. and Minniti, D. and Morelli, L. and Nikolaev, S. and Olsen, K. and Oasterle, L. and Pignata, G. and Prieto, J. and Smith, R. C. and Stubbs, C. and Suntzeff, N. B. and Welch, D. L. and Wood-Vasey, W. M. and Zenteno, A. 2007, in Bulletin of the American Astronomical Society, Vol. 38, 935

Rest, A. and Matheson, T. and Blondin, S. and Bergmann, M. and Welch, D. L. and Suntzeff, N. B. and Smith, R. C. and Olsen, K. and Prieto, J. L. and Garg, A. and Challis, P. and Stubbs, C. and Hicken, M. and Modjaz, M. and Wood-Vasey, W. M. and Zenteno, A. and Damke, G. and Newman, A. and Huber, M. and Cook, K. H. and Nikolaev, S. and Becker, A. C. and Miceli, A. and Covarrubias, R. and Morelli, L. and Pignata, G. and Clocchiatti, A. and Minniti, D. and Foley, R. J. 2008a, ApJ, 680, 1137

Rest, A. and Sinnott, B. and Welch, D. L. 2011, in prep.

Rest, A. and Sinnott, B. and Welch, D. L. and Foley, R. J. and Narayan, G. and Mandel, K. 2010, ArXiv e-prints, 1004.3783

Rest, A. and Stubbs, C. and Becker, A. C. and Miknaitis, G. A. and Miceli, A. and Covarrubias, R. and Hawley, S. L. and Smith, R. C. and Suntzeff, N. B. and Olsen, K. and Prieto, J. L. and Hiriart, R. and Welch, D. L. and Cook, K. H. and Nikolaev, S. and Huber, M. and Prochtor, G. and Clocchiatti, A. and Minniti, D. and Garg, A. and Challis, P. and Keller, S. C. and Schmidt, B. P. 2005a, ApJ, 634, 1103

Rest, A. and Suntzeff, N. B. and Olsen, K. and Prieto, J. L. and Smith, R. C. and Welch, D. L. and Becker, A. and Bergmann, M. and Clocchiatti, A. and Cook, K. and Garg, A. and Huber, M. and Miknaitis, G. and Minniti, D. and Nikolaev, S. and Stubbs, C. 2005b, Nature, 438, 1132

Rest, A. and Welch, D. L. and Suntzeff, N. B. and Oaster, L. and Lanning, H. and Olsen, K. and Smith, R. C. and Becker, A. C. and Bergmann, M. and Challis, P. and Clocchiatti, A. and Cook, K. H. and Damke, G. and Garg, A. and Huber, M. E. and Matheson, T. and Minniti, D. and Prieto, J. L. and Wood-Vasey, W. M. 2008b, ApJ, 681, L81

Richmond, M. W. and Treffers, R. R. and Filippenko, A. V. and Paik, Y. 1996, AJ, 112, 732

Richmond, M. W. and Treffers, R. R. and Filippenko, A. V. and Paik, Y. and Leibundgut, B. and Schulman, E. and Cox, C. V. 1994, AJ, 107, 1022

Roming, P. W. A. and Pritchard, T. A. and Brown, P. J. and Holland, S. T. and Immler, S. and Stockdale, C. J. and Weiler, K. W. and Panagia, N. and Van Dyk, S. D. and Hoversten, E. A. and Milne, P. A. and Oates, S. R. and Russell, B. and Vandrevala, C. 2009, ApJ, 704, L118

Ryle, M. and Smith, F. G. 1948, Nature, 162, 462

Schmidt, G. D. and Weymann, R. J. and Foltz, C. B. 1989, PASP, 101, 713

Sinnott, B. and Welch, D. and Rest, A. and Matheson, T. and Blondin, S. and Bergmann, M. and Suntzeff, N. B. and Smith, R. C. and Olsen, K. and Prieto, J. L. and Garg, A. and Challis, P. and Stubbs, C. and Hicken, M. and Modjaz, M. and Wood-Vasey, W. M. and Zenteno, A. and Damke, G. and Newman, A. and Huber, M. and Cook, K. H. and Nikolaev, S. and Becker, A. C. and Miceli, A. and Covarrubias, R. and Morelli, L. and Pignata, G. and Clocchiatti, A. and Minniti, D. and Foley, R. J. 2011, in prep.

Smith, N. and Davidson, K. and Gull, T. and Ishibashi, K. 2001, in Astronomical Society of the Pacific Conference Series, Vol. 242, Eta Carinae and Other Mysterious Stars: The Hidden Opportunities of Emission Spectroscopy, ed. T. R. Gull, S. Johannson, & K. Davidson, 117

Smith, N. and Davidson, K. and Gull, T. R. and Ishibashi, K. and Hillier, D. J. 2003, ApJ, 586, 432

Socrates, A. and Blaes, O. and Hungerford, A. and Fryer, C. L. 2005, ApJ, 632, 531

Soderberg, A. M. and Chevalier, R. A. and Kulkarni, S. R. and Frail, D. A. 2006, ApJ, 651, 1005

Stephenson, F. R. and Green, D. A. 2002, Historical Supernovae and their Remnants. International Series in Astronomy and Astrophysics, Vol. 5. Oxford: Clarendon Press

Sugerman, B. E. K. 2003, AJ, 126, 1939

Suntzeff, N. B. and Heathcote, S. and Weller, W. G. and Caldwell, N. and Huchra, J. P. 1988, Nature, 334, 135

Tananbaum, H. 1999, IAU Circ., 7246, 1

Wade, R. A. and Horne, K. 1988, ApJ, 324, 411

Wheeler, J. C. and Maund, J. R. and Couch, S. M. 2008, ApJ, 677, 1091

Willingale, R. and Bleeker, J. A. M. and van der Heyden, K. J. and Kaastra, J. S. 2003, A&A, 398, 1021

Willingale, R. and Bleeker, J. A. M. and van der Heyden, K. J. and Kaastra, J. S. and Vink, J. 2002, A&A, 381, 1039

Chapter 7

Conclusions

7.1 Summary of Contributions

The mechanism driving the explosive deaths of stars still eludes astronomers after more than 30 years of simulations. This thesis provides insight into two of the most-studied SNe in astronomy: SN 1987A and Cas A. Most importantly, however, it provides the community with a well-tested observational tool with which to observe SNe and stellar outbursts. In addition to characterizing explosions hundreds of years after the outburst has faded away, spectroscopy of multiple LEs from the same source provides direct asymmetry detections that cannot be made with traditional techniques such as spectropolarimetry. We refer to this technique of using LE spectroscopy to view a source from multiple perspectives as “3D LE spectroscopy” for the sake of brevity.

The primary contributions of Chapters 4 through 6 are twofold. First, we describe a model for interpreting spectroscopy of LEs using direct observables with minimal assumptions. We then directly test this model using high signal-to-noise LEs from SN 1987A. Secondly, we use this model to demonstrate the technique of 3D LE spectroscopy, directly observing early-epoch asymmetries in SN 1987A and Cas A.

Targeted spectroscopy of scattered LEs is an area of research still in its infancy.

Prior to this work, targeted spectroscopy of scattered LEs was performed on 6 astronomical sources, totaling 8 published spectra. Chapters 4 through 6 present over 18 LE spectra additions to the current literature, 14 of which are from the same astronomical source, SN 1987A. This latter database of spectra has allowed us to to validate theoretical interpretations of LE spectra to much greater detail than previously achieved.

To successfully interpret LE spectra, one needs to identify the relative flux contribution of each epoch in the observed integrated LE spectrum. Knowing the relative contributions is the only way to compare LE spectra to one another or to other sources. Prior to the work presented in Chapter 4, it was typically assumed only epochs where the source lightcurve was above some flux threshold were relevant for the integration (e.g. Sugerman, 2003). However, we show in Chapter 4 that the relative contributions in a LE spectrum depend on the scattering dust properties as well as the specifics of the observation. We show the inclination of the scattering dust, the location of the spectroscopic slit, and the seeing conditions are all *measurable* properties which can have a significant impact on the LE spectrum. We also show the non-measurable property, the width of the scattering dust filament, can be determined by modelling the LE flux profile as it appears on the sky. We therefore provide a direct path between observing LEs on the sky and determining the relative contributions of epochs in an observed LE spectrum.

The analysis of 14 LE spectra from a well-known source event, SN 1987A, enabled us to perform the first detailed test of LE spectroscopy observations. Chapter 4 and the first half of Chapter 5 provide a foundation for future LE spectroscopy observations. Most importantly for the field, LE spectra can be obtained for more exotic objects in the future with confidence that the technique is sound. The recent detection of LEs from η Car's 19$^{\text{th}}$-century "Great Eruption" (Rest et al., 2012) is an example where insight gained through these thesis contributions allowed for the interpretation and analysis of LEs of that event.

SN asymmetries are thought to play a key role in unearthing the explosion mechanism of core-collapse SNe. Chapters 5 and 6 demonstrate a direct observational tool for observing such asymmetries: 3D LE spectroscopy. Multiple LEs provide multiple viewing angles onto the same astronomical source, allowing for direct tests of asymmetry. For SN 1987A, we used this novel technique to discover early-epoch asymmetries in the explosion that appear to be correlated with the current 25-year-old expanding ejecta. Together with previous observations, a causally-connected picture of SN 1987A has emerged. The geometry of early polarization observations, the "mystery spots" detected in the first 50 days, heavy element mixing in the first few hundred days, the 25-year-old remnant, and the inner circumstellar ring all show roughly the same orientation in position angle, are blueshifted in the north, and redshifted in the south. The common orientation of the asymmetry signatures is not correlated with the rotation axis of the presumed progenitor system, ruling out many jet-driven models which would congregate heavy elements towards the poles of the rotation axis. Future modeling of the SN 1987A LE spectra could further constrain the geometry and implied velocities for early epochs of SN 1987A, allowing for direct comparison between explosion models.

In the case of Cas A, we discovered a velocity asymmetry in LE spectra that probe the first ~ 100 days of the explosion. We found a ~ 4000 km s^{-1} blueshift in He I $\lambda5876$ and Hα lines in only one LE line of sight, probing the north-west ejecta. Due to the contributions from Chapters 4 and 5, we were able to isolate the asymmetries to the explosion itself after taking into account the effects of LE scattering. We found the line of sight corresponding to the asymmetry to be roughly aligned with a Fe-rich outflow in the remnant ejecta, and roughly oppositely aligned with the motion of the compact remnant. An inherently asymmetric explanation for Cas A then emerged: the kick of the compact remnant, the excess ejecta velocity, and the orientation of bipolar Fe-rich outflows all appear to share a roughly north-west to south-east axis. The remnant also contains a prominent axis from north-east to south-west containing

Si-rich jet-like outflows. Our results are consistent with the Fe-rich axis representing the primary explosion axis.

Both asymmetry detections from SN 1987A and Cas A contribute significantly to the current understanding of these famous objects. However, together they show there appears to be a direct link between the explosion mechanism, the observed explosion itself, and the observed SNR for core-collapse SNe. This is a non-trivial discovery. Many different fluid instabilities are at work at very different spatial scales from the explosion in the core, to the propagation out to the stellar envelope, to the evolution into a SNR. Our observations appear to directly link Fe-rich asymmetries in the SNRs with early-epoch explosion asymmetries.

7.2 The Future of Scattered Light Echoes in Astronomy

Since a scattered LE was first used to type a historical SN by Rest et al. (2008a), the field of targeted LE spectroscopy has accelerated forward and shows no signs of slowing down. Below we highlight scientific goals that should be achievable in LE spectroscopy in the upcoming years.

Discovering LEs from Galactic SNe LEs from Kepler's SN (SN 1604) have yet to be discovered. Given that LEs have been observed for Cas A and Tycho, two SNRs with similar ages, there is no reason to suggest Kepler LEs will not be discovered. Thought to be a Type Ia SN with circumstellar interaction (Reynolds et al., 2007), LEs of Kepler's SN would provide valuable insight into the progenitor systems of Type Ia SNe. Surveys are ongoing to detect LEs from three remaining galactic SNe, SN 1006, SN 1054 (Crab), and SN 1181, although they are all significantly older than any previously discovered LE sources. All else being equal, LE brightness scales as $1/\mathrm{age}^2$, making LEs from older sources more difficult to detect. Nonetheless, discovery of LEs from the Crab SN offers scientific interest beyond any previously detected LE. It would mark the first LE discovery from a hydrogen-rich core-collapse SN (Chevalier, 1977). Finally, the technique of 3D LE spectroscopy would be invaluable for any source with more than one detected LE. Since multiple LEs exist for Tycho (Rest et al., 2008b; Krause et al., 2008b), an asymmetry study of the Type Ia SN similar to Chapter 5 and 6 should be possible. Additional LE spectra of Cas A could further constrain the nature of the explosion in the south-west direction.

Discovering LEs from Exotic Galactic Sources Spectroscopy of scattered LEs from a non-SN source was first performed recently by Rest et al. (2012), observing η Car's 19th-century "Great Eruption" with modern instruments. During this time η Car became the second brightest star in the sky and ejected more than $10M_\odot$ of material; an outburst with $\sim$ 10% of the energy of a traditional core-collapse SN (Smith et al., 2003; Smith, 2008). Yet the star did not explode. Acting as "SN impostors," these giant eruptions from luminous blue variables (LBVs) are rare, and the mechanism which drives them is not well understood. Rest et al. (2012) found the spectral type of η Car's "Great Eruption" was cooler than other extragalactic "SN impostors," even though η Car is considered the prototypical source for these kinds of outbursts. The 17th-century eruption of P Cygni, the only other galactic LBV known to have undergone such an eruption, is thought to be driven by a similar mechanism as η Car (Smith & Hartigan, 2006). The discovery of LEs from P Cygni's giant eruption, as well as future 3D LE spectroscopy of both sources, will undoubtedly help illuminate the nature of these "SN impostors."

Obtaining Time-Series Spectra of SNe As discussed in Sections 4.6.2 and 4.6.3, if a dust filament is favorably inclined, it acts to stretch out the source lightcurve on the sky. If the filament is thin and the seeing is excellent (i.e. HST-like), the lightcurve is minimally convolved and the source epochs are preserved as a function of distance across the sky. That is to say, the LE profile on the sky preserves the shape of the source lightcurve. In the case of core-collapse SNe, the shock breakout in the lightcurve could be detected using LE photometry, leading to constraints on the radius of the progenitor star. Under these conditions a LE spectrum probes $\sim 10 - 20$ days, rather than the > 100 days for typical dust conditions. Placing a spectroscopic slit *tangential* to the LE arc allows multiple spectra to be extracted with different slit offsets. LE spectroscopy as a function of time is therefore possible, with spectra probing photospheric pre-maximum, maximum, and late nebular epochs individually. The prospects of LE spectroscopy are tantalizing: spectra as a function of both *time* and *viewing angle* for a single astronomical source, hundreds of years after its light has faded from view. As the number of LEs discovered increases, this technique should be realized with HST within the next five years.

Shedding Light on Type Ia SN Progenitors Asymmetry observations for Type Ia SNe have recently provided insight into the explosion mechanism itself, as described in Section 2.6.2 above. Similar asymmetry studies in the future could provide insight into the unknown progenitor systems of these explosions. Both theoretical and observational work has already begun (e.g. Kasen, 2010; Chomiuk et al., 2012), but the field is still young. Known LEs exist for the following historical Type Ia SNe: Tycho (Galactic; Rest et al., 2008b; Krause et al., 2008b), SNR 0509-67.5 (LMC; Rest et al., 2008a), and SNR 0519-69.0 (LMC; Rest et al., 2008a). SNR 0509-67.5 is claimed to be due to a double-degenerate progenitor system based on a recent HST search for ex-companion stars (Schaefer & Pagnotta, 2012). A similar study on SNR 0519-69.0 found the progenitor system is either double-degenerate or a single-degenerate supersoft X-ray source (Edwards et al., 2012). For Tycho, the surviving ex-companion in a single-degenerate model may have been found (Ruiz-Lapuente et al., 2004; González Hernández et al., 2009; Lu et al., 2011). The progenitor system may not be common for all Type Ia SNe (Sternberg et al., 2011; Foley et al., 2012). These three historical sources represent a rare class of Type Ia SNe where the progenitor type may be *known*, if not now, in the future with deeper observations providing further constraints. A comparison of LE spectroscopy between these SNe, as well as asymmetry studies through 3D LE spectroscopy, offers the chance of linking spectroscopic signatures in the explosion with the progenitor system for Type Ia SNe.

Creating Detection Algorithms The current method for detecting LEs begs for an automated process. The detection of ancient LEs by our group is based on ongoing synoptic surveys on 4m-class telescopes. Our automated pipeline provides difference images which are viewed by eye to search for candidate LEs: diffuse, transient flux that (ideally) is detected in both images and thus has an apparent motion on the sky. In practice, it is extremely difficult to distinguish between a LE detection and scattered light from telescope optics. The problem is exacerbated when surveying for LEs near the galactic plane. Many bright stars saturate the CCD, resulting in imperfect image subtraction with an abundance of stray light. In searching for LEs, our group has combed through many tens of thousands of difference images by eye. This type of effort is not sustainable, especially considering the wealth of difference images that will be made available by upcoming synoptic surveys such as PanSTARRS and LSST. However, for the reasons stated above, traditional transient detection algorithms used for SNe or strong lensing are not adequate to rule out the many false-positive flux signatures in difference images. Future progress in this area will be critical if we desire real-time detection pipelines for scattered LEs in the upcoming era of synoptic surveys.

Towards Improved Observing Strategies Our group's current observing strategy is inefficient in that it is essentially random. Field choices are typically made by randomly selecting from an annulus on the sky, representing a range in source-to-LE distances along the line of sight. Previous attempts by our group at probability-based field selection (using, for example, dust distribution maps) have been unsuccessful (Oaster, 2008). There is presumably an observing strategy that takes into account dust concentration, scattering efficiency, and source-to-LE distances which can improve on random field selections, even if previous attempts were unsuccessful. Such a strategy warrants further pursuit. Observing strategies based on detecting the $\sim 90^\circ$ maximum-polarization ring have also been proposed (e.g. Sparks, 1994; Maslov, 2000). Romaniello et al. (2005) used this technique to search for LEs in the nearby, face-on spiral galaxy M83, but no LEs were detected. Krause et al. (2008a) detected a scattered LE from Cas A by following up on a successful infrared LE detection, but the correlation between infrared LEs and scattered optical LEs is currently unclear.

Detecting LEs from Type II SNe Using Narrowband Filters Multi-epoch difference imaging is currently used to detect scattered LEs from ancient sources. For most galactic sources, epoch spacing on the order of months is usually sufficient to resolve the apparent motion. Although surface brightness is independent of distance, the apparent motions of LEs scale inversely with distance. Therefore, for sources in the Local Group of galaxies, many years are required to resolve the motion. One detection strategy yet to be utilized, that does not require difference imaging, is to search for high-velocity Hα emission from Type II SNe using narrowband filters. The strategy would employ a custom filter which includes broad, high-velocity Hα emission from the P Cygni profile, yet masks the narrow, zero-velocity emission lines of H$\alpha\lambda$6563, [N II]λ6548, and [N II]λ6585. This method could allow the detection of LEs from galactic Type II SNe using deep, single-epoch photometry. LEs from ancient, hydrogen-rich, superluminous SNe may also be detectable within the Local Group with this strategy. Superluminous SNe are ~ 100 times brighter than their traditional counterparts, while the physical origin of these extremely luminous events is unclear (Quimby et al., 2011).

Bibliography

Chevalier, R. A. 1977, in Astrophysics and Space Science Library, Vol. 66, Supernovae, ed. D. N. Schramm, 53

Chomiuk, L. and Soderberg, A. M. and Moe, M. and Chevalier, R. A. and Rupen, M. P. and Badenes, C. and Margutti, R. and Fransson, C. and Fong, W.-f. and Dittmann, J. A. 2012, ApJ, 750, 164

Edwards, Z. I. and Pagnotta, A. and Schaefer, B. E. 2012, ApJ, 747, L19

Foley, R. J. and Simon, J. D. and Burns, C. R. and Gal-Yam, A. and Hamuy, M. and Kirshner, R. P. and Morrell, N. I. and Phillips, M. M. and Shields, G. A. and Sternberg, A. 2012, ApJ, 752, 101

González Hernández, J. I. and Ruiz-Lapuente, P. and Filippenko, A. V. and Foley, R. J. and Gal-Yam, A. and Simon, J. D. 2009, ApJ, 691, 1

Kasen, D. 2010, ApJ, 708, 1025

Krause, O. and Birkmann, S. M. and Usuda, T. and Hattori, T. and Goto, M. and Rieke, G. H. and Misselt, K. A. 2008a, Science, 320, 1195

Krause, O. and Tanaka, M. and Usuda, T. and Hattori, T. and Goto, M. and Birkmann, S. and Nomoto, K. 2008b, Nature, 456, 617

Lu, F. J. and Wang, Q. D. and Ge, M. Y. and Qu, J. L. and Yang, X. J. and Zheng, S. J. and Chen, Y. 2011, ApJ, 732, 11

Maslov, I. A. 2000, Astronomy Letters, 26, 428

Oaster, L. 2008, Master's thesis, McMaster University, Canada

Quimby, R. M. and Kulkarni, S. R. and Kasliwal, M. M. and Gal-Yam, A. and Arcavi, I. and Sullivan, M. and Nugent, P. and Thomas, R. and Howell, D. A. and Nakar, E. and Bildsten, L. and Theissen, C. and Law, N. M. and Dekany, R. and Rahmer, G. and Hale, D. and Smith, R. and Ofek, E. O. and Zolkower, J. and Velur, V. and Walters, R. and Henning, J. and Bui, K. and McKenna, D. and Poznanski, D. and Cenko, S. B. and Levitan, D. 2011, Nature, 474, 487

Rest, A. and Matheson, T. and Blondin, S. and Bergmann, M. and Welch, D. L. and Suntzeff, N. B. and Smith, R. C. and Olsen, K. and Prieto, J. L. and Garg, A. and Challis, P. and Stubbs, C. and Hicken, M. and Modjaz, M. and Wood-Vasey, W. M. and Zenteno, A. and Damke, G. and Newman, A. and Huber, M. and Cook, K. H. and Nikolaev, S. and Becker, A. C. and Miceli, A. and Covarrubias, R. and Morelli, L. and Pignata, G. and Clocchiatti, A. and Minniti, D. and Foley, R. J. 2008a, ApJ, 680, 1137

Rest, A. and Prieto, J. L. and Walborn, N. R. and Smith, N. and Bianco, F. B. and Chornock, R. and Welch, D. L. and Howell, D. A. and Huber, M. E. and Foley, R. J. and Fong, W. and Sinnott, B. and Bond, H. E. and Smith, R. C. and Toledo, I. and Minniti, D. and Mandel, K. 2012, Nature, 482, 375

Rest, A. and Welch, D. L. and Suntzeff, N. B. and Oaster, L. and Lanning, H. and Olsen, K. and Smith, R. C. and Becker, A. C. and Bergmann, M. and Challis, P. and Clocchiatti, A. and Cook, K. H. and Damke, G. and Garg, A. and Huber, M. E. and Matheson, T. and Minniti, D. and Prieto, J. L. and Wood-Vasey, W. M. 2008b, ApJ, 681, L81

Reynolds, S. P. and Borkowski, K. J. and Hwang, U. and Hughes, J. P. and Badenes, C. and Laming, J. M. and Blondin, J. M. 2007, ApJ, 668, L135

Romaniello, M. and Patat, F. and Panagia, N. and Sparks, W. B. and Gilmozzi, R. and Spyromilio, J. 2005, ApJ, 629, 250

Ruiz-Lapuente, P. and Comeron, F. and Méndez, J. and Canal, R. and Smartt, S. J. and Filippenko, A. V. and Kurucz, R. L. and Chornock, R. and Foley, R. J. and Stanishev, V. and Ibata, R. 2004, Nature, 431, 1069

Schaefer, B. E. and Pagnotta, A. 2012, Nature, 481, 164

Smith, N. 2008, Nature, 455, 201

Smith, N. and Davidson, K. and Gull, T. R. and Ishibashi, K. and Hillier, D. J. 2003, ApJ, 586, 432

Smith, N. and Hartigan, P. 2006, ApJ, 638, 1045

Sparks, W. B. 1994, ApJ, 433, 19

Sternberg, A. and Gal-Yam, A. and Simon, J. D. and Leonard, D. C. and Quimby, R. M. and Phillips, M. M. and Morrell, N. and Thompson, I. B. and Ivans, I. and Marshall, J. L. and Filippenko, A. V. and Marcy, G. W. and Bloom, J. S. and Patat, F. and Foley, R. J. and Yong, D. and Penprase, B. E. and Beeler, D. J. and Allende Prieto, C. and Stringfellow, G. S. 2011, Science, 333, 856

Sugerman, B. E. K. 2003, AJ, 126, 1939